Universitat Politècnica de València
Departamento de Máquinas y Motores Térmicos

Doctoral Thesis

Development of a test rig for the study of the atomization and combustion of a spray flame in an atmospheric annular spray burner at lean conditions

Presented by:
Santiago Cardona Vargas

Supervised by:
Dr. Jaime Gimeno García

in fulfillment of the requirements for the degree of
Doctor of Philosophy
Valencia, November 2021

Ph.D. Thesis

DEVELOPMENT OF A TEST RIG FOR THE STUDY OF THE ATOMIZATION AND COMBUSTION OF A SPRAY FLAME IN AN ATMOSPHERIC ANNULAR SPRAY BURNER AT LEAN CONDITIONS

Written by: Mr. Santiago Cardona Vargas
Supervised by: Dr. Jaime Gimeno García

Examination committee:

Chairman: Dr. José María García Oliver
Secretary: Dr. Octavio Armas Vergel
Member: Dr. Michele Bardi

Reviewing board:

Dr. Michele Bardi
Dr. María de los Reyes García Cabreras
Dr. Walter Martín Vera Tudela Fajardo

Valencia, November 2021

Abstract

The combustion process in spray flames is a highly complex multi-phase phenomenon that is still not completely understood since it involves several simultaneous events, such as atomization, vaporization, and chemical kinetics. Over the years, researchers have studied the combustion in spray flames thoroughly, in order to understand the fundamental processes as key to reduce pollutant emissions and improve the efficiency of aircraft propulsion. In recent years, the evolution in both injection and combustion technology has allowed to improve the spray mixing process and engine efficiency and hence, reducing pollutant emissions. Therefore, different configurations of injector type and air distribution inside the combustion chamber have proved capable of reducing fuel consumption, as well as emissions of nitrogen oxides and soot without affecting the engine performance.

This thesis provides an experimental methodology to study the effects of co-flow conditions, fuel mass flow rate, fuel type and air outlet diameter at the burner exit on the atomization and combustion behavior of the spray flame produced on an annular spray burner under lean conditions.

The characterization of the liquid spray without combustion was carried out using two different optical techniques. On the one hand, particle image velocimetry (PIV) was used to characterize the global velocity fields of the spray, evaluating the effect of varying the air co-flow conditions, fuel mass flow rate, fuel type and the air outlet diameter. On the other hand, Microscopic diffused back-illumination (MDBI) to measure the size and droplet velocity at a field of view close to the injector tip and again evaluating the effect of varying the parameters previously mentioned on the characteristics of the droplet. The results exhibited that both droplet size and droplet velocity are mainly controlled by the fuel type and fuel mass flow rate (injection pressure). Nevertheless, the variation of the co-flow velocity did not show a significant effect on droplet characteristics (size and velocity), which is likely due to the fact that the field of view of the Microscopic diffused back-illumination technique was located very close to the injector tip. Additionally, by increasing the co-flow temperature, it was observed that the mean droplet size decreased, which is caused by the fuel evaporation process. Finally, the variations in the droplet size and velocity profiles when varying the air outlet diameter were related to the velocity variation when modifying the cross-sectional area at the burner outlet, which affects the evaporation and drag of the drops.

On the spray development in reactive conditions, it was investigated in the operating conditions that promote stabilized flames, using three different optical techniques, all of which were triggered simultaneously. The light extinction

was used to determine the optical thickness through the soot cloud. In addition, OH* chemiluminescence and the Microscopic diffused back-illumination techniques were employed to measure the flame lift-off height and droplet characteristics, respectively. The results exhibited that the co-flow velocity, co-flow temperature and fuel type strongly influence the flame lift-off height. While in the soot formation the most influential parameters were the co-flow speed and the type of fuel. Additionally, thanks to the large number of operating conditions tested, experimental correlations, considering the parameters evaluated throughout the experiments, were calculated. These correlations make it possible to forecast the flame lift-off height trend. Regarding the results of the droplet evaporation, it was observed that the initial droplet sizes and the fuel properties control the droplet evaporation process. n-Dodecane fuel is the least volatile and also exhibited a larger initial droplet size and thus, the droplets took more time to evaporate than the other two fuels, resulting in a longer flame lift-off height and likewise higher soot formation by its greater tendency to form soot. Contrary, n-Heptane droplets evaporated faster, resulting in a shorter flame lift-off height and also less soot formation. Finally, n-Decane showed intermediate results for droplet evaporation, flame lift-off height, and soot formation.

Resumen

El proceso de combustión en llamas de difusión de combustible atomizado es un fenómeno multifásico altamente complejo que a día de hoy no se comprende en su totalidad, ya que involucra varios eventos simultáneos, como atomización, vaporización y cinética química. A lo largo de los años, los investigadores han estudiado a fondo la combustión en llamas de combustibles líquidos, con el fin de comprender los procesos fundamentales como clave para reducir las emisiones contaminantes y mejorar la eficiencia de la propulsión de las aeronaves. En los últimos años, la evolución tanto en la tecnología de inyección como en la de combustión ha permitido mejorar el proceso de mezcla por aspersión y la eficiencia del motor y, por tanto, reducir las emisiones contaminantes. Por lo que, diferentes configuraciones de tipo de inyector y distribución de aire dentro de la cámara de combustión, han demostrado ser capaces de reducir el consumo de combustible, así como las emisiones de óxidos de nitrógeno y hollín sin afectar el rendimiento del motor.

Esta tesis proporciona una metodología experimental para estudiar los efectos de las condiciones de co-flujo, el caudal másico de combustible, el tipo de combustible y el diámetro de salida de aire a la salida del quemador sobre el comportamiento de la atomización y la combustión de la llama producida en un quemador de combustible líquido atomizado en una configuración anular bajo condiciones de operación pobres.

La caracterización del chorro sin combustión se realizó mediante dos técnicas ópticas diferentes. Por un lado, se utilizó velocimetría de imagen de partículas (PIV) para caracterizar los campos de velocidad global del espray, evaluando los efectos de variar las condiciones de co-flujo de aire, caudal másico de combustible, tipo de combustible y diámetro de salida de aire. Por otro lado, retroiluminación microscópica difusa (MDBI) para medir el tamaño y la velocidad de las gotas en un campo de visión cercano a la punta del inyector y evaluando nuevamente el efecto de variar los parámetros mencionados previamente sobre las características de la gota. Los resultados mostraron que ambos, el tamaño de las gotas y la velocidad de las gotas están controladas principalmente por el tipo de combustible y el caudal másico de combustible (presión de inyección). Sin embargo, la variación de la velocidad de co-flujo no mostró un efecto significativo en las características de las gotas (tamaño y velocidad), lo que probablemente se deba a que el campo de visión de la técnica de retroiluminación difusa microscópica se ubicó muy cerca de la punta del inyector. Adicionalmente, al incrementar la temperatura de co-flujo se observó que el diámetro promedio de gota disminuía, lo cual es causado por el proceso de evaporación del combustible. Finalmente, las variaciones en los perfiles

de tamaño y velocidad de las gotas al variar el diámetro de salida de aire se relacionaron con la variación de la velocidad al modificar el área transversal a la salida del quemador, lo que afectaba la evaporación y el arrastre de las gotas.

Sobre el desarrollo de la llama en condiciones reactivas, se investigó en las condiciones de operación que permitían conseguir una llama estabilizada, utilizando tres técnicas ópticas diferentes, las cuales se activaron simultáneamente. La extinción de luz difusa se utilizó para determinar el espesor óptico de la nube de hollín. Además, se emplearon las técnicas de quimioluminiscencia OH* y de retroiluminación difusa microscópica para medir la altura de despegue de la llama y las características de las gotas, respectivamente. Los resultados mostraron que la velocidad del co-flujo, temperatura del co-flujo y el tipo de combustible influyen fuertemente en la altura de despegue de la llama. Mientras que en la formación hollín de los parámetros más influyentes fueron la velocidad del co-flujo y el tipo de combustible. Adicionalmente, gracias a la gran cantidad de condiciones de operación probadas, se calcularon correlaciones experimentales, considerando los parámetros evaluados a lo largo de los experimentos. Estas correlaciones permiten pronosticar la tendencia de la longitud de despegue de la llama. Con respecto a los resultados de la evaporación de las gotas, se observó que el tamaño de las gotas iniciales y las propiedades del combustible controlan el proceso de evaporación de las gotas. El combustible n-Dodecano es el menos volátil y también exhibió un tamaño de gota inicial más grande y, por lo tanto, las gotas tardaron más en evaporarse que los otros dos combustibles, lo que resultó en una mayor longitud de despegue de la llama y también una mayor formación de hollín debido a su mayor tendencia a formar hollín. Por el contrario, las gotas de n-Heptano se evaporaron más rápido, lo que resultó en una altura de despegue de la llama más corta y también en una menor formación de hollín. Finalmente, el combustible n-Decano mostró resultados intermedios para la evaporación de gotas, la altura de despegue de la llama y la formación de hollín.

Resum

El procés de combustió en flames de difusió de combustible atomitzat és un fenomen multifásico altament complex que a hores d'ara no es comprén en la seua totalitat, ja que involucra diversos esdeveniments simultanis, com a atomització, vaporització i cinètica química. Al llarg dels anys, els investigadors han estudiat a fons la combustió en flames de combustibles líquids, a fi de comprendre els processos fonamentals com a clau per a reduir les emissions contaminants i millorar l'eficiència de la propulsió de les aeronaus. En els últims anys, l'evolució tant en la tecnologia d'injecció com en la de combustió ha permés millorar el procés de mescla per aspersió i l'eficiència del motor i, per tant, reduir les emissions contaminants. Pel que, diferents configuracions de tipus d'injector i distribució d'aire dins de la cambra de combustió, han demostrat ser capaços de reduir el consum de combustible, així com les emissions d'òxids de nitrogen i sutja sense afectar el rendiment del motor.

Esta tesi proporciona una metodologia experimental per a estudiar els efectes de les condicions de co-flux, el cabal màssic de combustible, el tipus de combustible i el diàmetre d'eixida d'aire a l'eixida del cremador sobre el comportament de l'atomització i la combustió de la flama produïda en un cremador de combustible líquid atomitzat en una configuració anul·lar baix condicions d'operació pobra.

La caracterització del doll sense combustió es va realitzar per mitjà de dos tècniques òptiques diferents. D'una banda, es va utilitzar velocimetría d'imatge de partícules (PIV) per a caracteritzar els camps de velocitat global de l'espray, avaluant els efectes de variar les condicions de co-flux d'aire, cabal màssic de combustible, tipus de combustible i diàmetre d'eixida d'aire. D'altra banda, retroil·luminació microscòpica difusa (MDBI) per a mesurar la grandària i la velocitat de les gotes en un camp de visió pròxim a la punta de l'injector i avaluant novament l'efecte de variar els paràmetres mencionats prèviament sobre les característiques de la gota. Els resultats van mostrar que ambdós, la grandària de les gotes i la velocitat de les gotes estan controlades principalment pel tipus de combustible i el cabal màssic de combustible (pressió d'injecció). No obstant això, la variació de la velocitat de co-flux no va mostrar un efecte significatiu en les característiques de les gotes (grandària i velocitat), la qual cosa probablement se dega al fet que el camp de visió de la tècnica de retroil·luminació difusa microscòpica es va ubicar molt prop de la punta de l'injector. Addicionalment, a l'incrementar la temperatura de co-flux es va observar que el diàmetre mitjana de gota disminuïa, la qual cosa és causat pel procés d'evaporació del combustible. Finalment, les variacions en els perfils de grandària i velocitat de les gotes al variar el diàmetre

d'eixida d'aire es van relacionar amb la variació de la velocitat al modificar l'àrea transversal a l'eixida del cremador, la qual cosa afectava l'evaporació i l'arrossegament de les gotes.

Sobre el desenrotllament de la flama en condicions reactives, es va investigar en les condicions d'operació que permetien aconseguir una flama estabilitzada, utilitzant tres tècniques òptiques diferents, les quals es van activar simultàniament. L'extinció de llum difusa es va utilitzar per a determinar la grossària òptica del núvol de sutja. A més, es van emprar les tècniques de quimioluminiscencia OH* i de retroil·luminació difusa microscòpica per a mesurar l'altura d'envol de la flama i les característiques de les gotes, respectivament. Els resultats van mostrar que la velocitat del co-flux, temperatura del co-flux i el tipus de combustible influïxen fortament en l'altura d'envol de la flama. Mentres que en la formació sutja dels paràmetres més influents van ser la velocitat del co-flux i el tipus de combustible. Addicionalment, gràcies a la gran quantitat de condicions d'operació provades, es van calcular correlacions experimentals, considerant els paràmetres avaluats al llarg dels experiments. Estes correlacions permeten pronosticar la tendència de la longitud d'envol de la flama. Respecte als resultats de l'evaporació de les gotes, es va observar que la grandària de les gotes inicials i les propietats del combustible controlen el procés d'evaporació de les gotes. El combustible n-Dodecano és el menys volàtil i també va exhibir una grandària de gota inicial més gran i, per tant, les gotes van tardar més a evaporar-se que els altres dos combustibles, la qual cosa va resultar en una major longitud d'envol de la flama i també una major formació de sutja degut a la seua major tendència a formar sutja. Al contrari, les gotes de n-Heptano es van evaporar més ràpid, la qual cosa va resultar en una altura d'envol de la flama més curta i també en una menor formació de sutja. Finalment, el combustible n-Decano va mostrar resultats intermedis per a l'evaporació de gotes, l'altura d'envol de la flama i la formació de sutja.

"An Expert is the person who has made all the mistakes that can be made in a very narrow field"

Niels Bohr

A mi familia...

Es difícil encontrar las palabras para agradecer a todas aquellas personas que han contribuido de manera directa o indirecta en la consecución de esta tesis doctoral.

En primer lugar, me gustaría agradecer a mi tutor Jaime Gimeno, por darme la oportunidad de desarrollar este trabajo y por sus invaluables contribuciones durante todo su desarrollo. Asimismo, me gustaría exaltar su gran paciencia para resolver mis constantes dudas de manera sencilla y siempre aportando ideas para solucionar las dificultades. Me siento afortunado de contar con su ayuda y su simplicidad para enfrentar las dificultades durante el desarrollo de este trabajo. De igual forma, me gustaría agradecerle a Raúl Payri por ser un excelente líder del grupo de inyección del Centro de Investigación CMT-Motores Térmicos, siempre mostrando sus capacidades directivas, y por siempre llevar al equipo al límite de nuestras capacidades y el interés por el bienestar de todos sus integrantes. También me gustaría agradecer a Gaby, José María García-Oliver, Marcos, Pedro, Javi y Joaquín quienes, como los demás, estuvieron allí para brindarme una valiosa ayuda y positividad cuando fue necesario. No podría haber sido parte de un grupo mejor en la CMT y siempre me sentiré afortunado por ello. Además, quiero extender mi agradecimiento a todo el personal de CMT-Motores Térmicos, en especial a Francisco Payri, José María Desantes y Jesús Benajes, por brindarme la oportunidad de formar parte de uno de los institutos más reconocidos en el campo de la investigación de motores.

Con respecto a mis amigos en CMT, me gustaría empezar por mis compañeros de despacho: Jesús, Armando y Cesar por ser unos excelentes compañeros de despacho, por las discusiones científicas, las ayudas y motivación mutuas cuando surgían las dificultades y sobre todo por las risas y los consejos. Asimismo, a: Sebas (por su ayuda y recibimiento a mi llegada a Valencia), Juan Pablo, Dani, Abian, Alberto (por resolver mis constantes dudas y consejos), Mary, Vincenzo, María, Mario, Tomás, Marco, Enrique, Lucas, Rami y Victor por el tiempo compartido tanto en la CMT como fuera de esta. Igualmente Juan David por las discusiones y sus consejos. AdemÂ¡sicionalmente, me gustaría agradecer a José Enrique y Omar, por su ayuda en todo lo relacionado con los temas experimentales y con la puesta a punto de mi instalación, y a José "El torner" por estar siempre dispuesto a echarme una mano con los problemas que surgían de imprevisto. No podría dejar de mencionar a los estudiantes que he tenido la suerte de dirigir y que con su trabajo y apoyo han impulsado el avance de la investigación: Gregg, Jaime, Andrew, Kristopher, Mark, Juan Miguel, María, Carlos.

De igual manera debo mencionar aquí a las personas que me acogieron

y me ayudaron a desarrollar mi estancia de investigación en el Centro de investigación Complexe de Recherche Interprofessionnel en Aérothermochimie (CORIA), Francia: G. Cabot, Félix, B. Renou, Juan Pablo.

Finalmente, agradezco de manera especial a mi familia. A mi novia Carolina Londoño por su apoyo incondicional, por siempre estar en los momentos difíciles que esta etapa conlleva y por entender las largas jornadas de estudio. De manera especial a mis padres por ser figuras ejemplares de compromiso, trabajo, amor y dedicación. A mi hermano Arley por ser un modelo a seguir y por sus valiosos consejos. Y todos los miembros de mi familia, quienes siempre han estado atentos a mis progresos y han contribuido de una u otra manera para llegar donde estoy hoy. A si mismo todas las personas que me he conocido durante esta trayectoria que de alguna forma han contribuido.

Contents

List of Figures

List of Tables

Nomenclature

Acronyms

AF	Air-to-fuel.
APZ	Atmospheric Primary Zone.
CARS	Coherent Anti.Stokes Raman Scattering.
CCD	Charge-coupled device.
CFD	Computational Fluid Dynamics.
CO	Carbon monoxide.
CRZ	Corner Recirculation Zone.
DBI	Diffused back-illumination.
DGV	Doppler global velocimetry.
DLR	German Aerospace Center.
FWHM	Full width at halfmaximum.
GRT	Global Rainbow Refractometry Technique.
H	Hydrogen atom.
ICAO	International civil Aviation Organization.
ICCD	Intensified Charge-Coupled Device.
LDA	Laser Doppler Anemometry.
LDI	Lean-Direct Injection.
LD	Lean-Premixed.
LED	Light-emitting diode.
LEM	Laser extinction method.
LII	Laser-induced incandescence.

LOH   Lift-off height.
LPP   Lean premixed prevaporized.
MDBI   Microscopic diffused back-illumination.
MILD   Moderate or Intense Low-Oxygen Dilution.
NOx   Nitrogen oxides.
OPRs   Overall Pressure Ratios.
PAH   Polycyclic Aromactic Hydrocarbons.
PDA   Phase Doppler Anemometry.
PDPA   Phase Doppler Particle Analyzer.
PID   Proportional-Integral-Derivative.
PIV   Particle Image Velocimetry.
PLIF   Planar laser-induced fluorescence.
PRZ   Primary Recirculation Zone.
RMS   Root Mean Squaret.
RNG   Renormalization Group Theory.
RQL   Rich-burn, quick-quench, lean-burn.
RSM   Reynolds stress model.
SEM   Scanning Electronic Microscope.
SMD   Sauter mean diameter.
TCS   Turbulent Combustion of Sprays.
TEM   Transmission electron microscope.
TRL   Technologies Readiness level.
TSI   Threshold Soot Index.
UHC   Unbunred hydrocarbon.
UV   Ultra violet.
YSI   Yield Soot Index.

Greek symbols

ΔP Pressure difference throughout the nozzle.
Δp Pressure difference (general).
Δu_f Variation of fuel flow velocity.
δ_f Flame thickness.
δ_s Mean inter-droplet distance.
$\delta_{r,f}$ Radius of the flame.
λ_d Fuel conductivity.

λ_{opt}	Optimal wavelength.
$\mathcal{D}$	Binary diffusion coefficient.
μ_l	Dynamic viscosity of the liquid.
ν_l	Kinemactic viscosity of the fuel.
ϕ_{global}	Global equivalence ratio.
ρ	Density (general).
ρ_l	Density of the liquid.
σ_l	Surface tension of the liquid.
τ	Optical thickness.
τ_c	Chemical time scale.
τ_f	Characteristic time for combustion.
τ_t	Integral time scale.
τ_t	Kolmogorov time.
τ_v	Mean evaporation time of drops.
θ	Spray half-angle.
ε	Turbulent dissipation rate.

Latin symbols

$\dot{M}$	Momentum flux.
$\dot{m}$	Mass flow rate.
$\dot{Pr_t}$	Prandtl number.
$\overline{D}_o$	Average outlet diameter.
A	Cross-sectional area at the burner exit.
A_o	Outlet area of the nozzle.
B_i	Biot number.
B_Y	Dimensionless transfer number.
d	Droplet diameter.
d_j	Droplet initial diameter.
D_o	Initial droplet diameter.
d_o	Nozzle orifice diameter.
G_k	Kinectic energy.
h	Heat transfer.
I	Pixel-wise intensity distribution of the current image.
I_0	Pixel-wise intensity distribution of the reference image.
I_f	Pixel-wise intensity distribution of the flame.

I_t	Turbulent intensity.
K	Dimensional extinction coefficient.
K_e	Evaporation constant.
KA	Total amount of soot.
KL	Optical thickness related to soot.
KV	Soot horizontal sheet-of-sight perspective.
L	Path length through the soot cloud.
Oh	Ohnersoge number.
p	Pressure (general).
p_0	Reference pressure.
Re_p	Particle Reynolds number.
S	Seperation parameter.
S_L	Laminar flame speed.
S_N	Swirl number.
S_t	Stoke number.
S_{spray}	Flame propagation speed through quiescent multi-droplet mists.
T	Temperature (general).
t	Time (general).
T_0	Reference temperature.
T_f	Fuel temperature.
$T_{co-flow}$	Co-flow temperature.
u	Velocity (general).
U_L	Velocity liquid film.
U_R	Relative velocity.
u_t	Theoretical discharge velocity.
v_p	Particle velocity.
V_r	Resultant velocity.
$V_{co-flow}$	Co-flow velocity.
$V_{droplet}$	Velocity of droplet ejection.
We	Weber number.
We_c	Critical Weber number.
Da	Damköhler number.
G	Number of group.
X	Droplet diameter.

Chapter 1

Introduction

1.1 General context

The understanding of the combustion in spray flames is an essential factor to control the pollutant emissions generated during the burning of fossil fuels for several power generation and propulsion technologies (industrial and residential furnaces, internal combustion engines and propulsion engines). These applications adversely affect the environment, so that the laws about unhealthy exhaust emissions have become more stringent and their reduction is nowadays one of the main restrictions for the design of the coming generation of the combustion chambers. Therefore, researchers have investigated these processes trying to reduce pollutant emissions through continuous improvements in both combustion processes and combustor design. Additionally, the use and production of sustainable energy is currently a critical issue. Nevertheless, the aviation industry is not an exception in terms of rigorous emissions regulations, due to it uses traditional fossil jet fuel for aircraft propulsion. Since the fuels have to accomplish both physical and chemical requirements demanded by aircraft engines, being almost impossible to replace them safely. The certification of the next propulsion systems utilizing renewable fuels will consequently be difficult. Even though pollutant emissions decrease is essential, it must not affect the reliable operation of the engine. Even so, sustainable aviation fuel (SAF) is on the rise, this type of fuel is produced from sustainable feedstocks and is very similar in its chemistry to the traditional fuel and currently, SAF can be blended at up to 50% with conventional jet fuel and all quality tests are completed as per a traditional jet fuel. As the technology matures, it will

become more efficient and so the expectation is that it will become less costly for customers. Finally, these fuels must guarantee at ground level or high altitude conditions, some critical events may affect engine performance and even leading to the complete extinction of the combustion.Whatever the operating conditions, the aircraft engine must guarantee to ignite or re-ignite the flame in the combustion chamber almost immediately, and safely. The current specifications for the design of aircraft combustion chambers must ensure these safety standards at any adverse conditions. To guarantee these objectives, which are the protection and security of the environment, complete analysis and a significant understanding of the processes that take place in spray flames are necessary.

1.2 Objectives and methodology

Today, to predict and understand the atomization and combustion processes that take place in industrial applications, especially in combustion chambers of aircraft engines, numerical models are increasingly being used. Nevertheless, so that simulations can predict the multiple events that occur during the atomization and burning of liquid fuel, the simulation models must be validated by comparing them to experimental results. Using optical diagnostics in real applications is difficult due to their complex operating conditions. Therefore, it is necessary to develop simplified burner configurations to investigate the mechanisms that occur in combustion chambers, providing an understanding of the interaction between atomization and combustion and other phenomena. Also, to provide an experimental database to help to answer the hard points of the simulations.

In this perspective, this thesis follows the following main objective:

- Perform an experimental investigation in order to improve the understanding of the atomization and combustion processes involved in spray flames produced in an annular spray burner that uses a pressure swirl injector to atomize the fuel that is surrounded by a preheated air co-flow.

Therefore, the following three sub-objectives were developed in order to achieve the main objective:

- Development of a new experimental facility (chapter 4) for the study of the liquid spray flames through different experimental techniques. In such a facility, fundamental studies of atomization and combustion

process in spray flames will carry out in a simplified environment, controlling the surrounding conditions of the flame or the spray. For these studies, different optical techniques will be used simultaneously.

- To study the atomization and combustion process by using different optical and laser techniques, such as PIV, color diffused back-illumination and which results are presented in chapter 6 and chapter 7, respectively. Furthermore, to apply a new optical technique (microscopic diffused back-illumination) to measure the diameter and velocity of the fuel droplets.

- Conduct a wide range of experimental tests to investigate the influence of different parameters on the spray and combustion process, such as co-flow velocity, co-flow temperature, fuel mass flow rate, and air outlet diameter. Furthermore, the experimental campaign will carry out for three hydrocarbons fuels, which were chosen to cover a wide range of physical properties, such as density, viscosity, and surface tension, which influence the atomization (i.e., SMD), along with vapor pressures (P_v) and normal boiling temperatures, which impact the vaporization of the fuel.

To this objective, optical elements, the technologies and facilities available at CMT-Motores Térmicos were employed to investigate several aspects of the atomization and combustion processes. Based on their specific purposes, the experimental measurements performed can be divided into two groups:

- A spray characterization for multiple operating conditions and fuel types, visualizing the droplet properties such as size and velocity.

- A spray flame characterization for multiple operating conditions and fuel types, considering the flame lift-off height, soot formation and also droplet evaporation.

The experimental campaigns to study the effect of the variation of the surrounding condition (i.e., air co-flow velocity and temperature), injection pressure and liquid fuel type on the spray flame first consisted of a spray characterization (without combustion). Then, visualization of both the liquid region and combustion region of the spray flame was carried out simultaneously with microscopic diffused back-illumination and color diffused back-illumination, respectively. In addition, OH* chemiluminescence was applied to characterize the flame lift-off height. Finally, all cameras used in the optical setups were synchronized to record the same atomization event.

1.3   Thesis outline

The thesis is divided into eight chapters, opening with this brief introduction (**chapter 1**), which outlines the overall context and main objectives of the investigation performed.

Chapter 2 introduces an overview of elements employed in the atomization and combustion processes in aero-engine applications, using different combustion technologies in order to reduce the emissions in aircraft engines. The chapter concludes with a summary of the performance matrix for the combustion technologies discussed throughout this section.

Chapter 3 presents a literature review of fundamental concepts of atomization, spray combustion and soot formation, detailing each step of mechanisms present in spray flames, starting with the atomization process of fuel droplets up to the droplet combustion.

In **chapter 4**, a literature review of several test rigs around the world employed to study the atomization and combustion process of spray flames in confined and unconfined configurations was performed. Then the annular spray burner design is introduced, including some examples of the computational fluid dynamics results of non-reacting cold flow conditions. Additionally, different configurations, such as venturi/swirler and confinement/non-confinement, are presented. Finally, the test rig and injection system are described.

Chapter 5 is focused on describing the pressure swirl injector used in this study and its internal geometry measured through two different techniques. Then the annular spray burner configuration used to perform the experiments is presented. Finally, the measurement principles and procedures are described, as well as the optical setups and image processing methodologies.

Chapter 6 is focused on discussing the atomization process results, to analyze the effects of the co-flow conditions, fuel mass flow rate and the fuel type on the spray characteristic in order to understand the interaction between the fuel droplets and co-flow air. The results are given in terms of velocity fields, size and droplet velocity. Finally, a comparison between experimental results and predicted values of SMD calculated through theoretical correlations is introduced.

In **chapter 7**, the results from the combustion study are presented. Results are given in terms of flame lift-off height and soot attenuation by the soot cloud. Additionally, an experimental correlation for flame lift-off height

is introduced. Finally, a flame propagation speed through a quiescent multi-droplet mist was calculated and also the drop lifetime through the d^2 law for various fuels and initial droplet diameters.

Lastly, **chapter 8** provides a summary of the investigation performed and also main conclusions. Furthermore, various future directions are suggested base on experience and knowledge obtained through the development of this work.

Chapter 2

Technical background

2.1   Introduction

An aircraft engine is a complex machine composed of thousands of components and where multiple processes take place to ensure a safe operation of the engine. In this investigation, particularly the processes that occur inside the combustion chamber are of interest, and especially the phenomena associated with liquid fuel atomization. Therefore, the processes involved in the turbine and compressor are not treated in this study. The purpose of the combustion chamber is to create an enclosed space for burning the fuel-air mixture and then transfer the resulting gases to the turbine, i.e., where the potential energy of the fuel is converted into calorific energy. During the last years, the International Civil Aviation Organization (ICAO) has imposed a normative stricter in terms of emissions, forcing the engine manufacturers to optimize the combustor design and to reduce the specific fuel consumption of the aircraft engine. Nevertheless, there is a constant demand to continue reducing pollutant emissions. For these reasons, it is necessary to understand the phenomena which are involved during the combustion process. In this section, the multi-physical process occurring in aeronautical combustion is explained. Additionally, a general explanation of the two-phase combustion is introduced, starting from the fuel atomization up to different combustion regimes found in real combustion chambers.

2.2   Aircraft engine operation

The gas turbine engine is basically a heat engine that generates thrust by using air as a working fluid. The air passing through the engine must be accelerated to produce this thrust (i.e. that the air velocity is increased). This velocity increase is obtained as follows: Firstly, the pressure of the air is increased through the compressor, followed by the addition of heat energy at the combustion zone. Finally, kinetic energy is transformed in a high-velocity jet flow. Regardless of the propulsion mode, it must always include the following operating phases: (i) compression, (ii) combustion, and (iii) expansion. In aero-engines, these phases are performed through the following elements, which are depicted in Figure 2.1:

- Air intake.
- Compressor.
- Combustion chamber.
- Turbine.
- Exhaust.
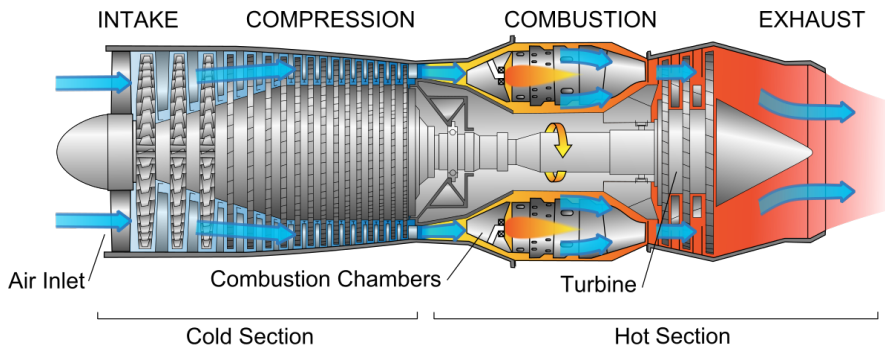
Figure 2.1: Schematic layout of an aero-engine.

In its most basic form, the turbine engine's operating cycle is described by the cycle indicated on the pressure-volume schematic diagram in Figure 2.2. Point A indicates air at atmospheric pressure, which passes through the compressor, increasing its pressure, as shown by line AB. Heat is added to the air from B to C by injecting fuel and burning it at constant pressure, significantly increasing the air volume. There are pressure losses in the combustion chamber, which are represented by the drop between B and C. The gases produced by the combustion process expand in the turbine and a jet pipe back

into the atmosphere, which takes place between Point C and D. Part of the energy from the expansion process of gases is converted into mechanical power through the turbine in this phase of the cycle, while the remainder is expelled to the atmosphere, creating a propelling jet.
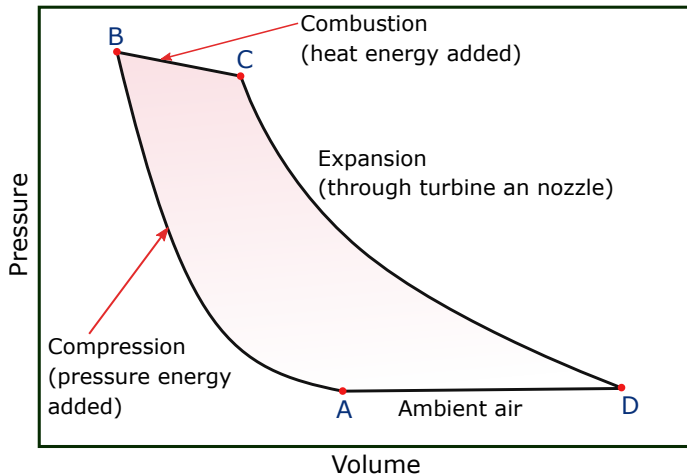
Figure 2.2: Schematic representation of the working cycle of the aircraft engine.

A combustor of a gas turbine must satisfy a variety of requirements, the relative significance of which changes depending on the engine type. Nevertheless, Lefebvre and Ballal [1] listed the fundamental requirements for all kinds of combustors:

- Reliable and quick ignition, regardless of the operating or ambient conditions.
- High-combustion efficiency (i.e., the fuel should be completely burned so that all its chemical energy is liberated as heat).
- Large flame stability limits.
- Low pressure losses.
- Temperature distribution at the engine outlet must be designed to extend the life of several components.
- Low levels of soot and gaseous pollutant emissions.
- Minimization of pressure pulsations and combustion instabilities.
- Dimensions and design must be consistent with the engine envelope.
- Engine design promoting a low cost and easy to manufacture.

- Durability and maintainability.
- Capability to use different types of fuels.

Size and weight are mandatory requirements for aero-engines, but other factors, such as extended operational life and the capacity to use multiple fuels, are more significant for industrial engines. Low pollutant emissions and fuel consumption are critical requirements for whatever type of engine.

2.2.1   Combustor types

The election of a suitable combustor kind and design is mainly determined by the engine design and the limitations of space and weight. According to Lefebvre and Ballal [1], there are two basic types of combustor: annular and tubular. An intermediate combustor between these two types is known as "tuboannular" or "can-annular," which uses numerous equispaced tubular liners within an annular air casing. The three basic combustor geometries are depicted in Figure 2.3.
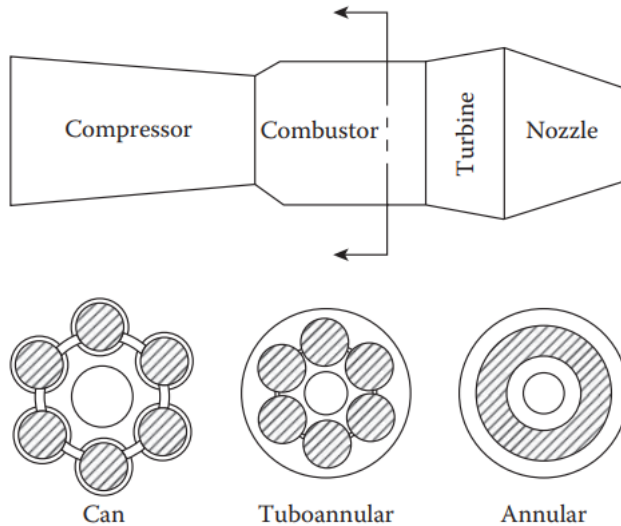
Figure 2.3: Illustration of Can, Tuboannular and Annular combustor types [1].

Tubular

This type of combustor is composed of a cylindrical liner that is concentrically installed inside a cylindrical casing. This type of combustor was used in

the majority of early jet engines and its fundamental advantage is the lower time and resources incurred in its development. Nevertheless, its considerable length and weight limit its employment in aero-engine applications, and its primary use is in industrial units where maintenance and maintenance are essential considerations.

Tuboannular

A tuboannular combustor aims to combine the tubular chamber's mechanical strength and the annular chamber's compactness. However, the necessity for interconnectors (i.e., cross-fire tubes) is a disadvantage found in this type of combustors, which it shares with tubular arrangements. On the other hand, compared with the annular design, it has a significant advantage in that much meaningful chamber development may be achieved with very little air supply, employing only a small portion of the overall chamber including one or more liners. Its disadvantages appear when attempting to establish a desirable and constant airflow distribution; in particular, the configuration of the diffuser can create significant challenges.

Annular

An annular combustor is composed of an annular liner installed concentrically inside an annular covering. Its efficient aerodynamic design results in a compact device, which is a suitable form of a combustion chamber and also presented less pressure loss than other types of combustors. However, its principal disadvantage is the severe buckling load on the outer liner.

2.3   Fuel injection

The jet engine performance seriously depends on the atomization and evaporation processes of the liquid fuel, which are fundamental in the combustion process. Therefore, the injection system needs to deliver the liquid fuel under specific conditions to guarantee engine efficient performance. Additionally, injectors have to provide a high quantity of small droplets since the liquid fuels can not generate enough vapor due to the limitations in fuel volatility. As the droplet size is smaller, the evaporation rate is enhanced. The effect of droplet diameter on ignition performance is considerably important because substantial rises in ignition energy are required to compensate for even small increases in mean droplet diameter. Spray quality also influences the flame stability limits, combustion efficiency and pollutant emission levels [1]. The

extreme operating conditions in jet engines are complex (high flow rates, temperatures and velocities), the design of the injector is more demanding than the basic principle it is based on would suggest. For the atomization of liquid fuels, three main physical concepts are employed according to the application:

- Liquid pressure driven atomization.
- Air driven atomization.
- Rotary atomization.

The first two types are most commonly employed in combustion applications. The diameter and droplet velocity characterize the spray atomized by the injector. The following are the features of an optimal injector [2]:

- Predefined uniform drop diameter and velocity distribution through the spray.

- Capacity to supply effective atomization over a large variety of fuel flow rates and also a fast reaction to variations in this flow rate

- No spray instabilities.

- Minimal of both power demand and obstruction sensitivity.

Two of the most common techniques for precisely dispersing the liquid fuel are to push it through either a tiny perforated disc or a narrow gap between two rings to produce some swirl, dispersion, or evaporation. The fuel must be supplied under high pressure, and in certain circumstances, it must also pass through a pre-injection chamber with fins that provide swirl motion to the fuel jet. The fuel would come out in a continuous, bubble-shaped flow at low injection pressure. As the injection pressure rises, the jet's boundary layer begins to break up, forming what is known as a tulip. Finally, at maximum operational pressure, the fuel jet fragments into many smaller pieces, essentially producing a finely atomized spray zone, shown in Figure 2.4.

2.3.1   Injectors for aircraft engine applications

In aircraft engines, and especially in ones that work under Lean-Direct Injection (LDI) combustion principle, high-quality atomization is required in order to produce quick evaporation of fuel droplets and thus allow an easy mix between fuel and airflow. The fuel atomization needs a force or a physical
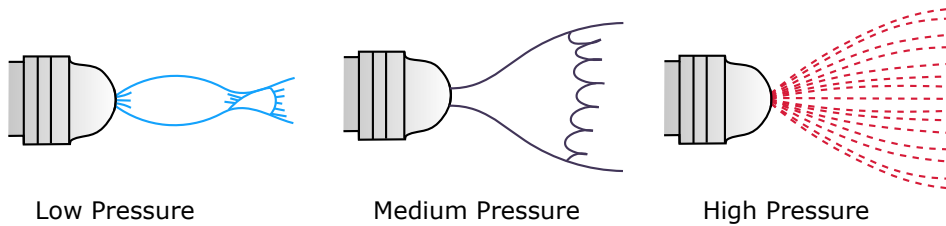
Figure 2.4: Spray patterns as a result of increasing the injection pressure.

interaction, capable of disintegrating the fuel jet into small particles. Therefore, different injectors have been developed in order to meet these technical requirements, which are classified depending on the elementary physical principle implemented to produce this disruptive force. In aircraft systems, two main types of atomizers are used:

- Pressure atomizers.
- Airblast atomizers.

The fuel atomization in these types of atomizers is based on the same working principle: gas-phase and fuel flow interact between them with a high relative velocity, producing strong aerodynamic interactions that yield jet disintegration into drops. In airblast injectors, the fuel jet is exposed to high-velocity airflow, whereas in pressure injectors, a high-velocity fuel jet or sheet is atomized into an inactive medium [3]. Additionally, different types of atomizers have been developed for technological uses (e.g., rotary atomizers, ultrasonic nozzle, electrostatic injectors, and other ones detailed in [4]). In the following, the two main types of atomizers employed in lean burn applications will be explained.

Pressure-swirl atomizer

The working principle of pressure injectors is based on the transformation of the fuel injection pressure into kinetic energy in order to generate a significant relative velocity between the surrounding air and the fuel jet. In addition, the fuel is forced to enter through a specially designed orifice. Several injectors are based on this working principle; one of the most commonly used in the industrial sector is the pressure-swirl atomizer. In this type of injector, a rotatory motion is forced on the fuel, the basic form of this type of injectors is the simplex atomizer (some designs are presented in Figure 2.5) in which the

fuel flow is first introduced axially through inlet ports. It then goes tangentially through tangential channels into a swirl chamber. Finally, the fuel flow is accelerated in the axial direction to pass through the discharge hole exit into the ambient air. The tangential channels have spirally shaped grooves and generate a rotating flow. Axial and swirl velocity components depend on these tangential channels [5]. The swirl chamber length does not affect the spray. Sheet shape and velocity are at most very weakly related to this parameter since the swirl strength decreases with a smaller chamber radius and reduces the cone angle and core radius [6].
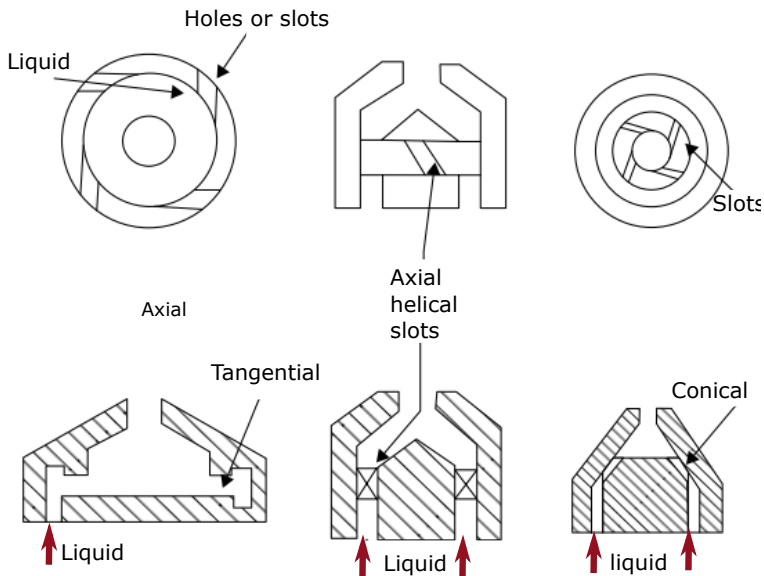
Figure 2.5: Various designs of simplex swirl atomizers [4].

Air-blast atomizer

Different from the pressure atomizers, the airblast injectors use the kinetic energy of the air stream to break-up the liquid jet into drops. *Plain-jet airblast* is considered the most basic type of airblast atomizers. Its working principle is that a plain jet is subjected to a high-velocity airstream that produces a jet disintegration into droplets. However, in aero-engine systems, most of the airblast atomizers are based on the so-called *prefilming airblast* configuration. In these types of atomizers, the fuel is initially injected as a thin continuous

sheet, which evolves through a prefilming surface under influence of a co-flowing air flow. As the liquid film approaches the atomizing edge, it is exposed on both sides to high-velocity air flow that breaks it up into ligaments and then droplets, resulting in very fine atomization. Figure 2.6.a depicts various schematic representations of prefilming airblast atomizers in aircraft engines where the fuel film immediately interacts with swirled air-stream implemented for the flame stabilization.
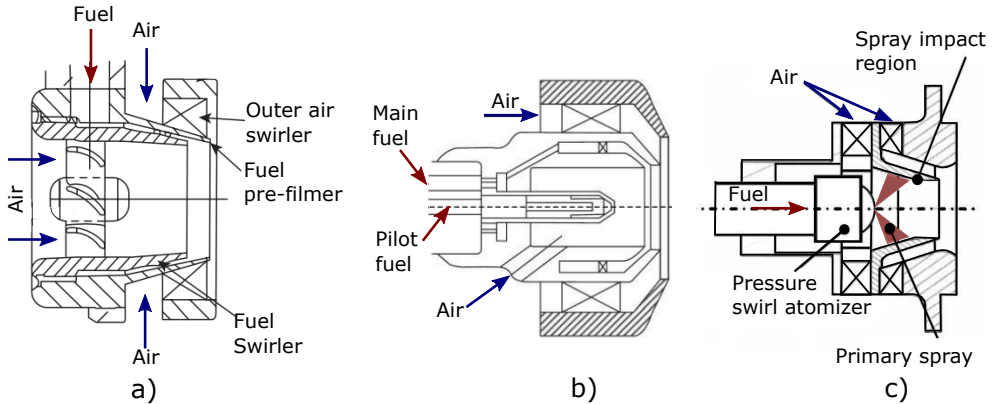
Figure 2.6: Various designs of airblast atomizers. a) prefilming airblast atomizer, b) piloted airblast atomizer, c) Impinging airblast. (Taken from [4])

Airblast atomizers have several advantages compared to pressure atomizers, especially in operating conditions at high pressure. The primary advantages include good atomization and slight variation in performance regardless of operating conditions [7]. Consequently, modern lean combustors employ injectors based on airblast atomizers [8]. However, this type of injector has some limitations that arise at engine startup produced likely by the lean blowout and poor atomization quality cause by the low velocity of the air flow [3]. To address these disadvantages, several injection systems employ a pre-filming airblast injector couple with a pressure injector in a configuration so-called *piloted airblast* system [4] (see Figure 2.6.b). For low fuel consumption, the majority of the fuel is injected by the pilot atomizer, but at high loads, the fuel is mostly supplied through the air blast atomizer. Moreover, in some airblast designs, the fuel atomization is created by the impact of drops injected by a pressure injector sometimes called *swirl cup* (see Figure 2.6.c).

2.4   Combustion regimes

In normal operating conditions, the global engine air-to-fuel (AF) ratio varies between 45:1 and 130:1. Kerosene-based fuels burn most efficiently at an AF ratio of around 15:1, and only a small portion of the air entering the combustion chamber is burnt. This is the primary combustion zone, which is depicted in Figure 2.7.
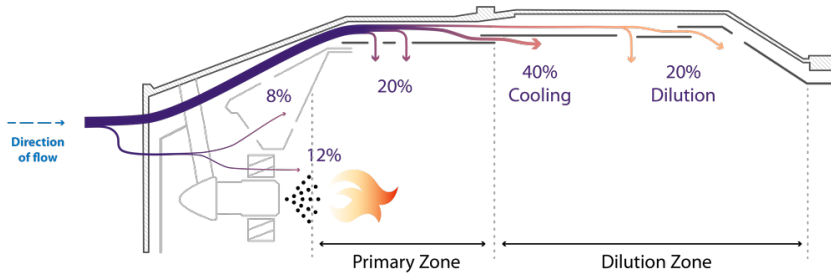
Figure 2.7: Air distribution in the combustion chamber [9].

The primary zone's major role is to anchor the flame and give enough time, turbulence, and temperature to ensure practically complete combustion of the entering fuel-air mix. The significance of the primary-zone airflow pattern in achieving these objectives cannot be emphasized. Various flow patterns are used, but one characteristic that all have in common is the formation of a toroidal flow reversal that entrains and recirculates a part of the burning gases to give continual ignition to the entering fuel and air.

The primary function of the dilution region is to admit the air that remains just after the combustion process and the wall-cooling and to supply an outlet flow with an appropriate temperature distribution to enter the turbine. This temperature distribution is commonly defined in terms of "pattern factor" or "temperature traverse quality." The quantity of air available for dilution is typically between 20 and 40 % of the whole combustor airflow. This air enters the hot gas flow via one or more lines of holes in the liner walls. The size and form of these holes are chosen to enhance air-jet penetration and the following mix with the mainstream. Theoretically, any specified traverse quality may be obtained by either using a large dilution zone or accepting a significant liner pressure-loss factor. In reality, nevertheless, it has been observed that increasing mixing zone length enhances mixedness significantly initially and then at a progressively slower rate. Consequently, the length/diameter ratios of dilution zones all tend to be within a limited range of 1.5 to 1.8 [1].

If the primary-zone temperature exceeds about 2000, dissociation processes will cause substantial quantities of hydrogen (H_2) and carbon monoxide (CO) to emerge in the efflux gases. If these gases are sent immediately to the dilution zone and quickly cooled by the insertion of huge amounts of air, the gas composition will be "frozen," and CO, which is a cause of combustion inefficiency and a pollutant and likewise expelled from the combustor unburned. Reducing the temperature to a medium level by adding small quantities of air promotes soot burnout and enables the burning of CO and any other unburned hydrocarbons (UHC) to continue to completion.

Although all combustion processes involve chemical interactions between the air (oxidizer) and fuels, the specifics of each process differ significantly, hence they must be treated in different ways. In aircraft engines, two main combustion categories can be found [10]:

- non-Premixed combustion is characterized by the separation of the combustion areas of oxidizer and fuel, with combustion taking place at the interface between the two. Different types of burners, in which a fuel jet is atomized into an area of air.

- When combustion takes place in premixed combustion, the oxidizer and fuel are molecularly mixed. In such a situation, the flame separates various zones of unburned and burnt mixes.

In industrial applications, the most advantageous regime is frequently somewhere in the middle, where the oxidizer and fuel are allowed for mixing partially but not completely previously combustion takes place. It is the so-called Partially Premixed Combustion. In real applications, such as aero-engine applications, all combustion regimes can occur simultaneously in the combustion chamber. Additionally, the two-phase combustion process involves an extra complexity regarding the combustion regime. Therefore, it must be thoroughly investigated.

2.5 Combustion technologies

Since the restrictions referred to the emissions are becoming stricter, the aircraft engine manufacturers have developed different combustion technologies for reducing the emissions. The most well-known are the Rich burn, quick Quench-Lean Burn (RQL), Lean Premix Pre-vaporized (LPP), Lean-Direct Injection (LDI) and Multipoint Lean-Direct Injection (MLDI). A short description of these technologies is presented as follow.

2.5.1   Lean premixed prevaporized (LPP)

The working principle of LPP combustors is first evaporating the fuel and then mix it with the airflow to generate a homogeneous mixture previously to enter the combustion zone, resulting in a low equivalence ratio near the lean blowout limit. The decrease in flame temperature and the removal of hot spots from the combustion zone promotes a substantial reduction of NO_x emissions. A schematic representation of a LPP combustor is presented in Figure 2.8. In general, a LPP combustor is composed of three principal stages: fuel atomization, vaporization, and fuel-air mixing in order to achieve both fuel evaporation and fuel-air mixing; the second is for combustion, where the flame is stabilized in the recirculation regions, and the third generally is a conventional dilution zone.
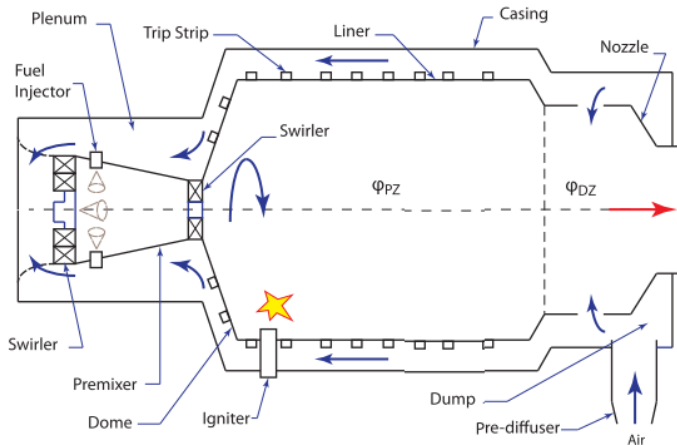
Figure 2.8: Schematic of an LPP combustor [11].

Figure 2.9 illustrated the physics of a typical LPP combustor. Vital features such as the recirculation zones, shear layers, and flame locations shown in the figure are common in this type of combustors. The main flame is stabilized in the layer of mixing while a pilot flame exists in the center, surrounding the Primary Recirculation Zone (PRZ). Also shown are the Lip Recirculation Zone (LRZ) and the Corner Recirculation Zone (CRZ). The main flame is designed to be premixed, and it is believed that the stability criteria is similar to that of a Bunsen flame, as explained by [12].

Generally, aero-engines work at higher overall pressure ratios (OPRs), under these operating conditions, LPP combustion concept has certain operational risks on the engine performance such as auto-ignition of the air-fuel

CRZ = Corner Recirculation Zone
LRZ = Lip Recirculation Zone
PRZ = Primary Recirculation Zone
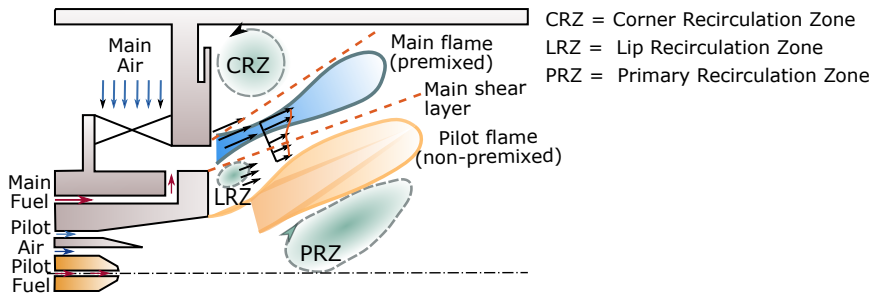
Figure 2.9: Air distribution in a LPP chamber [9].

mixture, narrow stability limits, and flame flashback. However, LPP combustors have been extensively employed in industrial gas turbines since their capacity to generate relatively low NO_x emissions.

2.5.2 Rich-burn, quick-quench, lean-burn (RQL)

The majority of combustors used in modern aircraft engines are based on RQL concept, which is illustrated in Figure 2.10, where combustion starts in a fuel-rich mixture at the primary zone with an equivalence ratio of 1.2-1. In general, the rich burn has two advantages: First, the rich burn produces a large concentration of energetic hydrogen and hydrocarbon radical species, which improves combustion stability. Second, because of the comparatively low flame temperatures and low concentrations of oxygen-containing intermediate species, NO_x generation is reduced. The hot efflux gas resulted from the primary zone has a high concentration of smoke, CO, and UHC that cannot be drained without further processing, according to Samuelsen et al. [13].

The basic characteristics of an RQL combustor are presented in Figure 2.11. The rich zone, as detailed in [14], provides a high degree of resistance to flame out, even maintaining the combustor alight at low power loads while the engine is operating under extremely lean conditions. Furthermore, adequate dilution holes design enables many of the soot produced in a rich zone at high power to be oxidized. The quenching zone is the most challenging section of the combustor because the combustor can reach stoichiometric conditions (which promote the rapid formation of thermal NO_x), being necessary to reduce the time employed by the mix in these zones. The lean-burn section is also responsible for regulating the combustor outlet temperature distribution quality. The typical equivalence ratio in the lean burn is in the range of 0.5-0.7.
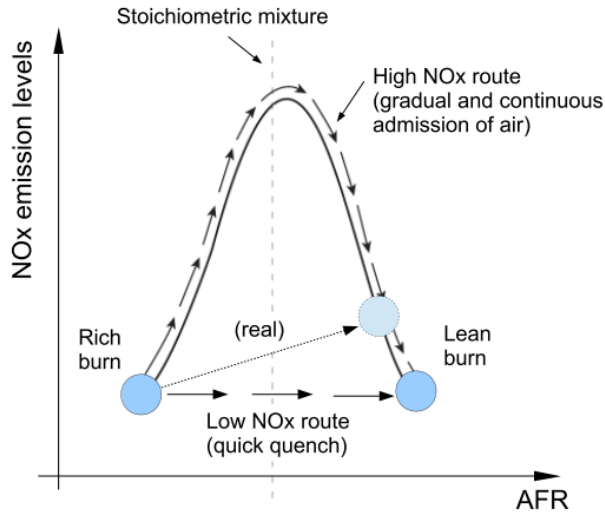
Figure 2.10: Principle of RQL combustion [3].
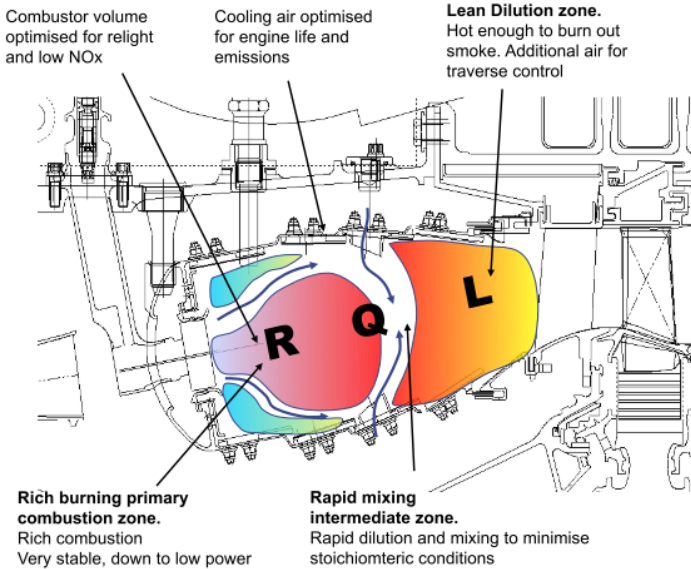
Figure 2.11: Fundamental characteristics of a combustor according to the RQL principle [3].

It is notable to mention that various novel designs, such as the Pratt & Whitney TALON X combustor, have been developed in recent years [15]. In this combustor, the quenching section is characterized by an improved design to improve the mixing process between the dilution air and combustion products derived generated in rich primary region, suggesting a significant potential for reducing NO_x emissions.

2.5.3 Lean-Direct Injection (LDI)

Even though classical RQL technology is widely used in aero-engines applications, it still has some improvement potentials, most of them related to the NO_x reduction targets. Therefore, the development of alternate combustion processes implementing the lean-burn combustion process is inevitable. The most appropriate solution for aero-engines can be LDI technology, which reduces the NO_x emissions considerably and, thus allowing to meet the emissions requirements. As a result, over the last year, the main engine manufacturers have intensified their efforts to investigate this type of technology in order to provide engines that are both safe and efficient.

In LDI combustors, the reduction of nitrogen emissions is achieved by a quick mixing of the fuel with a substantial portion of air in the combustor primary zone. In addition, before entering the combustion zone, the air and fuel must be precisely mixed to prevent the creation of diffusion flames, which occur under stoichiometric conditions. As mentioned in [3], lean combustion was firstly implemented in gas turbines for industrial applications with gaseous fuels. Nevertheless, the use of liquid fuel in aero-engine limits the direct implementation of this technology, due to the complications to form a homogenous mixture. Consequently, modern technologies must be developed to provide precise control of liquid fuel preparation and optimum fuel-air mixing. The main essential aspects of a combustor based on lean combustion technology are presented in Figure 2.12.

The injection system can be considered one of the most important components for the efficient operation of an LDI combustor since it includes the processes of fuel atomization, spray development, and evaporation that are critical to the success and implementation of lean-burn technology. Consequently, an important number of investigations in the lean combustion sector are dedicated to developing sophisticated injector systems capable of controlling the quality of liquid fuel preparation and promoting rapid mixing of fuel and air, enabling the combustion to be shifted toward lean premixed flames.

In LDI systems, approximately 70 % of the air provided by the compressor is employed in the primary zone and is delivered directly through the injection

Advanced injection
configurations to control the
quality of air-fuel mixing and
the characteristics of the
flow in the primary region.

Advanced cooling techiniques
due to the small amount of air
available for wall cooling.

Rich burning pilot zone.
Rich combustion zone generated
by the pilot stage for stable
operation at low power.

**Lean burning primary
combustion zone.**
Lean fuel-air mixture to max power.
Fuel staged out at lower powers.

Figure 2.12: The primary characteristics of a lean burn combustor. (Adapted from [3])

system. The air in the primary zone is not only essential for atomization and mixing, but it also contributes to flame stabilization, which is produced thanks formation of a swirl stabilized recirculation zone [16]. However, lean conditions in the primary region, along with the quick air-fuel mixing, may have a negative influence on the ignition, altitude relight, and flame stability at low power [8]. Hence, to ensure full operability, LDI combustor is provided with piloting systems that create relatively rich flames, stabilizing the combustion process, particularly under low power conditions.

2.5.4   Multi-point Lean-Direct Injection (MPLDI)

The working principle of the Multi-point Lean Direct Injection (MPLDI) systems is that fuel is distributed to small injectors, which form the multi-point fuel injector module, as shown in Figure 2.13. Each small injector is fitted with an air-swirler to produce a local quick and uniform mixing and small recirculation zone, resulting in a stable and short flame that minimizes the flame

residence time and, as a consequence, NO_x generation. The injection system allows reducing the fuel-air mixing time inside the combustor by spreading liquid fuel droplets rapidly and uniformly, which are quickly vaporized and mixed with the air. The uniform mixture additionally contributes to the uniform distribution of temperature profiles and the homogenous distribution of combustion products through the combustion chamber.
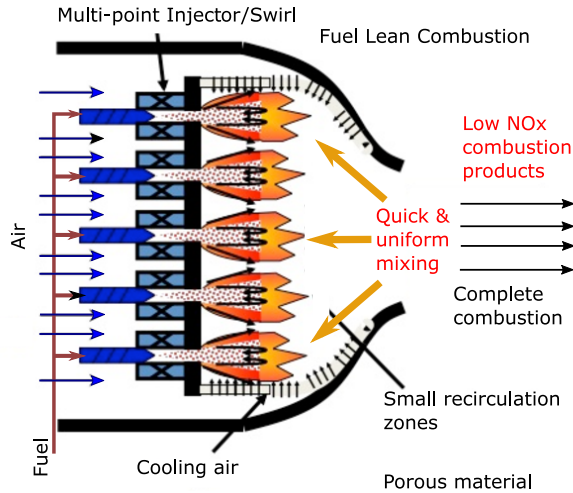
Figure 2.13: Sketch of Multi-swirler array [17].

In the MPLDI combustors, most of the air enters through the combustor dome, and the rest of the air is employed for liner cooling. Therefore, the mixture formed is lean, leading to reduce NO_x production. Additionally, an effective mixing process in this type of combustors also reduces CO production. Consequently, the combustor length can also be reduced (see Figure 2.14), reducing the flow residence time and hence reduces the NO_x production further. As a result of the shorter combustor, less liner cooling is required and a smaller engine shaft, resulting in a significant reduction in engine weight. Moreover, as was mentioned by Dewanji [11], the design of the MPLDI combustor allows controlling each fuel injector may be controlled to regulate the fuel in space and time, reducing local hot spots inside the combustion chamber. Finally, in addition to conventional aviation fuel, this system may run on alternative fuels like biofuels and gaseous hydrogen without requiring any design changes.

Liu et al. [18] summarized the advantages and design challenges of this kind of technology:
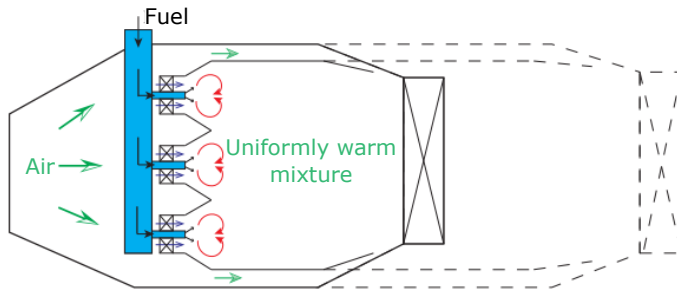
Figure 2.14: Schematic representation of an MPLDI combustor controlling [11].

- Local uniform fuel-air mixture with rapid mixing can be achieved through the distributed small recirculation of flame. The resulting benefit is the reduction of the combustor length and hence low NO_x. Little soot is formed as well.

- By adjusting the local fuel-air ratio in each small injector, temperature distribution may be continuously regulated.

- Both the recess and the outward canted arrangement reduce the local dilution of the stream at the borders of the fueled and unfueled zones, hence reducing the generation of excessive UHC and CO.

Technology design challenges:

- Densely packed structure demands high manufacturing technology to minimize the dimension discrepancy tolerance for each injector.

- A densely packed structure needs advanced manufacturing technique in order to decrease dimension discrepancy tolerance for each injector.

- With acceptable pressure losses, the mixing quality from this concept can not create a perfectly uniform fuel-air mixture.

- The reduced residence time added an extra design difficulty for altitude relight.
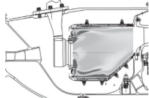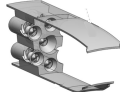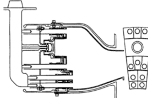
2.5.5   Review of performance characteristics

Although emissions may be a priority when constructing a conventional low emissions combustor, the value of other performance interactions with emissions should be extensively investigated. Therefore, while building a low emission combustor, concerns such as combustion efficiency, size, weight, combustion stability, altitude relight capacity, liner durability, pressure loss, and autoignition/flashback danger should not be ignored. Safety is usually the most critical requirement, and there is no exception in the design of low-emission combustors. The ability to relight at altitude and avoid autoignition/flashback should be considered early in the design process. In addition to emissions levels, several combustion performance parameters are evaluated qualitatively for the reviewed low emissions combustion technology. In addition to emissions levels, several combustion performance parameters are evaluated qualitatively for the reviewed low emissions combustion technology. A performance matrix for the combustor technologies mentioned previously is provided in Table 2.1 that would be utilized for design requirements. Explanations for each evaluation are discussed in [18].

2.6   Summary

This section presented a description of the fundamental concepts of the atomization and combustion process. Additionally, the main combustor types were introduced, highlighting the advantages and disadvantages of each one. Then, the injectors for aero-engine applications (pressure-swirl and airblast atomizers) and their working principle are described. Finally, the main combustion technologies used in the aeronautic sector are introduced, summarizing the performance aspects of each technology.

Table 2.1: Summary of the reviewed low emissions combustion performance based on qualitative evaluation. (Extracted from [18])

Criterion	RQL	LDI	MPLDI	LPP
Graphi				
TRL	9	≤ 7	≤ 5	≤ 5
Altitude relight capability	High	Moderate	Low	Moderate
Autoignition/ flashback risk	Low	Low	Low	High
Combustion stability	High	Moderate	Moderate	Low
Combustion efficiency (High-power)	High	High	High	High
Combustion efficiency (Low-power)	High	High	High	High
Pressure loss	Moderate	Moderate	High	Moderate
LTO NO_x (High-power)	Low	Even lower	Even lower	Lowest
LTO CO (Low-power)	Moderate	High	High	High
LTO UHC (Low-power)	Moderate	Low	Low	Low
Smoke number	High	Low	Low	Low
Weight	Moderate	Moderate	Moderate	Moderate
Fuel coking risk	Moderate	Moderate	Moderate	Moderate
Liner life	Moderate	Long	Long	Long
OTDF/RTDF quality	High	Higher	Higher	Higher

References

[1] Lefebvre, A. H. and Ballal, D. R. *Turbine Combustion Alternative Fuels and Emissions*. CRC Press, 2010, pp. 1–537.

[2] Verdier, A. "Experimental study of dilute spray combustion". PhD thesis. Normandie Université, 2018, pp. 1–175.

[3] Giusti, A. "Development of numerical tools for the analysis of advanced airblast injection systems for lean burn aero-engine combustors". PhD thesis. 2014.

[4] Lefebvre, A. and McDonell, V. *Atomization and Sprays*. 2017, p. 300. DOI: 10.1016/0009-2509(90)87140-N.

[5] Nonnenmacher, S. and Piesche, M. "Design of hollow cone pressure swirl nozzles to atomize Newtonian fluids". In: *Chemical Engineering Science* 55.19 (2000), pp. 4339–4348. DOI: 10.1016/S0009-2509(00)00043-9.

[6] Park, H. and Heister, S. D. "Nonlinear simulation of free surfaces and atomization in pressure swirl atomizers". In: *Physics of Fluids* 18.052103 (2006), pp. 1–11. DOI: 10.1063/1.2197876.

[7] Lefebvre, A. H. "Airblast atomization". In: *Progress in Energy and Combustion Science* 6.3 (1980), pp. 233–261. DOI: 10.1016/0360-1285(80)90017-9.

[8] Doerr, T. "Introduction to aero-engine gas turbine combustion". In: *Aero-engine design: from state of the art turbofans towards innovative architectures*. Rhode Saint Genese, 2008, p. 5.

[9] JetX Engineering. *https://www.jet-x.org/*.

[10] Tabor, G. *Combustion regimes*.

[11] Dewanji, D. "Investigation of flow characteristics in lean direct injection combustors". PhD thesis. 2012, pp. 181–196. DOI: 10.2514/1.B34264.

[12] Lewis, B. and Von Elbe, G. "Stability and structure of burner flames". In: *The Journal of Chemical Physics* 11.2 (1943), pp. 75–93. DOI: 10.1063/1.1723808.

[13] Samuelsen, G. S., Brouwer, J., Vardakas, M. A., and Holdeman, J. D. "Experimental and modeling investigation of the effect of air preheat on the formation of NOx in an RQL combustor". In: *Heat and Mass Transfer/Waerme- und Stoffuebertragung* 49.2 (2013), pp. 219–231. DOI: 10.1007/s00231-012-1080-0.

[14]   Haselbach, F. and Parker, R. "Hot end technology for advanced, low emission large civil aircraft engines". In: *28th Congress of the International Council of the Aeronautical Sciences 2012, ICAS 2012* 3 (2012), pp. 2479–2490.

[15]   McKinney, R. G., Sepulveda, D., Sowa, W., and Cheung, A. K. "The Pratt & Whitney TALON X low emissions combustor: Revolutionary results with evolutionary technology". In: *Collection of Technical Papers - 45th AIAA Aerospace Sciences Meeting.* Vol. 7. 2007, pp. 4697–4704. DOI: `10.2514/6.2007-386`.

[16]   Syred, N. and Beér, J. M. "Combustion in swirling flows: A review". In: *Combustion and Flame* 23.2 (1974), pp. 143–201. DOI: `10.1016/0010-2180(74)90057-1`.

[17]   Cai, J. "Aerodynamics of Lean Direct Injection Combustor with Multi-Swirler Arrays". PhD thesis. 2006.

[18]   Liu, Y. et al. "Review of modern low emissions combustion technologies for aero gas turbine engines". In: *Progress in Aerospace Sciences* 94 (2017), pp. 12–45. DOI: `10.1016/j.paerosci.2017.08.001`.

Chapter 3

Fundamentals of atomization, spray combustion and soot formation

3.1 Introduction

Two-phase combustion combines both multi-physical and chemical limitations, due to they involve different phenomena such as atomization, dispersion, evaporation, and combustion, which usually occur simultaneously or in narrow small areas within the combustion chambers. In addition, the existence of liquid fuel droplets adds another level of complexity compared to gas-fired flames.

The understanding of the spray flame is essential and also important, detailing each phase of the process, beginning with fuel drop atomization and extending up to the combustion process. All these processes take place in the combustion chamber. Figure 3.1 represents the interacting multi-scale mechanisms that governing droplet evaporation and combustion. Certain interactions are not described in detail in this section, and only those that can be addressed during this experimental investigation are detailed.

The purpose of modern combustors is firstly prevaporized the liquid fuel and then mixing the vapor of the fuel, which is produced by the fuel drops evaporation process. Unfortunately, the time necessary for properly prevaporization and pre-mixing is not available in most applications. If the liquid

distributed combustion

single–droplet combustion

coflow

spray

flame ignition

rich deflagration

Ω_{F}

Σ_f

Ω_{O}

diffusion flame (external group combustion)

air coflow

fuel film

hot recirculation region

liquid fuel

region $\alpha \gg 1$ (liquid fragmentation)

region $\alpha = O(1)$ (heating and vaporization starts)

extinction/reignition

region $\alpha \lesssim O(1)$ (vaporization and combustion)

secondary atomization

primary atomization

unburnt hydrocarbons

combustor wall

Figure 3.1: Schematic representation of the liquid spray-combustion processes in continuous-combustion systems [1].

fuel is not completely pre-vaporized and premixed in the combustion chamber, it will produce a lack of homogeneity of the mixture fraction and hence a variation of the flame temperature. This variation will adversely influence NO_x and soot emissions. Figure 3.2 summarizes the iterations between processes involved in the liquid fuel flames.

Both the atomization and fuel droplet dispersion are affected by the turbulent flow. Additionally, turbulence can increase the evaporation of the fuel droplets by promoting interaction with the surrounding air. By interacting with the carrier phase, the drops can influence local turbulence. The generation of fuel vapor during the evaporation stage results in a heterogeneous mixture fraction within the combustion chamber due to molecular diffusion. The combustion regime can be influenced by the variation in the local mixture. Moreover, due to inhomogeneities in the mixture fraction, it is quite possible to experience several combustion regimes simultaneously [2]. Consequently, it
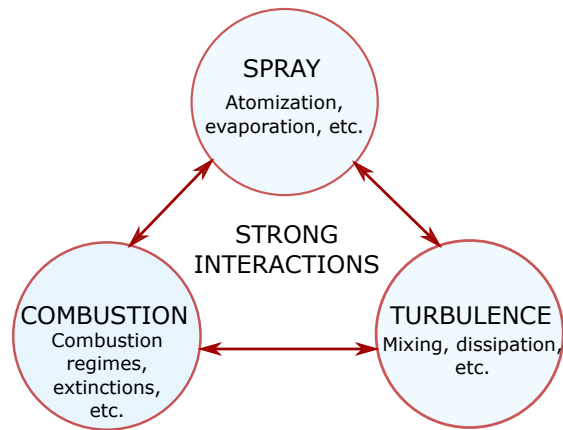
Figure 3.2: Schematic description of the interactions that take place in a turbulent spray flame.

is important to study these phenomena together in order to comprehend the physical mechanisms that occur during two-phase combustion.

3.2 Atomization process

As described in section 2.3, in order to produce a good air/fuel mixture and complete operability of the aircraft engine combustor, typical injection systems employed in gas turbine systems comprise pressure and airblast injectors, generally coupled with more sophisticated designs. In these kinds of systems, the fuel is often atomized as a plain jet or a thin sheet that disintegrates into small drops in a phenomenon known as *primary breakup*. This process occurs close to the injector tip and must be differentiated from *secondary breakup*, which characterizes the further disintegration of drops into smaller ones. Lefebvre and Ballal [3] suggested that both mechanisms define the precise properties of the fuel spray in terms of droplet size distributions and their velocities. The primary and secondary atomization processes will be detailed in further detail in the following sections, introducing to the fundamental principles of liquid fuel breakup. These concepts will be appropriate to explain the experimental results.

3.2.1 Useful non-dimensional numbers

Multiple interactions with the gas-phase and boundary walls control the liquid throughout the spray generation and evolution process, and more generally in

multi-phase flows. In several cases, it may be extremely convenient to perform an order-of-magnitude analysis to determine what the dominant interactions are. This type of analysis enables us to include certain non-dimensional numbers. Because a multi-phase flow is being studied, quantities linked to the liquid phase, in addition to conventional gas-phase characteristics, should be taken into consideration, as they play a significant role in many physical processes such as evaporation and breakdown.

Quantitative characterization of the processes implicated in the droplet disintegration may be stated according to the *Weber number* (*We*), which reflects the ratio of momentum force to surface tension force [4].

$$We = \frac{\rho_g U_R^2 l}{\sigma} \tag{3.1}$$

where ρ_g is the density of the gaseous-phase (air), l is a length scale parameter, generally the drop size (i.e., diameter), σ is the surface tension, and U_R is the relative velocity between the gas-phase and the liquid. This number is commonly used in breakup theory because it considers the relative relevance of surface tension and aerodynamic interactions.

The *Ohnesorge number* (*Oh*), which relates the internal viscous force to inertia and surface tension forces, is another important dimensionless number:

$$Oh = \frac{\mu_L}{\sqrt{\rho_L \sigma l}} \tag{3.2}$$

where l is a characteristic length scale, ρ_L and μ_L are the density and dynamic viscosity of the liquid-phase, respectively. Finally, in the investigation of drop dynamics, it may be convenient to introduce the *Particle Reynolds Number* (*Re_p*), which is given as:

$$Re_p = \frac{\rho_g d \|u - v\|}{\mu_g} = \frac{\rho_g d U_R}{\mu_g} \tag{3.3}$$

where d is the particle diameter, μ_g is the dynamic viscosity of the gas-phase, and U_R is the relative velocity between the carrier phase and the droplet.

3.2.2 Primary atomization

This is a complex phenomenon influenced by several parameters in which various breakup mechanisms can be identified, depending on the operating conditions and geometrical configurations. A literature review of the principal

mechanisms, describing injection configurations employed in aircraft engine technology, will be used to explain the primary breakup. The principal purpose is to provide a general analysis of the complex physical phenomena that govern the disintegration process, defining the most relevant characteristics of this liquid breakup. Therefore, classical atomization mechanisms of the liquid jet are detailed in this work. However, liquid sheets are not described but are fully explained in [3].

Liquid jets

Classical jet atomization theories are based on the propagation of disturbances, which results in jet fragmentation. It is crucial to remark that disturbances are inherent in jet dynamics since they occur spontaneously when the liquid flows through the injection system or as a result of interactions with the gas phase.

Rayleigh [5] conducted the first theoretical analysis of jet breakup, considering a laminar jet with a starting diameter equivalent to dj, emerging from a circular hole and exposed to surface disturbances. He observed that symmetric disturbances with an ideal wavelength of $\lambda_{opt} = 4.51dj$ are likely to grow with time, eventually leading the jet to break up into ligaments that finally form spherical droplets with a diameter of d equal to

$$\lambda_{opt}\frac{\pi}{4}d_j^2 = \frac{\pi}{6}d^3 \rightarrow d = 1.89d_j \tag{3.4}$$

Weber later extended Rayleigh's theory by incorporating the impact of liquid viscosity using the Ohnesorge number, as detailed in [3]. The optimum unstable wavelength, according to Weber's theory, is given by

$$\lambda_{opt} = \sqrt{2}\pi d_j(1 + 3Oh)^{0.5} \tag{3.5}$$

where the characteristic length scale in Equation 3.2 is the cylindrical jet diameter, the equation may be written as

$$Oh = \frac{\mu_L}{\sqrt{\rho_L \sigma d_j}} \tag{3.6}$$

It follows that:

$$\lambda_{opt}\frac{\pi}{4}d_j^2 = \frac{\pi}{6}d^3 \rightarrow d = \left(\frac{3\pi}{\sqrt{2}}\right)^{\frac{1}{3}} d_j(1 + 3Oh)^{\frac{1}{6}} \tag{3.7}$$

In addition to liquid viscosity, the initial velocity of the jet releasing from the injector orifice is another crucial parameter that has a considerable impact on the atomization process. The theories developed by Rayleigh and Weber are representative of disintegration only at low jet velocities. When the relative velocity of the air and the liquid increases, the aerodynamic interactions between the two fluids become more intense, resulting in smaller drops. According to recent experimental results, Reitz [6] proposed the following classification of breakup regimes (see also Figure 3.3, where the various jet breakup regimes are shown as a function of the liquid Reynolds and Ohnesorge numbers):
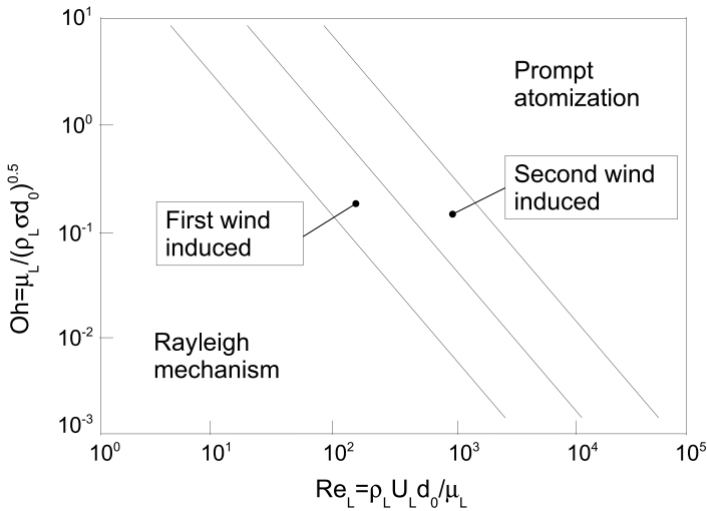
Figure 3.3: Jet breakup regime classification, where d_o is the orifice diameter. (Extracted from [7])

- *Rayleigh mechanism*: Rayleigh's breakup mechanism dominates at low velocities. The jet breakup is caused by the formation of symmetric oscillations under the influence of surface tension, which can enhance the amplitude of disturbance wavelengths larger than a certain value. Drops produced by this process are fairly uniform in size, with diameters about double the starting jet diameter. This breakup regime is commonly referred to as varicose due to the unique geometric shape of the jet, which is characterized by rotationally symmetric perturbations.

- *First wind-induced breakup*: the relative velocity between the gas-phase and the jet increases the surface tension effect, which decreases the optimal wavelength for jet disintegration, resulting in smaller droplets.

- *Second wind-induced breakup*: drops are formed when the jet velocity increases due to the unstable development of small waves on the jet surface induced by the interaction of the jet and the surrounding gas. The waves become unstable and disengage from the jet surface as ligaments, eventually disintegrating into droplets considerably smaller than the initial jet diameter.

- *Prompt atomization*: jet disintegrates entirely at the injector exit and hence drop sizes are significantly smaller than the jet diameter.

The preceding section examined the scenario of a liquid stream injected into an airflow. A plain jet exposed to a co-flowing airflow, on the other hand, might be found in particular injector configurations. In this scenario, also known as air-assisted cylindrical jet, various breakup mechanisms may be seen, as detailed in [8]. When we consider a liquid jet discharged from a cylindrical orifice with a coaxial air-stream, we may differentiate the following regimes:

- *Rayleigh mechanism*: when the relative velocities between the liquid jet and co-flowing airflow are extremely low ($We_j < 25$, with $We_j = \rho_g(U_g - U_j)^2 d_j/\sigma$), the jet disintegration apart via a mechanism similar to the one defined by Rayleigh. Droplet sizes are comparable to jet diameter. With axisymmetric deformation (as found for liquid jets in a still medium but with shorter breakup lengths) and non-axisymmetric structures, two distinct sub-regimes may be differentiated.

- *Membrane-type breakup*: this regime ($25 < We_j < 70$) is characterized by the formation of thin liquid sheets that generate Kelvin-Helmholtz waves and breakup into droplets with significantly smaller diameters than the preceding regime. The jet's shape resembles that of a thin liquid sheet.

- *Fiber-type breakup*: this case ($100 < We_j < 500$) is characterized by the formation of thin liquid fibers that peel off the jet and disintegrate by a process similar to the non-axisymmetric mode found at low relative velocities. Further downstream, the main liquid core turns wavy and ruptures into ligaments, from which new fibers are peeled. The drop sizes are pretty small and typically grow with the downstream distance.

- *Digitation*: Another mechanism characterized by the formation of digitations (ligaments) on the crests of an axisymmetric disturbance has also been reported in some studies [9]. These ligaments subsequently breakup by a non-axisymmetric Rayleigh-type mechanism (the digitations-type disintegration regime is noticed at the same We_j of the membrane-type breakup regime [8]).

Some atomization remarks

The liquid atomization process is a highly complex event in which small-scale interactions may impact the final droplet properties after jet disintegration, as was previously commented. Breakup mechanisms are indeed also affected by the injection configuration, adding a difficulty to establish a unified atomization theory. As a result, numerical methods have been developed in order to help in the understanding of the atomization process are often quite case-dependent.

In the configurations discussed in this section, the key parameter influencing atomization is the relative velocity between the air co-flow and the liquid fuel, and the atomization quality typically increases as the relative velocity increases. Regardless of the liquid configuration, all the studies indicate a similar tendency for higher relative velocity values. When the relative velocity is significantly large, the intense contact with the co-flow air immediately downstream of the injection point disintegrates the liquid jet. To emphasize that the liquid atomization occurs extremely near to the injection system, this atomization regime is often referred to as prompt atomization. An important feature of this atomization mode, as described in [3], is that the fuel is rapidly and violently disrupted, ensuring that the resultant droplet diameters are essentially independent of the original fuel dimension (sheet thickness or jet diameter). In addition, fuel atomization appears to be independent of its viscosity, which can not influence a quick process. Prompt atomization is always observed under operating conditions found in gas-turbine systems.

Factors that affect the fuel atomization

As stated previously, the relative velocity between the gas phase and the liquid flow and is the most significant parameter affecting atomization in configurations typical of pressure and airblast atomizers. Usually, a significantly higher velocity increases atomization quality. Nevertheless, numerous other parameters, such as the geometrical configuration of the injection system, can influence the atomization process. Lefebvre and McDonell [4] summarized the most important factors as follows:

- Injector geometry.
- Liquid properties.
- Gas medium properties.

The injection system geometry defines the interaction between the gas phase and the liquid fuel and is primarily responsible for the characteristics of the liquid spray and, as well as the distribution pattern within the combustion chamber. Significant attention must be given to the design of the geometrical characteristics in order to ensure the efficient operation of the injection system. The physical mechanism used to generate the destructive force that contributes to droplet production typically determines the shape and fundamental features of the injector (see section 2.3). The capacity to achieve effective atomization almost regardless of the fuel flow rates, low cost, lightweight, easy to maintain and removal for servicing, are common needs to consider in enhancing conventional injection designs and developing new ones.

Dynamic viscosity and surface tension are the two most significant fluid characteristics that influence atomization. The first is unfavorable to atomization because it resists any alteration in fluid geometry. In addition, inside the injector, the viscosity also affects the flow. An increase in liquid viscosity usually leads to a reduction of the atomization efficiency, with an increase in the diameter of the drop and a delay in the formation of the droplet. Furthermore, liquid density has only a minor impact on the breakup phenomena. On the other hand, surface tension is a force that tends to draw the liquid into the configuration of minimal surface energy (a sphere in the absence of external forces), inhibiting the formation of a new liquid surface. Therefore, a factor that acts against disturbance can be considered in equilibrium configurations (This is the case, of secondary atomization, for instance), whereas if the fluid is not in an equilibrium configuration, surface tension may become a significant parameter in liquid deformation and probable breakup (this is the case, of capillary instability of free liquid jets, for instance, [10]).

The atomization process is also influenced by the properties of the medium into which the liquid is atomized. Density and pressure seem to be the most essential properties to consider in the injection, although their influence is highly dependent on the injector's design. For instance, as mentioned in Giusti [7], increasing the liquid density improves atomization quality in airblast atomizers, while two different effects occur in pressure swirl atomizers. Increased density, as in airblast injectors, results in higher aerodynamic interactions, resulting in smaller drop sizes and shorter breakup lengths. The spray angle, on the other hand, decreases.

3.2.3   Secondary atomization

Aerodynamic forces regulate the movement of a droplet in a gaseous phase, which can result in deformation and fragmentation of the droplet. Secondary atomization is the process by which a droplet is fragmented into smaller particles. There are several research on secondary atomization in the literature. Ashgriz and Yarin [10] present a good overview of them. Some basic concepts will be presented following.

Critical Weber number

Considering a specific droplet exposed to a moving airflow, basic considerations about droplet stability can be defined. When the aerodynamic force (i.e., drag force) balances the surface tension force, the critical condition for drop breakup is reached [3]:

$$C_D \frac{\pi}{8} d^2 \rho_g U_g^2 = \pi d \sigma \tag{3.8}$$

where C_D is the drag coefficient of the liquid structure, d is the droplet diameter, ρ_g and U_g are the density and the velocity magnitude of the gas, respectively. By rearranging this equation, we can derive a critical Weber number, which allows us to provide a measure of the maximum diameter of stable drops that may be observed in a spray:

$$\left(\frac{\rho_g U_R^2 d}{\sigma} \right)_c = We_c = \frac{8}{C_D} \rightarrow d_{max} = \frac{We_c \sigma}{\rho_g U_R^2} \tag{3.9}$$

Experimental results on C_D imply a value for We_c of about 12 for low-viscosity liquids. To take into account the impact of fluid viscosity, the critical Weber number equation can be adjusted by inserting the Ohnesorge number (see subsection 3.2.1). The following expression is suggested by Brodkey [11]:

$$We_{c,lv} = We_c + 14 \left(\frac{\mu_L}{\sqrt{\rho_L \sigma d}} \right)^{1.6} = We_c + 14 Oh^{1.6} \tag{3.10}$$

as can be seen in Equation 3.10, an increase in the viscosity of the liquid typically results in a larger critical Weber number. Nevertheless, viscosity has a substantial influence on the critical Weber number only at high fuel viscosity.

Secondary breakup regimes

Different disintegration regimes may be identified based on the experimental data, as illustrated in Figure 3.4. The transition between regimes is determined by both the Weber droplet number ($We = \rho_g U_R^2 d/\sigma$) and the Ohnesorge number that takes the effects of liquid viscosity into account, as previously stated. Nevertheless, for extremely low Ohnesorge values, the effect of the liquid viscosity is minimal, and transitions between regimes could be defined using the Weber number [7]. Typical Weber values for disintegration regimens are also shown in Figure 3.4, for *Oh* less than 0.1.
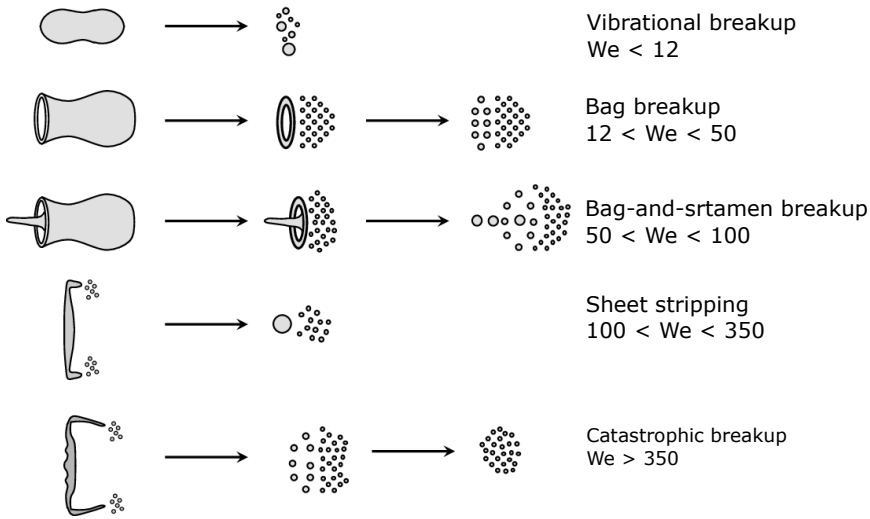
Figure 3.4: Five regimes of breakup for a low viscosity(inviscid) Newtonian drop in the presence of a horizontally flowing air stream. (Adapted from [12])

Significant deformation occurs with a Weber unit number. The surface tension and viscous forces resist the deformation caused by the contact of the gas flow and the droplet. If the aerodynamic forces are strong enough, over a certain number of the Weber value, the deformation of the droplet results in a breakup of it. The first regime, known as a vibrational breakup, is not always detected and comprises oscillations at the drop's natural frequency. The droplets formed after the breakup are comparable in size to the parent droplet. Droplet deformation leads to the development of a thin hollow bag connected to a thicker toroidal rim in the bag breakup regime. The bag-and-stamen disintegration is comparable to the bag disintegration, but with the inclusion of an anti-parallel stamen oriented in the direction of the drop le

movement. The bag is the first one to disintegrate, followed by the rim and the stamen. In the sheet stripping regime, creates on the droplet surface, a film is formed from which small drops are constantly torn off. This produces a cloud of tiny drops and, in certain instances, a core that is equivalent in size to the original drop. Finally, the catastrophic regime tends to appear for very large Weber numbers. Waves with large amplitude and long wavelengths corrugate the drop surface, resulting normally in the formation of small drops.

For $Oh > 0.1$, due to the impact of liquid viscosity, the critical Weber numbers that differentiate the distinct regimes may change. The critical Weber number as a function of the Ohnesorge number is often expressed in the form Equation 3.10. References [13] provide some indications regarding the transition between the different regimes as a function of both We and Oh numbers.

Effect of turbulence

The gas-phase turbulence plays a significant role in the droplet breakup. Turbulent oscillations could have length scales of the same order of magnitude of drop size, causing pressure gradients throughout the drop that may cause the droplet to disintegrate. One of the primary causes of vibrational breakup might be turbulent variations. Furthermore, airflow turbulence might affect the randomness of the disintegration process, but the Weber number based on mean velocity could not be as relevant since turbulence drops have different local velocities, which determine specific breakup performance. Besides, the internal turbulence of the fluid caused by the primary atomization process may affect droplet secondary breakup. To consider the influence of gas-phase turbulence, an approach based on a turbulent Weber number derived by calculating the square of the root mean square (RMS) of turbulent velocity fluctuations ($\bar{u}'$) inside the length scale that has the magnitude of the drop was proposed Hinze [14] .

$$We_{c,turb} = \frac{\rho_g \bar{u}'^2 d}{\sigma} \tag{3.11}$$

According to this concept, the critical Weber number at which a drop can disintegrate is significantly lower than the one seen for laminar flows, as also reported by Prevish and Santavicca [15]. Hinze [14] suggested a value for $We_{c,turb}$ equivalent to Equation 3.11, which is much lower than values obtained for laminar flows. As a result, reduced consistent diameters might be expected in turbulent flows.

Guildenbecher et al. [13] highlighted that despite efforts, the effect of turbulence on drop disintegration is not fully understood, and it remains an open investigation subject. According to Koch [16], typical breakup regimes encountered experimentally with a degree of turbulence equivalent to 2% - 3% are comparable to those mentioned previously and breakup models employed in computational solutions often follow the prior classification.

3.3 Representation of droplet

The combustor performance is strongly affected by the spray characteristics, which affect the fuel evaporation, and therefore its distribution inside the combustor. In addition, due to the randomness of the atomization process, the population of drops generated by atomizers used in gas turbine systems has a wide variety of droplet sizes. Therefore, the mathematical functions described following are used to characterize size distributions presented together with certain measurements of spray pattern and mean diameter.

3.3.1 Mean diameter

To evaluate the injector performance and to compare with other ones, some quantities capable of describing drop distribution characteristics must be defined. According to the application, a mean representative diameter and a value of the variation around it are suitable in many cases. Different definitions of the mean diameter are reported in the literature. A general definition of the mean diameter for a spray with a total number of N drops is given by the following expression:

$$D_{ab} = \left(\frac{\Sigma_{i=1}^{N} d_i^a}{\Sigma_{i=1}^{N} d_i^b} \right)^{\frac{1}{a-b}} \tag{3.12}$$

According to this formula, D_{10} is the arithmetic average including all spray drop diameters, and D_{30} is the size of a drop whose volume, if multiplied by the overall number of drops in the spray, represents the total liquid volume of the spray. In the same way, many additional diameters may be defined. Among the numerous potential definitions, the D_{32}, also known as *Sauter mean diameter* (SMD), is widely used in combustion applications since it is most relevant to evaporation and combustion rates [17]. SMD denotes

the diameter of a droplet whose volume-surface area ratio equals the volume-surface ratio of the complete spray.

$$D_{32} = \frac{\Sigma_{i=1}^{N} d_i^3}{\Sigma_{i=1}^{N} d_i^2} \tag{3.13}$$

Moreover, D_c (where c is a real value between 0 and 1) is often used to indicate the size such that the ratio of the volume of droplets with a size less than Dc to the entire volume of the spray equals c. For example, $D_{0.632}$ is the droplet diameter such that droplets of smaller diameter comprise 63.2 percent of the total liquid volume. The parameter X of the Rosin-Rammler Distribution (Equation 3.14), described in the following section, is equivalent to $D_{0.632}$. Finally, in a droplet size-frequency distribution curve, D_{peak} is utilized to identify the most probable diameter.

Finally, a mean size is required to provide a measurement of the spray's spread. Some parameters can be recognized, but in most cases, the variation between two distinct diameters (e.g., $D_{0.9}$ and $D_{0.1}$) or the dispersion factor of a distribution function (for example, q in the Rosin-Rammler formulation) are adequate.

3.3.2   Mathematical distributions

In the absence of a complete explanation of the atomization process, different functions have already been developed, each of which is based on probability and empirical factors that are validated by experimental observations. Standard spray formulas comprise normal, log-normal, chi-squared, and Rosin-Rammler distributions. Generally, the formulation that must be selected is the one that best fits the experimental diameter distribution. A short explanation of the Rosin-Rammler distribution is following presented, whereas further information about other formulations is detailed in [4].

The Rosin-Rammler function [18] is an empirical distribution which can be expressed in the following form (cumulative distribution):

$$1 - Q = exp\left[-\left(\frac{d}{X}\right)^q\right] \tag{3.14}$$

where Q is the portion of the overall volume included in drops with sizes less than d, X is the droplet size such that droplets with smaller diameters contain 63.2 % total liquid volume, and q is a measurement of droplet size dispersion. The larger the value of q, the more homogenous the spray, as depicted in Figure 3.5.
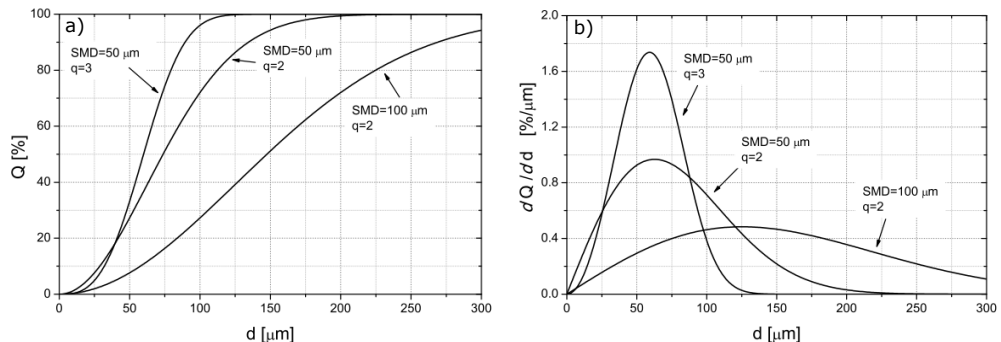
Figure 3.5: Examples of Rosin-Rammler distribution. a) Cumulative distributions, b)Frequency distributions. (Extracted from [7])

The two parameters X and q in the Rosin-Rammler distribution definition may be related to the most fundamental definition of representative sizes using the following expressions:

$$\frac{D_{32}}{X} = \left[\Gamma \left(1 - \frac{1}{q} \right) \right]^{-1} \tag{3.15}$$

$$\frac{D_{peak}}{X} = \left(1 - \frac{1}{q} \right)^{\frac{1}{q}} \tag{3.16}$$

where Γ represents the Gamma function. SMD is often provided in experimental correlations in order to compare different injectors, hence if the dispersion parameter is given (According to Lefebvre and McDonell [4] "for most sprays q ranges between 1.5 and 4.0"), Equation 3.15 can be employed to calculate the parameter X. Figure 3.6 shows an example of the position of the most relevant diameters along the drop size-frequency distribution curve.

3.4 Evaporation process

Predictive models of evaporation and heating of the fuel droplet are important to understand how drops interface with the gas phase, exchange mass, momentum, and energy during their dynamics. Because a dilute spray is assumed, the inter-particle spacing may be considered sufficiently large to remove the impact of neighbor particles on droplet dynamics. In the instance of evaporation, for example, if the inter-spacing is minimal, the liquid mass evaporated
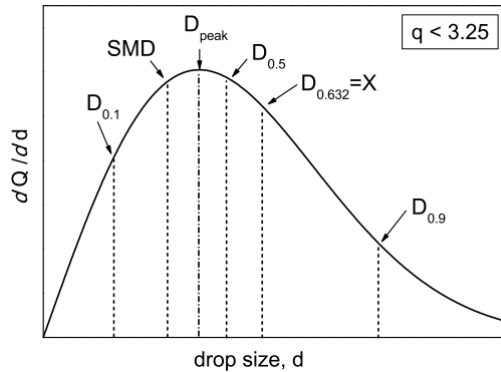
Figure 3.6: Position of different representative diameters throughout a Rosin-Rammler frequency distribution. (Extracted from [7])

from a droplet may impact the evaporation of nearby drops because the evaporated liquid increases the liquid mass fraction at the drop surface [7]. The dilute spray approach allows us to ignore drop interactions, and models established for a single drop may be used to the entire spray. Suitable models to manage the most essential interactions will be introduced in the following sections.

3.4.1   Drag forces

Gas-phase and droplet transfer momentum through *drag force*, which defines the aerodynamic interaction between both phases. The drag force is commonly expressed as follows:

$$F_D = \frac{1}{2} C_D \frac{\pi d^2}{4} \rho_g (\tilde{u} - v_p) \|\tilde{u} - v_p\| \tag{3.17}$$

where v_p is the particle velocity, $\tilde{u}$ velocity derived from the gas-phase solution, C_D is the drag coefficient which is calculated through equation derived for spheres with an additional correction to take into account the effects of particle distortion due to the interaction with the gas-phase (Particle shape may be significantly distorted and, if the distortion reaches a critical value, breakup may occur). The drag coefficient strongly dependent on particle form, measuring the impacts of droplet deformation is desirable. Meanwhile, the possibility of droplet deformation during the breakup process is consid-

ered, assuming that the drag coefficient changes linearly between the values of a sphere and a disk [19]:

$$C_D = C_{D.sphere}(1 + 2.632y) \qquad (3.18)$$

where y is the droplet distortion from sphericity, and which varies between 0 and 1. This value is calculated through the method implemented in the Taylor Analogy Breakup (TAB) model developed by O'Rourke and Amsden [20]. As regards the drag coefficient of a sphere, the following definitions have been employed [21–23]:

$$C_{D.sphere} = \begin{cases} \frac{24}{Re_p}(1 + \frac{1}{6}Re_p^{2/3}) & Re_p \leq 1000 \\ \\ 0.424 & Re_p > 1000 \end{cases} \qquad (3.19)$$

3.4.2   Evaporation models

Predictive models of fuel drop heating and evaporation are critical in several power systems that use spray combustion. Drop-to-drop interactions are important in the evaporation process because fuel atomization produces numerous droplets of different sizes. As a result of the high level of complexity involved in real configurations, developing models to analyze the evaporation process in a realistic spray is challenging. Consequently, most of the models implemented for real combustion chamber calculations ignore these interactions. In recent years, theoretical and experimental studies have been conducted to investigate these interactions. Castanet et al. [24] used an experimental and numerical method to study the interaction process that affects mass and heat transmission in a chain of regularly arranged monodisperse drops.

The droplet evaporation process has been widely studied by Miller et al. [25]. In this study, some models of drop evaporation, which are grouped into three types of models and here are globally described.

The models shown in Table 3.1 can be divided into three classes in which the complexity increased in ascending order. The evaporation models are globally described for each group, and the principal assumptions are provided.

- TYPE 1: The temperature of the fuel drop is maintained constant throughout the evaporation process. The droplet temperature is uniform inside it and constant along the time, as seen in Figure 3.7. Furthermore, various models of type 1 assume spherically symmetric fuel

Table 3.1: Nomenclature of models reported in [25].

Type	Model	Name
Type 1	M1	Classical rapid mixing
Type 1	M2	Abramzon-Sirignano
Type 2	M3	Mass analogy Ia
Type 2	M4	Mass analogy Ib
Type 2	M5	Mass analogy IIa
Type 2	M6	Mass analogy IIa
Type 3	M7	Langmuir-Knudsen I
Type 3	M8	Langmuir-Knudsen II

vapor diffusion in the carrier phase. The classical rapid mixing model, commonly known as the d^2 law, is based on kept drop temperature and comprises the quasi-steady assumption with infinite conductivity or the fast mixing model ($T = cste$) [25]. The model developed by Abramzon and Sirignano studies the rapid mixing model, incorporating evaporation adjustments on mass transfer and heat, including the impacts of Stefan flow.

- TYPE 2: The temperature within the drop is still consistent, but it varies with time, as shown in Figure 3.7. It is expected that the drop is warmed up to its boiling point before evaporating. The ambient energy transferred to the drop promotes its evaporation. Recent models [21, 26] incorporate correction variables in the spherically symmetric model for fuel vapor diffusion, which is different from type 1. These models also add the influence of convection around the drop in order to calculate the interface between the surrounding flow and the fuel vapor created by the evaporation process. Models M3-M6 are indeed variants on a simple heat-mass transfer analogy model that may be obtained immediately from the droplet's vapor fraction boundary condition. These are classified as TYPE 2 models.

- TYPE 3: In this sort of evaporation model, the gradient temperature within the drop is taken into account in addition to the temporal development of the droplet temperature (Figure 3.7). These models can be solved using a variety of approaches. For example, resolving the Navier Stokes equations within and outside the drop allows for an accurate determination of the droplet temperature inside a given environment. It is

essential to note, nevertheless, that this model is computationally highly costly and hence rarely applied in LES.
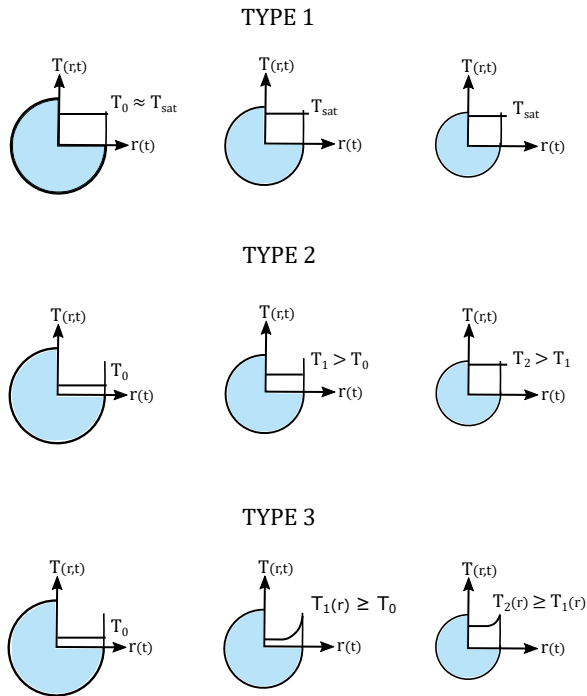
Figure 3.7: Schematic representation of spatial and temporal temperature evolution for three different droplet evaporation models. (Extracted from [2])

Finally, the first models (M1 to M6) are transient classical models with a heat-mass transfer analogy, but the latter two models (M7-M8) are non-equilibrium models based on the Langmuir-Knudsen evaporation law. The computation of the heat and mass transport terms differs between the eight models. A short overview of the different models was provided; however, they are extensively discussed in [25].

During the droplet evaporation, many simultaneous processes are acting [16]:

- Heat transfer between carrier phase and droplet.
- Mass transfer between gas-phase and droplet.
- Heat transfer by convection and conduction inside the droplet.

- Mass transfer inside the droplet (only for multi-component fuels).
- Phase change at the droplet interface.

Generally, a real model of the drop evaporation should consider all the transport processes inside and around the drop. Nevertheless, models able to take into account all relevant events are extremely complicated and imply high computational cost. Thus, they cannot be implemented for the calculation of spray evaporation. Therefore, in practical cases are used for the study the evaporation of a single droplet. If it is possible to identify some dominant transport processes, simplified models can be developed.

Droplet Biot number is generally implemented as a simplified measurement of the relative impact between internal conduction and outside heat transfer from the gas-phase to the drop:

$$Bi = \frac{hd}{2\lambda_d} \qquad (3.20)$$

where h denotes the heat transfer coefficient and λ_d denotes the liquid conductivity. If the Biot number is low ($Bi \to 0$) heat conduction within the drop takes priority over outside heat transfer, and the temperature within the drop rapidly levels out. *uniform temperature models*, in which the temperature of the drop is assumed to be constant and hence no internal transform is solved, can be employed in this scenario. Otherwise, when the Biot number is very large ($Bi \to \infty$), the conduction process within the drop is quite low, and only the drop surface may be considered heated by external heat transfer. The thin skin approach can then be used. In intermediate instances, conduction within the drop must be resolved, implying a considerable computational effort [7].

The temperature model usually results in a good explanation of evaporation in conditions of concern for jet engine applications, while requiring a minimal computational cost [16].

3.4.3   Spray-turbulence interactions

Interactions between the turbulent carrier phase and fuel spray can strongly influence the trajectory and motion, these interactions have been previously reported by Balachandar and Eaton [27]. The modulation intensity of the turbulence by droplets is affected by both the quantity and size of drops. Certainly, turbulence modulation is double. Firstly, friction at the droplet surface reduces the local turbulent kinetic energy. The turbulent kinetic energy is dissipated at the drop's surface. In fact, the preferred segregation of

drops is mostly determined by the interaction between turbulence and spray. Therefore, these interactions have been investigated numerically [28–30] and experimentally [31, 32].

In a turbulent gas flow, in which the drops are exposed to turbulent velocity fluctuations. It has been observed that small droplets have more tendency to follow the turbulent velocity fluctuation than the large droplets. Therefore, The Stoke number (S_t) has been created, which describes the inertia of the droplet compared to the carrier phase. i.e., the ratio of the aerodynamic response time (τ_p) of a droplet suspended in a flow field and the time scale associated to the large-scale flow vortices:

$$S_t = \frac{\tau_p}{\tau_f} \tag{3.21}$$

where $\tau_p = \frac{\rho_d D_d^2}{18\mu_g}$ rdenotes the relaxation time, which is the time required for drops to adjust to the new surrounding airflow velocity after a rapid change and τ_f is the characteristic time of the flow. Droplets that present low Stokes numbers ($S_t << 1$) tend to precisely follow the changes of the gas flow. On the other, droplets with a large Stokes number ($S_t >> 1$) hardly follow the fluctuations of the gas flow. This is typically the case for large droplets with ballistic trajectories. Droplets with a large Stokes number have difficulty following the variations of the gas flow. This seems to be common for big drops with ballistic trajectories.

3.5 Turbulence-gaseous flame interactions

Turbulent combustion is the consequence of a two-way interaction between chemistry and turbulence.

- The effect of flame on turbulence. When a flame interacts with a turbulent flow, the processes can either (i) produce turbulence, known as "flame-generated turbulence," or (ii) dampen turbulence by relaminarization because of the high temperature.

- Turbulence effect on the flame structure. Turbulence may modify the flame structure through wrinkling and straining processes [33–35], improving the chemical reaction, but it can also inhibit it and lead to flame quenching due to the critical value of turbulence.

Damköhler [36] was the first one to define turbulent combustion and include wrinkling as one of the primary processes influencing the impact of turbulence on flame fronts. It is important to examine different time scales in order to characterize the interactions between combustion and turbulence. To explain flame-vortex interactions, The Damköhler and Karlovitz number are used.

$$Da = \frac{\tau_t}{\tau_c} = \frac{l_t/u'}{\delta/s_L^0} \tag{3.22}$$

$$Ka = \frac{\tau_c}{\tau_k} \tag{3.23}$$

The Damköhler number (Da) is determined for the largest eddies and corresponds to the ratio of τ_t to τ_c, which are the integral and chemical time scales, respectively. The Karlovitz number (Ka), which is the ratio of the chemical time scale τ_c to the Kolmogorov time τ_k, represents the smallest eddies. The chemical time is greater than the turbulent time for $Da \ll 1$. Turbulence controls the mixing of the burnt gas and fresh air, whereas chemistry controls the total reaction rate. This is known as the Well stirred reactor regime. The chemical time scale, on the other hand, is less than the integral turbulence time when $Da \gg 1$. In this scenario, turbulence has no effect on the flame, and the burning rate is identical to that of a laminar flame. This is known as a flamelet regime, and the turbulence can wrinkle the flame front. These characteristics time have been used by some authors [37, 38] to explain the premixed turbulent combustion regimes illustrated in Figure 3.8.

Figure 3.8 shows several combustion regimes identified in terms of lenght (l_t/δ) and velocity (u'/s_L^0) ratios.

- When the Reynolds number is less than one, the premixed combustion regime is laminar. Nevertheless, the regime turbulent controls the other four regions.

- When the Ka value is less than one, the flame thickness is less than the lowest turbulent scale. Furthermore, all turbulent time scales are less than the chemical time scale. The flame front is narrow, near to a laminar flame, and wrinkled by the turbulence in this condition. This flamelet regime is separated into two regions: (i) Wrinkled flamelet regime, which corresponds to situations in which turbulent motion is insufficient to wrinkle the flame front. The flame is somewhat wrinkled
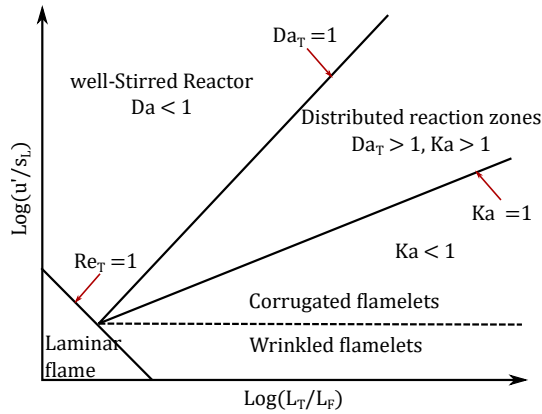
Figure 3.8: Diagram of combustion regimes and turbulent flame structure for pre-mixed flames.

in this configuration, and the structure is similar to that achieved in the laminar regime. (ii) Corrugated flamelet regime. The flamelet regime remains valid in this circumstance, but bigger turbulence structures might react with the flame front, leading to the creation of pockets of fresh or burnt gases.

- The thickened flame regime, also known as distributed reaction zones. When $Ka > 1$ and $Da > 1$, this regime arises. The turbulent integral time scale is still bigger than the chemical time scale throughout this regime, but the Komolgorov scales are shorter than the flame thickness and can perturb the flame front until it quenches if the stretch exceeds a critical threshold.

- For Damkölher numbers less than one, turbulent motion is lower than chemical time. The mixing is extremely fast, and the reaction rate is restricted by chemistry.

Other significant turbulence-flame interactions result in the risk of extinguishing the flame due to high turbulence intensity. In fact, flame quenching happens when a flame front is exposed to external disturbance, such as heat losses or sufficiently significant aerodynamic stretch, which causes the reaction rate to drop. It should be noted that the reduction in reaction rate might be caused by either thermal quenching caused by interactions of the flame-wall and low drop temperature or by strain quenching. When the local stretch

caused by turbulent movements on the flame front exceeds a certain value, the flame is extinguished. The combustion is modified at a specific point, and the new reactants mix with the products without combustion.

3.6   Spray combustion

Spray turbulent combustion is a complex process because it involves several physical phenomena that can interact and influence the local and global flame structures. Spray combustion is distinguished by the fact that the fuel is injected in the liquid state, and evaporation and dispersion of fuel vapor into the surrounding gas phase occur before chemical interactions between oxidizer and fuel. As a consequence, spray combustion involves aspects of both premixed combustion and non-premixed [39]. Lefebvre and McDonell [4] defined two different limiting cases:

- Heterogeneous combustion.
- Homogeneous combustion.

Although some authors have classified the two-phase flow combustion in three interaction levels [2, 40], as shown in Figure 3.9.
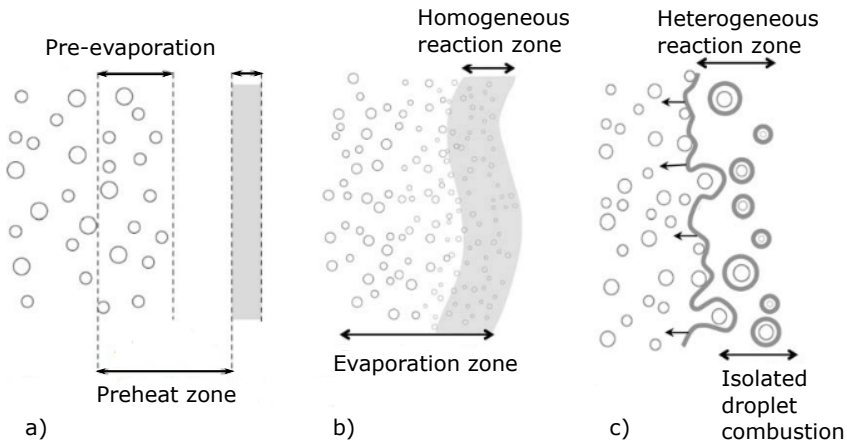
Figure 3.9: Illustration of the various interaction levels in two-phase combustion. a) Pre-vaporized flame. b) Homogeneous combustion. c) Heterogeneous combustion. (Adapted from [40])

In *pre-vaporized flame*, the combustion occurs after the complete droplet evaporation. This configuration results in a pure gaseous mixture at the front. This usual spray flame is only used to create a tiny, homogeneous droplet with a low density.

In *homogeneous two-phase combustion*, a concentrated and uniform spray of drops constantly supplies the flame front. Before reaching the reaction zone, the evaporation is not complete, and some drops interact with the flame front.

In *heterogeneous two-phase combustion*, the existence of drops has a significant wrinkling effect on the flame front. Furthermore, some of the biggest drops can exceed the reaction zone and burn in distinct combustion regimes, which will be discussed further below.

3.6.1   Combustion regime

The spray flame classification given by Chiu et al. [41] is a common one. The flame structure propagating throughout a drop spray within a pre-heated fuel at rest is defined in this classification. The combustion regimes are classified using a group number indicated G. The ratio between characteristic evaporation velocity to and the temperature diffusion velocity is represented by the number G. Candel et al. [42] provides the number of group G as a function of two parameters:

$$G \approx 5 \frac{N^{2/3}}{S} \qquad (3.24)$$

where N is the total number of drops and S is the separation factor, which is the ratio of the mean inter-droplet separation *deltas* to the flame radius δ_s that surrounds the single drop. If S decreases, the flame topology can transform from an individual combustion regime to a group regime. In Figure 3.10, two main types of spray flame may be recognized by fixing the separation number and changing the total number of droplets.

The first case is represented by $G >> 1$. Since the droplets are so close together, thermal diffusion inside the cloud is unlikely. Only an exterior fuel vapor layer is present in this configuration. Therefore, the flame occurs near the edge of the drop cloud. In the second instance, $G1$, it suggests that drops are sufficiently separated for hot gas to enter into the cloud. Each drop evaporates independently during this process, and combustion occurs surrounding each drop. Chiu (1982) incorporated novel combustion regimes. The first mode is characterized as external, while the second one as internal. In order to include the effect of the surrounding flow, Borghi [37, 43] completed

the initial classification proposed by Chiu et al. [41]. He incorporated three other parameters, which are: τ_f the characteristic time for combustion, δ_f is the flame thickness and τ_v the mean evaporation times of drops. If $\tau_f >> \tau_v$ the droplets evaporate quickly, and combustion is performed under a premixed regime.

In Figure 3.11 can be observed the combustion regimes proposed by Borghi [37, 43]. The organization of the droplets, which might be arbitrary, demands categorizing the mist of droplets into three groups:

- $S < 0.41$: The space between droplets is large enough for certain drops to burn independently.

- $0.41 < S < 0.73$: The existence of gas pockets and drop aggregation may be seen. The spray is comprised of dense and diluted regions.

- $S > 0.73$: Because of the drop concentration, combustion is difficult.
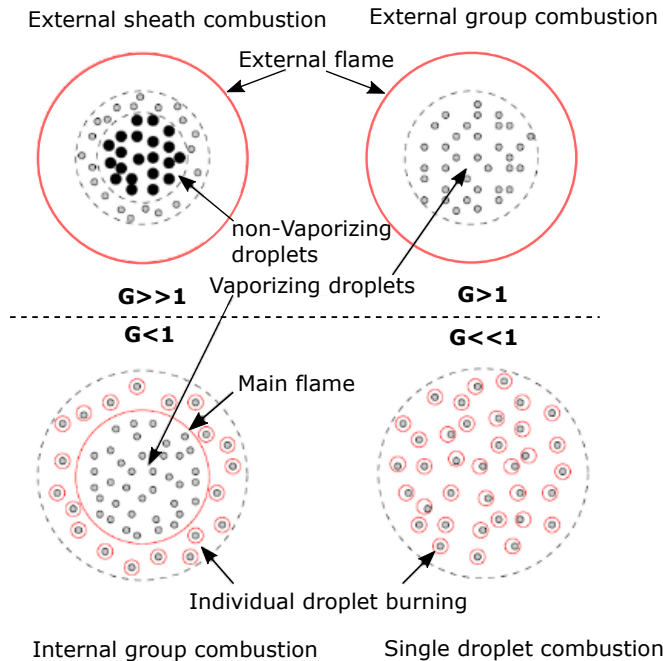
Figure 3.10: Schematic representation of the regimes of two-phase combustion based on the group number G. (Extracted from [41])
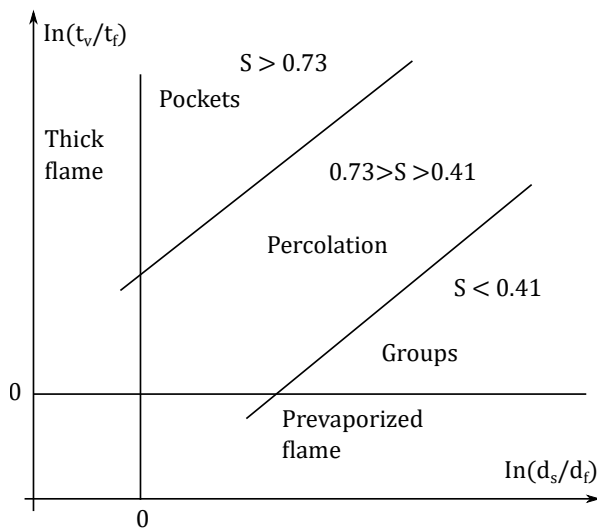
Figure 3.11: Borghi's diagram for laminar spray flames propagating through uniform and polydisperse drops. (Extracted from [43])

Some authorts recently made an improvement on the two previous approaches [44, 45]. Previous approaches proposed by Chiu and Borghi, in fact, are based on two significant assumptions: (*i*) the flow is initially at rest, and (*ii*) the concept of equivalence ratio is not incorporated. Domingo et al. [44] and Reveillon and Vervisch [45] offer three categories for combustion regime based on numerical studies and comparisons with the experimental work conducted by Cessou [46]. When the equivalency ratio is maximum, the external combustion regime is presented. The group combustion regime shows that drops form a rich zone in which combustion takes place first in premixed and subsequently in diffusion. The droplet groups burn under premixed conditions in this configuration, however, the large equivalence ratio restricts the diffusion flame's percolation inside the drop spray.

3.7   Soot formation

The use of liquid fuels in several applications is related to soot production, these fuels must be atomized and burned to perform a specific task, resulting in heterogeneous combustion, which generates favorable conditions that promote particle nucleation from Polycyclic Aromatic Hydrocarbons (PAH) and their subsequent growth [47]. The significant amount of soot results from interaction among several processes involved in real devices such as fuel evaporation

and combustion, convection, and radiation. Moreover, these phenomena occur simultaneously, being almost impossibility to decouple them, and making the direct investigation of such systems a truly challenging task.

In an attempt to understand the droplet combustion dynamics and soot formation, several computationally studies have been performed through Computational Fluid Dynamic (CFD) codes [48–51]. Some investigations have been directed towards the combustion of simpler, idealized systems like spherical droplets in microgravity conditions. Although they do not consider some phenomena and the sizes are still significantly larger, they give fundamental information about the complex coupling between the involved physical and chemical processes. For this reason, several experiments on soot formation in spherical droplets was performed through reduced-gravity experiments [52, 53]. The structure of the flame surrounding the droplet was next investigated by Mikami et al. [54], who used hooked thermocouples to show that the greatest temperature area, i.e., the reaction region, is situated outside of the yellow luminous zone, whose color is created by soot radiation. The transient evolution of soot volume fractions was quantified in succeeding investigations [55–57]: the highest values were found to be between 10 and 100 ppm, which is more than one order of magnitude larger than what was observed in gas-phase diffusion flames with the same fuels [58, 59].

Soot is a solid carbonaceous material formed during the pyrolysis of fuel at high temperatures [60, 61]. Soot is mostly formed of carbon, being C_8H a common empirical formulation [62]. However, additional elements can be detected in minimum amounts [62]. In terms of soot's structure, it is composed of soot particles grapes-like clusters of small spheres denominated primary particles or spherules [63, 64]. Recent studies in soot structure description have revealed that, despite the large diversity in spherule size, there is a relationship with aggregate size. These researches suggest that the growth of soot particles in conventional combustion systems follows a similar relation.

Although certain aspects remain unclear, significant research has contributed to the conclusion that soot formation originates with the formation of gas-phase molecular species from fuel, followed by the development of incipient rings, PAH growth, particle nucleation, heterogeneous surface reaction, and particle interactions [65]. Figure 3.12 depicts a theoretical schematic of this general physicochemical process, which is a frequently reviewed subject, with new results being added regularly.
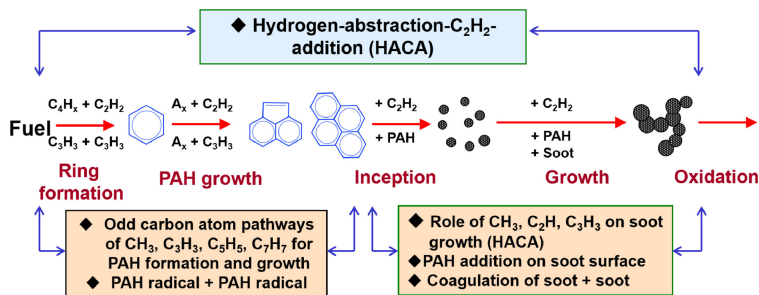
Figure 3.12: Schematic of overall pathways for soot formation. (Extracted from [65])

3.7.1 Gaseous soot precursors formation

The formation of PAHs is a crucial step between the solid soot particles and the gaseous fuel molecules. PAHs are produced from unsaturated hydrocarbons under fuel-rich conditions and serve as a basis upon which soot grows. Acetylene is the most important species among unsaturated hydrocarbons, not only for the production of PAHs and also for its growth [63, 66].

The formation of single-ring aromatic species is the initial point in the development of PAHs. While benzene is the initial aromatic ring, the chemical pathway to PAHs also includes the phenyl group and cyclopentadienyl. Numerous reactions have been proposed to define the first aromatic cycle generation, but it is still research in progress [67].

3.7.2 Physical phenomena

Figure 3.13 shows a graphical overview of the physical processes involved with the transition from gaseous soot precursors to the solid phase, with the consequent collisional phenomena. It includes processes that affect the overall mass-generated (nucleation and condensation), as well as processes that affect the soot number density (coagulation and agglomeration).

The appearance of the first soot particles is driven by nucleation. Several authors have underlined that even today particle nucleation is not well-known, and it is a frequent remaining review subject to understand the soot production. Glassman and Yetter [62] reported that nuclei do not contribute much to overall soot mass but are essential for mass expansion through surface growth. In fact, the rate of nuclei production is proportional to the amount of soot generated.
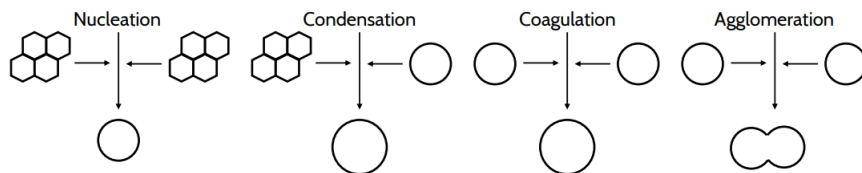
Figure 3.13: Physical phenomena in soot production. (Extracted from [68])

Both chemical growth and PAHs collision are the most fundamental mechanisms for explaining particle nucleation. In the first situation, nuclei arise as a consequence of PAHs chemical coalescence [69, 70], whereas, in the second instance, nuclei form as a result of physical coalescence [71, 72]. Neither of these pathways is capable of explaining the complex nucleation process on its own. On the one hand, the chemical coalescence pathways fail to describe nucleation in the presence of low H radical concentration. Nucleation through physical coalescence, on the other hand, is constrained by the necessity for difficult-to-form big PAHs, according to Wang and Chung [65].

Considering its limitations, physical coalescence of PAHs has been largely accepted as the primary source of soot nucleation. Pyrene dimerization has been frequently used in this context to describe the transition from the gaseous soot precursor phase to nuclei. Both computational and experimental results indicate that collisional events involving pyrene are an appropriate approach to synthesis the particle nucleation process [72–75].

Condensation is defined as the collision of PAHs in the gaseous phase with soot particles, and it is a process that contributes to the increase in soot mass. However, recent research has suggested that the condensation process is, to some extent, reversible [76]. These researches inspired computational investigations that provided promising findings while emphasizing the need for more research on the subject [73, 77–79].

Coagulation is the process through which soot particles collide with one another, which controls the soot number density, but it does not affect the total amount of soot generated. The border between colliding particles dissolves during the coagulation process, resulting in the formation of a new particle and a reduction in total surface area. According to Wang [47], the coagulation is more likely to produce a big soot particle (with a large surface area) and a compact soot particle (higher velocity in comparison to a big particle). As particles age, soot-soot interactions may result in an aggregation of stuck

particles rather than a new larger particle [80]. The latter stage is known as agglomeration, and it is a subprocess of coagulation.

3.7.3 Chemical phenomena

Surface growth and oxidation are two chemical processes that occur on the surface of soot particles. Both processes have an insignificant effect on soot number density, but their balance determines the majority of the overall soot mass-produced.

Surface growth is the process of adding mass to soot particles by the adsorption of gas-phase species, with acetylene being the most common contributor [81–83]. The surface growth process is not completely understood, although experimental studies have led to semi-empirical models based on first-order kinetics [83, 84]. Several authors [81, 85, 86], have suggested the presence of aging phenomena that produces surface growth rate to decrease with particle growth extent, adding to the subject's complexity.

Soot oxidation is known as the last phase described, despite the fact that it begins as soon as nuclei are formed and continues throughout the whole soot formation process. This is the only method that decreases the overall quantity of soot generated. Some species have been implicated in soot oxidation. Wang and Chung [65] suggested that OH and O_2 as the dominant species. According to Prieto [68], the first species is especially important for high-temperature oxidation. The second species demonstrated two different phenomena, one involving a reduction in reactivity as oxidation progressed and the other involving quicker oxidation for particles having curved PAH structures as opposed to planar PAHs. Several authors [63, 87, 88] have highlighted that OH an O_2 predominate on soot oxidation with less relevant contribution from O.

3.8 Summary

This section presented the fundamentals related to atomization, evaporation, spray combustion, and soot formation. The primary and secondary atomization regimes are defined and the factors that influence the atomization performance. Then, the mathematical functions used to describe diameter distributions are included. In order to understand how droplets, interact with the gas phase, exchange mass, energy, and momentum, the predictive models of evaporations and heating of the fuel droplet are also described. Additionally, essential characteristics of spray combustion are defined. Finally, soot formation and the pathways for soot are introduced.

References

[1]   Sánchez, A. L., Urzay, J., and Liñán, A. "The role of separation of scales in the description of spray combustion". In: *Proceedings of the Combustion Institute* 35.2 (2015), pp. 1549–1577. DOI: 10.1016/j.proci.2014.08.018.

[2]   Verdier, A. "Experimental study of dilute spray combustion". PhD thesis. Normandie Université, 2018, pp. 1–175.

[3]   Lefebvre, A. H. and Ballal, D. R. *Turbine Combustion Alternative Fuels and Emissions*. CRC Press, 2010, pp. 1–537.

[4]   Lefebvre, A. and McDonell, V. *Atomization and Sprays*. 2017, p. 300. DOI: 10.1016/0009-2509(90)87140-N.

[5]   Rayleigh, L. "On The Instability Of Jets". In: *Proceedings of the London Mathematical Society* s1-10.1 (1878), pp. 4–13. DOI: 10.1112/plms/s1-10.1.4.

[6]   Reitz, R. D. *Atomization and other breakup regimes of a liquid jet*. Princeton University, 1978.

[7]   Giusti, A. "Development of numerical tools for the analysis of advanced airblast injection systems for lean burn aero-engine combustors". PhD thesis. 2014.

[8]   Dumouchel, C. "On the experimental investigation on primary atomization of liquid streams". In: *Experiments in Fluids* 45.3 (2008), pp. 371–422. DOI: 10.1007/s00348-008-0526-0.

[9]   Marmottant, P. and Villermaux, E. "On spray formation". In: *Journal of Fluid Mechanics* 498.498 (2004), pp. 73–111. DOI: 10.1017/S0022112003006529.

[10]   Ashgriz, N. and Yarin, A. L. "Capillary Instability of Free Liquid Jets". In: *Handbook of Atomization and Sprays*. Springer US, 2011, pp. 3–53. DOI: 10.1007/978-1-4419-7264-4_1.

[11]   Brodkey, R. O. *The Phenomena of Fluid Motions*. Addison-Wesley, 1967, p. 737. DOI: 10.1017/S0022112068222267.

[12]   Pilch, M. and Erdman, C. A. "Use of breakup time data and velocity history data to predict the maximum size of stable fragments for acceleration-induced breakup of a liquid drop". In: *International Journal of Multiphase Flow* 13.6 (1987), pp. 741–757. DOI: 10.1016/0301-9322(87)90063-2.

[13] Guildenbecher, D. R., López-Rivera, C., and Sojka, P. E. "Secondary atomization". In: *Experiments in Fluids* 46.3 (2009), pp. 371–402. DOI: 10.1007/s00348-008-0593-2.

[14] Hinze, J. O. "Fundamentals of the hydrodynamic mechanism of splitting in dispersion processes". In: *AIChE Journal* 1.3 (1955), pp. 289–295. DOI: 10.1002/aic.690010303.

[15] Prevish, T. D. and Santavicca, D. A. "Turbulent breakup of hydrocarbon droplets at elevated pressures". In: *ILASS Americas, 11th annual conference on liquid atomization and spray systems*. Sacramento, CA, 1998, pp. 1–9.

[16] Koch, R. "Spray combustion". In: *Turbulent combustion*. 2011.

[17] Lefebvre, A. H. "Airblast atomization". In: *Progress in Energy and Combustion Science* 6.3 (1980), pp. 233–261. DOI: 10.1016/0360-1285(80)90017-9.

[18] Rosin, P. and Rammler, E. "The Laws Governing the Fineness of powdered coal". In: *Journal of the Institute of Fuel* 7 (1933), pp. 29–36.

[19] Liu, Z., Zheng, C., and Zhou, L. "A joint PDF model for turbulent spray evaporation/combustion". In: *Proceedings of the Combustion Institute* 29.1 (2002), pp. 561–568. DOI: 10.1016/S1540-7489(02)80072-4.

[20] O'Rourke, P. J. and Amsden, A. A. "The tab method for numerical calculation of spray droplet breakup". In: *SAE Technical Papers*. SAE International, 1987, pp. 1–10. DOI: 10.4271/872089.

[21] Abramzon, B. and Sirignano, W. A. "Droplet vaporization model for spray combustion calculations". In: *International Journal of Heat and Mass Transfer* 32.9 (1989), pp. 1605–1618. DOI: 10.1016/0017-9310(89)90043-4.

[22] Yuen, M. C. and Chen, L. W. "On Drag of Evaporating Liquid Droplets". In: *Combustion Science and Technology* 14.4-6 (1976), pp. 147–154. DOI: 10.1080/00102207608547524.

[23] Faeth, G. "Current status of droplet and liquid combustion". In: *Progress in Energy and Combustion Science* 3.4 (1977), pp. 191–224. DOI: 10.1016/0360-1285(77)90012-0.

[24] Castanet, G., Perrin, L., Caballina, O., and Lemoine, F. "Evaporation of closely-spaced interacting droplets arranged in a single row". In: *International Journal of Heat and Mass Transfer* 93 (2016), pp. 788–802. DOI: 10.1016/j.ijheatmasstransfer.2015.09.064.

[25]   Miller, R., Harstad, K., and Bellan, J. "Evaluation of equilibrium and non-equilibrium evaporation models for many-droplet gas-liquid flow simulations". In: *International Journal of Multiphase Flow* 24.6 (1998), pp. 1025–1055. DOI: 10.1016/S0301-9322(98)00028-7.

[26]   Yao, G. F., Abdel-Khalik, S. I., and Ghiaasiaan, S. M. "An investigation of simple evaporation models used in spray simulations". In: *Journal of Heat Transfer* 125.1 (2003), pp. 179–182. DOI: 10.1115/1.1517267.

[27]   Balachandar, S. and Eaton, J. K. "Turbulent Dispersed Multiphase Flow". In: *Annual Review of Fluid Mechanics* 42.1 (2010), pp. 111–133. DOI: 10.1146/annurev.fluid.010908.165243.

[28]   Zonta, F., Marchioli, C., and Soldati, A. "Direct numerical simulation of turbulent heat transfer modulation in micro-dispersed channel flow". In: *Acta Mechanica* 195.1-4 (2008), pp. 305–326. DOI: 10.1007/s00707-007-0552-7.

[29]   Elghobashi, S. and Truesdell, G. C. "On the two-way interaction between homogeneous turbulence and dispersed solid particles. I: Turbulence modification". In: *Physics of Fluids A* 5.7 (1992), pp. 1790–1801. DOI: 10.1063/1.858854.

[30]   Squires, K. D. and Eaton, J. K. "Particle response and turbulence modification in isotropic turbulence". In: *Physics of Fluids A: Fluid Dynamics* 2.7 (1990), pp. 1191–1203. DOI: 10.1063/1.857620.

[31]   Gore, R. and Crowe, C. "Effect of particle size on modulating turbulent intensity". In: *International Journal of Multiphase Flow* 15.2 (1989), pp. 279–285. DOI: 10.1016/0301-9322(89)90076-1.

[32]   Eaton, J. and Fessler, J. "Preferential concentration of particles by turbulence". In: *International Journal of Multiphase Flow* 20.SUPPL. 1 (1994), pp. 169–209. DOI: 10.1016/0301-9322(94)90072-8.

[33]   Bray, K. N. C., Champion, M., and Libby, P. A. "The Interaction Between Turbulence and Chemistry in Premixed Turbulent Flames". In: Springer, New York, NY, 1989, pp. 541–563. DOI: 10.1007/978-1-4613-9631-4_26.

[34]   Peters, N. *Turbulent Combustion.* Cambridge University Press, 2000. DOI: 10.1017/CBO9780511612701.

[35]   Poinsot, T. and Veynante, D. *Theoretical and numerical combustion.* 2005.

[36] Damköhler, G. "Der Einfluss der Turbulenz auf die Flammengeschwindigkeit in Gasgemschen". In: *Zeitschrift für Elektrochemie und angewandte physikalische Chemie* 46.11 (1940), pp. 601–652. DOI: `0.1002/bbpc.18980052102`.

[37] Borghi, R. "The links between turbulent combustion and spray combustion and their modelling". In: *8th International Symposium on Transport Phenomena in Combustion*. 1996, pp. 1–18.

[38] PETERS, N. "The turbulent burning velocity for large-scale and small-scale turbulence". In: *Journal of Fluid Mechanics* 384 (1999), pp. 107–132. DOI: `10.1017/S0022112098004212`.

[39] Jenny, P., Roekaerts, D., and Beishuizen, N. "Modeling of turbulent dilute spray combustion". In: *Progress in Energy and Combustion Science* 38.6 (2012), pp. 846–887. DOI: `10.1016/j.pecs.2012.07.001`.

[40] Damien, M. D. "Modelisation de la combustion d'un spray dans un bruleur aeronautique". PhD thesis. Université de Toulouse, 2016.

[41] Chiu, H. H., Kim, H. Y., and Croke, E. J. "Internal group combustion of liquid droplets". In: *Symposium (International) on Combustion* 19.1 (1982), pp. 971–980. DOI: `10.1016/S0082-0784(82)80273-7`.

[42] Candel, S., Lacas, F., Darabiha, N., and Rolon, C. "Group combustion in spray flames". In: *Multiphase Science and Technology* 11.1 (1999), pp. 1–18. DOI: `10.1615/MultScienTechn.v11.i1.10`.

[43] Borghi, R. "Turbulent combustion modelling". In: *Progress in Energy and Combustion Science* 14.4 (1988), pp. 245–292. DOI: `10.1016/0360-1285(88)90015-9`.

[44] Domingo, P., Vervisch, L., and Réveillon, J. "DNS analysis of partially premixed combustion in spray and gaseous turbulent flame-bases stabilized in hot air". In: *Combustion and Flame* 140.3 (2005), pp. 172–195. DOI: `10.1016/j.combustflame.2004.11.006`.

[45] Reveillon, J. and Vervisch, L. "Analysis of weakly turbulent dilute-spray flames and spray combustion regimes". In: *J. Fluid Mech* 537 (2005), pp. 317–347. DOI: `10.1017/S0022112005005227`.

[46] Cessou, A. "Simple description of the combustion structures in the stabilization stage of a spray jet flame". In: *Atomization and Sprays* 9.1 (1999), pp. 1–27. DOI: `10.1615/atomizspr.v9.i1.10`.

[47] Wang, H. "Formation of nascent soot and other condensed-phase materials in flames". In: *Proceedings of the Combustion Institute* 33.1 (2011), pp. 41–67. DOI: `10.1016/j.proci.2010.09.009`.

[48] Marchese, A., Dryer, F., and Nayaman, V. "Numerical modeling of isolated n-alkane droplet flames: initial comparisons with ground and space-based microgravity experiments". In: *Combustion and Flame* 116.3 (1999), pp. 432–459. DOI: 10.1016/S0010-2180(98)00109-6.

[49] Dietrich, D. L. et al. "Droplet Combustion Experiments Aboard the International Space Station". In: *Microgravity Science and Technology* 26.2 (2014), pp. 65–76. DOI: 10.1007/s12217-014-9372-2.

[50] Kumar, S., Ray, A., and Kale, S. R. "A soot model for transient, spherically symmetric n -heptane droplet combustion". In: *Combustion Science and Technology* 174.9 (2002), pp. 67–102. DOI: 10.1080/00102200290021380.

[51] Avedisian, C. T. "Recent Advances in Soot Formation from Spherical Droplet Flames at Atmospheric Pressure". In: *Journal of Propulsion and Power* 16.4 (2000), pp. 628–635. DOI: 10.2514/2.5619.

[52] Jackson, G. S. and Avedisian, C. T. "The effect of initial diameter in spherically symmetric droplet combustion of sooting fuels". In: *Proceedings of the Royal Society of London. Series A: Mathematical and Physical Sciences* 446.1927 (1994), pp. 255–276. DOI: 10.1098/rspa.1994.0103.

[53] Shaw, B., Dryer, F., Williams, F., and Haggard, J. "Sooting and disruption in spherically symmetrical combustion of decane droplets in air". In: *Acta Astronautica* 17.11-12 (1988), pp. 1195–1202. DOI: 10.1016/0094-5765(88)90008-2.

[54] Mikami, M., Niwa, M., Kato, H., Sato, J., and Kono, M. "Clarification of the flame structure of droplet burning based on temperature measurement in microgravity". In: *Symposium (International) on Combustion* 25.1 (1994), pp. 439–446. DOI: 10.1016/S0082-0784(06)80672-7.

[55] Choi, M. Y. and Kyeong-Okk, L. "Investigation of sooting in microgravity droplet combustion". In: *Symposium (International) on Combustion* 26.1 (1996), pp. 1243–1249. DOI: 10.1016/S0082-0784(96)80341-9.

[56] Lee, K. O., Manzello, S. L., and Choi, M. Y. "The effects of initial diameter on sooting and burning behavior of isolated droplets under microgravity conditions". In: *Combustion Science and Technology* 132.1-6 (1998), pp. 139–156. DOI: 10.1080/00102209808952013.

[57] Manzello, S. L. et al. "The burning of large n-heptane droplets in microgravity". In: *Proceedings of the Combustion Institute* 28.1 (2000), pp. 1079–1086. DOI: 10.1016/S0082-0784(00)80317-3.

[58] Kashif, M., Guibert, P., Bonnety, J., and Legros, G. "Sooting tendencies of primary reference fuels in atmospheric laminar diffusion flames burning into vitiated air". In: *Combustion and Flame* 161.6 (2014), pp. 1575–1586. DOI: 10.1016/j.combustflame.2013.12.009.

[59] Kashif, M., Bonnety, J., Matynia, A., Da Costa, P., and Legros, G. "Sooting propensities of some gasoline surrogate fuels: Combined effects of fuel blending and air vitiation". In: *Combustion and Flame* 162.5 (2015), pp. 1840–1847. DOI: 10.1016/j.combustflame.2014.12.005.

[60] Marchal, C. "Modélisation de la formation et de l'oxydation des suies dans un moteur automobile". PhD thesis. 2009, pp. 1–177.

[61] Carbonell, D. "Numerical studies of diffusion flames. Special emphasis on flamelet concept and soot formation". PhD thesis. Universitat Politècnica de Catalunya, 2008. DOI: 10.13140/2.1.1581.7924.

[62] Glassman, I. and Yetter, R. A. "Environmental Combustion Considerations". In: *Combustion.* Elsevier, 2008, pp. 409–494. DOI: 10.1016/B978-0-12-088573-2.00008-7.

[63] Warnatz, J., Maas, U., and Dibble, R. W. *Combustion: Physical and chemical fundamentals, modeling and simulation, experiments, pollutant formation.* Springer Berlin Heidelberg, 2006, pp. 1–378. DOI: 10.1007/978-3-540-45363-5.

[64] Heywood, J. *Internal Combustion Engine Fundamentals.* 2018, p. 1056.

[65] Wang, Y. and Chung, S. H. "Soot formation in laminar counterflow flames". In: *Progress in Energy and Combustion Science* 74 (2019), pp. 152–238. DOI: 10.1016/j.pecs.2019.05.003.

[66] H. Bockhorn, ed. *Soot Formation in Combustion.* Vol. 59. Springer Series in Chemical Physics. Berlin, Heidelberg: Springer Berlin Heidelberg, 1994. DOI: 10.1007/978-3-642-85167-4.

[67] Aubagnac-karkar, D. "Sectional soot modeling for Diesel RANS simulations". PhD thesis. IFP - Energies Nouvelles, 2015, p. 152.

[68] Prieto, L. M. P. "CFD Modeling of Combustion and Soot Production in". PhD thesis. UPV, 2020, pp. 1–157.

[69] Violi, A., Sarofim, A. F., and Voth, G. A. "Kinetic monte carlo-molecular dynamics approach to model soot inception". In: *Combustion Science and Technology.* Vol. 176. 5-6. Taylor and Francis Inc., 2004, pp. 991–1005. DOI: 10.1080/00102200490428594.

[70]   D'Anna, A. "Combustion-formed nanoparticles". In: *Proceedings of the Combustion Institute* 32.1 (2009), pp. 593–613. DOI: 10.1016/j.proci.2008.09.005.

[71]   Frenklach, M. and Wang, H. "Detailed modeling of soot particle nucleation and growth". In: *Symposium (International) on Combustion* 23.1 (1991), pp. 1559–1566. DOI: 10.1016/S0082-0784(06)80426-1.

[72]   Schuetz, C. A. and Frenklach, M. "Nucleation of soot: Molecular dynamics simulations of pyrene dimerization". In: *Proceedings of the Combustion Institute* 29.2 (2002), pp. 2307–2314. DOI: 10.1016/S1540-7489(02)80281-4.

[73]   Aubagnac-Karkar, D., El Bakali, A., and Desgroux, P. "Soot particles inception and PAH condensation modelling applied in a soot model utilizing a sectional method". In: *Combustion and Flame* 189 (2018), pp. 190–206. DOI: 10.1016/j.combustflame.2017.10.027.

[74]   Wang, H. et al. "A comparison study on the combustion and sooting characteristics of base engine oil and n-dodecane in laminar diffusion flames". In: *Applied Thermal Engineering* 158.113812 (2019), pp. 1–6. DOI: 10.1016/j.applthermaleng.2019.113812.

[75]   Mitra, T., Zhang, T., Sediako, A. D., and Thomson, M. J. "Understanding the formation and growth of polycyclic aromatic hydrocarbons (PAHs) and young soot from n-dodecane in a sooting laminar coflow diffusion flame". In: *Combustion and Flame* 202 (2019), pp. 33–42. DOI: 10.1016/j.combustflame.2018.12.010.

[76]   Siegmann, K., Sattler, K., and Siegmann, H. "Clustering at high temperatures: carbon formation in combustion". In: *Journal of Electron Spectroscopy and Related Phenomena* 126.1-3 (2002), pp. 191–202. DOI: 10.1016/S0368-2048(02)00152-4.

[77]   Eaves, N., Dworkin, S., and Thomson, M. "The importance of reversibility in modeling soot nucleation and condensation processes". In: *Proceedings of the Combustion Institute* 35.2 (2015), pp. 1787–1794. DOI: 10.1016/j.proci.2014.05.036.

[78]   Veshkini, A., Eaves, N. A., Dworkin, S. B., and Thomson, M. J. "Application of PAH-condensation reversibility in modeling soot growth in laminar premixed and nonpremixed flames". In: *Combustion and Flame* 167 (2016), pp. 335–352. DOI: 10.1016/j.combustflame.2016.02.024.

[79]   Eaves, N. A., Dworkin, S. B., and Thomson, M. J. "Assessing relative contributions of PAHs to soot mass by reversible heterogeneous nucleation and condensation". In: *Proceedings of the Combustion Institute* 36.1 (2017), pp. 935–945. DOI: 10.1016/j.proci.2016.06.051.

[80]   Frenklach, M. "Reaction mechanism of soot formation in flames". In: *Physical Chemistry Chemical Physics* 4.11 (2002), pp. 2028–2037. DOI: 10.1039/b110045a.

[81]   Haynes, B. and Wagner, H. "Soot formation". In: *Progress in Energy and Combustion Science* 7.4 (1981), pp. 229–273. DOI: 10.1016/0360-1285(81)90001-0.

[82]   Calcote, H. "Mechanisms of soot nucleation in flames - A critical review". In: *Combustion and Flame* 42.C (1981), pp. 215–242. DOI: 10.1016/0010-2180(81)90159-0.

[83]   Harris, S. J. and Weiner, A. M. "Surface Growth of Soot Particles in Premixed Ethylene/Air Flames". In: *Combustion Science and Technology* 31.3-4 (1983), pp. 155–167. DOI: 10.1080/00102208308923637.

[84]   Sunderland, P. and Faeth, G. "Soot formation in hydrocarbon/air laminar jet diffusion flames". In: *Combustion and Flame* 105.1-2 (1996), pp. 132–146. DOI: 10.1016/0010-2180(95)00182-4.

[85]   Harris, S. J. and Weiner, A. M. "Determination of the Rate Constant for Soot Surface Growth". In: *Combustion Science and Technology* 32.5-6 (1983), pp. 267–275. DOI: 10.1080/00102208308923661.

[86]   Homann, K. and Wagner, H. "Some new aspects of the mechanism of carbon formation in premixed flames". In: *Symposium (International) on Combustion* 11.1 (1967), pp. 371–379. DOI: 10.1016/S0082-0784(67)80161-9.

[87]   Cavaliere, A., Barbella, R., Ciajolo, A., D'anna, A., and Ragucci, R. "Fuel and soot oxidation in diesel-like conditions". In: *Symposium (International) on Combustion* 25.1 (1994), pp. 167–174. DOI: 10.1016/S0082-0784(06)80641-7.

[88]   Stanmore, B. R., Brilhac, J. F., and Gilot, P. "The oxidation of soot: a review of experiments, mechanisms and models". In: *Carbon* 39.15 (2001), pp. 2247–2268. DOI: 10.1016/S0008-6223(01)00109-9.

Chapter 4
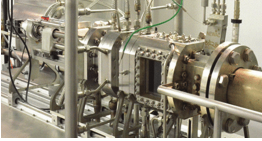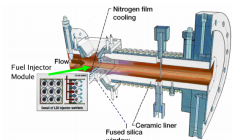
Review of experimental configurations and annular spray burner design

4.1 Introduction

Experimentally research is essential to understand the theoretical issues of spray combustion and necessary to support engine suppliers in designing high-performance, low-emission combustors for engine propulsion systems. It is becoming more important to do research work in combustion sciences and exploratory development of combustors for gas turbine systems. Therefore, several experimental test benches have been developed to work at extreme conditions (i.e., high temperature and high pressure) found in both ground and aeronautical gas turbines. Nowadays, several test facilities capable of recreating these extreme operating conditions are now available at various combustion research institutes throughout the world. In Table 4.1 are listed some facilities with similar operational capabilities and combustion chamber sizes.

In facilities listed in Table 4.1 and others, Lean-Premixed (LP) aero-engine injection system has been investigated experimentally through optical techniques. Therefore, several experiments are carried out under appropriate operating conditions up to high pressures and utilizing commercial kerosene as fuel [5]. Nevertheless, because of critical conditions such as high pressure

Table 4.1: Summary of high-pressure and high-temperature facilities, where h, w, and l are the height, width, and length of the combustion chamber, respectively.

Image Investigation center (test bench)	Maximum air mass flow rate [kg s^{-1}]	Maximum Pressure [MPa]	Maximum air inlet temp. [K]	Chamber size (h, w) l [mm]
CORIA (HERON)	0.3	2	900	(90, 100) l= 50
DLR (BOSS)[1]	2.3	2	900	(140, 140) l= 50
ONERA (LACOM) [2]	1	5	900	(105, 105) l= 82
NASA Glenn Research Center (CE-5) [3]	4.5	2.5	870	(76, 76)
LUND (HPC rig) [4]	1.3	1.6	650	(100, 100)

and temperature, optical diagnostics are more difficult to implement than on canonical setups, and some diagnostics would not be conducted under these conditions. Furthermore, these extreme conditions demand the use of a combustion chamber design able to resist these critical conditions. In most situa-

tions, combustion chambers have very limited optical access to conduct laser diagnostics, and combustion chamber confinement is necessary to support the load produced by the pressure. Computational Fluid Dynamics (CFD) has taken an active essential role in the design of modern aircraft engines in the last decades, particularly in the development phase. These studies have confirmed that numerical simulations are efficacy for understanding the mechanisms that control the combustion process. Nowadays, the numerical results accord with the experimental measurements for the description of the carrier phase and dispersed. Nevertheless, because of the complexity of the combustion models, predicting flame structures is more challenging. The absence of experimental results in the real configurations complicates the task of selecting the appropriate model. In this context, many laboratories have produced several experimental measures in order to have a better understanding of the mechanisms of combustion. Finally, when novel diagnoses are developed, databases are becoming more prevalent. The following section provides a review of some current test benches for studying the spray jet flame; these studies provide databases to contrast the CFD results. Also, this section introduces the annular spray burner design, injection system and high-flow and high-temperature facility.

4.2 Spray jet flame experimental configurations

4.2.1 Unconfined burners

To overcome the difficulties encountered in real geometries (e.g., small optical accesses and measurements that are likely affected by extreme conditions such as pressure and temperature), the spray flame structure is mostly explored experimentally through canonical setup. This configuration consists of a central pressure swirl atomizer or air-blast atomizer surrounded by an air co-flow stream with varying thermo-physical characteristics (temperature, composition, and velocity). This co-flow allows for the stabilization of a flame downstream of the injection with a wide range of flame structures. The pioneer works of Cessou [6] and Goix et al. [7] investigated the flame structures in the stabilization zones of a two-phase jet flame atomized by a coaxial air-blast atomizer. They proposed that the flame had a structure of two diverging and opposing diffusion-like fronts based on quantitative OH-PLIF observations. They also observed that both the atomization process and the spatial distribution of fuel drop had a significant impact on flame structures. Friedman and Renksizbulut [8] also observed that the spray flame in their jet spray flame burner working with a pressurized fuel injector and a big bluff-body had a

double reaction zone structure with air co-flow off but a single reaction zone with air co-flow on (Figure 4.1).
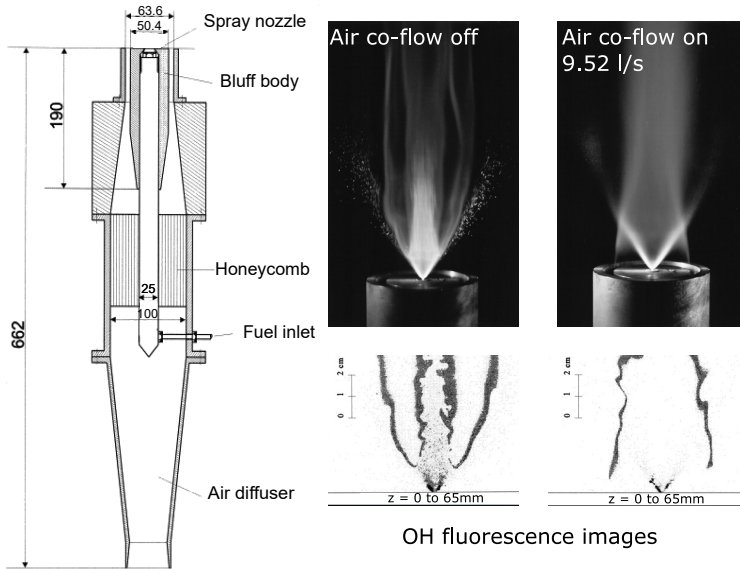
Figure 4.1: Burner system cross section studied by Friedman and Renksizbulut [8] with all dimensions in millimeters.

Marley et al. [9, 10] studied the impact of air co-flow rate in a spray burner designed to provide a flat air velocity profile at the exit of the co-flow region, and the conclusions were slightly different. They observed through OH-PLIF measurements distinct flame behaviors for co-flow and no co-flow conditions because of the changes in the oxidizer flow field. A double flame structure, visible as two diverging flame fronts, was also seen, comprised of an outer diffusion flame and an interior structure that changes from mixing governed to partially premixed combustion downstream of the leading edge. The structure was modified in the absence of co-flow, and a double reaction zone was still detected, but with an inner structure that burned sporadically with areas of local extinction, which occurred often at the most upstream places towards the leading edge. Cléon et al. [11] examined experimentally the influence of CO_2 dilution on the structure and stability of a spray oxyfuel flame experimentally. The amount of CO_2 had a significant impact on the chemical time and flame temperature, as well as the vaporization time and size dispersion of fuel droplets. Reddy et al. [12] studied experimentally the effect of co-flow conditions, fuel injection pressure and nitrogen dilution on liquid spray

flame characteristics, reporting that increasing the SMD causes variations in the lifted flame's stability point. The flame lift-off height increases with N_2 dilution as contrasted to ambient air co-flow. Preheating the co-flow stream improves drop evaporation and mixing, resulting in increased flame stability. Experiments using academic setups like counterflow flames [13], have also been conducted, allowing for the study and isolation of specific physical processes to help to understand such as flame structure and stability.

Several investigation institutions have designed new experimental facilities to conduct measurements of the disperse and carrier phase, for both non-reactive and reactive conditions, in order to better understand the droplets/turbulence/flame interactions and to enhance the modeling capabilities of turbulent spray reacting flows. Most of these recent researches have been coordinated by international workshops on Turbulent Combustion of Sprays (TCS) [14].

Sydney Spray Burner designed by Masri and co-workers [15–17], is presented in Figure 4.2. It includes a pilot spray burner in which liquid fuel (ethanol or acetone) is atomized into the air co-flow by a nebulizer positioned upstream within the spray nozzle. Their study has generated large data on the phenomena of interest in dilute sprays, including drop dispersion, drop evaporation, turbulence/drop interaction, and drop/flame interactions. Several of the experimental conditions are concerned with the extinction limits close to the blow-off limits. Broad OH areas, and also holes in the OH profile indicate potential local extinction. Additionally, a detailed study of the spray boundary conditions was conducted, including a systematic modification of variables, resulting in a large database suitable for rigorous validation tests of spray flame models.

Figure 4.3 shows the CORIA Rouen Spray Burner (CRSB) developed in CORIA research institute, which is an atmospheric unconfined burner, composed of an external annular non-swirling air co-flow and a pressurized swirl injector to atomize liquid fuels. This burner has been used to study the spray combustion, from the carrier and dispersed phase characterization to the flame and stabilization mechanisms. Verdier et al. [18] used laser techniques such as PDA, Laser-Induced Fluorescence of OH radical (HS-OH-PLIF) and High-Speed Particle Image Velocimetry (HS-PIV) to measure drop size and velocity, flame structure and velocity fields, respectively, of an n-Heptane spray jet flame. They observed a double flame structure with inner and outer reactions zones, where fuel drops are still present and interact with the reaction zones. Additionally, Verdier et al. [19] also employed Global Rainbow Refractometry Technique (GRT) to measure drop temperature in different regions of
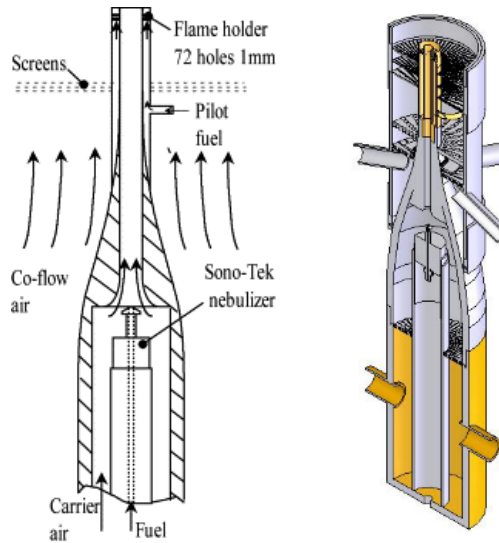
Figure 4.2: Schematic of the Sydney University spray burner [15].

the spray jet flame, reporting that the fuel temperature distribution near the flame front has a bimodal structure. It is primarily due to the contribution of drops placed in fresh gases as well as drops that may have already exceeded the flame front.
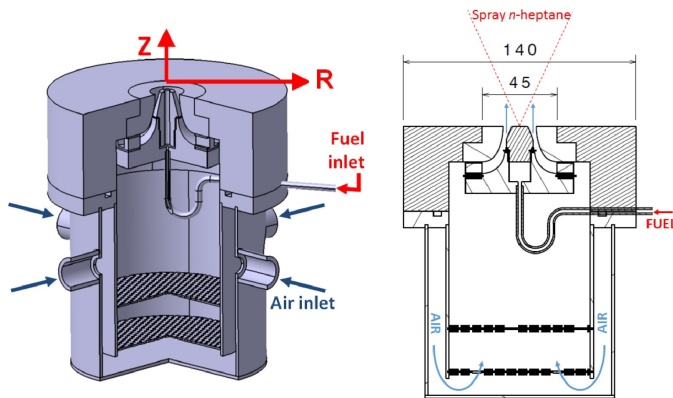
Figure 4.3: Schematic representation of the CORIA Rouen Spray Burner with relevant dimensions in millimeters [18].

Figure 4.4 depicts a schematic of the Delft Spray burner, which was designed by Gounder et al. [16] and Correia Rodrigues et al. [20] to study spray

combustion in Moderate or Intense Low-Oxygen Dilution (MILD) conditions, which are based on the massive recirculation of hot combustion products into the reactants. The burner consists of a pressure-swirl atomizer that produces a spray of fine fuel droplets issuing in a co-flow of either air or hot combustion products, which are generated by a secondary burner. It consists of a hexagonal packing arrangement of identical 5 mm diameter vertical pipes with each end welded to perforated plates. Laser Doppler Anemometry (LDA), Phase Doppler Anemometry (PDA) and Coherent Anti-Stokes Raman Scattering (CARS) techniques were used to evaluate the spray flame structure and provide an explanation of the stabilization characteristics of sprays. They found that the variation of both oxygen dilution and co-flow temperature generates a change in the local flame type. They also observed an increase of the flame lift-off height for lower co-flow bulk temperatures, which was related to the increased in the time needed for the droplet vaporization and an increased in the chemical time scale.
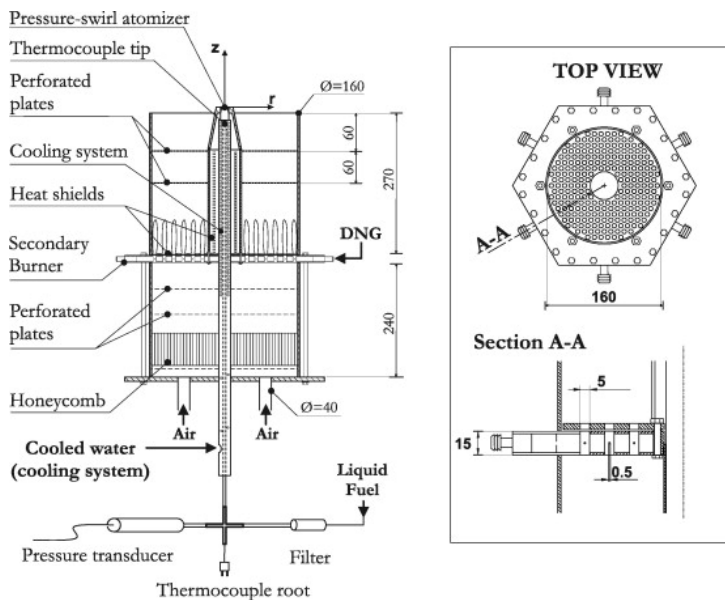
Figure 4.4: Schematic of the burner facility with relevant dimensions in millimeters [20].

4.2.2   Confined burners

In order to increase the performance and reduce emissions of the combustion chambers, new experimental configurations have been explored, as well as new combustion methodologies, which will use in the next generation of gas turbines. The LDI combustion technology is designed to operate under extreme operating conditions (compression ratios up to 60:1 and peak temperature of approximately 1900 K)[21]. In the LDI combustor, all the air flow is forced to pass through an air swirler and the fuel-air mixing process is carried out inside the combustor without premixing. In this part, homogenous and quick mixing of the fuel is decisive for the combustion performance and emission production. For this aim, several research groups have designed atmospheric confined test benches supplied with swirling air co-flow for various purposes, such as providing a database for numerical analysis on the LDI combustion, to understand the fuel-air mixing process in a specific configuration and provide a departure point for future combustor design.

The Cambridge Spray Burner presented in Figure 4.5 consists of a confined swirl burner arrange with a pressurized swirl hollow cone injector to produce an n-Heptane spray flame. Yuan et al. [22] used some optical techniques such as high-speed OH-PLIF and joint PLIF measurements of CH_2O and OH in a spray flame at conditions close to the extinction to explore the local flame structure, the reaction zones and local extinction holes. They found that $CH_2O \times$ OH regions followed very well the OH regions, indicating that high-speed OH-PLIF measurements could be a reliable marker for heat release regions in swirling spray flames.

ONERA has designed the Mercato test rig to study two-phase combustion in a realistic helicopter engine configuration [24]. This experimental facility can operate at pressures ranging from 0.5 to 1 bar and air temperatures ranging from 233 to 473 K, allowing it to simulate high altitude conditions and therefore test the reignition reliability. The fuel is liquid kerosene that is atomized at temperatures ranging from 233 K to ambient temperature. The combustion chamber is a square section chamber of $130{\times}130\,mm^2$ and incorporates Quartz windows for optical access. The air is injected into the plenum via a channel before passing through the swirler, where it is forced into a rotating motion. A Simplex pressure-swirl atomizer injects fuel into the chamber at the intake. Finally, for ignition, a spark plug installed on the combustion chamber's wall is employed. Figure 4.6 shows a schematic of the test rig. Despite its simplicity, the Mercato design includes a swirler, an injection system, and a spark plug, all of which are typical of true aviation engines.
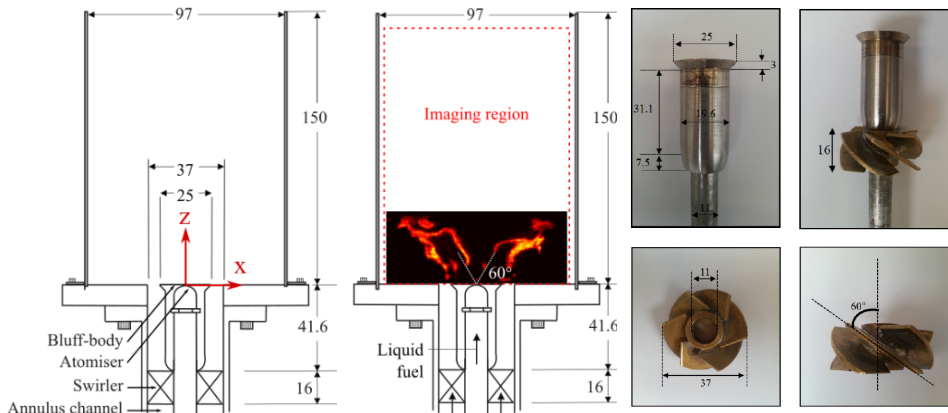
Figure 4.5: Swirling spray burner geometry of the Cambridge University with relevant dimensions in millimeters [23].
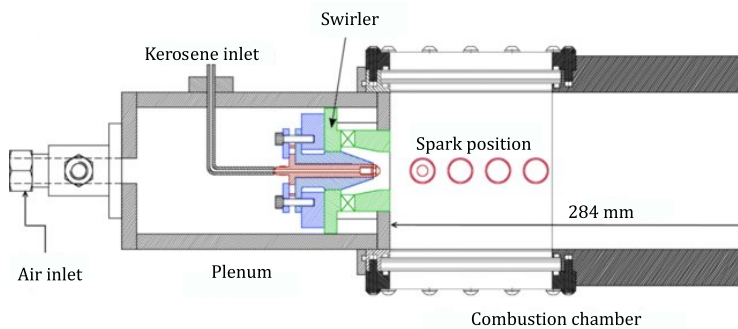
Figure 4.6: Schematic representation of the Mercato test rig [24].

The single-injector KIAI-Spray facility in CORIA research lab is the two-phase flow version of the original KIAI burner, which was designed to operate in gaseous configuration, previously investigated by Cordier [25]. The burner consists of a square section chamber of $100 \times 100 \, \mathrm{mm^2}$ and a height of $260 \, \mathrm{mm}$, as shown in Figure 4.7. The burner has been equipped with an exhaust convergent nozzle at the top of the chamber to avoid possible external air entries. In addition, the swirl co-flow is generated by a radial swirler coupled at the air duct and composed of 18 rectangular channels inclined at 45°. The injector system has been provided with a simplex pressure swirl injector, which atomized a hollow cone spray pattern with an 80° opening. Marrero-Santiago et al. [26, 27] investigated the spray ignition and local fuel flow properties of

an n-heptane spray flame under ultra-lean conditions ($\phi_{global} = 0.61$) through different optical techniques (e.g., PIV, PDA and Toluene-PLIF). They found that the outer recirculation zone (ORZ) has a flammability factor close to 1 and is the region with the highest ignition probability of success ($\sim 80\,\%$). They also reported a very high correlation between de ignition probability and the air velocity and turbulent kinetic energy.
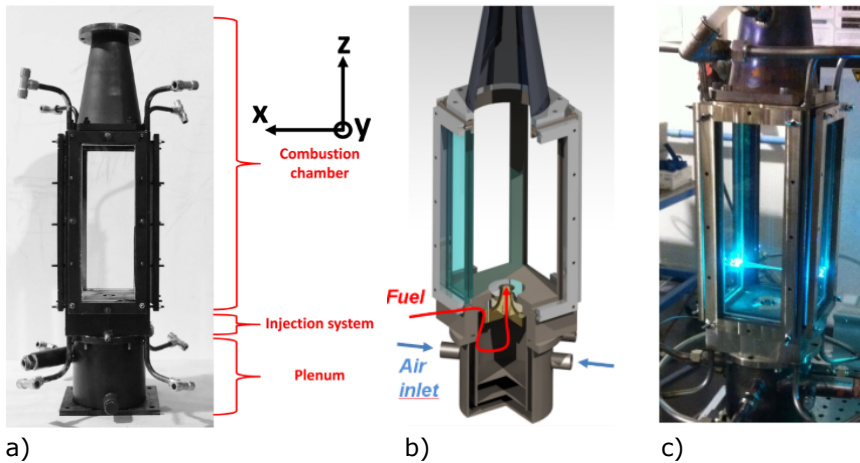
Figure 4.7: a) Original KIAI burner [25], b) Render of the KIAI-Spray burner CAD design with detail of the air plenum and fuel injection system, c) photograph of the burner during the PDA measurements [28].

The Institute of Propulsion Technology at the German Aerospace Center (DLR) has also developed an Atmospheric Primary Zone (APZ) test rig in order to investigate and characterize the burner flow filed at atmospheric pressure, depicted in Figure 4.8, in which the single fuel nozzle is located in the center of the square base area. Additionally, this test bench has been used to study air-blast atomizers, cooling methods, and wall materials. Willert et al. [29] performed an experimental investigation using both PIV and Doppler Global Velocimetry (DGV) to obtain volumetric, three-component velocity data sets of reacting flow field.

To evidence the potential of the LDI combustor, the NASA Glenn Research Center has extensively investigated this type of combustor, both experimentally and computationally. Tacina et al. [21] studied the LDI concept in a single injection configuration for both reactive and non-reactive conditions at ambient pressure and temperature. Figure 4.9 shows the single-element LDI test bench (flame tube), which consists of a fuel injection system, air swirler,
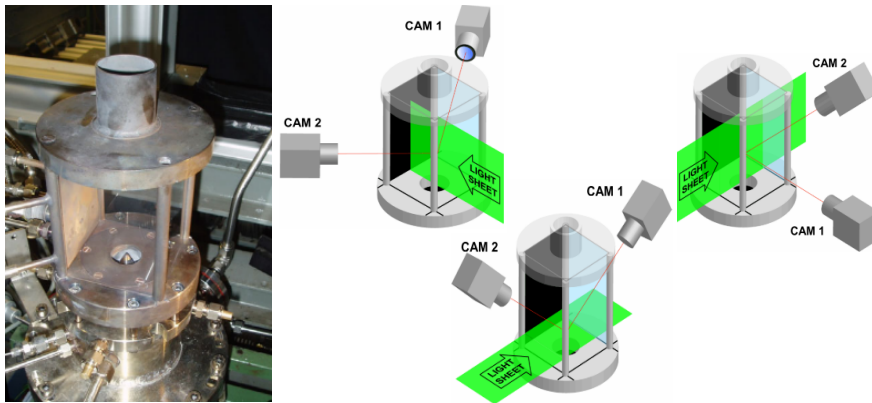
Figure 4.8: Atmospheric Primary Zone (APZ) and three stereoscopic PIV configurations [29].

and a converging-diverging venturi. The air swirler is a vane-annular swirler including six helicoidal axial vanes with downstream vane angles of 60°. They conducted Phase Doppler Particle Analyzer (PDPA) measurements to determine the spray velocity and droplet size distribution at different axial locations within the combustion chamber. They also reported that the strong swirl flow produced by the helicoidal vanes affects the mean droplet diameter profiles, resulting in more uniform drop sizes. Finally, they found that the interaction between liquid and gas phases produces a decrease in the recirculation zone during the combustion process.
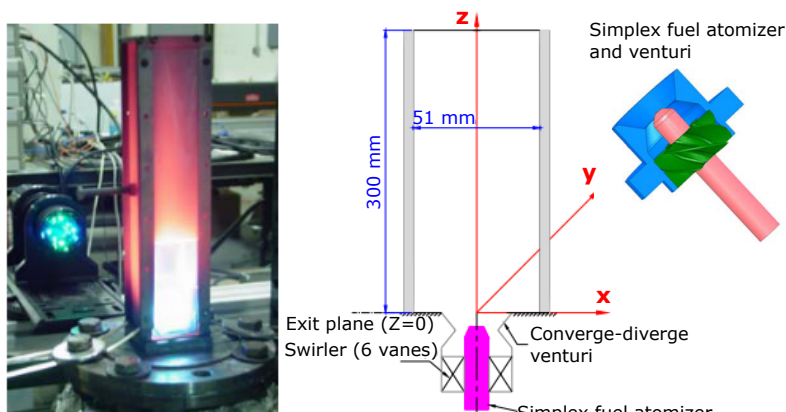
Figure 4.9: NASA's single-element LDI burner [21].

4.3 Spray burner design

As was mentioned previously, the LDI concept is a potential technology to replace the existing combustion systems for aircraft engines. This technology has evidenced a promise reduction of NO_x emissions more than the systems used currently in the aero gas turbine. Additionally, the experiments have demonstrated good flame-holding ability and extensive stability limits. The results are very encouraging, but the measurements are limited and complex to perform (i.e., the experiments have not described completely the mixing and combustion processes). The experiments for the single-element LDI are necessary to validate the computational models and then move much more complex configurations. Therefore, the interest in continuing investigating this type of technology, leading to consider the present research to aim to understand the fundamental characteristics of the LDI concept, which contribute to the reduced NO_x emissions. In this regard, a combustor has been designed to investigate experimentally under both non-reacting cold flow and reacting spray combustion. The design was based on the burners presented previously introduced [21, 25] and was designed in such a manner that a wide number of geometrical configurations can be employed.

Previously to the design step, some computational analyses were performed in ANSYS fluent model to study the flow dynamics at non-reacting conditions. In addition, the modeling results may provide an understanding of the flow structures generated in the combustion chamber as well as the probable impact on fuel/air mixing. Furthermore, a parametric analysis of several geometrical configurations of swirler/venturi was conducted, which can be employed to evaluate the operational capability of the chosen design and the diversity of experiments the hardware might be capable of with basic modifications. For the modeling mesh, a similar geometry of the atmospheric single injection test bench from the NASA Glenn Research Center was reproduced. This geometry was chosen by the simplicity of the design and the availability of both computational and experimental results [21], allowing us to compare the results and to evaluate additional configurations.

Figure 4.10 shows an example of the computational results, where the swirler blade angle at the inlet was modified by varying the flow's tangential component direction. Swirler blade angle was varied from 40 to 65°, producing a swirl number range of 0.62 to 1.59. The swirl number, S_N, can calculated by

$$S_N = \frac{2}{3} \left[\frac{1 - (D_i/D_o)^3}{1 - (D_i/D_o)^2} \right] \tan \alpha \qquad (4.1)$$

where α is the vane angle of the swirler, D_o and D_i are the outlet diameter and internal diameter of the swirler, respectively. Considerable changes occur when the swirler blade angle is modified from 40 to 60°, as depicted in Figure 4.10. In terms of overall flow structure, there is little to no difference between 60 and 65°. Additionally, a core recirculation zone was identified at swirl angles equal to or higher than 50° was observed, as a consequence of a vortex breakdown phenomenon caused by the strong whirling flow. The overall size of the central recirculation region grows as the swirl angle increases, whereas the corner recirculation zone region decreases. Although weaker in terms of backflow, a single central recirculation will be more beneficial in creating a homogenous mixture, particularly at the combustor's entrance area, where ignition occurs. The flow patterns of the 60 and 65° swirlers are beneficial in that they draw the flow back into the burn region of the combustor and prevent corner recirculations (as observed in the 50 and 55° flow patterns) which force the fuel away from the burn zone. Furthermore, it can be noted that the 40 and 45° swirler blade angles are inadequate to create any recirculation, with all axial flow in the positive direction. This is due to the swirling flow being unable to provide a sufficient adverse pressure gradient to induce a recirculation zone. A swirl angle of 50° created a favorable pressure gradient large enough to cause recirculation in the combustion chamber.

Several venturi angles were also computationally investigated and the configurations were chosen to study the effect that the converging/diverging venturi has on the overall flow structure. The converging venturi section accelerates the flow while simultaneously increasing the length of the vortex breakdown bubble. Some configurations appear to allow the flow to properly flow around the corner as it diverges, pushing the air to the outside of the chamber and allowing the larger center recirculation zone to start.

After performing the initial computational study, the design was adapted to allow the use of commercial injectors. Therefore, it was necessary to scale the characteristics dimensions of the initial geometry used for the computational study in order to keep the same cross-section. Additionally, both the cross-section size and length of the combustion chamber were also modified. The cross-section was increased up to $70{\times}70$ mm to keep the initial relationship and it is also in the range of cross-sections of the burners previously reviewed that use similar atomizers. In addition, this dimension is essential to avoid that the fuel being sprayed on the silica windows. The windows length was reduced up to 180 mm to minimize both the price and the complexity of manufacturing weak windows. Since these geometrical modifications could affect flow dynamics within the combustion chamber, both were computationally studied before the test bench design to observe that the new design will
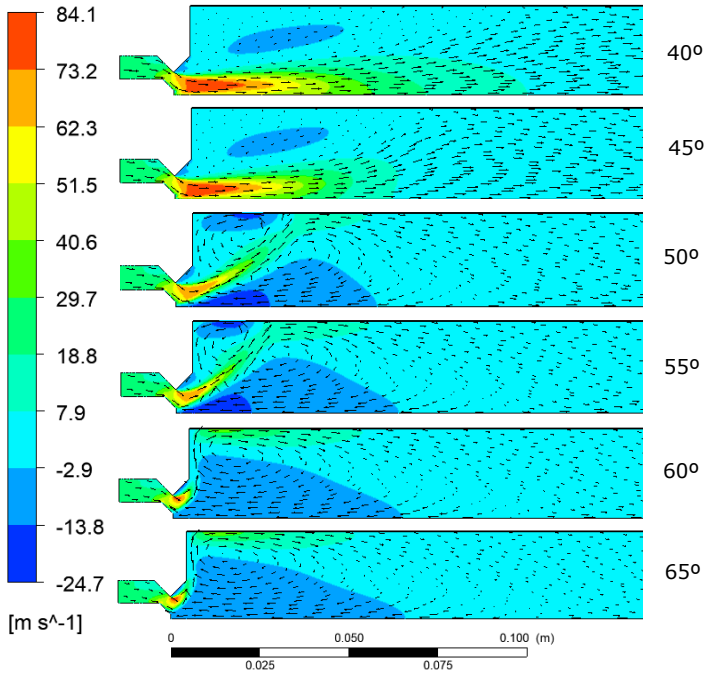
Figure 4.10: Axial velocity comparison of varying inlet swirl numbers.

present a similar fluid dynamic as the ones used by the initial computational study, an example of the comparison is shown in Figure 4.11.
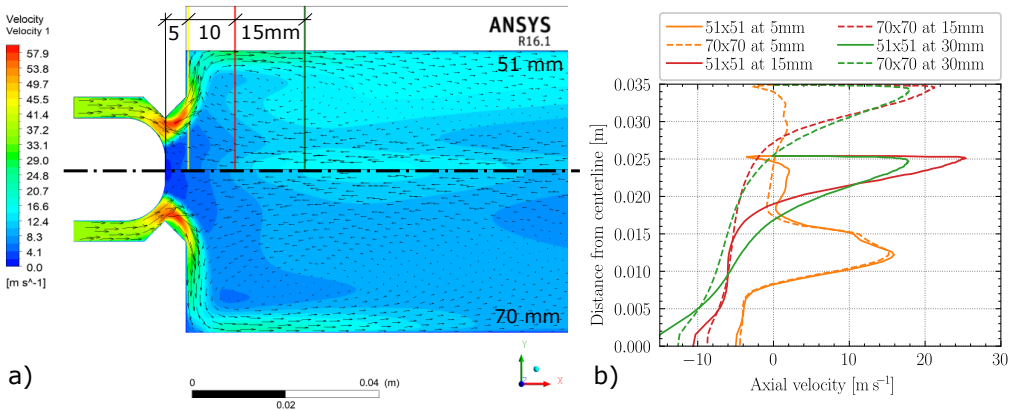
Figure 4.11: a) Chamber size comparison, b) Axial velocity profiles comparison at different downstream distances from the injector tip.

In Figure 4.11 both cross-section chamber sizes are compared to observe the differences between them and check if both present similar flow dynamic structures, in Figure 4.11.a are compared the magnitude of velocity. Additionally, three lines were plotted at different lengths from the nozzle tip to compare the axial velocity at these distances, as depicted in Figure 4.11-b, where colors refer to the distance along the axis. There are no significant differences in both figures, besides a slight variation in the axial velocity profile close to the burner axis, which is more noticeable at 15 mm from the nozzle tip.

After testing that the variations of the length and cross-section of the combustion chamber do not affect the fluid dynamics considerably, the test bench design is performed, which is based on the single point LDI test bench identified in the literature [21], but also in other similar as [25, 29]. Dimensions for important pieces such as swirler inner and outer hub diameters, venturi throat/exit regions, and fuel nozzle offset were supplied. An important aspect of the test bench design must be optical access using silica windows in the immediate entrance to the chamber. These optical accesses allow using different optical techniques such as Schlieren, DBI, PVI, LDA to measure density gradients, spray silhouette, velocities fields and droplet properties, respectively. This must extend from the venturi's mouth to the end of the flame burn zone. Silica glass, which is employed in many other combustion chambers, was chosen as a suitable window material. It is ideally suited for this application due to its remarkable optical and thermal characteristics, high compressive stress, and machinability. The windows were designed to be exchangeable with steel plates during testing in order to avoid excessive wear of the glass. The final design has to be adaptable while minimizing the need to completely rebuild the combustor or modify significant components between tests. For this reason, a modular design was used so that the specific functional requirements of each module could be explicitly outlined and designed appropriately and then integrated. In this way, the number of permanent components might be increased while ensuring the interfaces with interchangeable parts have similar joining techniques, as shown in Figure 4.12.

Since of their proximity, the venturi and swirler were considered as a single sub-system. To maintain flow velocity, the air must enter the combustion chamber quickly after passing through the swirler, therefore the venturi nozzle is located as near to the swirler outlet as possible. The fuel supply pipe runs through the center of the swirler hub, with the nozzle tip positioned near the venturi's throat, as illustrated in Figure 4.12. Additionally, the swirler is fixed through the screw mechanism to avoid rotational and translational movement. The venturi is designed as an individual piece, which is coupled to the plenum
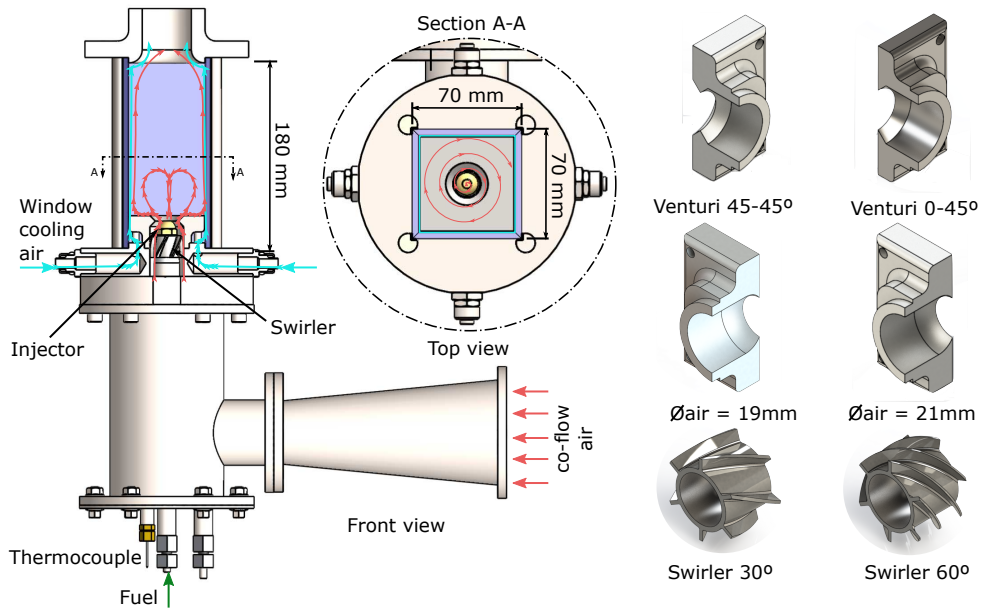
Figure 4.12: Annular spray burner and multiple components.

that is positioned at the immediate entrance to the combustion chamber. Figure 4.13 shows some swirler/venturi configurations, which were designed in order to investigate their effect on the flow structure and therefore fuel atomization and combustion. These components can be replaced easily and can be arranged in multiple configurations. In addition to the configurations depicted in Figure 4.13 a non-swirl flow and rounded shape at the exit of the burner can also be arranged to explore additional flow structures.
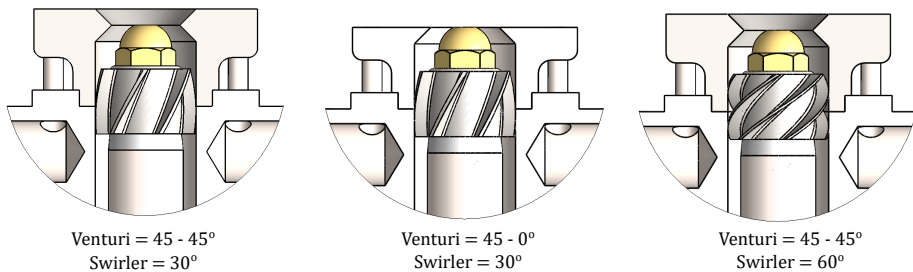
Figure 4.13: Swirler/venturi configurations.

The optical section had the greatest number of design requirements re-

garding the size and positioning of the windows. The chamber has a square section of 70×70 mm and a heigh of 180 mm and is composed by three large quartz windows and one metallic, which enclose the combustion chamber and providing full optical access. The metallic window is used to install the spark plug, pressure sensor sampling, and thermocouple. A window cooling system has been installed on the burner to protect the windows from hot combustion gases and to prevent fuel from being sprayed on the silica windows. The air is supplied as a film (thickness of 1 mm) to all four sides at ambient temperature. Mass flow of the cooling can be regulated independently. Therefore, the effect of the cooling air on combustion is limited and can also be investigated. Depending on the operating conditions, the cooling air mass flow ranges between 10 % and 30 % of the main air mass flow. In addition, an exhaust convergent nozzle is incorporated at the top of the chamber to avoid possible air entries. The burner is equipped with one thermocouple in the airflow, close to the exit of the air duct, in order to control the inlet co-flow temperature. Additionally, the burner can be arranged without walls to perform a no flow confinement configuration and therefore investigate the more canonical configuration for the study of spray flame, removing the flow/wall interactions. In the confinement flow configuration, the optical access to the spray/flame is possible from three sides over the full width of the combustion chamber. At the fourth side is placed an stain steel plate to install some devices. The Figure 4.14 shows both flow configurations.

No flow confinement   Flow confinement
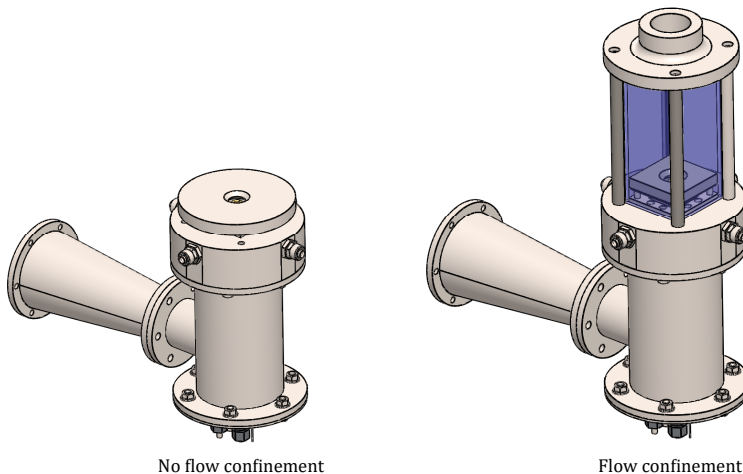
Figure 4.14: No flow confinement and flow confinement configurations.

The airflow enters the burner horizontally and must be redirected to create an ascending flow inside the inner cylinder. Figure 4.15 shows how the airflow is forced to change direction by a succession of elements, including a volute, a metallic grid, and a space filled with 3 mm diameter stain steel spheres (red region in Figure 4.15), which are used to break any large turbulent flow structures. Finally, it flows through guiding vanes to ensure a uniform flow structure and continues toward the upper end of the plenum where is forced to enter the axial swirler, which is composed of 6 vanes inclined at a certain angle. This part is placed around the fuel injection system, on top of the atomizer holder and the liquid spray is immediately surrounded by the airflow after entering the chamber.
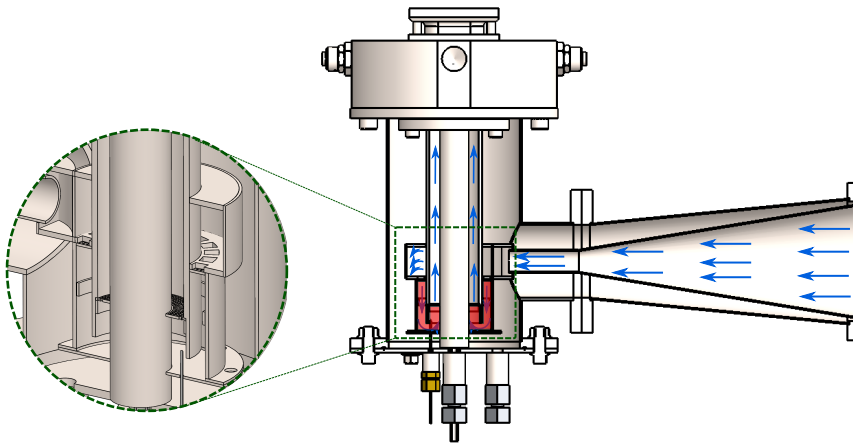
Figure 4.15: Airflow trajectory.

In order to avoid the heat losses of the heated air co-flow, an isolating material was placed between the main air duct and the external casing and also to prevent the external casing from heating up. Also, a layer of isolating material was installed between the air duct and fuel line to prevent the overheating of the fuel.

4.3.1 Injection system

The fuel injection system consists of a pressurized vessel (2 L capacity) that can be pressurized up to 5 MPa through a nitrogen bottle couple with an extra bottle to minimize the pressure fluctuations. Pressure is maintained through a pressure regulator. The vessel has been provided with multiple input

connection ports, allowing to attach different sensors (e.g., thermocouples, pressure sensor) and valves to it. A safety valve also has been installed to prevent an over-pressure in the system, releasing the pressure when it reaches 7 MPa. An electronic Coriolis mass flow meter (Bronkhorst, CORI-FLOW) has been arranged at the fuel pipeline for accurate measurement of the fuel mass flow rate. Additionally, two electro-valves were installed upstream of the injector to control the fluid flow through it; during the injection event, the first one allows passing the fuel meanwhile the second valve is closed, to stop the injection event, the first one closes meanwhile the second one is open, releasing the pressured fuel to the ambient to prevent the dribble effect in the injector. The fuel temperature was measured with a K-type thermocouple at a point just before entering the nozzle. The fuel is injected through a hollow cone spray injector. The subsection 5.2.1 describes the injector characteristics used in the experiments in detail.
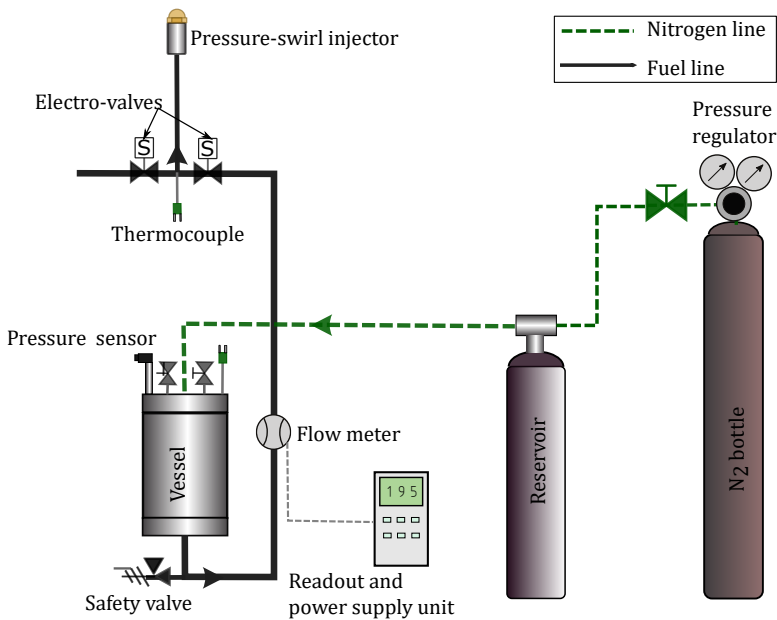
Figure 4.16: Pressurized system schematic diagram.

4.3.2 High-flow and high-temperature facility

A schematic layout of the facility used to study the behavior of the atomization and combustion processes in spray flames at atmospheric conditions is
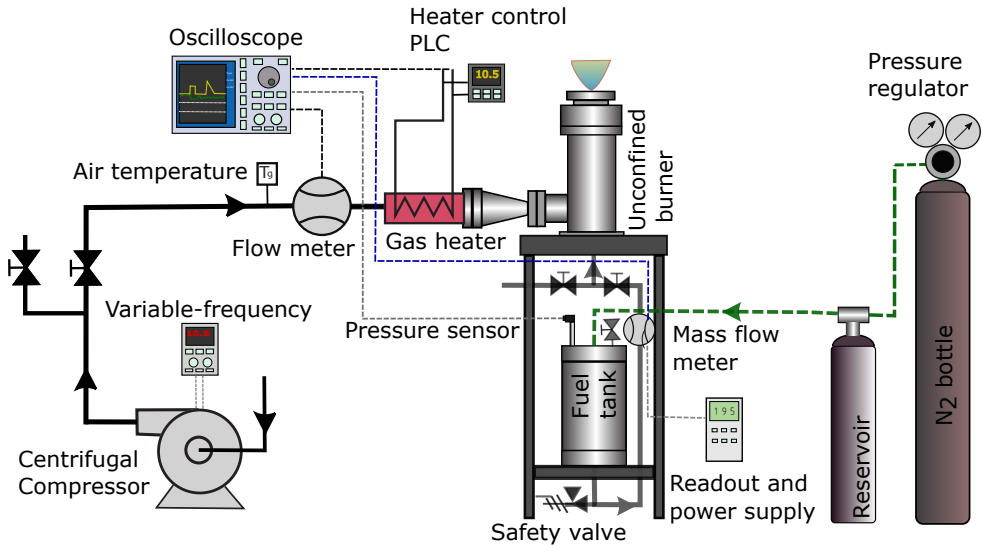
Figure 4.17: Schematic representation of the high-flow and high-temperature facility.

presented in Figure 4.17. Air co-flow is supplied through a centrifugal blower with an air blowing capacity of 0 - 400 kg h^{-1} and measured through a flow meter. A 15 kW electric heater has been installed at the air pipeline to increase the air temperature up to 673 K, allowing to investigate its effect on the combustion and atomization processes. The air co-flow temperature is measured with K-type thermocouples at different locations and controlled by a PID module. The burner is located after the electric heater and also under an extraction combustion gases system, which evacuates the gases during the combustion studies. The burner can be fitted with a particle seeder system to seed particles in the main air stream to apply the PIV technique.

Another important system is the fuel supply, which consists of pressurized lines and a pressurized vessel fitted to a nitrogen bottle at high pressure, as was described in subsection 4.3.1.

4.4   Summary

This chapter presents a literature review of several test benches around the world used to study both the atomization and combustion process at atmospheric conditions and different experimental configurations, mainly no confinement and confinement flow configurations. The next section presents

the annular spray burner design, introducing the different setups such as swirler/venturi, confinement or no confinement flow, and also examples of results of a computational fluid dynamics study into various geometrical configurations of the swirler/venturi to investigate the operational capacity of the chosen design. Finally, the injection system and high-flow and high-temperature facility are included, describing each component and its function.

References

[1]   Schneider, D. et al. "A new test rig for laser optical investigations of lean jet engine burners". In: *27th Congress of the International Council of the Aeronautical Sciences 2010, ICAS 2010*. Vol. 4. 2010, pp. 2667–2676.

[2]   Cochet, A. et al. "ONERA test Facilities for Combustion in Aero Gas Turbine Engines, and Associated Optical Diagnostics". In: *Aerospace-Lab* 11 (2016).

[3]   Chi-Ming, L., Kathleen M., T., and Changleie, W. "High pressure low NOx emissions research: Recent progress at NASA Glenn Research Center". In: *fuel* 4.1 (2007), pp. 1–8. DOI: `10.1007/s13398-014-0173-7.2`.

[4]   Seyfried, H. et al. "Optical diagnostics applied to a gas turbine pilot burner". In: *AIAA Journal* 45.11 (2007), pp. 2702–2709. DOI: `10.2514/1.30032`.

[5]   Malbois, P. et al. "Experimental Investigation With Optical Diagnostics of a Lean-Premixed Aero-Engine Injection System Under Relevant Operating Conditions". In: *ASME Turbo Expo 2017*. Vol. 4B. Charlotte, North Carolina: American Society of Mechanical Engineers, 2017. DOI: `10.1115/GT2017-64484`.

[6]   Cessou, A. "Simple description of the combustion structures in the stabilization stage of a spray jet flame". In: *Atomization and Sprays* 9.1 (1999), pp. 1–27. DOI: `10.1615/atomizspr.v9.i1.10`.

[7]   Goix, P. J., Edwards, C. F., Cessou, A., Dunsky, C. M., and Stepowski, D. "Structure of a methanol/air coaxial reacting spray near the stabilization region". In: *Combustion and Flame* 98.3 (1994), pp. 205–219. DOI: `10.1016/0010-2180(94)90236-4`.

[8]   Friedman, J. A. and Renksizbulut, M. "Investigating a methanol spray flame interacting with an annular air jet using phase-Doppler interferometry and planar laser-induced fluorescence". In: *Combustion and Flame* 117.4 (1999), pp. 661–684. DOI: 10.1016/S0010-2180(98) 00136-9.

[9]   Marley, S. K., Welle, E. J., Lyons, K. M., and Roberts, W. L. "Effects of leading edge entrainment on the double flame structure in lifted ethanol spray flames". In: *Experimental Thermal and Fluid Science* 29.1 (2004), pp. 23–31. DOI: 10.1016/j.expthermflusci.2004.01.009.

[10]   Marley, S. K., Lyons, K. M., and Watson, K. A. "Leading-Edge Reaction Zones in Lifted-Jet Gas and Spray Flames". In: *Flow, Turbulence and Combustion* 72.1 (2004), pp. 29–47. DOI: 10.1023/B: APPL.0000014906.91990.4e.

[11]   Cléon, G., Honoré, D., Lacour, C., and Cessou, A. "Experimental investigation of structure and stabilization of spray oxyfuel flames diluted by carbon dioxide". In: *Proceedings of the Combustion Institute* 35.3 (2015), pp. 3565–3572. DOI: 10.1016/j.proci.2014.06.028.

[12]   Reddy, V. M., Trivedi, D., and Kumar, S. "Experimental investigations on lifted spray flames for a range of coflow conditions". In: *Combustion Science and Technology* 184.1 (2012), pp. 44–63. DOI: 10.1080/ 00102202.2011.615770.

[13]   Massot, M., Kumar, M., Smooke, M. D., and Gomez, A. "Spray counterflow diffusion flames of heptane: Experiments and computations with detailed kinetics and transport". In: *Symposium (International) on Combustion.* Vol. 27. 2. Elsevier, 1998, pp. 1975–1983. DOI: 10. 1016/S0082-0784(98)80042-8.

[14]   TCS. *Workshop on Measurement and Computation of Turbulent Spray Combustion.* 2015.

[15]   Stårner, S. H., Gounder, J., and Masri, A. R. "Effects of turbulence and carrier fluid on simple, turbulent spray jet flames". In: *Combustion and Flame* 143.4 (2005), pp. 420–432. DOI: 10.1016/j.combustflame. 2005.08.016.

[16]   Gounder, J. D., Kourmatzis, A., and Masri, A. R. "Turbulent piloted dilute spray flames: Flow fields and droplet dynamics". In: *Combustion and Flame* 159.11 (2012), pp. 3372–3397. DOI: 10.1016/j. combustflame.2012.07.014.

[17] Masri, A. R. and Gounder, J. D. "Turbulent spray flames of acetone and ethanol approaching extinction". In: *Combustion Science and Technology* 182.7 (2010), pp. 702–715. DOI: 10.1080/00102200903467754.

[18] Verdier, A. et al. "Local extinction mechanisms analysis of spray jet flame using high speed diagnostics". In: *Combustion and Flame* 193 (2018), pp. 440–452. DOI: 10.1016/j.combustflame.2018.03.032.

[19] Verdier, A. et al. "Experimental study of local flame structures and fuel droplet properties of a spray jet flame". In: *Proceedings of the Combustion Institute* 36.2 (2017), pp. 2595–2602. DOI: 10.1016/j.proci.2016.07.016.

[20] Correia Rodrigues, H., Tummers, M. J., Veen, E. H. van, and Roekaerts, D. J. "Effects of coflow temperature and composition on ethanol spray flames in hot-diluted coflow". In: *International Journal of Heat and Fluid Flow* 51 (2015), pp. 309–323. DOI: 10.1016/j.ijheatfluidflow.2014.10.006.

[21] Tacina, R., Cai, J., and Jeng, S.-M. "The Structure of a Swirl-Stabilized Reacting Spray Issued from an Axial Swirler". In: *43rd AIAA Aerospace Sciences Meeting & Exhibit*. January. 2005, pp. 1–14.

[22] Yuan, R., Kariuki, J., Dowlut, A., Balachandran, R., and Mastorakos, E. "Reaction zone visualisation in swirling spray n-heptane flames". In: *Proceedings of the Combustion Institute* 35.2 (2015), pp. 1649–1656. DOI: 10.1016/j.proci.2014.06.012.

[23] Sidey, J. A. M., Giusti, A., Benie, P., and Mastorakos, E. *The Swirl Flames Data Repository*.

[24] Hervo, L., Senoner, J. M., Biancherin, A., and Cuenot, B. "Large-Eddy Simulation of Kerosene Spray Ignition in a Simplified Aeronautic Combustor". In: *Flow, Turbulence and Combustion* 101.2 (2018), pp. 603–625. DOI: 10.1007/s10494-018-9924-4.

[25] Cordier, M. "Allumage et propagation de flamme dans les écoulements fortement swirlés : études expérimentales et numériques". PhD thesis. INSA, 2013.

[26] Marrero-Santiago, J. et al. "Spray Ignition and Local Flow Properties in a Swirled Confined Spray-Jet Burner: Experimental Analysis". In: *ILASS-Europe 2017, 28th Conference on Liquid Atomization and Spray Systems*. Valencia (Spain), 2017. DOI: 10.4995/ILASS2017.2017.4674.

[27] Marrero-Santiago, J. et al. "Experimental study of aeronautical ignition in a swirled confined jet-spray burner". In: *ASME. J. Eng. Gas Turbines Power*. Vol. 140. American Society of Mechanical Engineers (ASME), 2017, pp. 1–14. DOI: 10.1115/GT2017-64476.

[28] Santiago, J. M. "Experimental study of lean aeronautical ignition. Impact of critical parameters on the mechanisms acting along the different ignition phases." PhD thesis. 2018, pp. 1–215.

[29] Willert, C. et al. "Combined PIV and DGV applied to a pressurized gas turbine combustion facility". In: *Measurement Science and Technology* 17.7 (2006), pp. 1670–1679. DOI: 10.1088/0957-0233/17/7/005.

Chapter 5

Experimental tools and methodologies

5.1 Introduction

In this chapter, all the experimental tools and analytical methodologies are described. First, the pressure swirl injector specifications and two different techniques to measure the internal geometry of the injector orifice are detailed. Then, the annular spray burner configuration used to perform the experiments is presented, detailing mainly the conditions of the air co-flow and diameters at the burner exit. Finally, the optical setups and image processing strategies carried out to measure each parameter are explained. It is also important to mention that all measurements were performed in the facilities of CMT-Motores Térmicos.

5.2 Fuel atomizer

Fuel needs to be atomized into the ambient at specific conditions (e.g., pressure, mass flow rate). Additionally, these conditions need to be stable, to some extent, through a wide range of operating conditions. To this end, the injection system is composed mainly of a pressurized vessel, Coriolis mass flowmeter, and a simplex pressure-swirl injector, as was detailed in subsection 4.3.1.

5.2.1 Simplex pressure-swirl atomizer

The injector chosen to perform all the experiments is a Fluidics simplex pressure-swirl injector with the following fabrication specifications: $0.57\,\mathrm{kg\,h^{-1}}$ at $1\,\mathrm{MPa}$ for calibration fluid (ISO 4113), hollow cone with an 80° opening. Figure 5.1 presents a schematic cut view of this injector type on the left side and a real image on the right side. The main components of the atomizer are the primary filter, secondary filter, swirler, and head. The swirler part has three slots that guide the flow tangentially into a small swirling chamber and a tiny conical opening in which the swirling liquid is forced to exit.
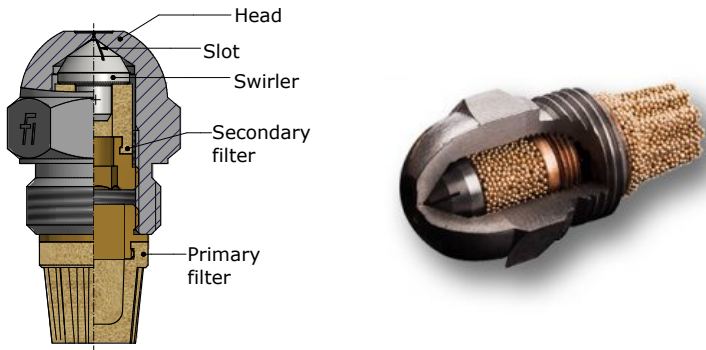
Figure 5.1: Pressure-swirl atomizer.

The small dimensions inside the injector promote high liquid velocities at the injector outlet. Since the fluid flow in the atomizer chamber has a strong rotational motion, pressures at the centre are forced to decrease and the liquid spills out of the conical opening along the cone walls, forming a thin liquid conical sheet (80°) immediately at the atomizer outlet. The injector was selected in order to provide good atomization quality and low fuel mass flow rate, allowing us to generate lean mixtures in the burner to approach the principle used in lean-direct-injection combustion systems. Furthermore, the injector provides other advantages such as simplicity of its construction, reliability, and good quality atomization with low pumping power requirements. Figure 5.2 shows from a frame recorded through the Microscopic Diffused Back-Illumination technique (MDBI) how the liquid-sheet evolves. Filaments can be appretiated at the first $2\,\mathrm{mm}$ (primary atomization). Then the secondary atomization takes place until $\approx 4\,\mathrm{mm}$, where no further ligaments are observed, and the majority of droplets are already spherical. It is important mentioning that the atomization process is due to the velocity difference between air and fuel, and the fuel velocity is caused by the pressure differential.
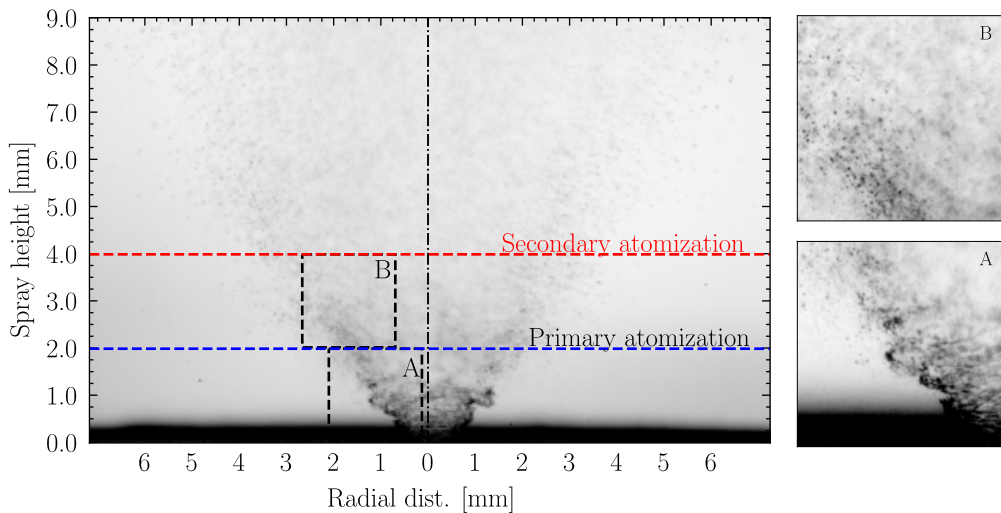
Figure 5.2: *Liquid-sheet evolution. The frame shown is at first millimeters, for n-Heptane fuel, injection pressure of 1 MPa, air mass flow of 0.5 kg min^{-1} and temperature of 328 K.*

Since the notorious effect of the injection pressure and liquid type on the atomization process and injection performance, the pressure swirl atomizer was tested at different injection pressure levels, measuring the mass flow rate, as depicted in Figure 5.3. Moreover, the experiment was carried out with several liquid types, which have different physical properties. From Figure 5.3 can be appreciated that as the injection pressure is increased, the mass flow rate increases. This figure also shows the effect of the liquid type on the mass flow rate.

5.2.2 Injector orifice

Since the injector orifice diameter has a notorious effect on the atomization process, different experimental techniques such as x-ray tomography, silicone moulding, or optical microscopy have been developed to measure internal geometry, and thus allowing to measure relevant dimensions of the orifice. For this aim, silicone and x-ray were used and introduced following.

Silicone methodology

This methodology is based on the one developed to measure the internal geometry of the diesel injectors [1], which uses a specific type of silicone to
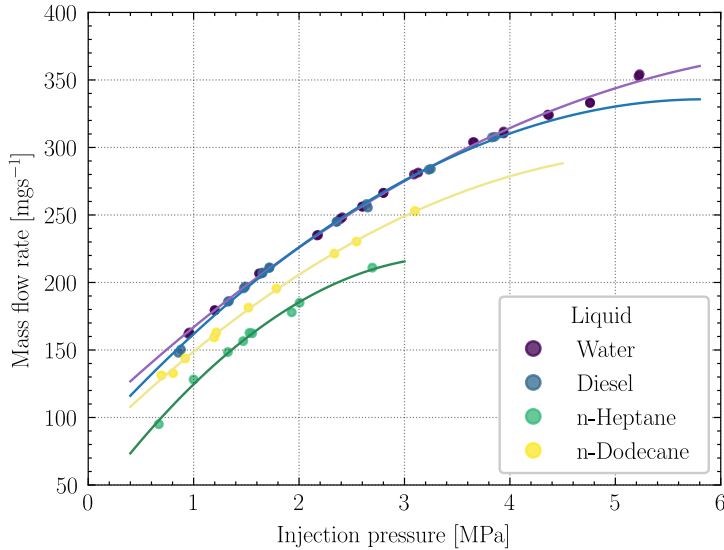
Figure 5.3: Injector performance, mass flow rate for different liquids at different levels of injection pressure (Ambient pressure = 0.1 MPa).

introduce inside the injector and thus obtain the internal geometry. Once the molds are obtained and extracted, they are coated with gold to create an electricity conductive layer, allowing to image them by Scanning Electronic Microscope (SEM) as depicted in Figure 5.4. The result will not be affected by this gold deposition because the thickness of the gold coating is less than $0.1\,\mu\mathrm{m}$. Finally, CAD software was used to measure the dimensions of the orifice, taking into account the reference dimension (magnification factor) on the images to load them with the appropriated scale factor.

X-ray tomography

Static x-ray tomography was used in order to characterize the three-dimensional internal shape of the pressure swirl injector, mainly at the outlet section, as shown in Figure 5.5. For this task, a commercial x-ray tomography system Nikon XT H 160 was used, which was equipped with $160\,\mathrm{kV}/60\,\mathrm{W}$ micro-focus x-ray tube to view the internal geometry of the injector from multiple viewing angles. Finally, the tomography images were loaded and analyzed through a volume graphics software, allowing to measure the internal geometry (especially the outlet diameter and angles).
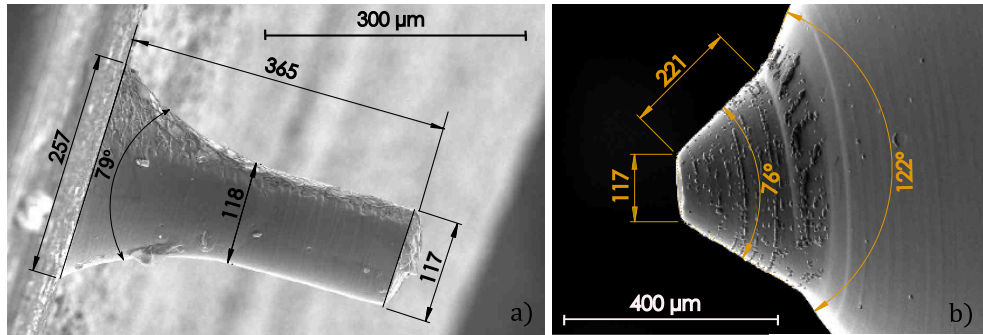
Figure 5.4: SEM images of the internal geometry of the pressure-swirl atomizer; external cone and orifice a) and internal cone b).
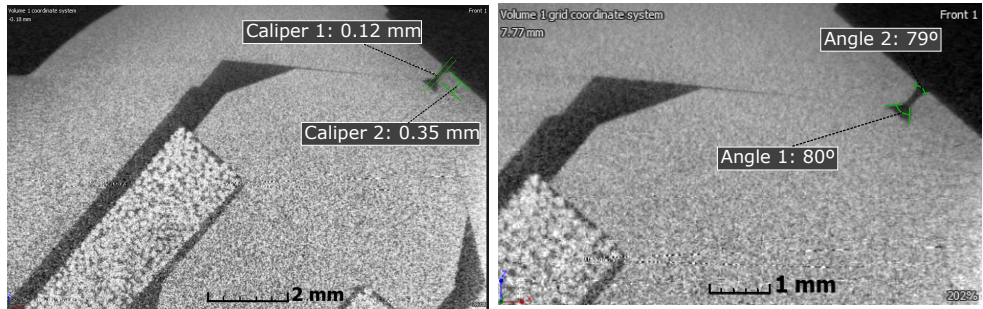
Figure 5.5: X-ray images of the internal geometry of the pressure-swirl atomizer.

The characteristic dimensions of the internal geometry of the pressure swirl injector measured through both silicone technique and X-ray tomographic are summarized in Table 5.1.

Table 5.1: Characteristic dimensions of the internal geometry of the pressure swirl atomizer.

Parameter	SEM images	X-ray
Internal cone	76°	80°
External cone	79°	79°
Orifice diameter [µm]	117	120

From the results of both techniques to measure the internal geometry of the injector, the diameter of the injector orifice can be considered to be

approximately 120 μm and opening angle of 80°. This small dimension in the diameter orifice results in high liquid velocities at the exit.

5.3   Annular spray burner

A new high-flow and high-temperature facility was used to perform the experimental measures, allowing visualization and characterization of both spray and flame. The test facility is described section 4.3 and was designed to supply air at high-flow and high-temperature to the burner, enabling to test a wide range of co-flow conditions. The test section, where the spray flame takes place, is fully accessed optically, allowing to set up different optical techniques, even simultaneously.

The burner design is modular, as shown in Figure 5.6, allowing rearranged the burner easily to simulate various air co-flow configurations, as was previously explained in section 4.3. For this work, the burner was settled vertically in order to have full access to the spray/flame and to avoid the gravity effect on the spray flame, also no confinement and no swirler flow configurations were chosen to perform the experimental campaign. In addition, two air outlet diameters were tested 19 mm and 21 mm, which have a rounded shape, as depicted in Figure 5.6. In order to avoid heat loss, a cross-section of insulating material was settled between the external housing and the internal flow duct, likewise between the co-flow channel and the fuel line avoiding the fuel heating. Finally, the injector was placed such that it was flush with the air outlet diameter piece, allowing the whole spray to be registered from the nozzle tip.

5.4   Measured parameters through optical techniques

In this section, the optical techniques and image processing methodologies are detailed, which are classified regarding the parameter to measure. Optical diagnostic is usually implemented to investigate several parameters, considering a useful tool, as they generally yield a non-intrusive way for experimental investigation. Furthermore, with recent advancements in cameras, laser, x-ray, optics, and illumination technologies, different optical arrangements are possible, depending on the variable to be measured in the spray flame, such as droplet size and velocity, spray angle, flame lift-off height, velocity fields, soot concentration, and others. The methodology for image processing depends substantially on the parameters to extract from the images recorded. For the non-reactive conditions, the primary aim is the segmentation of the
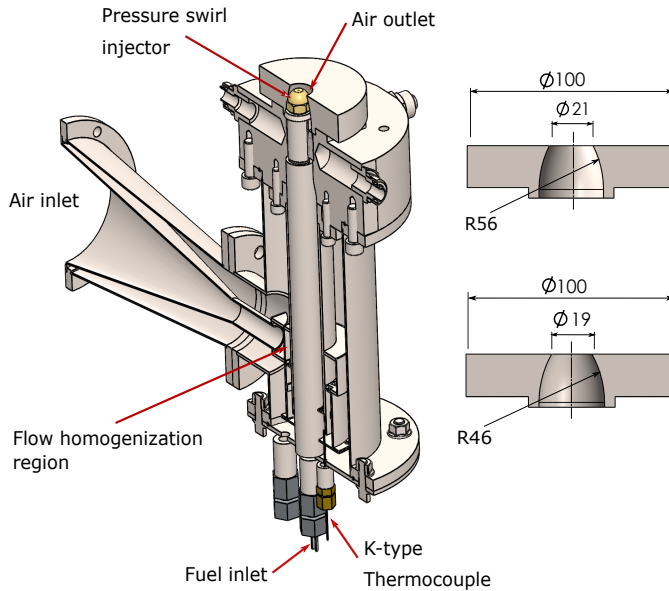
Figure 5.6: Annular spray burner and both air outlet diameters.

spray and the background, and for reactive conditions, it is the segmentation of the combustion phase and liquid phase. All the routines were purpose programmed with PYTHON. For this work, the Microscopic diffused back-illumination (MDBI), PIV, Diffused back-illumination extinction (DBI), and OH* chemiluminescence techniques were used to measure droplet size and droplet velocity, velocity fields, soot concentration, and flame lift-off height, respectively.

5.4.1 Velocity fields

The PIV method was used to obtain instantaneous velocity fields. The PIV measurement can be used to calculate 2D velocity fields. This diagnostic consists of capturing two consecutive frames with a CCD camera separated by a time interval Δt that varies depending on the experimental settings (i.e., flow velocity, magnification ratio). The signal recorded by the camera corresponds to the Mie scattering of particles illuminated by a thin laser sheet. The optical arrangement shown in Figure 5.7 was used to carry out this technique. A double-head 15 Hz Nd: YAG laser with 135 MJ/pulse at 532 nm gave two laser beams separated by $\Delta_{PIV} = 15\,\mu s$). The Mie scattering signal from droplets is collected with a TSI PowerView Plus 4MP camera equipped with

a Nikon f/1.4 50 mm objective coupled with a narrow band-pass filter with a wavelength of 532 nm.
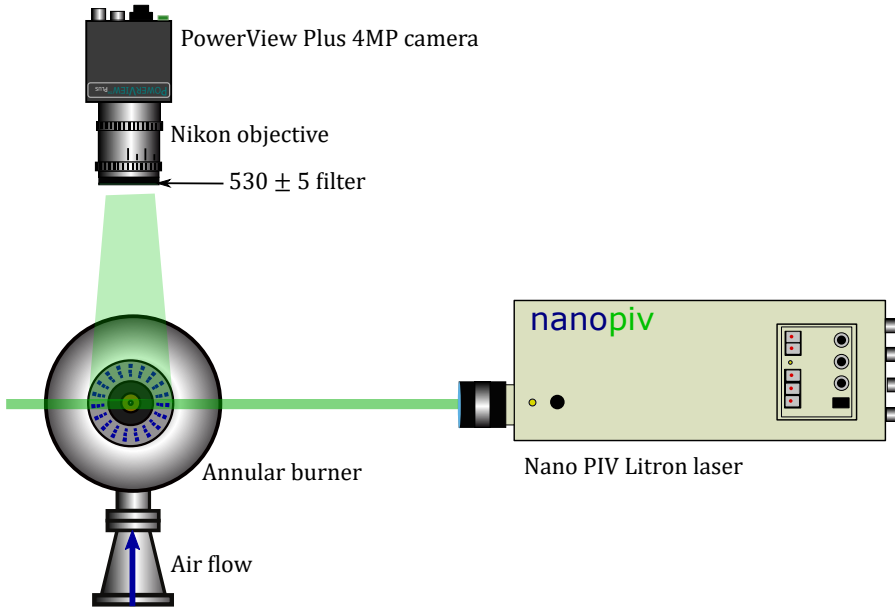
Figure 5.7: Schematic diagram of the particle image velocimetry setup.

The camera resolution was set at 2048×2048 pixel, leading to a magnification ratio equal to $19 \, \text{pixel} \, \text{mm}^{-1}$. The post-treatment was performed with PIV-lab code, which was developed in MATLAB by Thielicke and Sonntag [2], with a cross-correlation algorithm with a window size of 32×32 pixel and a 50 % overlap. Finally, a coherent filter is also applied to correct isolated false vectors. It should be noted that the PIV technique does not estimate the velocity of individual particles, but instead the velocity of a group of particles. Taking particle displacement and the Δt into account, a velocity vector can be calculated for each interrogation window through the following equation:

$$u = \frac{\Delta x_t^{t+\Delta t}}{\Delta t} \tag{5.1}$$

where u, $\Delta x_t^{t+\Delta t}$, Δt are the velocity vector estimated in one interrogation window, the statistical displacement of particles, and the time between the two images recorded, respectively. To calculate the statistical displacement of particles in all interrogation windows, the cross-correlation technique and

the position of the correlation peak were employed [3]. The schematic representation of the concept of PIV measurements, including the cross-correlation technique, is shown in Figure 5.8.
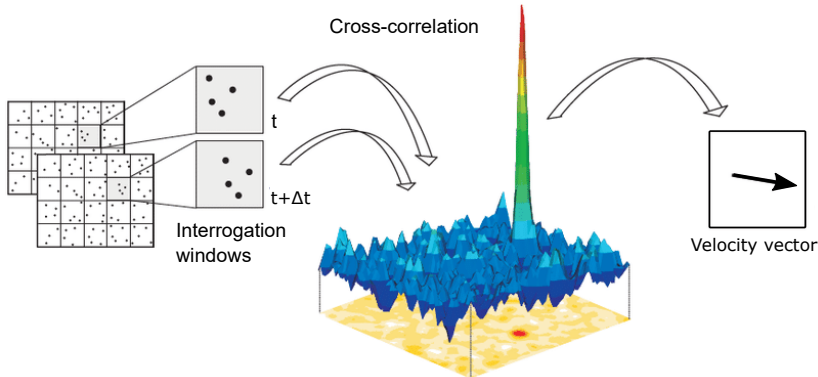
Figure 5.8: Principle of PIV measurement, extracted from [4].

PIV is based on a simple principle, but it must be appropriately implemented in order to get reliable measurements and decrease uncertainties. Special consideration should be given to the many aspects that might influence the PIV technique results. The size of the interrogation window, out-of-plane particle motion, signal-to-noise ratio, and flow seeding affect the final velocity vector field [3, 5, 6]. In the present configuration, the aerodynamic of the flow is measured in nominal condition with fuel droplets, i.e. the droplets were used as tracers. Indeed, in this setup, the poly-disperse spray distribution produces small drops along the centerline axis, while the most of the mass is distributed as big droplets around the spray borders. The relatively small droplets in the center have a Stoke Number of $<< 1$, implying that they completely follow the co-flow of air. The big inertial droplets are placed outside the air co-flow and have enough velocity to be tracked by the Δ_{PIV} imposed to collect information in the spray's center. It is important to remember that the velocity vector fields provided in the following study are the results of droplet velocity.

5.4.2 Droplet size and droplet velocity

Droplet size and droplet velocity were measured throughout the Microscopic diffused back-illumination technique (MDBI), which is based on the principle

of measuring the amount of light attenuated or extinguished by the interference of some features like droplets, soot particles, etc. In this case, when the background is illuminated by a diffused light, the droplets and ligaments appear as black silhouettes. The MDBI setup was composed of a light source, diffuser, field lens, long-distance microscopic lens, and a high-speed camera, as shown in a simplified schematic diagram in Figure 5.9. The camera (Phantom VEO640) and light source were arranged on opposite sides of the liquid spray, allowing a line-of-sight visualization arrangement. The camera was coupled with a microscopic lens (Infinity K2 Distamax) that allows the magnification of the field of view and therefore record the droplets. Furthermore, a white LED unit capable of producing short and high-power pulses of light at high repetition rates was used as a light source. The light rays from the LED were directed to an engineered diffuser with 20.5° of divergence angle and 100 mm of diameter. The light was then projected on a Fresnel lens (focal length of 67 mm) to reproduce and concentrate the diffused illumination at the middle plane of the spray.
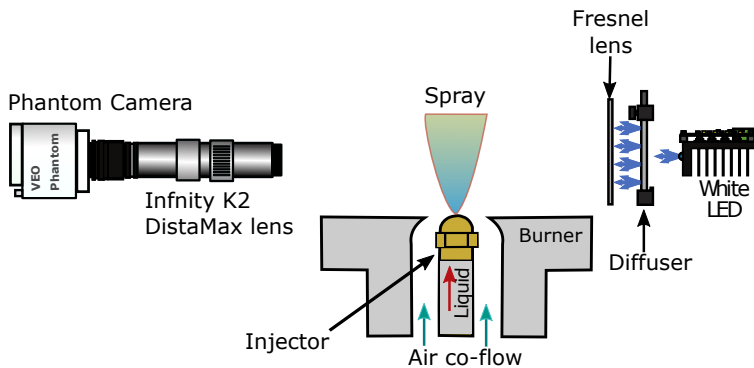
Figure 5.9: Schematic diagram of the Microscopic diffused back-illumination setup.

This technique has been arranged to capture the microscopic features of the liquid spray (droplets, filaments). Therefore, the camera was run at full-frame (2560x1600 pixels) and an acquisition rate of 1,000 frames per second (fps). This relatively low camera acquisition rate was chosen to be able to use all the camera sensor. Energizing time of the LED was set to 300 ns as a compromise between the illumination intensity and the recording speed. Therefore, this speed must be sufficient to "freeze" the droplet, and the illumination needs to be relatively good to provide acceptable contrast at the middle plane of the spray near the nozzle exit. The camera captures the light that is not blocked

by the spray (i.e., droplets, and ligaments), and thus rendering the liquid phase of the spray as a shadow or dark pixels in the images. The use of high-speed pulsating LED as a light source makes this optical setup the best option for liquid phase visualization. This technique also allows capturing images sharper than continuous light sources, reducing the spatial uncertainties [7, 8].

This optical technique is also used to estimate the droplet velocity, as seen in section 6.3, which is calculated by recording two consecutive frames with a small time gap between them and controlling the background illumination by the LED pulses, similar to the principle implemented in the PIV technique. Therefore, to achieve this small time gap between consecutive frames, the exposure time of the camera was set to PIV mode to provide a high resetting velocity of the sensor and therefore minimize the time gap between the consecutive frames. Figure 5.10 shows a schematic representation of the camera and LED pulses. Note that an LED pulse is sent at the end of frame A and the following one at the start of frame B, resulting in two frozen instants of the droplets separated by a relatively short time (2.5 µs).
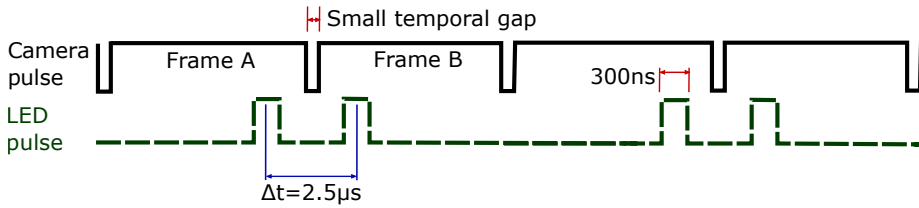
Figure 5.10: Schematic diagram of both the camera and LED pulses.

During the experimental campaign, different fields of view (FOV) were tested in order to find one with sufficient magnification but also an adequate FOV size. Figure 5.11 shows two magnifications FOV evaluated. The big one has a width of 14 mm and height of 9 mm, resulting in a digital resolution of 5.6 µm per pixel. The other FOV has a width of 3.5 mm and a height of 5.5 mm, resulting in a digital resolution of 2.1 µm per pixel. As can be observed in Figure 5.11.a provides a good size of the FOV, enabling to record a suitable spray length. However, it can not record the smallest droplets. Therefore, FOV with the highest magnification was chosen to perform the main study of the droplet size and droplet velocity due it can record those smallest droplets. Furthermore, since the sprays show a high symmetry, as shown in Figure 5.11.a, the FOV was located on the right side of the spray to take advantage of the highest length recording the spray evolution vertically.
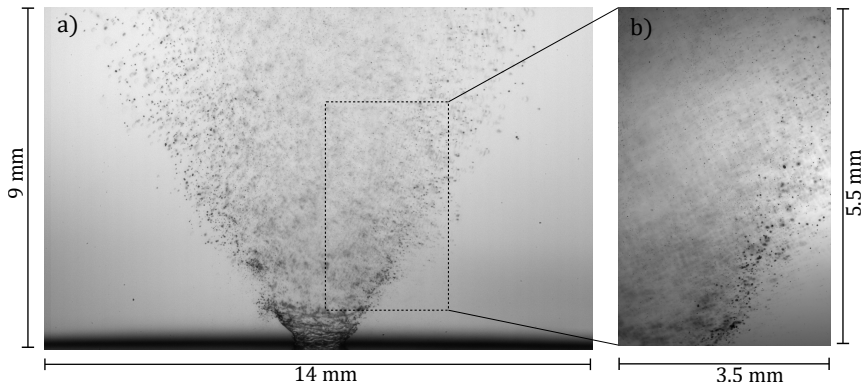
*Figure 5.11: Two FOVs with different digital resolution; 5.6 μm per pixel (a)
and 2.1 μm per pixel (b). The frame shown is a n-Dodecane spray at air
surrounding temperature of 328 K.*

After defining the FOV, which was located to register the first millimeters
of the jet spray, registering from 2 mm above the injector tip with a FOV of
5.5 mm height and 3.5 mm width, which provides a pixel size of 2.1 μm, the
images were recorded, using the technique previously detailed, which used a
K2 DistaMax microscopic lens to provide a large magnification. This magnifi-
cation allows recording the droplets generated during the atomization process.

5.4.3   Image processing

This section presents the image processing methodology used to identify the
droplets in the focused plane and then measure the diameters and velocities
of these droplets. Figure 5.12 presents an example of the processing steps for
the frame depicted in Figure 5.12.a and the steps are the following:

- Figure 5.12.b: is the raw image of the spray recorded through the MDBI
  technique.

- Figure 5.12.c: is the frame after the background subtraction (i.e.,
  $I_{inv} = I_0 - I_{raw}$). This to remove both reflections and background
  objects, which could generate bad estimations of the spray characteris-
  tics. Additionally, the subtraction was computed in that way to obtain
  the particles as white features, as presented in Figure 5.12.c. The back-
  ground was determined as an average of the images captured before the
  start of the injection (I_0).

- Figure 5.12.d: a rolling average was computed for resulting images from the previous step (I_{inv}) in order to smooth the images (I_{smooth}), i.e., reduce the image noise. Then, a subtraction was carried out ($I_{clean} = I_{inv} - I_{smooth}$) to filter out the blurred/cloudy areas, which have a low frequency and thus highlight particles with higher frequencies.

- Figure 5.12.e and Figure 5.12.f: a gradient estimation was calculated for each particle (I_{grad}) to identify which ones are located at the middle plane of the spray jet (i.e., focused particles), the depth of field is approximately 0.032 mm. High gradients represent particles defined and focused, as shown in Figure 5.12.e. Additionally, a one-step dilation was used to move the maximum intensity of the gradient to the particle center ($I_{dilgrad}$).

- Figure 5.12.g: a method was established to select both the valid and focused particles and hence no considering the other ones not in the focus plane. They are fleeting peaks in brightness that are not actually particles. Thus, in order to determine the "good" particles at the central plane, it was used some thresholds and the information from I_{inv}, I_{clean} and $I_{dilgrad}$. Then, the coordinates of the center for each particle were calculated through the determination of the local maximum intensity.

- Finally, after distinguishing real particles from invalid ones with the criteria presented previously, the droplet locations ($[x, y]$) in the measuring plane are determined. Then, using the image moment principle with the intensity of the pixels, several characteristics of the droplet can be calculated.

Droplet size and droplet position

After distinguishing the valid particles in the captures by using the previously described methodology, the particles bigger than 5 μm were identified and their location in the measuring plane. However, the small particles (lower than 5 μm) were not treated. The particle size captured is limited by the optical setup, which was optimized to favor the size of the field and hence recording a reasonable spray length. Additionally, a method based on a threshold is used to determine the pixels that belong to the droplet and which are around the location of maximum intensity. Finally, multiple droplet properties, such as equivalent diameter, mass center, eccentricity, and so on, may then be calculated for these pixels using the image moment concept. Figure 5.13 shows an example of the droplet size distribution for each fuel at given operating conditions.

(a) Raw image   (b) I_{raw} (c) I_{inv} (d) I_{clean}

(e) I_{grad} (f) $I_{dilgrad}$ (g) I_{locate}
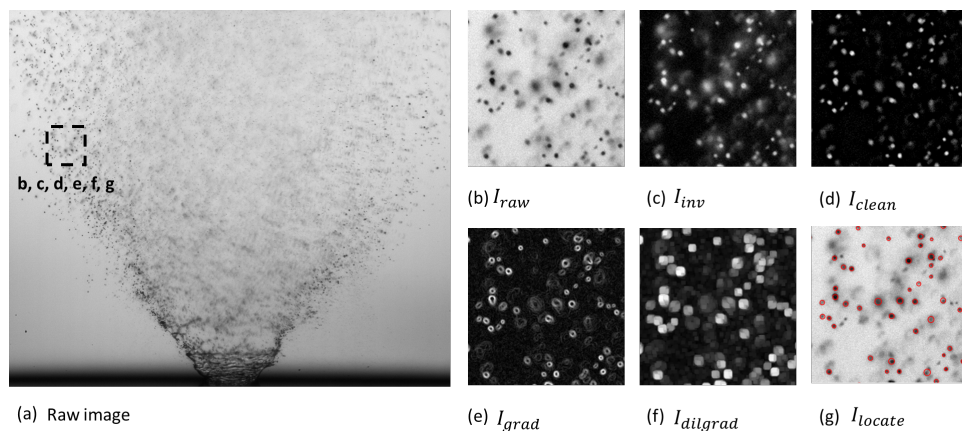
Figure 5.12: a) Raw image of the n-Dodecane spray jet at an injection pressure of 1.1 MPa, air flow of 28.5 kg/h and air temperatures of 328 K using MDBI technique and FOV of 14 mm × 9 mm, the dashed rectangle in the figure indicates the location of the next images, only to appreciate easily the procedure followed. b)Section of the raw image. c) Image with background subtraction and inverting of the pixels. d) Smoothing background subtraction. e) The gradient for each particle was calculated. f) Dilate in order to move the maximum intensity of the gradient. g) Particles that overcome the thresholds set.

Droplet tracking

After separating the good droplets from the spurious ones, it is necessary to find the most likely set of assignments that match each droplet in the previous frame with its counterpart in the current frame. This is not always trivial: the correct match for a droplet is not always the one closest in distance, and some droplets disappear or are introduced with each new frame, leaving droplets without counterparts. Therefore, a Python package was used for this task, Trackpy, which was developed by Allan et al. [9]. The tracking algorithm, at its simplest level, takes each particle in the previous frame and tries to find it in the current frame. This requires knowing where to look for it; if we find an actual particle near that spot, it is probably a match. The basic algorithm (Crocker & Grier) was developed to track particles undergoing Brownian diffusion, which ideally means that a particle's velocity is uncorrelated from one frame to the next. As a result, the best prediction for where a particle will move is that it will be close to its most recent position, as shown in Figure 5.14.

After identifying which particles are matched in both frames, the trajectory of them can be determined. Additionally, taking into account the time gap
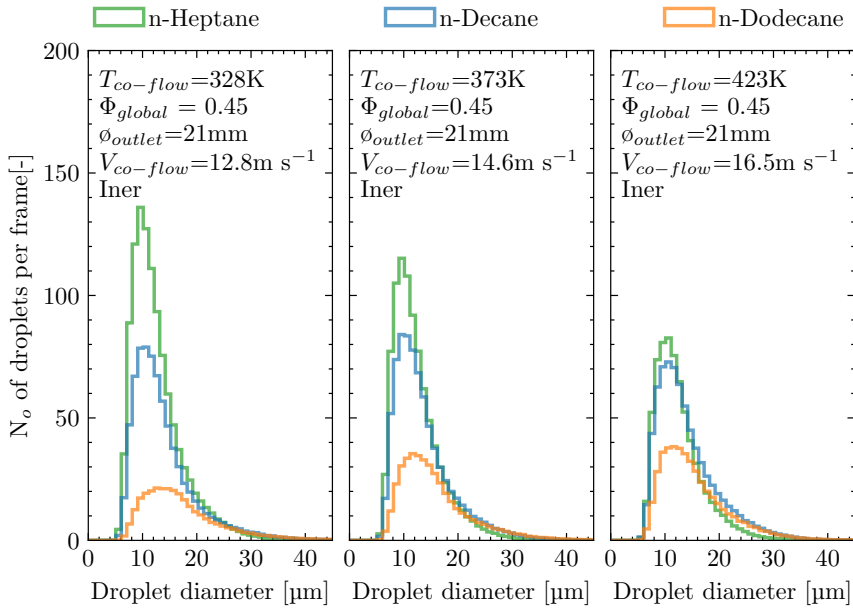
Figure 5.13: *Mean droplet distribution per frame for n-Heptane, n-Decane and n-Dodecane fuels at different air co-flow temperatures: 328 K a), 373 K b), and 423 K c).*
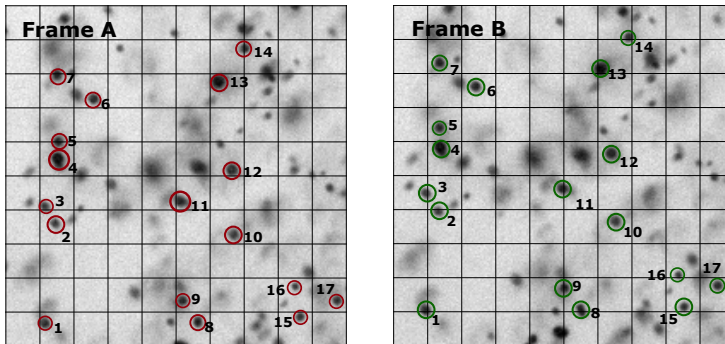
Figure 5.14: *Location and identification of the particles in Frame A and frame B (images captured through the MDBI technique). The frame shown is a n-Dodecane spray, for an injection pressure of 1.1 MPa, air co-flow of 28.5 kg h⁻¹ and air co-flow temperature of 328 K. Please note that the darker regions or spots captured in the pictures are not necessarily focused droplets.*

between the two frames allows calculating the droplet velocity. Figure 5.15 shows droplets of two successive frames, droplets in the initial time are colored

in green and the ones after the delay time between two consecutive frames in purple. Arrows and their color represent the magnitude of the droplet velocity.
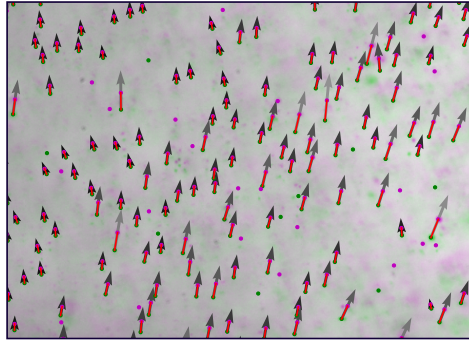
Figure 5.15: Droplet trajectory obtained through MDBI. The frame shown is a n-Dodecane spray, for an air mass flow of 11.9 kg h⁻¹ , and fuel mass flow of 135 mg s⁻¹ and air surrounding temperature of 328 K.

5.4.4   Soot formation

The soot formation in the spray flames was measured through the diffused back illumination technique, which is based on using a visible wavelength light as the source of illumination to observe any feature that attenuates this illumination. Nowadays, diffused back-illumination is widely employed in experimental setups that enable line-of-sight visualization. In this technique, the light extinction is the physical process, the optical depth (τ) or optical density is the metric to measure it, for instance, thus using the Beer-Lambert law, this extinction can be determined for each frame with the following equation:

$$\frac{I}{I_0} = e^{-\tau} \tag{5.2}$$

where I is the current pixel-wise intensity distribution of the frame that accounts for spray attenuation and I_0 is the background intensity without any attenuation. However, since the technique is used to measure the soot formation in a spray flame, some adjustments to the original technique were necessary. On the one hand, to measure the broad-band intensity from the flame (I_f) recorded and needed for calculating light extinction by the soot cloud, the light source was set to in an on-off configuration, i.e., the camera records a

frame with the light-on and the consecutive one with the light-off. Therefore, to include the broad-band intensity from the flame, the Equation 5.2 becomes

$$\frac{I - I_f}{I_0} = e^{-\tau} \tag{5.3}$$

where I_f accounts for the light emitted by the flame for the same time step with light-off. On the other hand, thanks to the advancement of new technologies such as fast light-emitting diodes (LED), it is now possible to improve the quality of images generated using the DBI technique. Since the light pulse duration may be adjusted to very low values (nanoseconds), the quantity of light available for each frame from the LED is controlled by the pulse length, but the light from soot incandescence is controlled by the camera's shutter time. Therefore, a DBI configuration was chosen for qualitative or even quantitative measurements of the soot concentration [10–13], as the optical thickness can also be represented as:

$$\tau = K \cdot L \tag{5.4}$$

where K is the dimensional extinction coefficient, and L is the path length through the soot. Thus, conditions with higher concentrations present a higher KL factor, although it is limited to the dynamic range of the images gathered. Furthermore, in the case of soot formation, it is essential to minimize the quantity of light captured by the camera from the flame; thus, the following configurations were used: First, a color LED unit was used as a light source, and a narrow band-pass filter with the same wavelength of the LED unit was coupled to the camera in order to record only a narrow portion of the broadband luminosity from the flame. Second, a short light-pulse was set, allowing to reduce the exposure time of the camera, thus recording less light from the flame. However, the configurations adopted to avoid recording the broad-band intensity from the flame are insufficient, and some of this intensity is captured by the camera, requiring removal in the image processing step by using Equation 5.3. Therefore, a LED pulse configuration was implemented (see Figure 5.16) to measure the light emitted from flame, which is estimated when the LED is turned off. The LED pulse configuration consists of 600 frames with LED-on and 600 frames with LED-off (recorded in successive batches of 20 frames as depicted in Figure 5.16), which were averaged to obtain proper mean images of the flame. A graphic explanation of how the KL factor was calculated for the case of the soot concentration is presented in Figure 5.17.
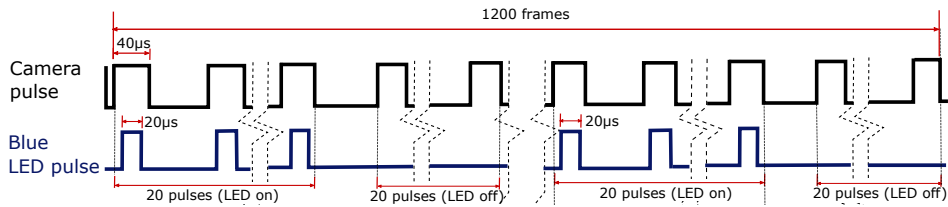
Figure 5.16: Schematic representation of the camera and LEDs pulses, movies consist of successive batches of 20 frames with LED-on and the following 20 frames with LED-off up to record 1200 frames.
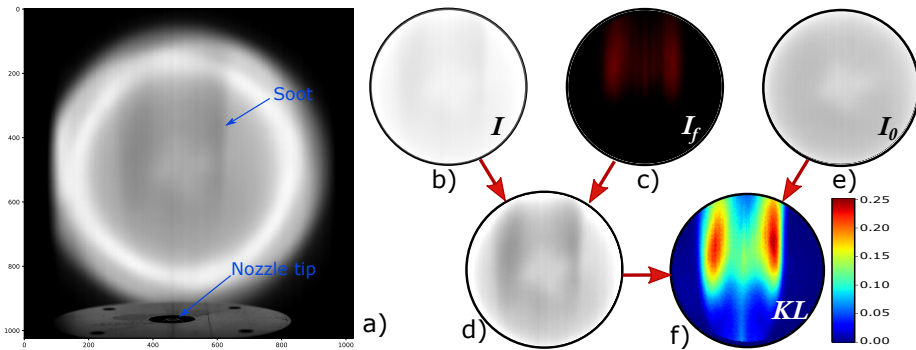
Figure 5.17: a) Raw image, b) Light attenuation by the soot cloud, I , c) Light emitted by the flame, d) Result from the subtraction of c) to b), true attenuation, e) Reference illumination, I_0, f) Optical thickness. Frames b), c) and d) same level of intensity. The frame shown is a Dodecane flame, for an injection pressure of 0.91 MPa, an air mass flow of 0.2 kg min^{-1} , and fuel mass flow of 135 mg s^{-1} and air surrounding temperature of 328 K.

The optical setup is formed mainly of a light-emitting diode (LED) as an illumination source and a high-speed camera (Photron SAZ) on opposing sides of the spray flame in a line-of-sight arrangement, as shown in a simplified schematic diagram Figure 5.18. A blue LED unit with a wavelength centered at 460 nm was mounted to the rays were directed to a Fresnel lens, with a focal length of 67 mm. Then a big square diffuser was placed in such a manner that the diffused background created was relatively large (more than 100 mm in diameter) and uniformly at the optical test plane of the spray flame. This blue LED unit can produce short and high-power pulses of light, with a high rate of repetition, the duration of the pulse was set at 20 µs, as a compromise

between intensity illumination and camera speed. Also, it allows for a higher signal-to-noise ratio in soot DBI measurements [14].
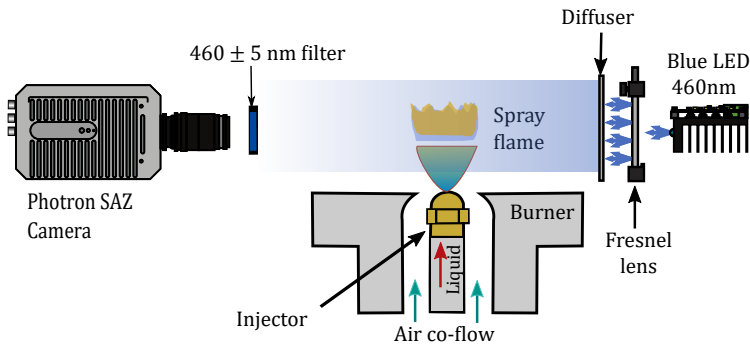
Figure 5.18: Schematic diagram of a simple diffused back-illumination setup.

The camera was equipped with a 24 - 70 mm Sigma lens, adjusted at a focal length of 60 mm. The camera was set with an acquisition rate of 250 fps and an exposure time of 40 μs to acquire the full period of the LED illumination. To effectively image the extinction signals, a filter must be placed in front of the camera objective. Therefore, a bandpass filter that transmits from 455 nm to 465 nm (measured at FWHM) was selected, which rejects most of the broadband luminosity from the flame. This technique has limitations, one of them is that some cameras have problems with fully resetting the sensor after the readout process when recording at relatively high speeds, as depicted in Figure 5.19. For such reasons, the movies were recorded in packs of 20 repetitions up to record 1200 frames and then averaged them, removing the first frame after each pack to avoid this effect. Manin et al. [15] studied this effect, highlighting the complexity of the process and the difficulty to quantify them.

After setting as well possible configuration to measure the soot attenuation as 1 explained previously, the images must be processed. However, quantitative soot measurements as a measure of the light extinction can be dominated by large uncertainties. For example, the calculation of the dimensionless optical extinction coefficient (k_e) can be mentioned. This coefficient has considerable control over the result of the soot volume fraction (f_v). This uncertainty comes from the dependence on a high number of parameters (e.g., soot morphology, the complex refractive index of soot, fuel sooting propensities) and the complexity to measure them experimentally. For these reasons, the present work presents the results related to the light extinction measures
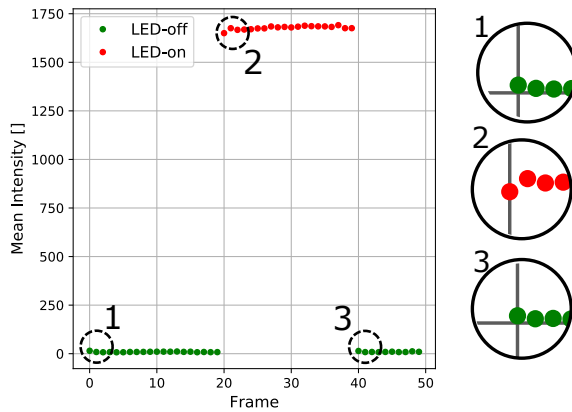
Figure 5.19: Schematic diagram of the camera performance.

in terms of the dimensional extinction coefficient, *K*. The dimensional extinction coefficient was calculated through the Abel Transform on the *KL* image results, which were obtained with the Equation 5.4, for which several methods have been developed. This makes it challenging to select the proper method for a specific application. Therefore, three methods (`Basex, Onion peeling, Three points`) out of the eight methods implemented in the PyAbel open source package for Python [16] were compared at random height. They are depicted as a yellow line in Figure 5.20.a and are commonly used in the analysis of flames and plasma plumes. Firstly, the inverse transform is computed at this height, i.e. it takes a 2D projection of the object to calculate a slice of the 3D object (Figure 5.20.b). Secondly, the forward transform is calculated for the previous step, i.e. to transform a slice of a 3D object into a 2D projection of the object (Figure 5.20.c). For this work, the `Basex` method was chosen and the "Tikhonov regularization" was set to 50, which provides reasonable noise suppression while still preserving the fine features in the image, as depicted in Figure 5.20. Furthermore, this method is computationally cheap.

Next to computing the Abel transform, a slice of the flame at the focal plane is obtained. As shown in Figure 5.21.a, light attenuation by both liquid phase and soot cloud appears in this slice. Therefore, as the combustion zone is the zone of interest, the following methodology was used to find the border between the two zones through a thresholding method: First, a threshold was set to split the image into two zones (as seen in Figure 5.21.b). Then, the border between them was then determined using a purpose algorithm.
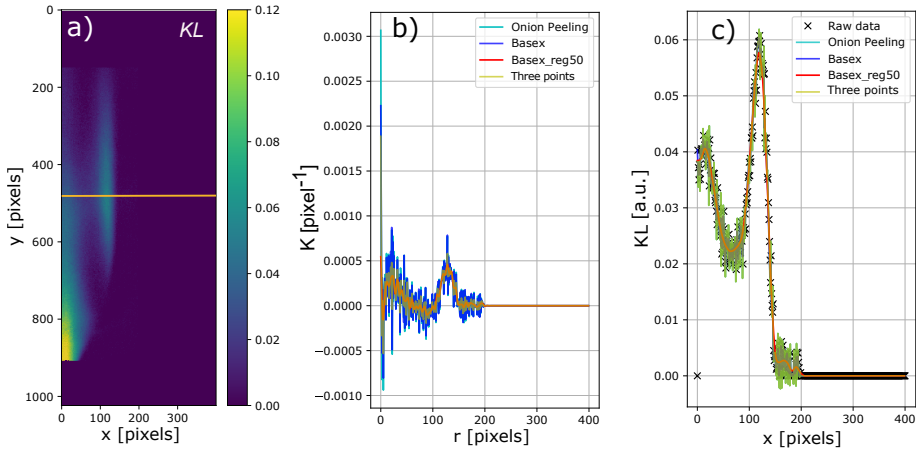
Figure 5.20: a) Soot attenuation presented in terms of the optical thickness (KL), yellow line represents the height to compute the Abel transform, b) Inverse transform computed at the chosen height, c) Forward transform of the inverse results presented in b). The frame shown is a n-Dodecane flame with an air surrounding temperature of 328 K, for an injection pressure of 0.1 MPa, an air mass flow of 0.2 kg min^{-1} and fuel mass flow of 135 mg s^{-1}.

Finally, the picture was masked such that just the combustion zone could be seen (Figure 5.21.c).

5.4.5   Flame lift-off height

The flame lift-off height was measured by recording the OH* Chemiluminescence, which is defined as a light emission phenomenon resulting from a chemical reaction, commonly associated with a release of heat. This technique has been extensively used in combustion research since OH radicals emit luminescence when they decay at their ground state. This luminescence can be captured and used in several diagnostics such as detection of high-temperature regions and estimations of the equivalence ratio [17–19]. OH* chemiluminescence occurs mostly at high-temperature stoichiometric combustion, and it is present in the flame stabilization region of lifted flames. The OH radical has the strongest emittance band at approximately 306 nm far away from the soot incandescence as shown in the right side of Figure 5.22. Thus, with the suitable optical setup, OH* chemiluminescence is an excellent marker to determine the flame lift-off height [20]. Therefore, an ICCD Andor iStar camera equipped with a 100 mm f/2.9 UV-capable lens and with the corresponding filter for OH* chemiluminescence (narrow band-pass filter of 310 ± 5 nm).
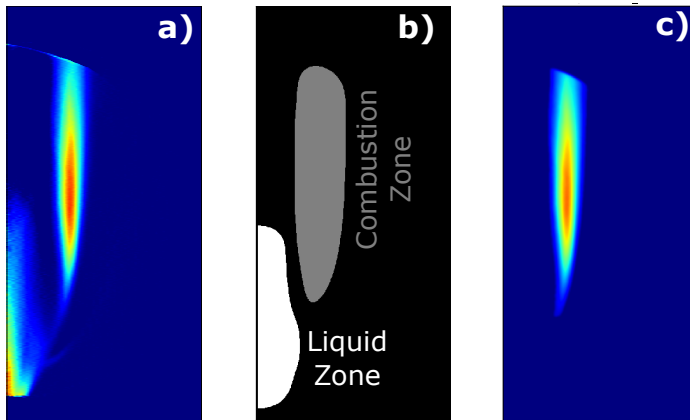
Figure 5.21: Example of the segmentation algorithm: Abel transform image a), combustion and liquid regions b), and combustion region c). The frame shown is a n-Decane flame, for an air mass flow of 0.2 kg min^{-1}, and fuel mass flow of 135 mg s^{-1} and air surrounding temperature of 328 K.

The camera was arranged shaping a slight angle to the optical axis to avoid the diffuser used to DBI technique. The chemiluminescence configuration has been extensively reported in the literature [20–26].
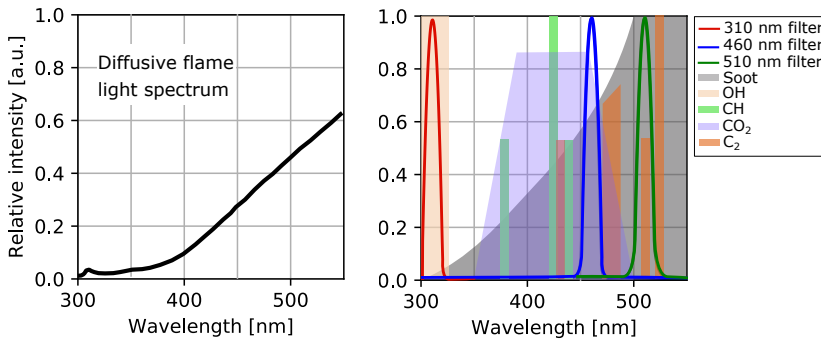
Figure 5.22: Example of the light spectrum distribution of a diffusive flame (left) [27], with peak injection pressure of 68 MPa, chamber density of density of 16.6 kg m^{-3} and temperature of 900 K. Emission wavelengths and relative radiation intensities of species in different phases of ignition and combustion. Emission wavelengths and relative radiation intensities of species in different phases of ignition and combustion (right) [28, 29].

As mentioned previously, the field of species concentration can be recorded by viewing the reacting zone through an appropriate optical band-pass filter, allowing only the spectrum of light emitted by the species of interest to pass. Nevertheless, such an image contains the concentration of the entire volume, since each pixel captures the integrated light from the entire volume passing through its line of sight. In order to resolve an axisymmetric integrated line-of-sight data distribution to one at a given azimuthal plane, the mathematical Inverse Abel Transform was used [30]. This method takes a 2D projection and reconstructs a slice of the cylindrically symmetric 3D distribution as shown in Figure 5.23. Since the spray flame is not completely axisymmetric, the Abel transform was computed for each half of the image separately, as shown in Figure 5.23.b. The Figure 5.23 also shows that the flame shape is well defined, suggesting that the effects of the non-axisymmetric do not seem to modify the flame morphology. The inverse Abel method plays a significant role in analyzing the projection flames [30–32]. Therefore, the processing step started by calculating the Abel inversion, using the Basex method, which provides appropriate advantages for this study, as described in the preceding section, for each recorded frame of OH* chemiluminescence.

a)   b)   c)
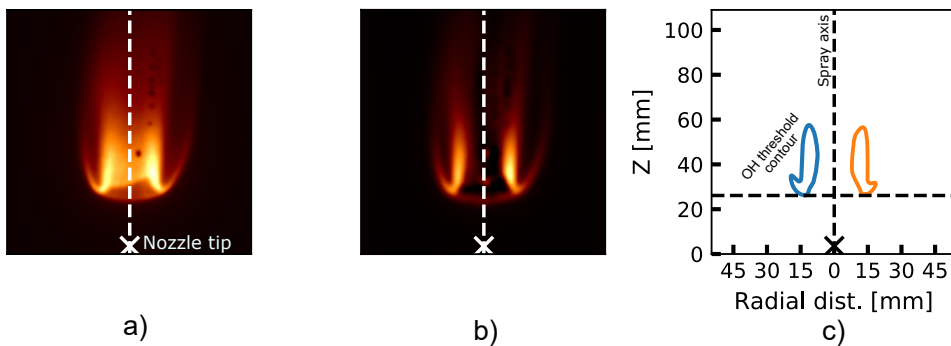
Figure 5.23: a) Raw image of OH* chemiluminescence, b) OH* chemilumi-nescence image after computing the Inverse Abel Transform, using a Basex method, c) Contour of the flame at central plane (image b) with a set thresh-old. The frame shown is a n-Dodecane flame, for an air mass flow rate of $0.2\,kg\,min^{-1}$, and fuel mass flow rate of $135\,mg\,s^{-1}$ and air co-flow temper-ature of $328\,K$.

The flame lift-off height is determined by averaging 30 OH* chemilumines-cence frames per operating condition. These frames were captured through an ICCD camera for each stabilized period of the combustion in order to obtain a proper mean image of the flame. The exposure time of the camera was set

at 0.3 s, integrating the flame radiation for a long time gap thus averaging turbulent fluctuations of the flame lift-off height. The images then represent spatial and temporal averages of radiation. The processing methodology to measure the flame lift-off height has been done following the methodology proposed by Siebers [33] for diesel fuel jets. After computing the Abel transform and averaging all repetitions, both sides of the resultant image are averaged and filtered with a Gaussian filter. Then, the mean intensity is traced for each height position, generating an intensity profile of the flame. Finally, two thresholds are defined as 25% and 50% of the difference between the first levelling-off peak and background noise. The background noise is calculated by averaging the first 7 mm from the nozzle tip, where no flame is present. The flame lift-off height is defined as the distance between the nozzle tip and the closest point in the flame above the calculated thresholds as shown in Figure 5.24.b. Even though no large differences in *LOH* were found when processing with the two chosen thresholds, the results presented in chapter 7 correspond to the threshold of 25%, which is slightly more sensitive to the intensity changes.

a)   b)
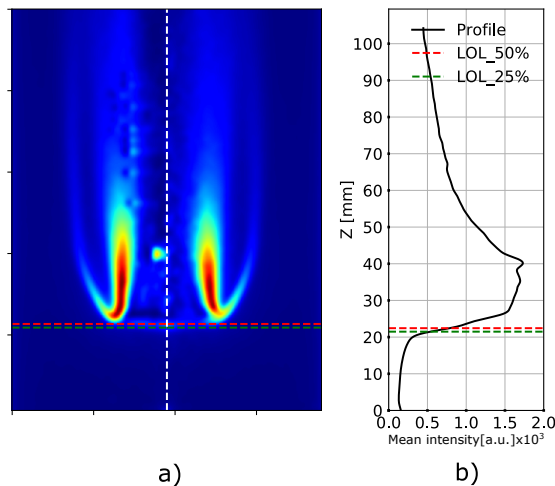
Figure 5.24: a) OH* chemiluminescence image after computing the Inverse Abel Transform, using the Basex method, b) Intensity profile of averaged flame, dashed lines represent the flame lift-off measured with both thresholds. The frame shown is a n-Decane flame with an air surrounding temperature of 328 K, for an air mass flow of 0.23 kg min^{-1} and fuel mass flow of 189 mg s^{-1}.

5.4.6 Simultaneous optical setup

All the techniques previously introduced were performed simultaneously (not the PIV technique) in order to measure the same injection event. PIV was implemented previously to this setup and was used to measure the velocity field of the atomization process. Additionally, taking advantage of the DBI configuration implemented to measure the soot concentration, the setup was also used to try determining the droplet concentration and was carried out simultaneously with Microscopic diffused back-illumination (MDBI) used to determine the droplet diameter and droplet velocity at the first millimeters near the nozzle exit, before the combustion zone (i.e., upstream the flame). In the case of the reactive spray diagnostic the MDBI, DBI, and OH* chemiluminescence techniques were carried out simultaneously and just after recording the frames at non-reactive conditions. MDBI was used to measure the diameter and velocity of the droplet at the region upstream from the flame lift-off height where there is no combustion. Likewise, DBI was applied to study the soot concentration within the spray flame. Finally, an ICCD Andor iStar camera, with the corresponding filter for OH* chemiluminescence, was positioned to the spray flame with a slight angle to avoid the diffuser of the DBI setup and thus record the OH* images to determine the flame lift-off height. Figure 5.25 shows a schematic representation of the optical setup used to carry out the simultaneous measurements of the different parameters.

The camera configurations for each optical technique used in the experimental campaign are summarized in Table 5.2.

Table 5.2: Summary of the configuration settings for each of the optical techniques performed.

Parameter	MDBI	DBI	OH*
Camera	Phantom VEO 640	Photron SAZ	Andor iStar
Camera lens	K2 DistaMax	Sigma 24-70 mm f/2.8	100 mm f/2.9 UV
Frame rate [fps]	1000	250	30*
Exposure [µs]	PIV mode	40	3×10^4
Field of view [pixels]	2560x1600	1024x1024	1024x1024
Pixel-mm	465	7.45	9.45
Filter CWL [nm]	-	460	310

* Per injection event.
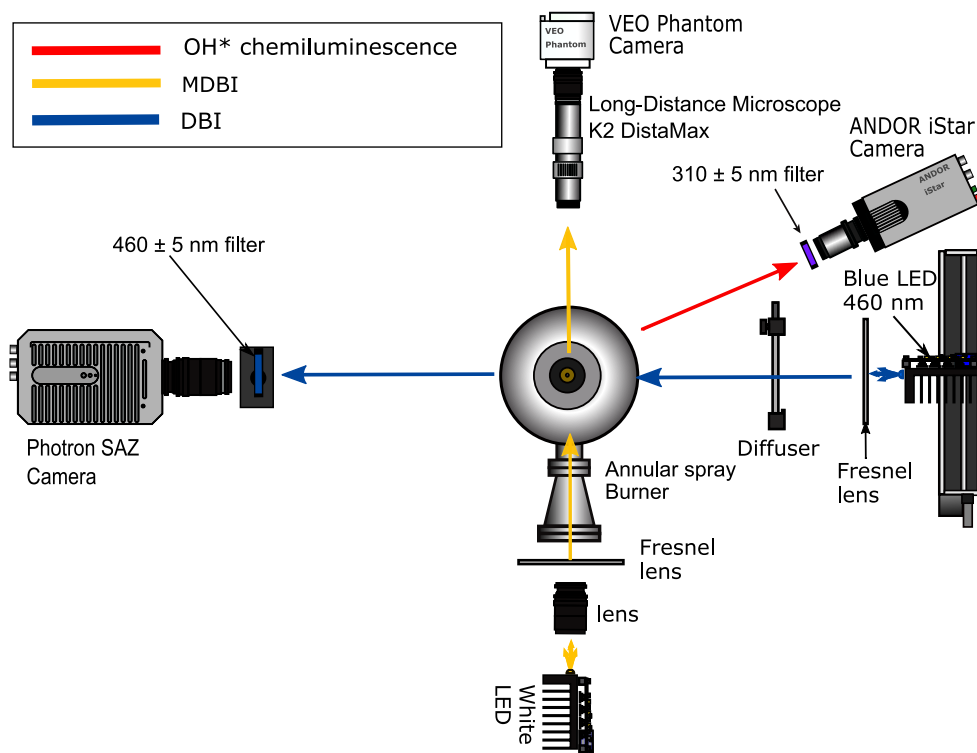
Figure 5.25: Schematic representation of the optical setup used to measure simultaneously MDBI, DBI, and OH* chemiluminescence.

5.5   Summary

This chapter presents all the experimental tools, optical setups and data processing routines used throughout the experimental campaign. First, the specifications of the injector and its internal geometry determination were detailed. The next section presents the annular spray burner, detailing the configuration used to perform the experimental campaign. Then, the optical diagnostic setups image processing methodology are discussed for each parameter measured, i.e., droplet velocity, droplet diameter, velocity fields, soot formation, and flame lift-off height, detailing cameras settings and the measuring strategies (e.g., synchronization of the light source signal and the camera). Finally, the optical arrangement used to carry out simultaneously the MDBI, DBI, and OH* chemiluminescence is introduced with a table that summarizes the camera's settings for the three techniques.

References

[1] Macian, V., Bermúdez, V., Payri, R., and Gimeno, J. "New technique for determination of internal geometry of a Diesel nozzle with the use of silicone methodology". In: *Experimental Techniques* 27.April (2003), pp. 39–43. DOI: 10.1111/j.1747-1567.2003.tb00107.x.

[2] Thielicke, W. and Sonntag, R. "Particle Image Velocimetry for MATLAB: Accuracy and enhanced algorithms in PIVlab". In: *Journal of Open Research Software* 9 (2021), pp. 1–14. DOI: 10.5334/JORS.334.

[3] Willert, C. E. and Gharib, M. "Digital particle image velocimetry". In: *Experiments in Fluids* 10.4 (1991), pp. 181–193. DOI: 10.1007/BF00190388.

[4] LaVision. *https://www.piv.de/index.php.*

[5] Prasad, A. K., Adrian, R., Landreth, C. C., and Offutt, P. W. "Effect of resolution on the speed and accuracy of particle image velocimetry interrogations". In: *Experiments in Fluids* 13 (1990), pp. 105–116.

[6] Raffel, M. et al. *Particle Image Velocimetry.* Cham: Springer International Publishing, 2018, pp. 1–664. DOI: 10.1007/978-3-319-68852-7.

[7] Payri, R., Bracho, G., Gimeno, J., and Moreno, A. "Spray Characterization of the Urea-Water Solution (UWS) Injected in a Hot Air Stream Analogous to SCR System Operating Conditions". In: *WCX SAE World Congress Experience.* 1. 2019, pp. 1–9. DOI: 10.4271/2019-01-0738.

[8] Manin, J., Bardi, M., Pickett, L., Dahms, R., and Oefelein, J. "Microscopic investigation of the atomization and mixing processes of diesel sprays injected into high pressure and temperature environments". In: *Fuel* 134 (2014), pp. 531–543. DOI: 10.1016/j.fuel.2014.05.060.

[9] Allan, D. B., Caswell, T., Keim, N. C., Wel, C. M. van der, and Verweij, R. W. *Trackpy v0.5.0.* 2021. DOI: 10.5281/ZENODO.4682814.

[10] Payri, R., Gimeno, J., Cardona, S., and Ayyapureddi, S. "Measurement of Soot Concentration in a Prototype Multi-Hole Diesel Injector by High-Speed Color Diffused Back Illumination Technique". In: *SAE Technical Paper 2017-01-2255.* 2017, pp. 1–11. DOI: 10.4271/2017-01-2255.

[11]   Skeen, S. A., Manin, J., Dalen, K., and Pickett, L. M. "Extinction-based Imaging of Soot Processes over a Range of Diesel Operating Conditions". In: *8th US National Combustion Meeting*. Utah, USA, 2013, pp. 1–13.

[12]   Manin, J., Skeen, S. A., and Pickett, L. M. "Two-color diffused back-illumination imaging as a diagnostic for time-resolved soot measurements in reacting sprays". In: *SAE Int. J. Engines* 6.4 (2013), pp. 1908–1921. DOI: 10.4271/2013-01-2548.

[13]   Pastor, J. V., Garcia-Oliver, J. M., Novella, R., and Xuan, T. "Soot Quantification of Single-Hole Diesel Sprays by Means of Extinction Imaging". In: *SAE International Journal of Engines* 8.5 (2015), pp. 2068–2077. DOI: 10.4271/2015-24-2417.

[14]   Manin, J., Bardi, M., and Pickett, L. M. "Evaluation of the liquid length via diffused back-illumination imaging in vaporizing diesel sprays". In: *The Proceedings of the International symposium on diagnostics and modeling of combustion in internal combustion engines*. Fukuoka, 2012, pp. 665–673.

[15]   Manin, J., Pickett, L. M., and Skeen, S. A. "Toward quantitative spray measurements using high-performance high-speed video cameras". In: *ILASS Americas 2016* (2016), pp. 511–518.

[16]   Hickstein, D. D., Gibson, S. T., Yurchak, R., Das, D. D., and Ryazanov, M. "A direct comparison of high-speed methods for the numerical Abel transform". In: *Review of Scientific Instruments* 90.6 (2019), pp. 1–9. DOI: 10.1063/1.5092635.

[17]   Orain, M. and Hardalupas, Y. "Influence du combustible sur la mesure de richesse par chimiluminescence dans les flammes prémélangées". In: *Comptes Rendus - Mecanique* 338.5 (2010), pp. 241–254. DOI: 10.1016/j.crme.2010.05.002.

[18]   Panoutsos, C. S., Hardalupas, Y., and Taylor, A. M. "Numerical evaluation of equivalence ratio measurement using OH* and CH* chemiluminescence in premixed and non-premixed methane-air flames". In: *Combustion and Flame* 156.2 (2009), pp. 273–291. DOI: 10.1016/j.combustflame.2008.11.008.

[19]   Liu, H. et al. "Influence of temperature and mixture stratification on HCCI combustion using chemiluminescence images and CFD analysis". In: *Applied Thermal Engineering* 33-34.1 (2012), pp. 135–143. DOI: 10.1016/j.applthermaleng.2011.09.026.

[20] Higgins, B. and Siebers, D. L. "Measurement of the Flame Lift-Off Location on DI Diesel Sprays Using OH Chemiluminescence". In: *SAE Technical Paper* (2001).

[21] Bardi, M. "Partial needle lift and injection rate shape effect on the formation and combustion of the Diesel spray". PhD thesis. Valencia (Spain): Universitat Politècnica de València, 2014. DOI: `10.4995/Thesis/10251/37374`.

[22] Benajes, J., Payri, R., Bardi, M., and Martí-aldaraví, P. "Experimental characterization of diesel ignition and lift-off length using a single-hole ECN injector". In: *Applied Thermal Engineering* 58.1-2 (2013), pp. 554–563. DOI: `10.1016/j.applthermaleng.2013.04.044`.

[23] Payri, R., Bracho, G., Martí-Aldaraví, P., and Viera, A. "Nozzle geometry size influence on reactive spray development: from Spray B to heavy duty applications". In: *SAE Technical Paper 2017-01-0846*. 2017, pp. 1–12. DOI: `10.4271/2017-01-0846`.

[24] Payri, R., Salvador, F. J., Manin, J., and Viera, A. "Diesel ignition delay and lift-off length through different methodologies using a multi-hole injector". In: *Applied Energy* 162 (2016), pp. 541–550. DOI: `10.1016/j.apenergy.2015.10.118`.

[25] Payri, R., Viera, J. P., Pei, Y., and Som, S. "Experimental and numerical study of lift-off length and ignition delay of a two-component diesel surrogate". In: *Fuel* 158 (2015), pp. 957–967. DOI: `10.1016/j.fuel.2014.11.072`.

[26] Bardi, M. et al. "Engine combustion network: comparison of spray development, vaporization, and combustion in different combustion vessels". In: *Atomization and Sprays* 22.10 (2012), pp. 807–842. DOI: `10.1615/AtomizSpr.2013005837`.

[27] Dec, J. E. and Espey, C. "Chemiluminescence Imaging of Autoignition in a DI Diesel Engine". In: *SAE Technical Paper* 724 (1998). DOI: `10.4271/982685`.

[28] Gaydon, A. G. *The Spectroscopy of Flames*. Springer Netherlands, 1974. DOI: `10.1007/978-94-009-5720-6`.

[29] Pittermann, R. "Spectroscopic Analysis of the Combustion in Diesel and Gas Engines". In: *MTZ worldwide* 69.7 (2008), pp. 66–73. DOI: `doi.org/10.1007/BF03227907`.

[30] Verma, S. and Basu, S. *Application of Inverse Abel Transform on flame image*. Tech. rep. Indian Institute of Science.

[31] Cignoli, F., De Iuliis, S., Manta, V., and Zizak, G. "Two-dimensional two-wavelength emission technique for soot diagnostics". In: *Applied Optics* 40.30 (2001), p. 5370. DOI: 10.1364/ao.40.005370.

[32] De Iuliis, S., Barbini, M., Benecchi, S., Cignoli, F., and Zizak, G. "Determination of the soot volume fraction in an ethylene diffusion flame by multiwavelength analysis of soot radiation". In: *Combustion and Flame* 115.1-2 (1998), pp. 253–261. DOI: 10.1016/S0010-2180(97)00357-X.

[33] Siebers, D. L. "Liquid-Phase Fuel Penetration in Diesel Sprays". In: *SAE Technical Paper*. 1998, pp. 1–23. DOI: 10.4271/980809.

Chapter 6

Experimental study of the atomization process

6.1 Introduction

In this chapter, the findings of using the Microscopic diffused back-illumination (MDBI) optical technique described in section 5.4 to measure the parameters related to the droplet properties (i.e., size and velocity) are introduced. The tests were conducted for both non-reactive and reactive conditions, but no significant differences were found since the field of view (FOV) was too close to the injector tip and therefore far away from the combustion area and thus, the data reported in this chapter correspond to non-reactive conditions. Previous to the MDBI study, a small PIV study was performed in order to investigate the effect of the co-flow conditions and fuel type on droplet velocities of the global spray since the MDBI technique was carried out only for a small region close to the tip of the injector. The chapter is organized as follows: First, the results of the PIV technique, which was used to measure the velocity fields formed by the liquid atomization in a wide range of operating conditions and three fuels (n-Dodecane, n-Heptane, and n-Hexadecane), are presented. Then, the results of droplet size and droplet velocity for three fuels (n-Decane, n-Dodecane, n-Heptane) are presented, which were measured by using the MDBI technique and also carried out for a wide range of operating conditions, however, the conditions are different to the ones used to perform the PIV study because the first ones do not provide conditions to stabilize the flame.

Furthermore, a comparison between measured and calculated SMD is included to compare theoretical and experimental results. The chapter ends with a summary and conclusions.

6.2   Velocity fields

As described in section 5.4, the PIV technique was used to measure 2D velocity fields using liquid droplets as tracers and was applied to investigate the global spray characteristics. Therefore, the conditions listed in Table 6.1 were selected to investigate the effect of co-flow temperature, injection pressure, and fuel type on droplet velocity in a long FOV (105×105 mm). The proposed test matrix has 72 test points and was performed for three different fuels, n-Heptane, n-Dodecane, and n-Hexadecane, which were chosen to cover a wide range of physical properties (provided in Table 6.2), such as density, viscosity, and surface tension. However, some operating conditions at high temperatures were not measured for the n-Heptane fuel since these conditions promote the complete evaporation of the fuel practically instantly after the fuel injection. PIV technique was carried out before performing simultaneously the MDBI, DBI, and OH* chemiluminescence techniques as the first approach to understand the behavior of the spray with the variation of the parameters tested.

Table 6.1: Test plan for PIV campaign.

Parameter	Value	Units
Air temperature (T_{air})	328 - 373 - 423 - 473	K
Injection pressure (P_{inj})	1.1 - 1.7 - 2.9	MPa
Air mass flow	26.4 - 34.2 - 44.4	kg h^{-1}
Air outlet diameter	19 and 21	mm

Table 6.2: Physical and chemical properties of the fuels. Most of the properties were extracted from the NIST database at normal temperature an pressure (i.e., 293.15 K and 1 atm) [1].

Properties	n-Heptane	n-Dodecane	n-Hexadecane
Formula	C_7H_{16}	$C_{12}H_{26}$	$C_{16}H_{34}$
Density (ρ_l) [kg m^{-3}]	683.94	749.5	773.7
Dynamic viscosity (μ_l) [Pa s]	0.00041	0.00149	0.00349
Surface tension (σ_l) [N m^{-1}]	0.0206^a	0.0254^a	0.0275^a

[a] Along the saturation curve

6.2.1 Results

As a result of applying the PIV technique, which provides velocity fields of the two mean velocity components (radial and axial) of the carrier phase of the fuel droplets, as shown in Figure 6.1. However, to compare the effect of varying the parameters on the droplet velocity effectively, the data provided in this section are presented in terms of velocity profiles at various spray jet heights (see Figure 6.1). Consistent with earlier works [2–5], the mean axial co-flow velocity provides two peaks at the exit of the injector. Further downstream ($Z > 30$ mm), the co-flow air jets merge to produce a unique larger jet with a flat axial velocity profile at the core of the jet. Note that the air co-flow jet also generates radial velocities, approximately 5 times smaller than the axial velocities at $Z = 10$ mm, which rapidly decrease down to zero at $Z = 30$ mm.
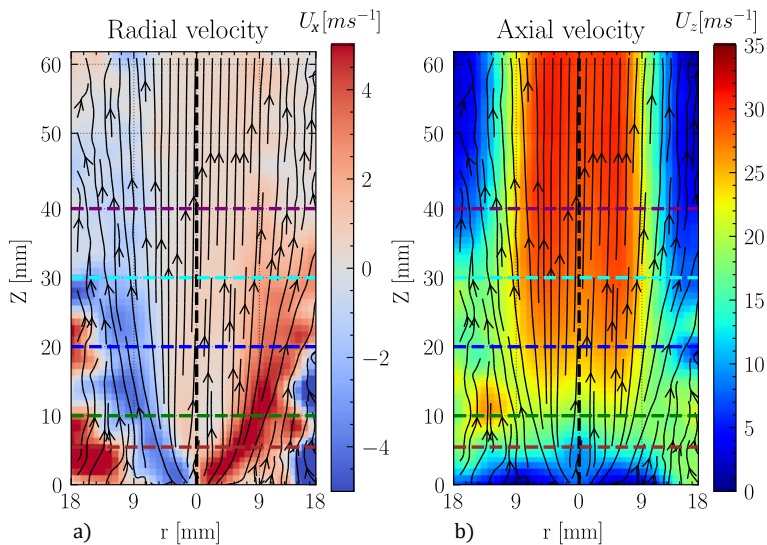
Figure 6.1: Mean components of fuel droplet velocity obtained with PIV technique; mean radial velocity a) and mean axial velocity b). The frame shown is a n-Hexadecane spray with an air surrounding temperature of 328 K, for an air mass flow of 0.44 kg min^{-1} and injection pressure of 1.1 MPa.

The liquid spray exhibits a complex heterogeneous distribution, with droplets sizes between 2 and 80 µm. The mean velocity profiles at three different heights, $Z = 10$, 20 and 30 mm are represented in the following Figures (6.2, 6.3, 6.4). Droplets are atomized at a cone with a 80° aperture, in a direction that forces them to interact with the air co-flow rapidly. Because of

the centrifugal movement induced by the swirling fluid injection inside the atomizer, the center area has a very low number of small droplets. Due to their low Stokes number, the smallest droplets formed by the liquid jet breakup are sensitive to the air velocity field and follow the flow. Additionally, in this area, the extremely small drops constitute only a small proportion of the liquid mass and evaporate slowly, resulting in a lean heterogeneous mixture near to the lean flammability limit [6]. Nevertheless, larger drops with higher Stokes numbers are less influenced by aerodynamic conditions and follow ballistic trajectories.

Figure 6.2 depicts that the droplets are expelled from the injector with relatively high radial velocities mainly at the spray borders where the big droplets are located, forming two radial velocities peaks and a central region at constant velocity formed by the small droplets. At the height of 10 mm, the droplets exhibit important radial velocities but father downstream small droplets adjust their velocity to the air co-flow. Big drops follow more ballistic trajectories and maintain radial centrifugal velocities until $Z = 30$ mm. When the spray is overlapped to the air stream, the droplet axial mean velocities are lower for the spray than for the air, and as a result, small droplets are significantly accelerated by the co-flow, while big droplets continue to fly at slower speeds until farther downstream. When fuel droplets leave the high-velocity zone, they enter a quiescent zone where they may decelerate. Additionally, it can be noted that air co-flow temperature, air co-flow and injection pressure variations at $Z = 30$ mm do not affect significantly the radial velocity since, at this height, the radial component of the droplet velocity has been reduced by the airflow an droplets are controlled by the air stream.

Figure 6.3 shows the effect of the variation of the air co-flow temperature, injection pressure, and air co-flow on the axial velocity at different heights of the spray jet. By increasing the air co-flow temperature, the air density is decreased, and thus the air co-flow velocity is increased for a fixed cross-section, resulting in a higher axial droplet velocity. The air mass flow rate is directly related to the axial velocity, i.e., increasing the air mass flow rate, the co-flow velocity increases. In Figure 6.3, it is evident this parameter has an important effect on the axial velocity. On the other hand, there are no significant differences in the axial velocity with the variation of the injection pressure, it only slightly at the first millimeters. The velocities profiles were calculated, recording the light scattering of all droplet sizes in a field of view (FOV) of 105 ×105 mm. However, measures were not possible at heights lower than $Z = 10$ mm due to the high concentration of fuel droplets and ligaments that avoid tracking the particles properly.
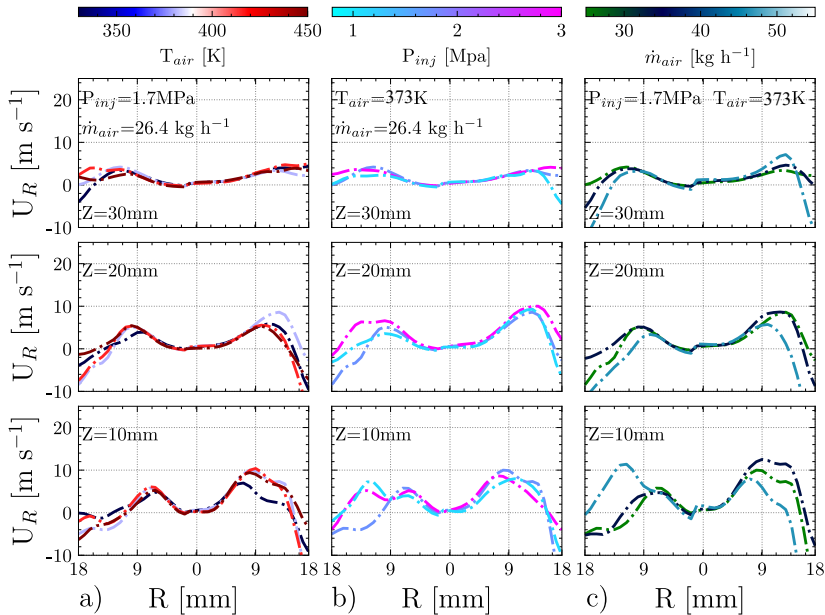
Figure 6.2: n-Dodecane sprays at constant conditions to observe the influence of co-flow temperature (a), injection pressure (b), and air mass flow rate (c) on the mean radial velocity at three different heights.

Figure 6.4 shows the axial velocity for three different fuels (n-Dodecane, n-Heptane and n-Hexadecane). When comparing fuel droplet profiles, it can be observed that n-Heptane droplets follow more closely the air velocity due to the small droplet size, as shown in section 6.3. Large droplets such as those generated by atomizing the n-Dodecane and n-Hexadecane fuels follow more ballistic trajectories and continue to present significant axial and centrifugal velocities until $Z = 30\,\mathrm{mm}$, where they nearly join the other groups. The differences in droplet size for the different fuels are associated with the physical property variations, especially differences in density, viscosity, and surface tension, as shown in Table 6.2. The effect of the co-flow rate can also be observed in Figure 6.4, evidencing its direct influence on the axial velocity of the droplets for all fuels, i.e., increasing the air mass flow rate the droplet velocity increases.
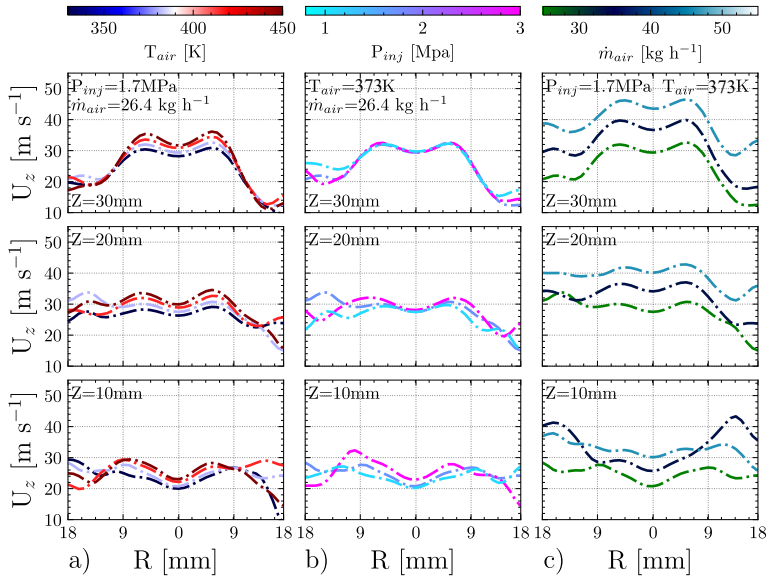
Figure 6.3: *n-Dodecane sprays at constant conditions to observe the influence of co-flow temperature a), injection pressure b), and air mass flow rate c) on the mean axial velocity.*
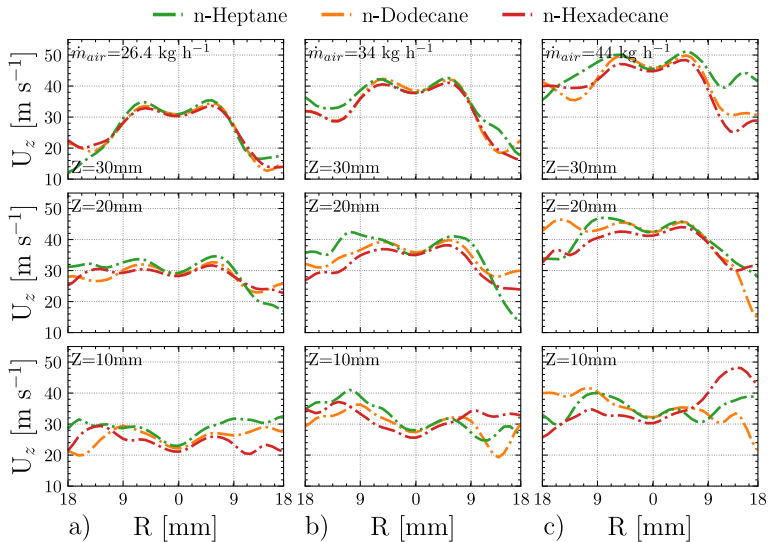
Figure 6.4: *Fuel comparison at air surrounding temperature of 423 K and injection pressure of 1.7 MPa and different air mass flow rate 26.4 a), 34 b), and 44 kg h^{-1} c).*

6.3   Droplet size and droplet velocity

After applying the PIV technique, which was used to study the global spray properties (velocity fields), the MDBI technique was carried out to measure the droplet size and droplet velocity in the region close to the injector tip (2 mm above the injector tip). Furthermore, The MDBI technique was performed for both non-reactive and reactive conditions. The results in this section, however, only refer to non-reactive conditions since no significant differences were found, which is likely due to the FOV was located so close to the nozzle tip and thus far away from the combustion zone. Figure 6.5 shows examples of the raw images captured through the MDBI technique, which records a FOV of 3.5×5.5 mm positioned on the right side of the spray concerning the spray axis, as was explained in section 5.4. Also, it is important to remember this technique is based on recording two consecutive frames with a small time interval between them, allowing to measure the droplet displacement and thus droplet velocity.
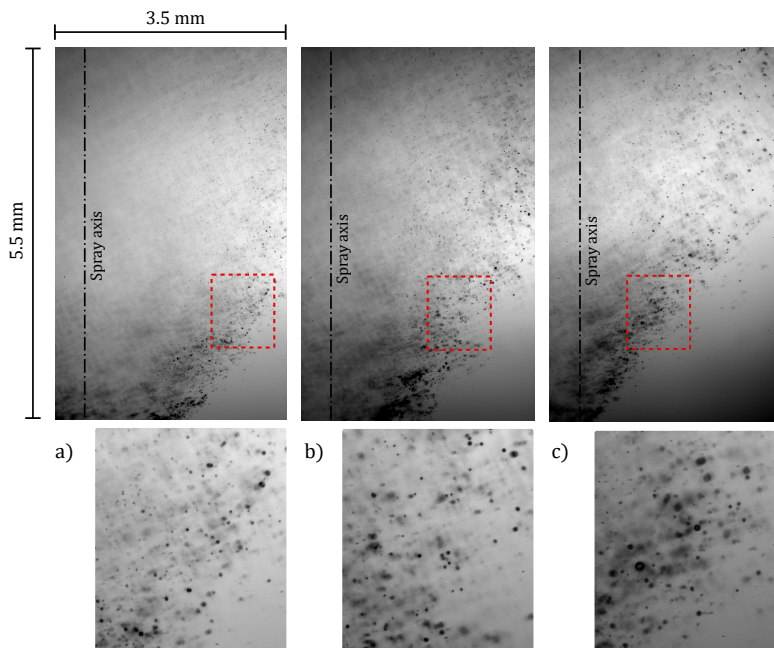
Figure 6.5: Raw images at fixed conditions for the three fuels: n-Heptane a), n-Decane b), and n-Dodecane c). The frames shown are sprays with an air surrounding temperature of 423 K, for an air co-flow velocity 12.6 m s^{-1} and a global equivalence ratio of 0.6.

The MDBI technique was performed for a wide range of operating conditions summarized in Table 6.3, which includes three air temperatures (328, 373 and 423 K) and nine global equivalence ratios (which are directly related to air mass flow rate, injection pressure and fuel type) for each air outlet diameter. Note these conditions are different from the ones used to carry out the PIV study since they did not provide conditions to stabilize the flame. Additionally, All experiments were performed for three different fuels (n-Heptane, n-Decane, and n-Dodecane) injected through a commercially hollow cone spray injector, described in section 5.2.

Table 6.3: Test conditions matrix.

Parameter	Value
Fuel mass flow rate $(\dot{m}_l)[\mathrm{mg\,s^{-1}}]$	$(130, 159, 187.6)^a$ $(130.8, 159.83, 188.89)^b$ $(131.23, 160.4, 189.54)^c$
Air mass flow rate $(\dot{m}_{air})$ [kg h^{-1}]	11.9, 13.6, 15.6
Global equivalence ratio (ϕ_{global})	0.45, 0.52,0.55, 0.6, 0.63, 0.65, 0.73, 0.75, 0.86
Co-flow temperature $(T_{co-flow})$ [K]	328, 373, 423
Air outlet diameter $(\varnothing_{outlet})$ [mm]	19 and 21

[a] n-Heptane,   [b] n-Decane,   [c] n-Dodecane

In Table 6.3, the global equivalence ratio (ϕ_{global}) is defined as the ratio of the actual fuel/air ratio to the stoichiometric fuel/air ratio and was calculated as follow:

$$\phi_{global} = \frac{\frac{\dot{m}_l}{\dot{m}_{air}}}{\left(\frac{\dot{m}_l}{\dot{m}_{air}}\right)_{St}} \tag{6.1}$$

where $\dot{m}$ is the mass flow for air and fuel, St, refer to stoichiometric conditions. The equivalence ratio was varied in a range of fuel-poor conditions from 0.45 to 0.86. Note that the fuel mass flow rate is controlled by the injection pressure. Since the air equivalence ratio and the air co-flow velocity are directly linked, the co-flow velocity was theoretically calculated at the burner outlet as

$$V_{co-flow} = \frac{\dot{m}_{air}}{A \cdot \rho_{air}} \quad \left[\frac{m}{s}\right] \tag{6.2}$$

where $\dot{m}_{air}$ is the air mass flow rate, A is the area of the cross-section of the burner exit, and ρ_{air} is the air density. This velocity has a strong effect on the

flame lift-off height (and hence soot formation, as will be seen in chapter 7) and it also significantly varies as a result of the variation of some parameters such as the air co-flow temperature. Note these parameters were varied throughout this study (see Table 6.3), resulting in a wide range of velocities that covering from 7.5 to 20.5 m s^{-1}.

Three hydrocarbon fuels were used in this study: n-Heptane, n-Decane, and n-Dodecane. The fuels were chosen to cover a wide range of physical properties (summarized in Table 6.4), such as density, viscosity, and surface tension, which influence the atomization (i.e., SMD), along with vapor pressures (P$_v$) and normal boiling temperatures, which impact the vaporization of the fuel. n-Heptane is the most volatile fuel, followed by n-Decane and then n-dodecane, which has a normal boiling higher than the other fuels. The reactivity of the fuel is marked by the laminar flame speed (S_L), which is a significant factor that can influence the flame stability, especially flame lift-off.

Table 6.4: Physical and chemical properties of the fuels. Most of the properties were extracted from the NIST database at normal temperature an pressure (i.e., 293.15 K and 1 atm) [1]. Laminar flame speed values were reported in previous works at 400 K, at 1 atm, and stoichiometric equivalence ratio [7, 8].

Properties	n-Heptane	n-Decane	n-Dodecane
Formula	C$_7$H$_{16}$	C$_{10}$H$_{22}$	C$_{12}$H$_{26}$
Density (ρ_l) [kg m^{-3}]	683.94	730.53	749.5
Dynamic viscosity (μ_l) [Pa s]	0.00041	0.00091	0.00149
Surface tension (σ_l) [N m^{-1}]	0.0206[a]	0.0238[a]	0.0254[a]
Normal Boiling point [K]	371.53	447.27	489.3
P$_v$ [kPa]	160[b]	16,5[b]	3.8[b]
S_L [m s^{-1}]	0.6413	0.6410	0.6405
Stoichiometric fuel/air ratio	1/15.1	1/15	1/14.95

[a] Along the saturation curve,   [b] At 387 K

6.3.1   General considerations

Using the MDBI technique and the processing methodology, the droplet size, position and velocity can be determined, as was previously described in section 5.4. For example, Figure 6.6 shows a scatter representation of the results applying this technique, which records droplets resulted from the atomization process at the first millimeters of the spray for the three fuels at fixed operating conditions. Figure 6.6 exhibits that fuel spray presents a complex

heterogeneous distribution, with droplets ranging from 2 to 80 μm, and with most of the droplets and mainly the big ones at the spray borders, which is expected due to the hollow spray pattern of the pressure swirl atomizer used. Additionally, it can be observed that droplets close to the spray axis are mostly small since the droplets are expelled from the injector with a spray opening angle of 80°, forcing them to interact quickly with the air co-flow, which drags the small ones to this region. Finally, from the figure can be noted that as lighter the fuel, the opening angle of the spray increases and also produces a higher quantity of droplets.
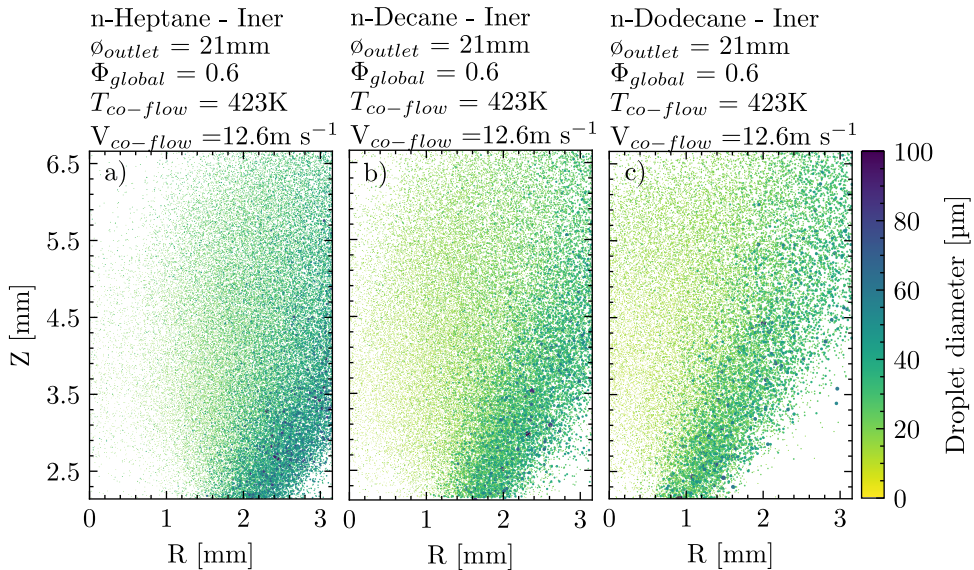
Figure 6.6: Schematic representation of the droplet size at fixed conditions for the three fuels: n-Heptane a), n-Decane b), and n-Dodecane c).

The MDBI technique was used to record 300 pairs of consecutive frames, which allows performing and statistical analysis, such as calculating mean droplet diameter, Sauter Mean Diameter (SMD), and mean velocities. Therefore, the frame's domain has been split into cells to calculate a specific parameter in each one. Figure 6.7 shows the SMD in each cell for the three fuels at the same operating conditions, evidencing again that most of the big droplets are at the spray borders and also that the heavier fuel (n-Dodecane) produces bigger droplets, followed by n-Decane and then n-Heptane.

Regarding the droplet velocity, it was calculated in the same way that the SMD, i.e., calculating the mean droplet velocity for each cell. Consequently,
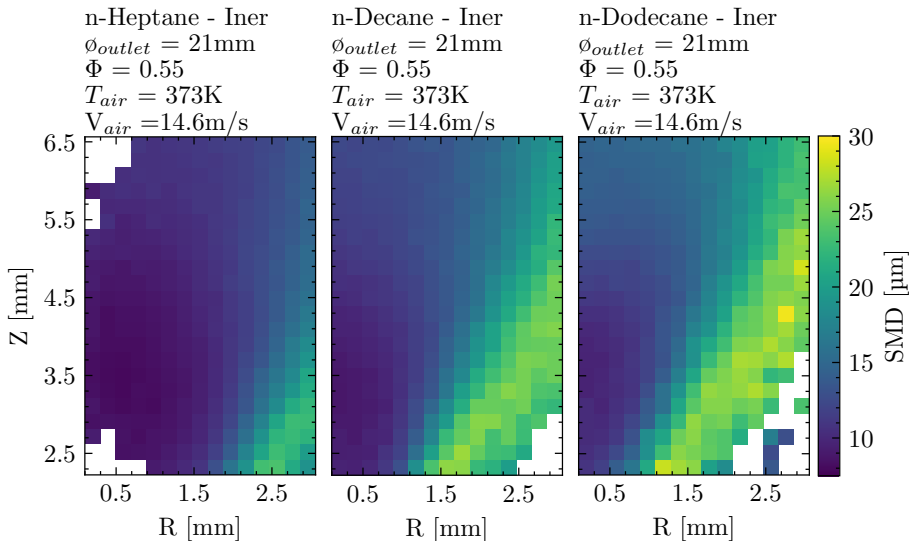
Figure 6.7: SMD calculated for each cell and for each of the three fuels at the same operating conditions.

the results presented throughout this section correspond to velocity in the cells at a certain height, resulting in a droplet velocity profile at this selected height. Previous to the results, it is significant to mention some relevant facts such as the droplet trajectory behavior regarding its size, as shown schematically in Figure 6.8, where it is represented the mean velocity for small and big droplets. This behavior is due to the centrifugal movement inside the atomizer that forces the liquid to be expelled in a hollow cone pattern with most of the droplets at the spray borders and relatively few droplets at the core zone (see Figure 6.6). The ones that appear in the spray core are mainly small, which are more influenced by the air co-flow that drives them to follow its streamline due to their small Stokes number, as shown in Figure 6.8, where both green and blue arrows represent the trajectory and velocity of the small droplets (i.e., droplet diameters below 12 µm). Furthermore, in this area, drops account for just a minimal portion of the liquid mass and evaporate slowly, resulting in a lean heterogeneous mixture close to the lean flammability limit [6]. Nevertheless, larger drops with higher Stokes numbers are less influenced by the aerodynamic conditions and follow ballistic trajectories, as observed in Figure 6.8, where red arrows represent the velocities and trajectories of the big droplets (droplet diameters above the 14 µm).

From these results, they can be represented such as histograms or profiles
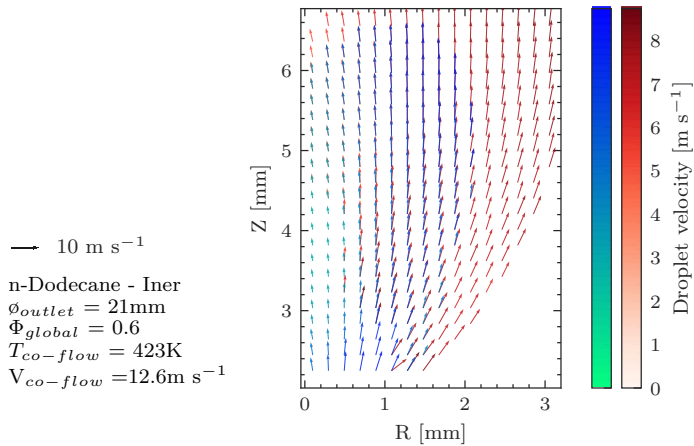
Figure 6.8: Droplet trajectories for n-Dodecane fuel; red arrows represent the trajectory of droplets with a diameter higher than 14 µm and blue or green arrows diameters lower than 12 µm.

of the droplet sizes or droplet velocities, like the example shown in Figure 6.9, where a comparison of these histograms for both droplet size and droplet velocity and even a combination of both in a 2D representation for the three fuels can be seen, evidencing the significant differences in droplet sizes and theirs velocities regarding the fuel type. Another important point to mention is that the global equivalency ratio was chosen as the constant parameter in order to compare the fuels because it is widely used in combustion research to compare different fuels. However, when this parameter is chosen, the fuel mass flow rate must be higher for the fuel with a lower stoichiometric fuel/air ratio, leading to an increase in injection pressure to supply this demand and therefore increasing droplet ejection velocity (see Anexo 6.A), which is higher for n-Heptane fuel, followed by n-Decane and then n-Dodecane, as shown in Figure 6.9. Nevertheless, this trend regarding droplet velocity does not coincide with the findings stated in the PIV results (see section 6.2) likely due to the measurements were performed at heights above 10 mm where the droplets are more influenced by the air co-flow than the results presented throughout this section, which are more related to the droplet ejection velocity since it was measured very close to the injector tip (2 mm above the injector tip), also, the PIV study was performed at higher both injection pressures and air mass flow rates. In addition, Figure 6.9 shows that for any fuel, the small droplets with low Stokes numbers have lower velocities than the big ones with

higher Stoke numbers and also that the heavier fuel promotes the formation of bigger droplets (n-Dodecane).
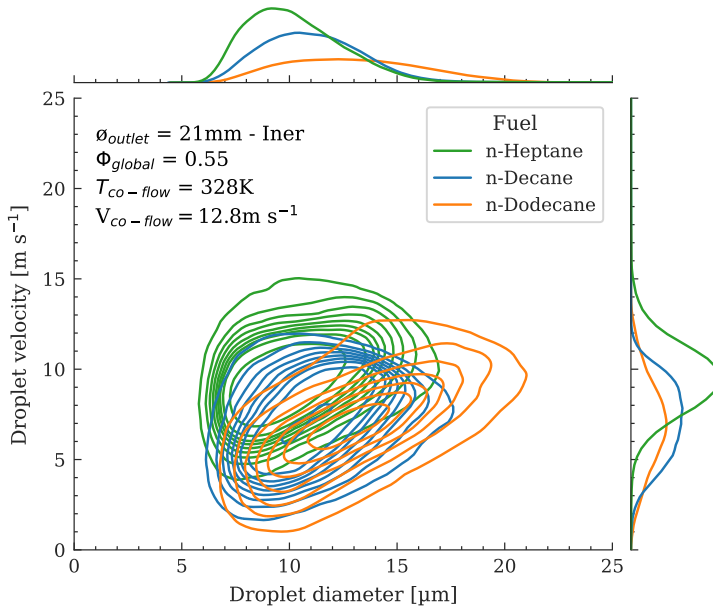
Figure 6.9: Probability density function for the three fuels at fixed conditions.

The last relevant fact is related to the classification of the breakup regimes, which were introduced in section 3.2. Regarding this classification, all operating conditions tested are controlled by the second wind-induced regimen, which is characterized by the small droplets generated by the unstable growth of short waves on the jet surface by the interaction between the jet and the surrounding air, as shown in Figure 6.10. The droplets generated under this regimen are much smaller than the initial jet diameter, and the breakup occurs several diameters downstream of the nozzle exit. The atomization characteristics were observed experimentally, showing that n-Heptane fuel generates the smallest droplet diameters since it was injected at a higher pressure, which increases both higher liquid ejection velocity and Reynolds number. Therefore, n-heptane is the closest to the Prompt atomization regime, which produces a droplet size much less than the jet diameter.

The following findings presented throughout this section result from using the microscopic diffused back-illumination technique and the image processing methodology to measure droplet size and droplet velocity, as described
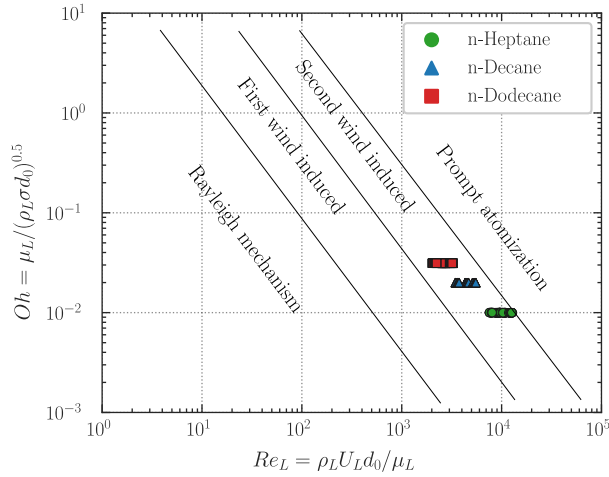
Figure 6.10: Classification of the breakup regimes for the three fuels at fixed conditions.

in section 5.4, and showing the effect of air co-flow conditions (temperature and velocity), fuel mass flow rate, air outlet diameter and fuel type on the droplet characteristics (i.e., diameter and velocity). The SMDs presented in the following figures are the mean of the cells, as was explained previously. However, only the cells between R=0 to R=3.1mm and Z=2.1 to Z=3.5mm were averaged in order to compare a spray region with similar characteristics and thus avoid the spray behavior stated before that the fuels produce different opening angles of the spray. Furthermore, since the droplet velocity measurements were performed close to the injector tip, they are affected by the aerodynamic close to the injector tip. Therefore, a small study of the aerodynamic conditions at exit of the burner and close to the injector tip is first introduced in order to help to understand the following results.

Aerodynamic conditions at the burner exit

As was mentioned previously, the droplet velocity profiles presented following are affected by the flow dynamic close to the burner exit since the measurements of spray characteristics were carried out very close to the injector tip, where the air recirculation are stronger. Therefore, a small aerodynamic study was performed in this region in order to determine the effect of the injector geometry on the air stream. This study comprises a basic computational simulation of the airflow and focuses on evaluating the flow dynamics. The findings exhibit that a recirculation zone close to the injector tip is formed,

which affects the droplet velocity profiles presented in the following section. Figure 6.11 shows that increasing the air mass flow rate or reducing the air outlet diameter, the recirculation zone is intensified, which is due to the acceleration of the surrounding air stream. Additionally, the Figure 6.12 depicts the axial velocity profile at the height of 3.8 mm above the injector tip, exhibiting that as the co-flow velocity is increased (e.g., by an air mass flow rate increased or air outlet diameter reduction), a more intense recirculation zone close to the injector tip is created. However, regardless of the operating condition, the size of the vortex is only slightly affected, as seen in Figure 6.12.
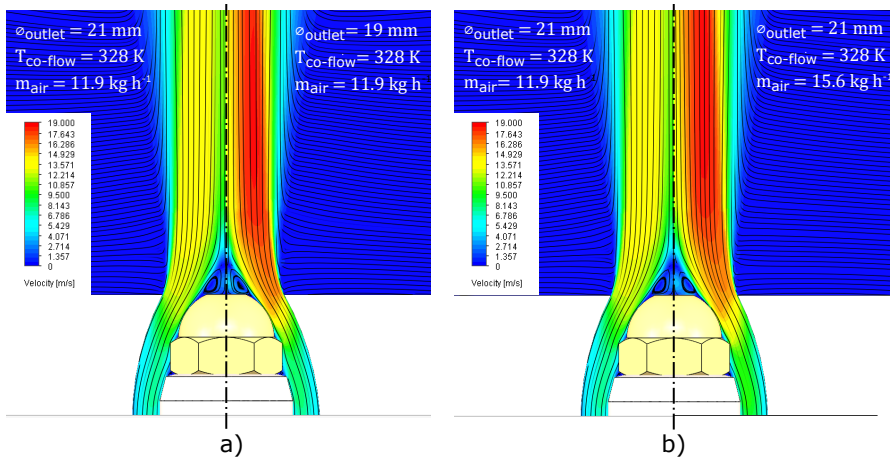
Figure 6.11: Axial velocity map at constant co-flow temperature of 328 K, and different test conditions: two air outlet diameter a) and two air mass flow rate b).

6.3.2   Results

The effects of varying the co-flow conditions, fuel type, and air outlet diameter on both droplet size and droplet velocity are presented following. The results shown through this section are presented in terms of the Sauter mean diameter (SMD) for droplet size and the velocity data through velocity profiles at different heights. Each parameter has been isolated so that its influence on the droplet characteristics may be easily identified.
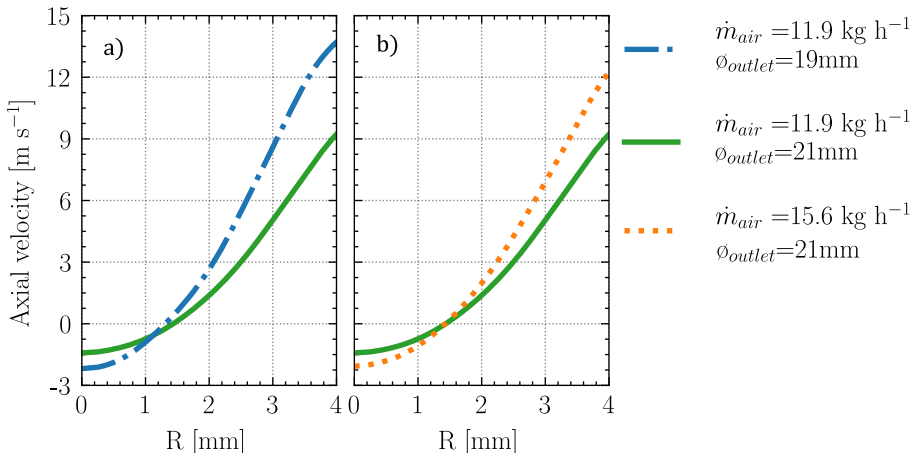
Figure 6.12: Axial velocity profile of air flow at height of 3.8 mm, constant co-flow temperature of 328 K, and different test conditions: two air outlet diameter a), and two air mass flow rate b).

Effect of air mass flow rate and fuel mass flow rate on the droplet diameter

Figure 6.13.a shows the SMD variation with the air mass flow rate for a given fuel (n-Decane) at a co-flow temperature of 328 K and three different fuel mass flow rates. On the other hand, Figure 6.13.a shows the SMD variation with the fuel mass rate for both the same fuel and co-flow temperature and three different air mass flow rates. Figure 6.13.a exhibits that the droplet diameters for a given fuel mass flow rate are slightly affected by the air mass flow rate (i.e., co-flow velocity), it is likely due to the measurements were performed very close to the burner exit, (2 mm above the burner exit), and thus the differences are almost imperceptible. Please note that a related work [9] reported that as a result of the vaporization of smaller droplets by increasing the air mass flow rate, the mean droplet size increases. In general, increasing the fuel mass flow rate, the SMD decreases, as shown in Figure 6.13.b. This is due to the pressure rise across the nozzle orifice, which enhances the atomization process of the liquid fuel and generates smaller droplets, and therefore the global SMD is reduced.

Figure 6.14.a shows the effect of varying the air mass flow rate on droplet velocity for a given fuel mass flow rate and n-Decane fuel. In general, the mean droplet velocities experience a dramatic rise, as the radial position is increased, which is expected due to the spray pattern that promotes the long
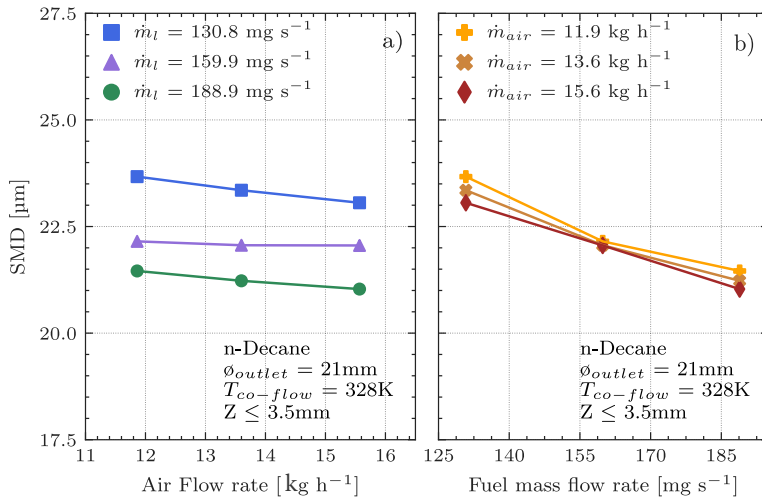
Figure 6.13: Variation of SMD with the air mass flow rate a), and fuel mass flow rate b), both for n-Decane fuel and a fixed air co-flow temperature of 328 K.

droplets at the outer edge of the spray (droplets with high Stokes number). Surprisingly, the mean droplet velocity decreases as the air mass flow rate is increased, especially at the centerline of the spray, and becomes nearly similar after the radial distance of 1.5 mm. This behavior is due to the recirculation zone formed close to the injector tip and which is intensified as the co-flow velocity increases, as was previously explained (see Figure 6.12).

The influence of varying the fuel mass flow rate on the droplet velocity was analyzed at a constant air mass flow rate (e.g., $11.9\,\mathrm{kg\,h^{-1}}$). The mean droplet velocities increase as the fuel mass flow rates are increased, as shown in Figure 6.14.b, which is attributed to the increase in droplet ejection velocity caused by increasing the fuel mass flow rate and so injection pressure. Regarding the mean velocity profiles for the case of the $188.9\,\mathrm{mg\,s^{-1}}$, it exhibits a drastic rise after passing the radial position at 1.6 mm. [9, 10] used pressure swirl nozzle and annular spray burners to perform similar experiments, reporting similar trends of the effect of the fuel mass flow rate on both droplet size and droplet velocity.

Effect of co-flow temperature on the droplet diameter

Figure 6.15.a shows the effect of varying the temperature of the air co-flow on the SMD at fixed air mass flow rate (e.g., $11.9\,\mathrm{kg\,h^{-1}}$). For a constant
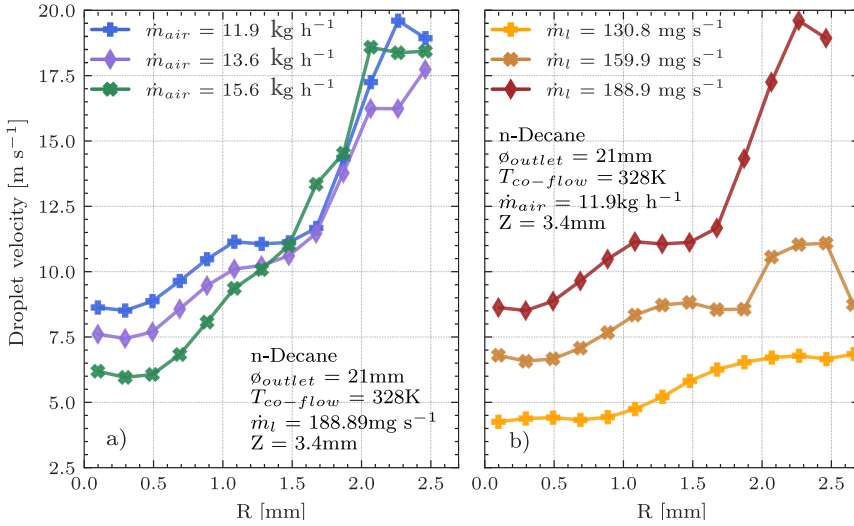
Figure 6.14: Droplet velocity profiles at height of 3.4 mm for different air mass flow rate a) and different fuel mass flow rate b), both for n-Decane fuel and a fixed air co-flow temperature of 328 K.

fuel mass flow rate, increasing the co-flow temperature results in a significant reduction in the SMD caused by the enhancement in the droplet evaporation. In addition, there is an SMD difference between the different fuel mass fuel rates due to the variation in the injection pressure and its effect on the atomization quality. This difference becomes lower at high temperatures since its dominant influence on droplet evaporation. However, it is important to note that the previously observed trend is likely affected by the co-flow velocity: increasing the co-flow temperature reduces the air density, and therefore the co-flow velocity increases (9.8, 11.1 and 12.6 m s^{-1} for the co-flow temperatures 328, 373, and 423 K, respectively).

In order to isolate the effect of the co-flow temperature on SMD, the Figure 6.15.b was introduced, where it can be seen that, for a constant air co-flow velocity, increasing the co-flow temperature significantly reduces the SMD. This trend is due to the droplet vaporization rate is enhanced by increasing the co-flow temperature, resulting in an SMD reduction [11]. Furthermore, it is interesting to notice that at the co-flow temperatures of 328 and 373 K, increasing the co-flow velocity reduces the SMD because increasing the co-flow velocity enhances the fuel jet breakup, resulting in smaller droplets diameters and therefore SMD values (see Figure 6.15.b). However, the previous trend is not observed with the co-flow temperature of 423 K likely because the high
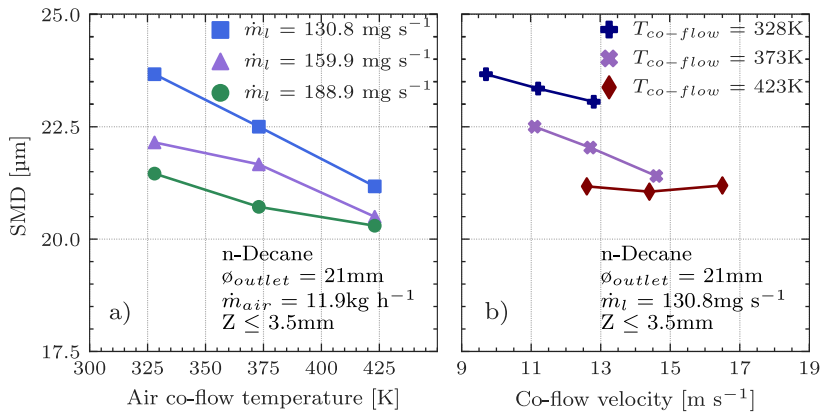
Figure 6.15: Variation of SMD with the air co-flow temperature a) and co-flow velocity b), both for n-Decane fuel.

co-flow temperature enhances the droplet evaporation, mainly the small ones, which keeps the SMD values almost constant regardless of the co-flow velocity. To further understand why SMD decreases as co-flow temperature increases, the droplet size histograms for each fuel are shown in Figure 6.16, to support the facts previously stated.

By increasing the co-flow temperature for each fuel, the evaporation process is enhanced, affecting principally the small droplets and resulting in a general reduction in the number of droplets. Furthermore, it is worth noting that for the n-Decane and n-Dodecane fuels, the effect of increasing the co-flow temperature is observed in droplets with small diameters(i.e., lower than 18 µm). However, for the n-Heptane fuel, although the bigger effect is observed in the smaller droplets, there is also a noticeable effect in big ones (i.e., higher than 18 µm), which is due to the physical properties of the fuel, mainly the volatility. Finally, Figure 6.16 exhibits that n-Heptane fuel produces smaller droplets than the other two fuels, increasing the quantity of the droplets.

To observe the effect of varying co-flow temperature on the droplet velocity, in Figure 6.17 the various velocities profiles at different co-flow temperatures were shown for two different fuel mass flow rates at a constant air mass flow rate. As shown in Figure 6.17, the mean droplet velocities increase as the co-flow temperatures are increased. For a given air mass flow rate, increasing the co-flow temperature leads to a reduction of the air density, which results in a raising of the co-flow velocity since the cross-section of the burner exit was kept constant. Figure 6.17 also shows that increasing the fuel mass flow
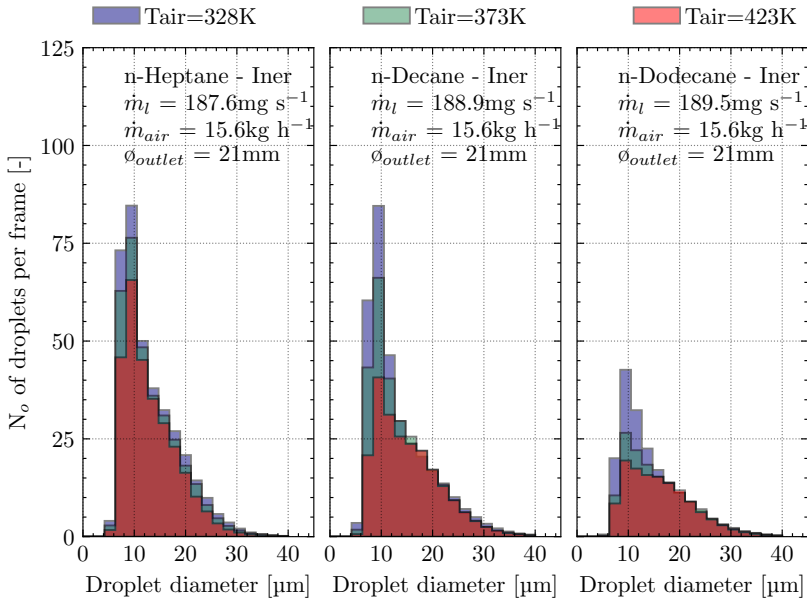
Figure 6.16: Mean droplet distribution variation per frame with the co-flow temperature for the three fuels: n-Heptane a), n-Decane b), and n-Dodecane c) at same operations conditions.

rate, the mean droplet velocity is raised, which is caused by the increase of the injection pressure (i.e., fuel mass flow rate) that enhances the droplet ejection velocity. Please note that velocities profiles shown correspond to at the height of 3.5 mm above the injector tip.

Effect of fuel type on the droplet size and droplet velocity

Figure 6.18 shows the influence of the fuel type on SMD, in which the fuels exhibit different droplet sizes for a constant fuel mass flow rate, with n-Dodecane presenting the largest droplet sizes of the group. This variation is due to the difference in the physical properties, specifically differences in density, viscosity, and surface tension. Since n-Dodecane has the highest viscosity, density and surface tension (see Table 6.1), it generates droplets with relatively big droplet size, compared to n-Decane and n-Heptane. These physical properties influence the global SMD, as was reported in three well-known correlations to predict the global SMD in pressure swirl atomizers [12–14].

The droplet velocity profiles plotted versus the radial positions for the three fuels are shown in Figure 6.19. n-Hepatne exhibits higher mean droplet
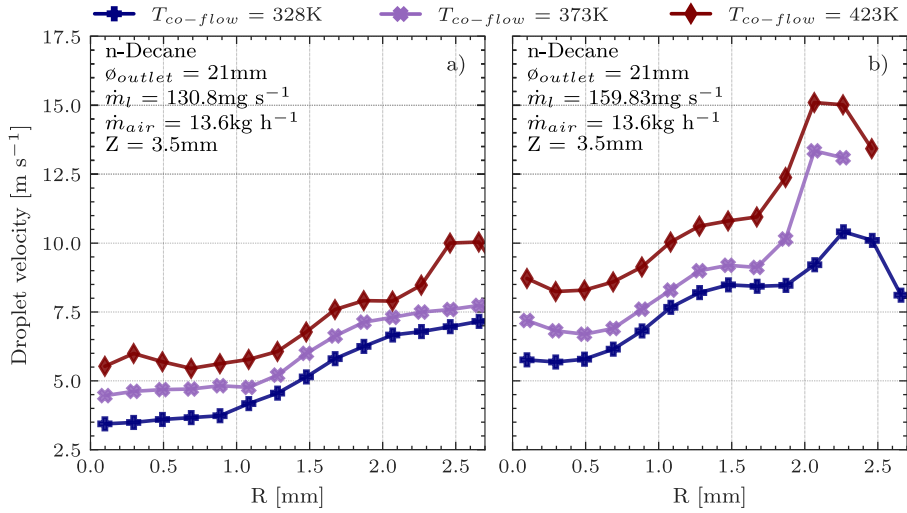
Figure 6.17: Mean radial profile profiles of droplets velocities for two fuel mass flow rates 130.8 a), and 159.83 mg s⁻¹ b), both for n-Decane fuel.
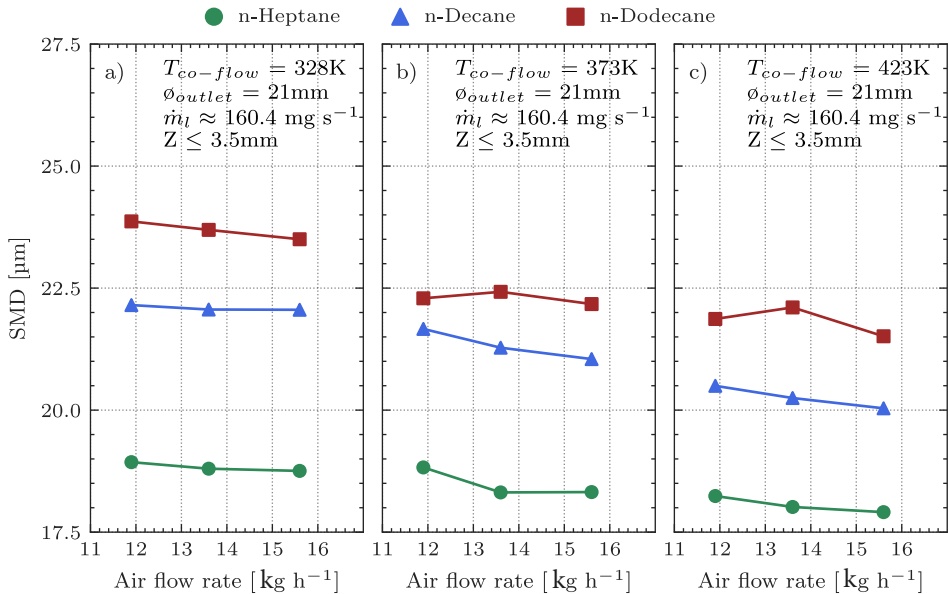
Figure 6.18: Variation of SMD with the fuel type at different co-flow temperatures of 328 K a), 373 K b), and 423 K c).

velocity, followed by n-Decane and then n-Dodecane. This trend is caused by the increase of the droplet ejection velocity, which is assumed to be related to the injector pressure drop, ΔP. Calculating the total velocity through Equation 6.6 and k value of 0.7, the resultant values are: 47.7, 45.3 and $41.6\,\mathrm{m\,s^{-1}}$ for the conditions shown in Figure 6.19.a and 60.2, 53.1 and $50.1\,\mathrm{m\,s^{-1}}$ for the conditions shown in Figure 6.19.b, for n-Heptane, n-Decane and n-Dodecane, respectively. These differences in the droplet ejection velocity among the fuels explain the trends observed in Figure 6.19.
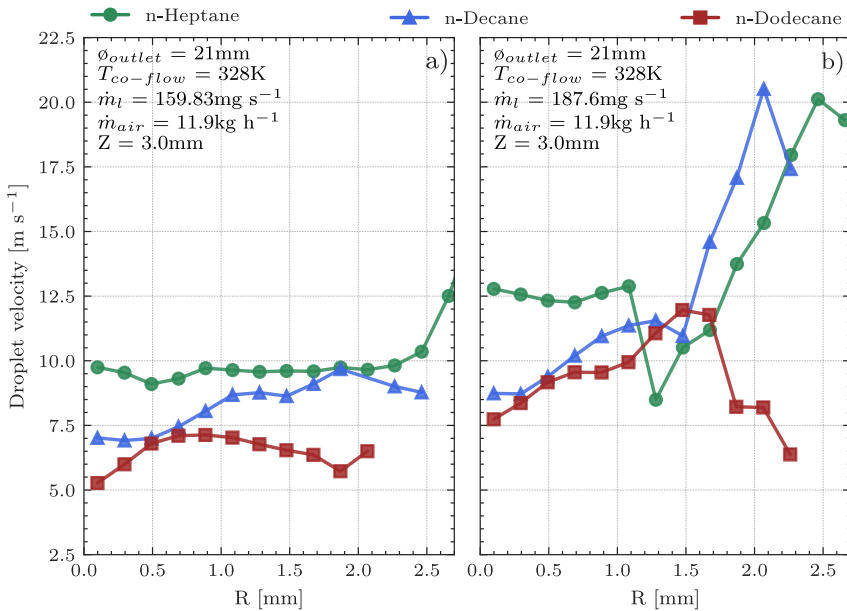
Figure 6.19: Variation of droplet velocity profiles for the three fuels at different fuel mass flow rates: $159.8\,mg\,s^{-1}$ a), and $187.6\,mg\,s^{-1}$ b).

Diameter outlet effect on the droplet diameter

The effect of replacing the air outlet diameter on the droplet size is depicted in Figure 6.20 for the three fuels at constant conditions. The trends observed in the figure can be due to two factors. On the one hand, the effect of the co-flow velocity, which increases when the air outlet diameter is reduced since the cross-section at the burner exit is smaller, accelerating the airflow and therefore enhancing the droplet evaporation, particularly the small droplets. This tendency is more notorious for n-heptane and n-Decane fuels because they produce smaller droplets than the n-Dodecane fuel, which exhibits larger

droplets in size and also is the less volatile fuel (see Table 6.1). On the other hand, due to the shape of the burner exit and also to the increase in the co-flow velocity, by the reduction in the cross-section at the burner exit, the airflow drags more droplets of higher size to the spray core, displacing the SMD profiles to the left side, it for of the lowest air outlet diameter, i.e., for the air outlet diameter of 19 mm regards to the air outlet diameter of 21 mm. This trend is more clear for the n-heptane fuel since it presents the lowest size droplets, as seen in Figure 6.21, which is a schematic representation of the droplets for n-Heptane and n-Dodecane fuels and the two air outlet diameters at same operation conditions.
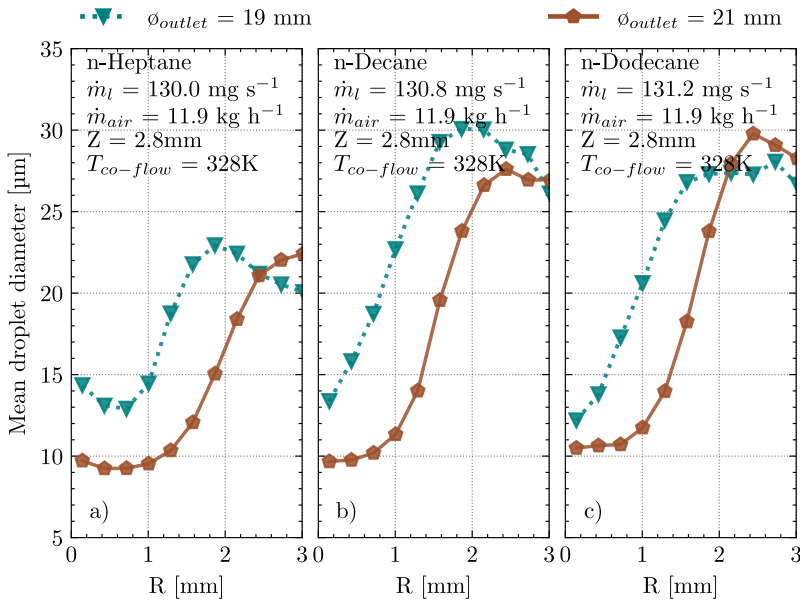
Figure 6.20: Mean radial droplet diameter profiles at constant co-flow temperature of 328 K at height of 2.8 mm for the three fuels: n-Heptane a), n-Decane b), and n-Dodecane c).

When the air outlet diameter changes from 21 mm to 19 mm, the external spray borders shift to the left side, and several droplets from the exterior edge drag close to the spray axis, increasing droplet concentration in the spray core (see Figure 6.21). These tendencies result from the cross-section reduction at the burner exit, which accelerates the airflow, as was previously explained. Furthermore, in Figure 6.21 is observed again that the n-Heptane fuel produces more droplets with a lower diameter regards the n-Dodecane fuel.
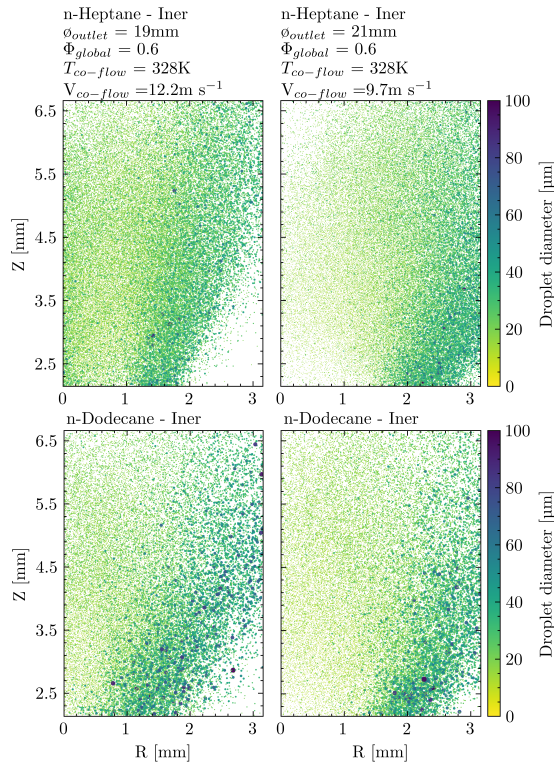
Figure 6.21: Droplet representation at constant co-flow temperature for n-Heptane and n-Dodecane fuels and both air outlet diameters.

Figure 6.22 shows the effect of varying the air outlet diameter of the burner on the mean droplet velocity at constant conditions of air mass flow rate and fuel mass flow rate. The mean droplet velocity increases as air outlet diameter decreased (smaller cross-section at the burner exit) since the air mass flow rate was kept constant. However, close to the spray axis, an opposite behavior is observed, which is caused by a recirculation zone formed close to the injector tip. This region is formed by the interaction between the air stream and the injector geometry and intensified by increasing the co-flow velocity, as was explained previously.

6.3.3   Comparison between measured and calculated SMD

For comparison between the measured and calculated SMD results, a global Sauter Mean Diameter (SMD_{global}) is defined as a single parameter to describe the global spray droplet size. Note that related works refer to this
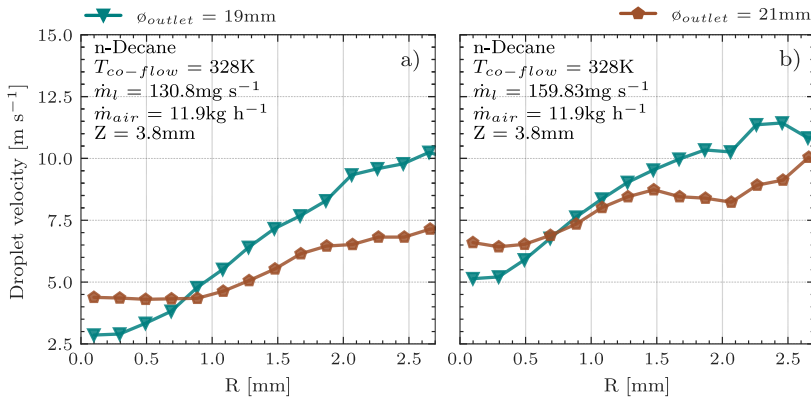
Figure 6.22: Droplet velocity profiles at constant co-flow temperature of 328 K at height of 3.8 mm and two different fuel mass flow rates: 130.8 mg s⁻¹ a) and 159.8 mg s⁻¹ b).

parameter such as integral, or overall SMD [15–17]. SMD_{global} was calculated through Equation 3.13. The measured SMD_{global} using microscopic diffused back-illumination technique, described in section 5.4, comparing the SMD calculated by three well-known correlations for pressure swirl atomizer: Radcliffe [12], Jasuja [13], and Lefebvre and McDonell [14].

$$SMD_{Radcliffe} = 7.3\sigma_l^{0.6}\nu_l^{0.2}\dot{m}_l^{0.25}\Delta P^{-0.4} \tag{6.3}$$

$$SMD_{Jasuja} = 4.4\sigma_l^{0.6}\nu_l^{0.16}\dot{m}_l^{0.22}\Delta P^{-0.43} \tag{6.4}$$

$$SMD_{Lefebvre} = 2.25\sigma_l^{0.25}\mu_l^{0.25}\dot{m}_l^{0.25}\Delta P^{-0.5}\rho_{air}^{-0.25} \tag{6.5}$$

where σ_l is the liquid surface tension, μ_l and ν_l are the dynamic and kinematic liquid viscosities, respectively; $\dot{m}_l$ is the liquid mass flow rate, ΔP is the pressure drop across the spray nozzle and ρ_{air} is the surrounding air density. All properties used in the SMD calculations are listed in Table 6.1. Since the fuel injection is in the ambient, the pressure drop is measured through a pressure sensor installed upstream from the nozzle.

The measured SMD_{global} for three fuel mass flow rates are compared to the predicted SMD in Figure 6.23. These correlations have been widely used in both experimental [10, 18] and computational [19] studies, and the predicted SMD followed the same trends between the different fuels observed in the

measurements. The fuels show different droplet sizes at an almost constant fuel mass flow rate: n-Dodecane exhibits the largest droplet sizes, followed by n-Decane and then n-Heptane. This variation is due to the differences in physical properties, particularly ones which are included in Equations 6.3-6.5 (density, surface tension, and viscosity). Amongst the fuels, viscosity is the property that varies more importantly. Since n-Dodecane has the highest viscosity (see Table 6.4), it exhibits the largest droplet size. Figure 6.23 also shows the effect of modifying the fuel mass flow rate on SMD, evidencing that increasing $\dot{m}_l$ reduces the SMD. This fact can be directly related to the associated increasing injection pressure, which enhances the atomization quality. Despite the fact that the global value of the measurements is more than the predicted diameters, the predicted SMD closely follows the measurement trend. The differences between the measured and predicted SMDs are lower for n-Dodecane fuel at every fuel mass flow rate, indicating that correlations are more accurate for heavier fuels. Consistently, the SMD predicted by Radcliffe's correlation is closest to the measured values, follow by Jasuja's correlation and then Lefebvre's correlation.

6.4   Summary and conclusions

This chapter collects all the results describing the spray characterization such as droplet size and velocity for multiple operating conditions. The measurements were carried out in an annular spray burner, with the Microscopic diffused back-illumination technique to visualize both droplet size and droplet velocity for n-Heptane, n-Decane and n-Dodecane hydrocarbon fuels. The field of view allowed for an optical limit of 3.25×4.75 mm width and height, respectively. The field of view achieved is relatively big, allowing the measurement of the initial droplet sizes and their velocities, i.e., close to the injector tip and after the primary breakup. In general, the trends follow the expected behavior by the variation of the co-flow conditions, fuel mass flow rate and fuel type. Based on the results and observations, the following conclusions can be drawn:

- The spray pattern promotes big droplets at the edge of the spray and small droplets close to centerline, larger droplets with higher Stokes number are less affected by the aerodynamic conditions and follow ballistic trajectories.

- Isolating the effect of the air mass flow rate, it has been observed that varying the air mass flow rate, the global SMD is only slightly affected.
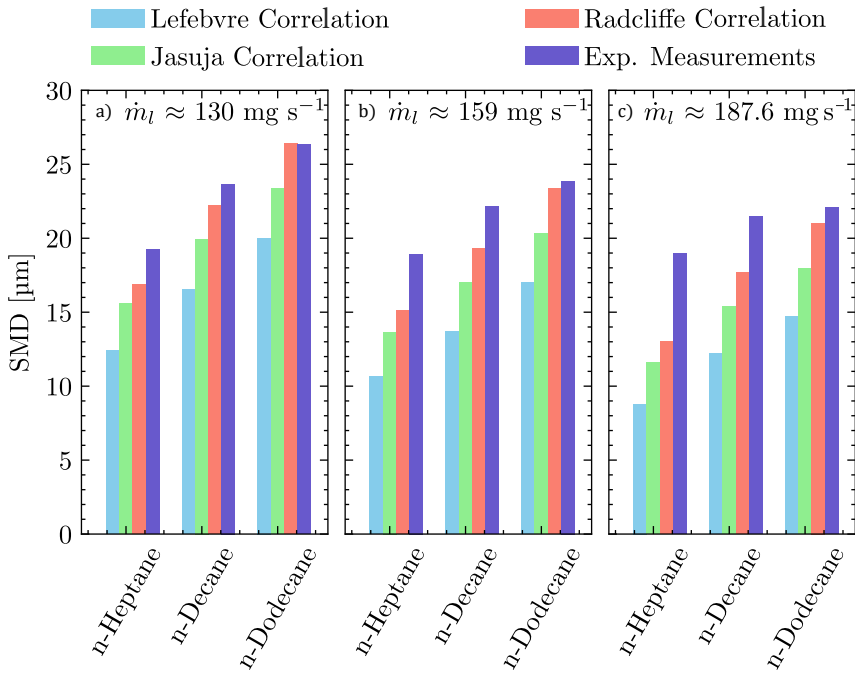
Figure 6.23: Comparison between the measured an predicted SMD for a constant air mass flow rate of $11.9\,kg\,h^{-1}$ and different fuel mas flow rates: $130\,mg\,s^{-1}$ a), $159\,mg\,s^{-1}$ b), and $1187.6\,mg\,s^{-1}$ c). The accurate fuel mass flow rates for each fuel are listed in Table 6.3.

This behavior is likely due to the fact that those measurements were carried out very close to the injector tip, where the influence of the air co-flow on global SMD is minimal. Furthermore, as the air mass flow rate increases, the droplet velocity is increased. This is attributed to an increase in the co-flow velocity that accelerates the droplets since the cross-section at the burner exit was kept constant. However, a recirculation zone was formed close to the injector tip that influences the droplet velocity profile and is intensified by increasing the air mass flow rate.

• The influence of the fuel type on the global SMD is clear, and it is related to the physical fuel properties, especially differences in density, viscosity and surface tension. n-Dodecane exhibits the largest droplets, followed by n-Decane and then n-Heptane. Moreover, n-Dodecane droplets evidence lower velocity since the droplet ejection velocity is lower than

the other two fuels since the fuel mass flow rate is lower and thus the injection pressure.

- For constant operating conditions, it has been observed that as the air outlet diameter reduces, the global SMD is reduced. This trend is attributed to the increase in the co-flow velocity that enhances the evaporation rates of the fuel droplets, especially the smaller ones, resulting in a larger global SMD. As a result of reducing the air outlet diameter, the air co-flow velocity is increased. Therefore, the droplets are also accelerated, exhibiting higher droplet velocities.

- The correlations do well at predicting the relative change of the SMD with varying the fuel mass flow rate. However, since the correlations do not take to account the influence from the co-flow conditions, the current formulas do not predict the variations in the global SMD when the air mass flow rate or co-flow temperature are raised.

6.A   Appendix: velocity of the liquid film

In the current work, the velocity of the liquid film (U_l) is given by the following equation:

$$U_l = kv\sqrt{\frac{2\Delta P}{\rho_l}} \tag{6.6}$$

where ΔP is the pressure differential and kv is a multiplying factor. The actual definition of "kv," a scale value for estimating the liquid film velocity, was given by Lefebvre [20], who noted that kv is a function of the injector design and injection pressure. However, later Senecal et al. [21] and Schmidt et al. [22] found that Lefebvre's correlation led to unphysical values, such as velocity coefficient being greater than 1. Equation 6.7 is then an expression for the coefficient of discharge for the swirl ports, assuming that most of the pressure drop through the injector occurs at the ports. The discharge coefficient for a single-phase nozzle with sharp inlet corners and a L/D of 4 is typically 0.78 or less by reported by Senecal et al. [21] and under cavitation it can be as low as 0.61. Therefore, 0.78 should be a practical upper bound for k. Considering 10% loss in discharge coefficient due to other momentum losses across the injector, Senecal et al. [21] calculated a value of 0.7 as the upper limit, the same valued used in this study. Furthermore, there are some physical limits on k such as that it must be less than unity by conservation of

energy, and it must be large enough to permit sufficient mass flow. To satisfy that the size of the air core non-negative, the following expression is used:

$$kv = max \left[0.7, \frac{4\dot{m}_l}{\pi d_0^2 \rho_l cos\theta} \sqrt{\frac{\rho_l}{2\Delta P}} \right] \qquad (6.7)$$

where $\dot{m}_l$ is the liquid mass flow rate and θ is the spray half-angle. In our experiments, we found this value to be always 0.7.

References

[1] Linstrom, P. J. and Mallard, W. G. "The NIST Chemistry WebBook: A chemical data resource on the Internet". In: *Journal of Chemical and Engineering Data* 46.5 (2001), pp. 1059–1063. DOI: 10.1021/je000236i.

[2] Verdier, A. "Experimental study of dilute spray combustion". PhD thesis. Normandie Université, 2018, pp. 1–175.

[3] Cléon, G., Honoré, D., Lacour, C., and Cessou, A. "Experimental investigation of structure and stabilization of spray oxyfuel flames diluted by carbon dioxide". In: *Proceedings of the Combustion Institute* 35.3 (2015), pp. 3565–3572. DOI: 10.1016/j.proci.2014.06.028.

[4] Correia Rodrigues, H., Tummers, M. J., Veen, E. H. van, and Roekaerts, D. J. "Spray flame structure in conventional and hot-diluted combustion regime". In: *Combustion and Flame* 162.3 (2015), pp. 759–773. DOI: 10.1016/j.combustflame.2014.07.033.

[5] Mansour, M. S., Alkhesho, I., and Chung, S. H. "Stabilization and structure of n-heptane flame on CWJ-spray burner with kHZ SPIV and OH-PLIF". In: *Experimental Thermal and Fluid Science* 73 (2016), pp. 18–26. DOI: 10.1016/j.expthermflusci.2015.08.019.

[6] Shum-Kivan, F. et al. "Experimental and numerical analysis of a turbulent spray flame structure". In: *Proceedings of the Combustion Institute* 36.2 (2017), pp. 2567–2575. DOI: 10.1016/j.proci.2016.06.039.

[7] Naik, C. V. et al. "Detailed chemical kinetic mechanism for surrogates of alternative jet fuels". In: *Combustion and Flame* 158.3 (2011), pp. 434–445. DOI: 10.1016/j.combustflame.2010.09.016.

[8] Kumar, K., Freeh, J. E., Sung, C. J., and Huang, Y. "Laminar flame speeds of preheated iso-octane/O2/N2 and n-heptane/O2/N2 mixtures". In: *Journal of Propulsion and Power* 23.2 (2007), pp. 428–436. DOI: 10.2514/1.24391.

[9]   Alsulami, R. A., Nates, S., Wang, W., Won, S. H., and Windom, B. "Effects of varying liquid fuel and air co-flow rates on spray characterisation of an annular co-flow spray burner". In: *Proceedings of the ASME Turbo Expo*. Vol. 4B-2019. American Society of Mechanical Engineers (ASME), 2019. DOI: `10.1115/GT2019-90989`.

[10] Alsulami, R. et al. "Investigating the role of atomization on flame stability of liquid fuels in an annular spray burner". In: *Fuel* 265 (2020). DOI: `10.1016/j.fuel.2019.116945`.

[11] Reddy, V. M., Trivedi, D., and Kumar, S. "Experimental investigations on lifted spray flames for a range of coflow conditions". In: *Combustion Science and Technology* 184.1 (2012), pp. 44–63. DOI: `10.1080/00102202.2011.615770`.

[12] Radcliffe, A. "Section D. Fuel Injection". In: *Design and Performance of Gas Turbine Power Plants*. Princeton University Press, 2015, pp. 92–118. DOI: `10.1515/9781400875603-008`.

[13] Jasuja, A. K. "Atomization of crude and residual fuel oils". In: *Journal of Engineering for Gas Turbines and Power* 101.2 (1979), pp. 250–258. DOI: `10.1115/1.3446480`.

[14] Lefebvre, A. and McDonell, V. *Atomization and Sprays*. 2017, p. 300. DOI: `10.1016/0009-2509(90)87140-N`.

[15] Im, J. H., Kim, D., Han, P., Yoon, Y., and Bazarov, V. "Self-pulsation characteristics of a gas-liquid swirl coaxial injector". In: *Atomization and Sprays* 19.1 (2009), pp. 57–74. DOI: `10.1615/atomizspr.v19.i1.40`.

[16] Tratnig, A. and Brenn, G. "Drop size spectra in sprays from pressure-swirl atomizers". In: *International Journal of Multiphase Flow* 36.5 (2010), pp. 349–363. DOI: `10.1016/j.ijmultiphaseflow.2010.01.008`.

[17] Jedelsky, J. and Jicha, M. "Energy considerations in spraying process of a spill-return pressure-swirl atomizer". In: *Applied Energy* 132 (2014), pp. 485–495. DOI: `10.1016/j.apenergy.2014.07.042`.

[18] Wei, X. and Yong, H. "Improved Semiempirical Correlation to Predict Sauter Mean Diameter for Pressure-Swirl Atomizers". In: *Journal of Propulsion and Power* 30.6 (2014), pp. 1628–1635. DOI: `10.2514/1.B35238`.

[19] Dikshit, P. S. B., Kulshreshtha, D. D. B., and Channiwala, D. S. A. "Numerical Analysis and Empirical Correlations to Predict SMD of Pressure Swirl Atomizer for Small Scale Gas Turbine Combustion Chamber". In: *International Journal of Applied Engineering Research* 13 (2018), pp. 4531–4537.

[20] Lefebvre, A. H. "Airblast atomization". In: *Progress in Energy and Combustion Science* 6.3 (1980), pp. 233–261. DOI: 10.1016/0360-1285(80)90017-9.

[21] Senecal, P. K. et al. "Modeling high-speed viscous liquid sheet atomization". In: *International Journal of Multiphase Flow* 25.6-7 (1999), pp. 1073–1097. DOI: 10.1016/S0301-9322(99)00057-9.

[22] Schmidt, D. P. et al. "Pressure-swirl atomization in the near field". In: *SAE Technical Papers*. SAE International, 1999. DOI: 10.4271/1999-01-0496.

Chapter 7

Spray combustion

7.1 Introduction

The fuel atomization process was discussed in the previous chapter, showing the effects of the variation of several parameters on the droplet size and droplet velocity. In this chapter, the results of also varying these parameters on the combustion process are presented. Therefore, the operating conditions and fuels are the same ones used in the atomization study, which are summarized in Table 6.3 and Table 6.4, respectively. The test matrix comprises the variation of the fuel mass flow rate, air co-flow temperature, air mass flow rate, and air outlet diameter. First, the lift-off height measurements were introduced, which were determined by recording OH* chemiluminescence by using a suitable optical setup. Then, the soot measurements resulted from applying the diffused back-illumination technique are presented. The quantification of light extinction by the soot cloud is given in terms of K or KV (i.e., after computing Abel inversion transform on the KL extinction images). Finally, the chapter ends with a summary and conclusions.

7.2 Lift-off height

This section presents the results of varying different parameters on the flame lift-off height, which have been determined by recording the OH* chemiluminescence with a suitable optical setup, as was described in section 5.4. Figure 7.1 shows examples of the raw images captured through this technique for

the three fuels, recording 30 frames for each operating point. These frames are then averaged to measure the flame lift-off height, which is the point where the local flame propagation speed and the air-fuel mixture velocity are the same. This point can be affected by the interconnection of several processes, such as atomization, vaporization, and chemical kinetics, which are in turn influenced by the operating conditions tested and fuel type. Therefore, the effects of varying these parameters on the flame lift-off height will be addressed throughout the current study.
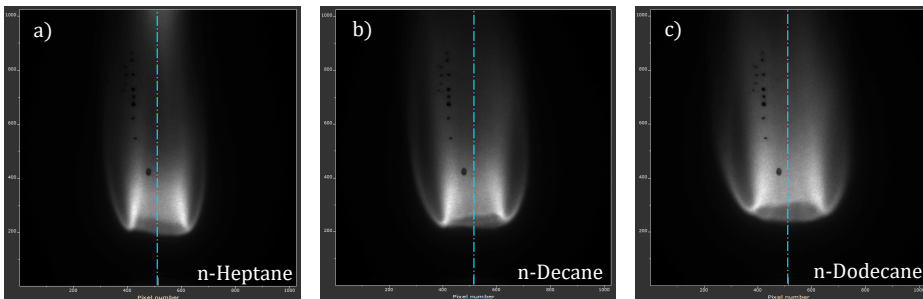
Figure 7.1: Raw images of the OH* chemiluminescence for the three fuels: n-Heptane a), n-Decane b), and n-Dodecane c). The frames shown are sprays with an air surrounding temperature of 328 K, an air mass flow rate of 11.9 kg h^{-1} and a fuel mass flow rate of 131 mg s^{-1}.

7.2.1 Results

By recording the OH* chemiluminescence and using the processing methodology, the flame lift-off height is measured for a wide range of operating conditions and different fuels. Figure 7.2 shows a representation of how the flame lift-off was determined. The flame lift-off height was measured in each Abel inverted image and then all results were averaged, as explained previously in section 5.4. Finally, the following results are presented in such a way that the effect of each variable on the flame lift-off height can be easily observed. Note that the flame lift-off heights in the following results have a maximum relative standard deviation from the mean value equal to 2%.

Effect of fuel mass flow rate and air mass flow rate on the flame lift-off height

Figure 7.3 shows the effect of varying the air mass flow rate (Figure 7.3.a) and fuel mass flow rate (Figure 7.3.b). Meanwhile, co-flow temperature and
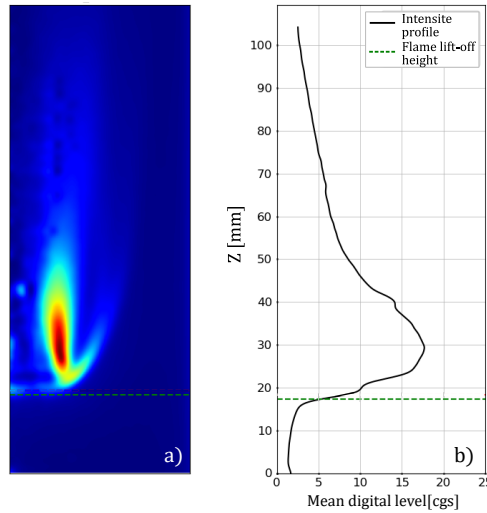
Figure 7.2: Image processing methodology; Abel inverted image a) and intensity profile on the resultant from the abel inverted image b). The frame shown is a n-Decane spray flame with an air surrounding temperature of 328 K, an air mass flow rate of 11.9 kg h^{-1} and a fuel mass flow rate of 131 mg s^{-1}.

air outlet diameter, were kept constant. Please note that Figure 7.3 only show results for the n-Decane fuel, allowing to readily visualize the trends. The other two fuels follow the same trends presented here. Some observations from Figure 7.3 can be made:

- In Figure 7.3.a, it is seen that the flame lift-off height has a direct relationship with the air mass flow rate, which is in turn related to the co-flow velocity calculated at the exit burner through Equation 6.2 (for this case 9.8, 11.1 and 12.6 m s^{-1} for the air mass flow rates, i.e., 11.9, 13.6 and 15.6 kg h^{-1}, respectively). Various works [1–3] reported the same trend. Please note that the droplets move in a co-flow field with a resultant velocity (V_r), which is the resultant of droplet ejection velocity ($V_{droplet}$) and the air co-flow velocity ($V_{co-flow}$). Assuming both constant fuel mass flow rate (i.e., same injection pressure) and air co-flow temperature for a specific fuel, as the air co-flow velocity increases the resultant velocity of the mixture drives the droplets straight to a downstream position. As a result, the flame stabilization point changes (i.e., higher flame lift-off height). Additionally, Kumar et al. [3] introduced the effect of the air co-flow velocity on the computational estimation
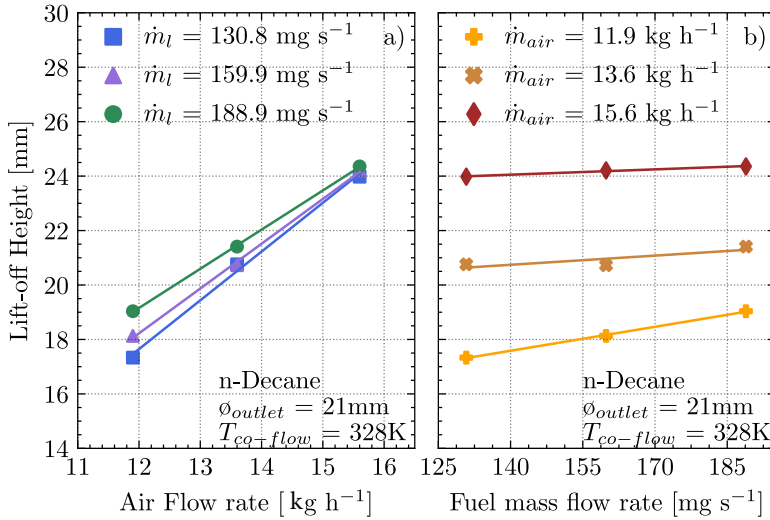
Figure 7.3: Variation of the flame lift-off height with the air mass flow rate a) and fuel mass flow rate b), both for n-Decane fuel and a fixed air co-flow temperature.

of the flame lift-off height, finding that increasing this velocity leads to an increase in the chemical time scale, thus reducing the global reaction rate of the mixture. This leads to a reduction of the laminar flame speed (S_L) and hence an increase in the flame lift-off height.

- Figure 7.3.b shows the effect of increasing the fuel mass flow rate on the flame lift-off height. In this study, the variation in the fuel mass flow rate is generated by varying the injection pressure of the system. Please recall Figure 6.13 that increasing the fuel mass flow rate for a given fuel leads to a reduction in the SMD [4, 5]. Thus, the droplet evaporation time is reduced, which should result in a decrease in flame lift-off height (this trend was reported by Reddy et al. [1], who used a similar injector type but with a bigger injector orifice diameter, lower injection pressures, and also lower velocities of co-flow). However, the trends shown here do not follow this criterion. This is most probably due to the fact that increasing the fuel mass flow rate at a constant air mass flow rate increases the velocity of droplet ejection ($V_{droplet}$), thus increasing V_r [5] moves the flame stabilization point to a downstream position (i.e., higher flame lift-off height). Furthermore, it can be noted that as the air mass flow rate increases, the resultant velocity V_r is

mainly controlled by the co-flow velocity rather than the droplet ejection velocity, e.g., for an air mass flow rate of $11.9\,\mathrm{kg\,h^{-1}}$, increasing the fuel mass flow rate results in a significant variation in flame lift-off height, which is due to the droplet ejection velocity still ha a significant effect on V_r, however, this effect for the case of the air mass flow rate of $15.6\,\mathrm{kg\,h^{-1}}$ is almost negligible since the V_r is mainly controlled by the air-co-flow velocity.

Effect of the co-flow temperature on the flame lift-off height

Figure 7.4.a shows the effect of varying the air co-flow temperature on the flame lift-off height at fixed air mass flow rate (e.g., $11.9\,\mathrm{kg\,h^{-1}}$) and different fuel mass flow rates. By increasing the fuel mass flow rate at constant co-flow temperature, the flame lift-off increases due to the increases in the fuel injection pressure, as was observed in the previous statement. However, in Figure 7.4.a co-flow temperature for any of the fuel mass flow rates does not exhibit a significant influence on the flame lift-off height, which is unusual. This effect can be explained by the co-flow temperature modifies the co-flow velocity, i.e., increasing the co-flow temperature reduces the air density, thus increasing the co-flow velocity (9.8, 11.1 and $12.6\,\mathrm{m\,s^{-1}}$ for the co-flow temperatures 328, 373, and 423 K, respectively), masking the real effect of the co-flow temperature on the flame lift-off height. Therefore, to isolate the effect of the co-flow temperature on flame lift-off height, the Figure 7.4.b is introduced, where it can be seen that, for a constant air co-flow velocity, increasing the co-flow temperature significantly reduces the flame lift-off height. This fact evidences again that the stabilization position of the flame strongly depends on the fuel vapor/air mixture formation and its resultant velocity (V_r). The droplet vaporization rate is enhanced by the increasing the co-flow temperature, which purely depends on droplet number density and entrainment rate of hot co-flow [1]. On the other, increasing the co-flow temperature increases the laminar flame speed (S_L), which in turn affects the rate of flame propagation through the spray as will be explained in section 7.3. To calculate this flame propagation through the quiescent multi-droplet mist, Myers and Lefebvre [6] derived a correlation to predict it, S_{spray}, taking into account the evaporation rates and chemical reaction rates (related to S_L). As the laminar flame speed increases, S_{spray} also increases, causing stabilization of the flame closer to the injector tip (i.e., lower flame lift-off height) [2].
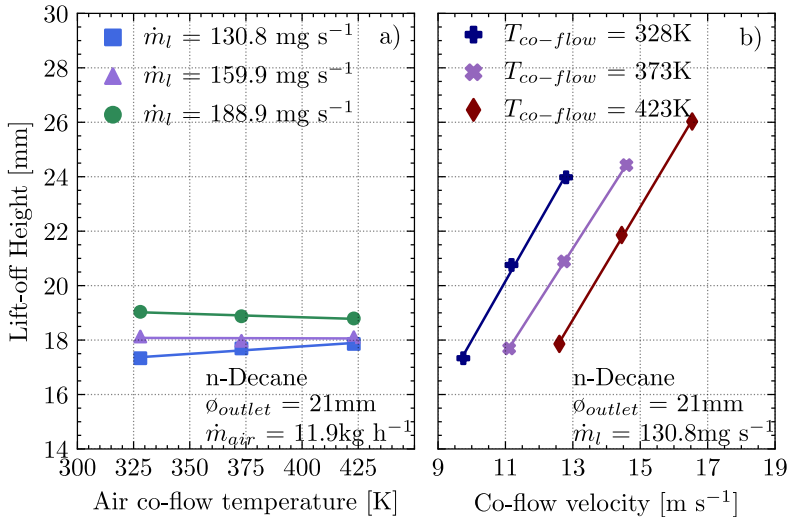
Figure 7.4: Variation of the flame lift-off height with the air co-flow temper-ature a) and co-flow velocity b), both for n-Decane fuel.

Effect of fuel type on the flame lift-off height

Since previous subsections have not yet shown the effect of the fuel type on the flame lift-off height, this subsection has been introduced. In Figure 7.5, flame lift-off height is plotted against air mass flow rate for the three co-flow temperatures tested. From the results, it is possible to observe some trends previously discussed, such as the air mass flow rate influence, but the purpose here is to remark the effect of fuel type on the flame lift-off height.

In general, larger droplet sizes and less volatile fuels exhibit higher lift-off heights as depicted in Figure 7.5. For instance, this is seen for a fixed nozzle size in the n-Dodecane fuel (the volatility of the fuel is represented by the fuel vapor pressure in Table 6.4 and it was described in subsection 6.3.3, the droplet size depending on fuel properties such as density, viscosity and surface tension). This is due to n-Dodecane needing more time/length to evaporate and generate enough vapor to stabilize the flame against the incoming reactant stream. n-Heptane exhibits a lower lift-off height, which can be attributed to its higher volatility and its smaller droplet size, which enhances the fuel/air mixing, resulting in a higher fraction of localized pre-mixed fuel-lean regions [7, 8]. The same behavior was noticed in a related work [2]. Since the n-Decane presents intermediate values of both volatility and droplet size, it is expected for n-Decane to present intermediate lift-off heights, as shown in Figure 7.5.
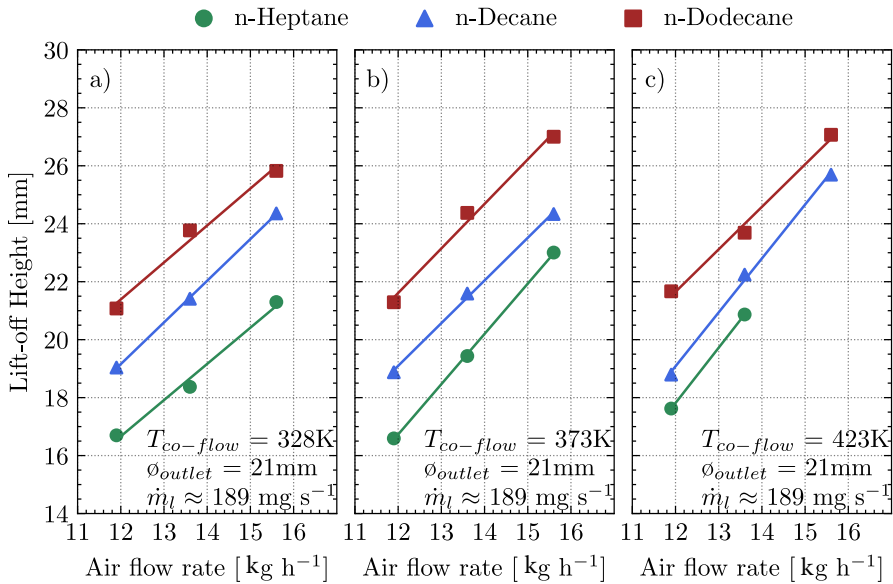
Figure 7.5: *Flame lift-off heights against the air mass flow rate for the different fuels, at co-flow temperatures of 328 K a), 373 K b), and 423 K c) at constant fuel mass flow rate (accurate values for each fuel are listed in Table 6.3). Symbols correspond to the fuel type and fit lines were plotted for each fuel.*

Air outlet diameter effect on the flame lift-off height

The effect of replacing the air outlet diameter on flame lift-off height is shown in Figure 7.6 for the three fuels and the three air mass flow rates tested under fixed conditions of fuel mass flow ratre and air co-flow temperature. Figure 7.6 also shows fit lines for each outlet diameter. In order to examine the effect that the air outlet diameter over the lift-off height, the co-flow velocity must remain constant. For every fuel shown in Figure 7.6 and a fixed co-flow velocity, the flame lift-off height increases as the outlet cross-section is increased (i.e., air outlet diameter). The difference between these points is the global equivalence ratio, which in the case of the air outlet diameter of 21 mm is considerably leaner than for the 19 mm one. This reduction is attributed to the increase in the air mass flow rate needed to achieve the same co-flow velocity. Myers and Lefebvre [6] reported that flame speed (S_{spray}) increases with the overall equivalence ratio up to the stoichiometric value for a wide range of fuels and test conditions. Consequently, as the flame speed increases, the flame lift-off height decreases [2]. Myers and Lefebvre [6] also observed that for heavier fuels, the flame speed is more sensitive to the fuel/air ratio.
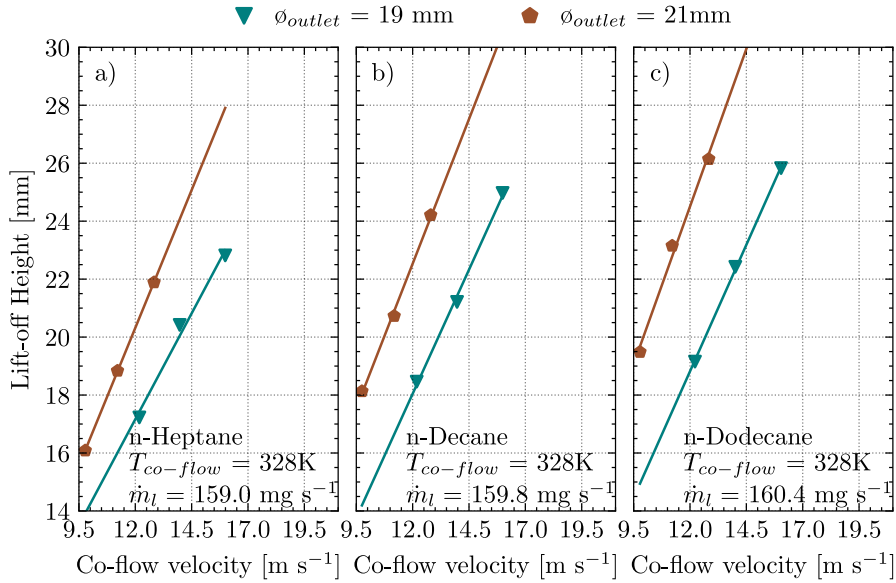
Figure 7.6: Flame lift-off heights against the co-flow velocity for the different fuels, n-Heptane a), n-Decane b), and n-Dodecane c) at constant fuel mass flow rate and co-flow temperature.

7.2.2   Experimental correlation

The wide range of operating conditions tested allows performing a statistical analysis in order to establish an empirical correlation from the variables set throughout the experimental campaign. Empirical correlations have been used by many researchers as an attempt to explain the effect of varying the surrounding conditions, injection pressure, and fuel type on the flame lift-off height [1, 9–11]. From the results presented earlier, it can be assumed that the flame lift-off height is probably controlled by the air co-flow velocity, fuel type (droplet size and volatility), co-flow temperature and also the global equivalence ratio. Reddy et al. [1] studied the effect of these parameters on the lift-off height, reporting that the lift-off height is a strong function of co-flow velocity and Sauter mean diameter. The first statistical analysis was performed individually for each fuel and each air outlet diameter. With the rest of the parameters, the outcomes showed that only air co-flow velocity and co-flow temperature are significant in the flame lift-off height estimation as presented in Equation 7.1:

$$LOH \propto T_{co-flow}^{a} \cdot V_{co-flow}^{b} \tag{7.1}$$

where *LOH* [mm] corresponds to the flame lift-off height, $T_{co-flow}$ [K] to air co-flow temperature, and $V_{co-flow}$ [m s^{-1}] corresponds to mean air co-flow velocity at the burner exit. Equation 7.1 seems to be reasonable due to the fact that the droplet evaporation time is a function of the air temperature, droplet diameter and air entrainment, which in turn depends on co-flow velocity. Therefore, the variation of the coefficients between fuels (Table 7.1), is likely related to fuel volatility and reactivity on the one hand, and to droplet size (which is a direct function of all liquid properties, i.e., surface tension, density, and viscosity), mass flow rate and the injection pressure on the other hand. Table 7.1 summarizes the results from Equation 7.1 for each fuel and both air outlet diameters. From the results, it is observed that the flame lift-off height varies linearly with the air velocity, whereas the air temperature has an inverse effect as expected by the findings mentioned earlier. In any case, the values of R^2 confirm the good repeatability and reliability of the results gathered. Nevertheless, there is relatively less reliability for the air outlet diameter of 19 mm, as seen in Figure 7.7. This is because a significant number of operating conditions are close to the conditions that promote the blow-off phenomenon, leading to flame instabilities. This blow-off phenomenon occurs when the fuel vapor-air mixture is too lean to burn and the co-flow velocity is too high to stabilize the flame. It was principally observed for n-Heptane fuel at both high co-flow velocities and high co-flow temperatures. Hence, many points for the n-Heptane fuel under these conditions could not be measured.

Table 7.1: Results of empirical correlation for flame lift-off height.

Fuel	Air outlet diameter	a	b	R^2
n-Heptane	19 mm	-0.874	1.205	0.94
	21 mm	-0.67	1.0977	0.97
n-Decane	19 mm	-0.82	1.09	0.95
	21 mm	-0.963	1.14	0.98
n-Dodecane	19 mm	-0.655	0.953	0.8
	21 mm	-0.9307	1.06	0.96

As the second attempt to explain differences in flame lift-off height regardless of the fuel type, the Sauter Mean Diameter (SMD) was used to correlate them, as reported in Reddy et al. [1]. Since SMD is a direct consequence of all liquid characteristics (i.e., density, surface tension, and viscosity), injection pressure, the effect of the fuel type and its mass flow rate is included in the
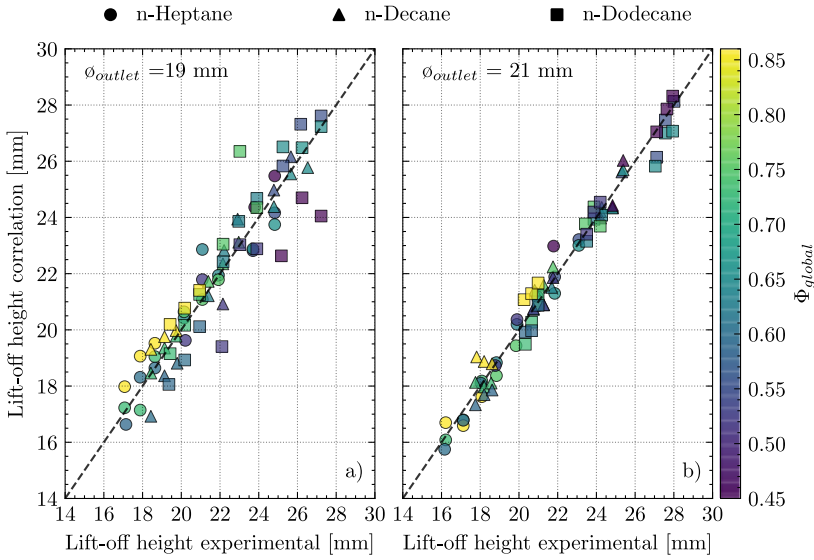
Figure 7.7: Comparison between experimental results and the correlation ones for the air outlet diameters of 19 mm a), and 21 mm b), all fuels, and all operating conditions.

calculation of the SMD. Thus, including SMD in Equation 7.1, it becomes

$$LOH \propto T_{co-flow}^{a} \cdot V_{co-flow}^{b} \cdot SMD^{c} \qquad (7.2)$$

where SMD [µm] is the Sauter mean diameter. Table 7.2 summarizes the results from Equation 7.2 for each air outlet diameters. From the results, it is observed that the flame lift-off height varies linearly with the air velocity and SMD, whereas the air temperature has an inverse effect, as expected by the findings mentioned earlier. In any case, the values of R^2 confirm the good repeatability and reliability of the results gathered. Nevertheless, there is again less reliability for the air outlet diameter of 19 mm, as seen in Figure 7.8, and due to the facts previously explained. Additionally, the p-values of the variables reported in Equation 7.1 and Equation 7.2 are long lower than 0.05, evidencing that the variables included in the correlation are quite significant.

In order to correlate all the experimental data regardless of the operating condition, fuel type, and air outlet diameter, the global equivalence ratio was included to explain the differences in flame lift-off height between the two air outlet diameters. However, the results exhibit that the equivalence ratio does not completely explain the difference between them ($R^2 = 0.53$), which

Table 7.2: Results of empirical correlation for flame lift-off height.

Air outlet diameter	a	b	c	R^2
19 mm	-0.83	1.15	0.19	0.87
21 mm	-0.83	1.25	0.7	0.91
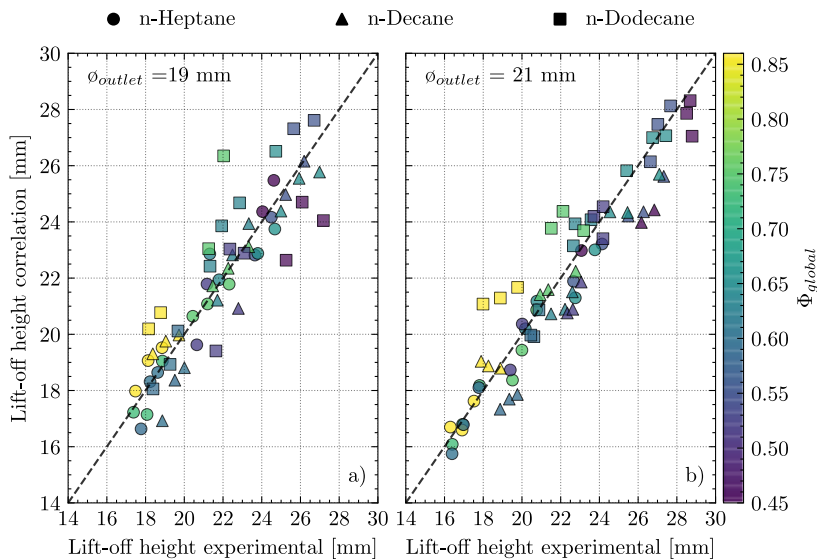
Figure 7.8: Experimental flame lift-off heights plotted against predicted flame lift-off heights using Equation 7.2.

suggests that there is another fact, such as the velocity profiles at the burner exit, that could explain the differences between the two air outlets' diameters.

7.3 Flame propagation speed

As was previously mentioned, the flame lift-off height has a significant relationship with the laminar flame speed and hence, with the rate of the flame propagation through a quiescent multi-droplet mist. Therefore, a correlation derived by Myers and Lefebvre [6] is introduced, which accounts for the effect of the droplet sizes on the rate of flame propagation through quiescent multi-droplet mists in concern with the gas phase flame speed. Since this correlation involves the fuel vapor mass fraction and the droplet diameter just before entering the flame, the following section introduced the droplet evaporation evolution necessary to calculate both using the d^2 law.

7.3.1   Droplet evaporation

The droplet evaporation is a source of fuel vapor that burns with the surrounding oxidant. The local flame structure influences the evaporation process [12] and the burning characteristics. To explain the effect of the droplet diameter and fuel type on droplet evaporation, droplet lifetime has been calculated using d^2 law for different initial droplet diameters (see appendix 7.A). Figure 7.9 shows the droplet lifetimes for different initial droplet sizes and also for the SMDs measured through the MDBI for different fuel mass flow rates, the plot has divided by the fuel type, note that the x-axis scale is different since the enormous differences in the evaporations time due to the variations in fuel properties. Here it is noticeable that smaller droplets (e.g., 5 µm) take less time compared to the larger droplet (e.g., 25 µm) as a result of the differences in the surface area-to-volume ratio. In addition, it is clear that n-Heptane droplets evaporate quickly compared to n-Dodecane droplets since the fuel properties are different and as well the initial droplet size. It is worth noting that the lifetime of the droplets presented in Figure 7.9 does not consider convection or radiation and thus should not be applied to represent the complete dynamics of droplets here but serves the primary purpose of highlighting the non-linear time scales that govern droplet evaporation.

During their dynamics, droplets interact with the gas phase, exchanging mass, energy, and momentum. Since a dilute spray is considered, the interparticle spacing can be considered sufficiently high to make negligible the influence exerted on the droplet dynamics by the neighbor particles. For example, as mentioned by Giusti [13], in the case of evaporation, if the interspacing is small, the fuel mass evaporated from a particle could influence the evaporation of the near droplets since the evaporated fuel enhances the fuel mass fraction near the droplet surface.

7.3.2   Flame propagation speed

The following correlation was derived by Myers and Lefebvre [6] to consider the effect of the droplet sizes on the rate of propagation through the quiescent multi-droplet mist concerning the gas phase flame speed:

$$S_{spray} = \alpha_g \left[\frac{(1 - f_v)\rho_F D^2}{8\rho_g^2 \ln(1 + B)} + \frac{\alpha_g^2}{S_L^2} \right]^{-0.5} \tag{7.3}$$

In Equation 7.3, S_{spray} is the two-phase flow (spray) flame speed, α_g and ρ_g are the thermal diffusivity and density of the air, respectively, at an average
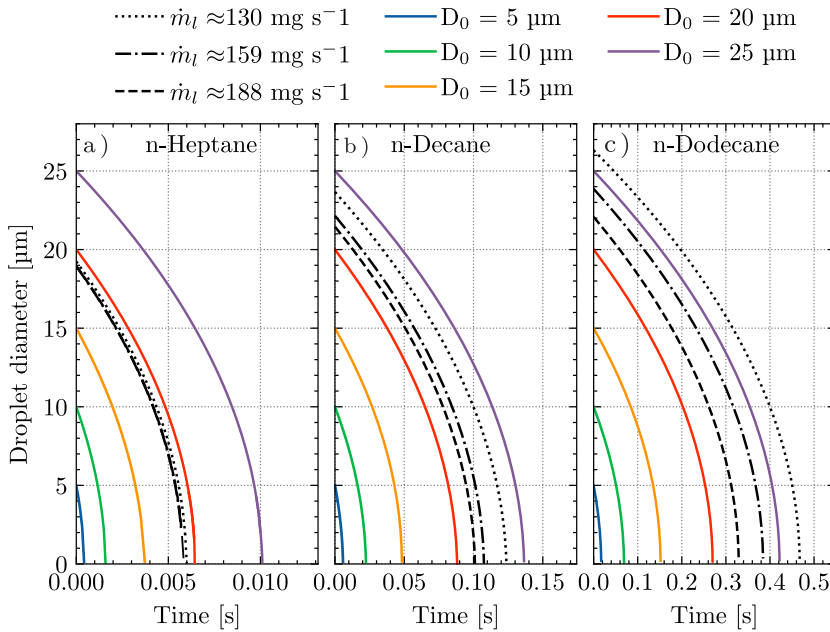
Figure 7.9: Lifetimes for different droplet sizes calculated using d^2 law for the three fuels: n-Heptane a), n-Decane b) and n-Dodecane c). The accurate fuel mass flow rates for each fuel are listed in Table 6.3.

temperature $\sim 1200K$, which was suggested by Myers and Lefebvre [6] and Neophytou and Mastorakos [14], f_v is the fuel vapor mass fraction and D is the droplet diameter at the preheated zone (just before to enter the flame), both estimated using the d^2 law, as was explained previously. The initial droplet sizes (D_0) used in the evaporation model were taken from the Microscopic Diffused Back-Illumination measurements. the values for each parameter are listed in Table 7.3. The residence time (from the injector tip to flame preheated zone) used to predict f_v and D was estimated based on the measured drop velocity and the location of the primary zone from the nozzle exit, ρ_F is the fuel density at $298\,\mathrm{K}$, and B is the heat transfer number (Spalding number), calculated using the following formula:

$$B = \frac{c_{pg}(T_\infty - T_{boil})}{h_{fg}} \tag{7.4}$$

where c_{pg} is the specific heat of the fuel at average temperature (e.g., $\overline{T} = \frac{T_\infty - T_{boil}}{2}$) and was taken from the NIST database [15]. T_{boil} and T_∞ are the fuel

boiling temperature and the temperatures of the preheated zone ($\sim$ 1200 K), respectively, and h_{fg} is the fuel's heat of vaporization. All of the parameters used in Equation 7.3 and 7.4 are listed in Table 6.4 and 7.3.

Table 7.3: Some values of parameters used in Equation 7.3 to calculate the spray flame speed, at air mass flow rate of $\approx 11.9\,kg\,h^{-1}$, fuel mass flow rate of $131\,mg\,s^{-1}$ and co-flow temperature of 328 kelvin.

Fuel	n-Heptane	n-Decane	n-Dodecane
Measured droplet diameter at nozzle exit (D_o) [µm]	19.4	23.74	26.45
Predicted droplet diameter at preheated zone (D) [µm]	15.9	23.4	26.35
Predicted vapor volume fraction entering the flame (f_v)	0.45	0.04	0.02
Specific heat (C_p) [kJ kg^{-1} K] at average temperature ($\overline{T}$)	3.37	3.42	3.47
Air density (ρ_{air}) at 1200 K [kg m^{-3}]	0.2902		
Air thermal diffusively (α_{air}) at 1200 K [m s^{-1}]	2.24E-04		

Figure 7.10 shows the effect of the air mass flow rate and co-flow temperature on the S_{spray} for a constant mass flow rate and all fuels tested. n-Heptane fuel exhibits the highest S_{spray}, followed by n-Decane fuel and then n-Dodecane fuel. The reason for this can again be attributed to the differences in the fuel physical properties and initial droplet size.

Figure 7.10 also shows the effect of the co-flow temperature, which increases slightly the S_{spray} as a result of the droplet evaporation enhancement. Note that some operating conditions did not promote conditions for the flame stabilization, resulting in a lack of points in Figure 7.10 for n-heptane and n-Decane. The effect of varying the fuel mass flow rate on the S_{spray} for a given fuel (e.g., n-Dodecane) is shown in Figure 7.11. Since the fuel mass flow rate is controlled by the injection pressure, increasing the fuel mass flow rate, the atomization quality is enhanced, which results in a droplet diameter decreases. This decrease in the droplet size increases the S_{spray}. In Figure 7.11 exhibits again the effect of the co-flow temperature, which was described previously in the explanation of the Figure 7.10. Figures 7.10 and 7.11 show that enhancing the droplet evaporation propensity, by either increasing the co-flow temperature or using more volatile fuels, the flame propagation speed increases (e.g., Figure 7.10.a n-Dodecane vs n-Heptane).

Normalizing the flame lift-off height measurements by the two-phase flame speed, calculated from Equation 7.3, resulted in a linear correlation with R^2
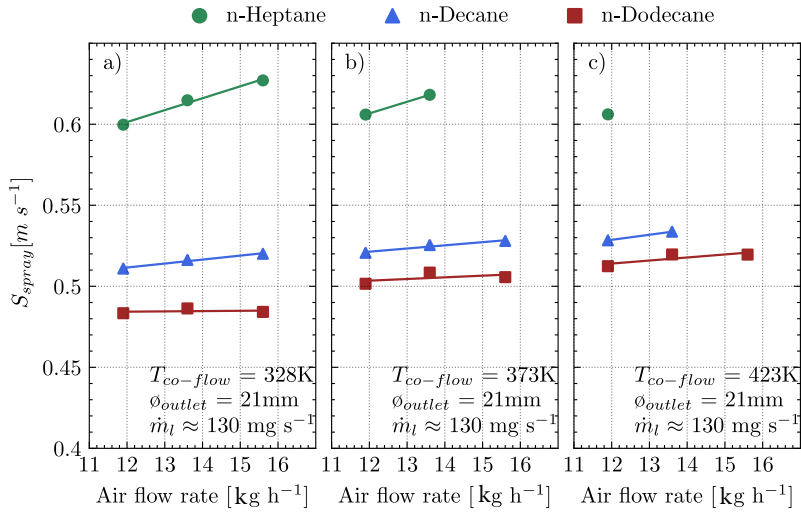
Figure 7.10: Flame propagation speed against air mass flow rate for three different co-flow temperatures: 328 K a), 373 K b) and 423 K c).
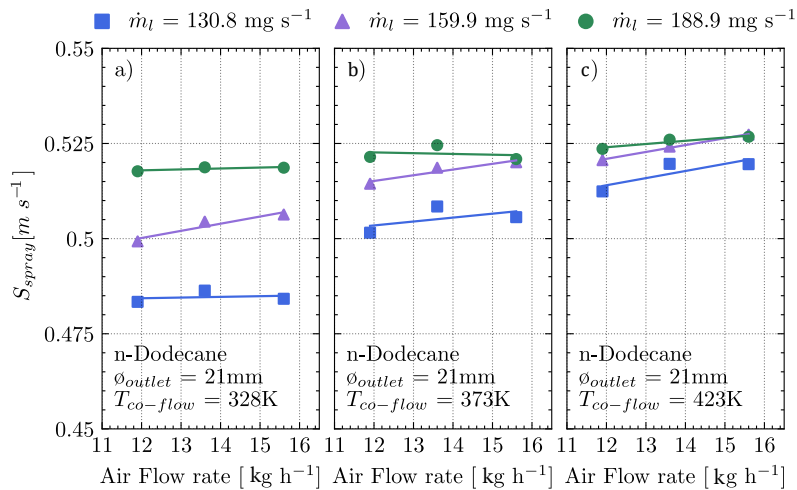
Figure 7.11: Flame propagation speed against air mass flow rate for three different co-flow temperatures: 328 K a), 373 K b) and 423 K c).

range from 0.72 to 0.94, as shown in Figure 7.12. The results exhibit that the ratio between the co-flow velocity and the S_{spray} can be enough to predict the spray flame lift-off height. As was observed in section 7.2, there is relatively less reliability for the air outlet diameter of 19 mm, as seen in Figure 7.12. This is because a significant number of operating conditions promote the flame blow-off phenomenon for the air outlet diameter of 19 mm and was principally observed for n-Heptane due to its high volatility and the increase in co-flow velocity.
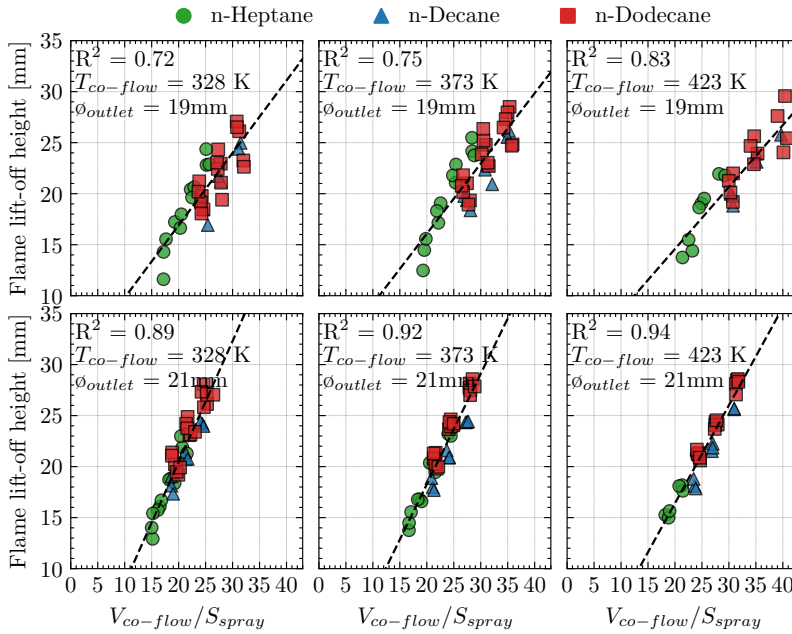
Figure 7.12: Flame lift-off heights plotted against $V_{co-flow}/S_{spray}$ for both air outlet diameters 19 mm (top) and 21 mm (bottom), all fuels, and all operating conditions.

Since the significant relationship between the flame lift-off height and S_{spray}, this variable is included in the Equation 7.1, which accounts for the droplet size in concert with the gas phase flame speed. Therefore, Equation 7.1 becomes

$$LOH \propto T_{co-flow}^{a} \cdot V_{co-flow}^{b} \cdot S_{spray}^{c}. \tag{7.5}$$

Table 7.4 summarizes the results from Equation 7.5 for both air outlet diameters. Note that comparing the values between Table 7.3 and Table 7.4, the

coefficient for the co-flow velocity remains almost similar. Additionally, the coefficient of the S_{spray} is negative, which is expected since it goes upstream regards the fuel stream. However, the coefficient of the co-flow temperature decreases because part of its effect is included in the S_{spray} effect. As seen in Figure 7.13, comparing the experimental flame lift-off height and the predicted flame lift height, using Equation 7.5, seems to be a good predictor with $R^2 = 0.88$ and $R^2 = 0.93$ for the air outlet diameter of 19 mm and 21 mm, respectively. Additionally, the p-values are long lower than 0.05, evidencing that the variables included in the correlation are quite significant.

Table 7.4: Results of empirical correlation for flame lift-off height.

Air outlet diameter	a	b	c	R^2
19 mm	-0.84	1.15	-0.36	0.88
21 mm	-0.87	1.17	-1	0.93
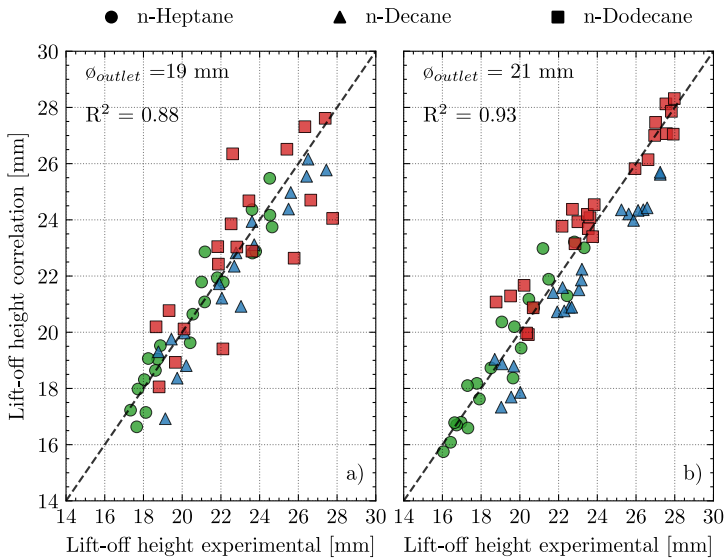
Figure 7.13: Experimental flame lift-off heights plotted against predicted flame lift-off heights using Equation 7.5.

Again, in order to correlate the data regardless of the air outlet diameter, the global equivalence ratio was used. However, the results exhibit that the global equivalence ratio does not completely explain the difference between them, as was informed in section 7.2.

7.4 Soot measurements through diffused back-illumination

This section presents the results of varying different parameters on the soot formation, which have been measured by recording the light attenuation by the soot cloud using a suitable optical setup, as was described in section 5.4. Figure 7.14 shows examples of the raw images captured through this technique for the three fuels, recording 1200 frames for each operating point in batches of 20 frames with LED-on and LED-off. These frames are then averaged to calculate the optical thickness (KL), which accounts for the quantity of light attenuated. This attenuation is affected by the operating conditions and mainly by the fuel type. Therefore, the effects of varying these parameters on soot formation will be introduced throughout the current study. According to Figure 7.14, the fuel that produces the most soot under identical conditions is n-Dodecane, followed by n-Decane, and then by n-Heptane.
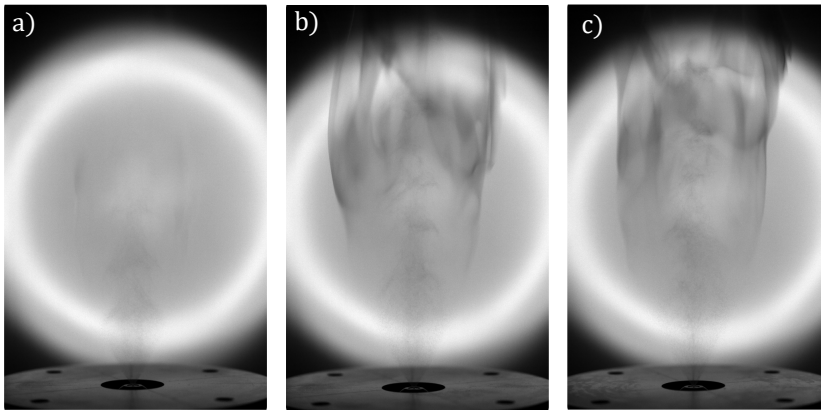
Figure 7.14: Raw images of the soot attenuation of the three fuels: n-Heptane a), n-Decane b), and n-Dodecane c). The frames shown are sprays with an air surrounding temperature of 328 K, an air mass flow rate of 11.9 kg h^{-1} and a fuel mass flow rate of 188 mg s^{-1}.

7.4.1 Results

In order to help to understand the influence of the parametric variations on soot formation, the effects are isolated regarding each parameter. The results presented throughout this section are the result of processing the images captured by the diffused back-illumination extinction technique and following

the methodology detailed previously in section 5.4. Furthermore, the results are given in terms of the amount of light attenuated (by the soot cloud) in a horizontal sheet-of-sight perspective (KA), i.e., the KL resultant image has been divided into rows, calculating the attenuation for each one and thus, allowing to obtain an attenuation profile through the flame height (blue line in Figure 7.15.b). The total amount of soot (KV), is calculated by summing the values from each row. Figure 7.15 also shows the location of the maximum value of KA, the flame lift-off height, and the soot starting position.
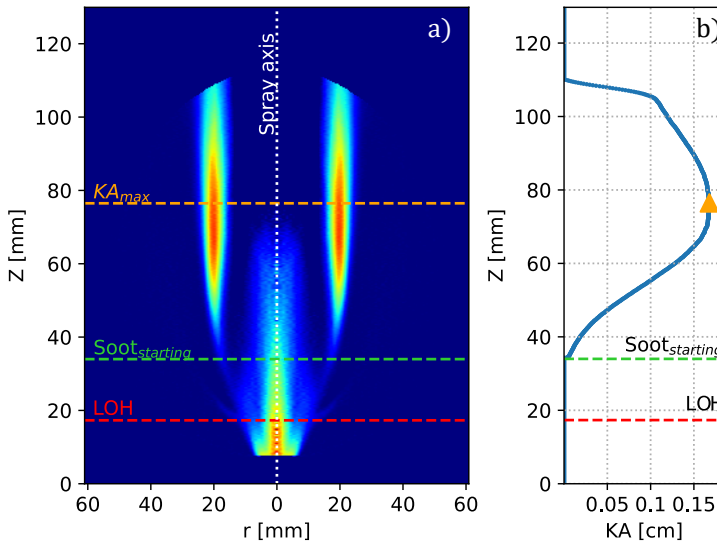
Figure 7.15: a) Light attenuation by the soot cloud in terms of K, b) KA evolution profile through the flame height. The frame shown is a n-Decane flame with an air co-flow temperature of 328 K, for an air mass flow of 11.9 kg h^{-1} and fuel mass flow of 131 mg s^{-1}.

Soot originates from the incomplete combustion of hydrocarbons fuels, indicating in most cases inefficient combustion conditions, where not all the fuel can be completely oxidized. Experimental results from different studies of liquid fuel spray combustion have shown the effect of operating conditions and fuel type on soot formation [16–19]. Unfortunately, as described Wang and Chung [19] soot formation during the burning of fuel sprays depends not only on soot chemistry but on many other physical processes such as spray penetration, droplet size distribution, and velocity field of the entrained air. Therefore, it is challenging to isolate these factors to obtain quantitative information on soot behaviors. Some relationships have been observed between

the operating conditions and soot formation, one of them being the strong relationship between the lift-off height and soot formation [10, 20, 21]. For a particular fuel, as the lift-off height increases, the air entrainment increases, providing a less-rich reaction zone just downstream of the flame lift-off height, thus resulting in less soot formation.

Effect of co-flow conditions and fuel mass flow rate on soot formation

Figure 7.16 shows the effect of varying the air co-flow temperature, air mass flow rate (co-flow velocity), and fuel mass flow rate on soot formation for a given air outlet diameter of 21 mm and n-Decane fuel. At the top of the figure are represented the soot evolution through the flame height, at the bottom are presented the total light attenuation and the figure is also divided regarding the fuel mass flow rate. From the figure, some observations can be made:

- Air co-flow velocity seems to be the parameter driving soot formation. As the air co-flow velocity increases, the flame stabilizes further away from the injector tip (Figure 7.16.a), i.e., the amount of air entrainment increases. Thus, there are less-rich conditions at the reaction zone just downstream of the flame lift-off height, which results in less soot formation due to the major availability of O_2 to oxidize the fuel molecules.It can be observed that as co-flow velocity decreases, the location of the maximum *KA* value is moved further downstream. A reduction in the co-flow velocity results in a longer flame length with a larger yellow-sooting diffusion region and a smaller blue region (partially premixed), moving the location of the maximum *KA*.

- Surprisingly the effect of the co-flow temperature observed here is almost negligible for a constant velocity. Soot formation is a process highly sensitive to temperature [19]. Also, an increase in the co-flow temperature increases the evaporation rate, which in turn reduces the flame lift-off height (see Figure 7.16.a). Thus, it reduces the amount of air entrainment, leading to an establishment of a rich primary zone likely contributing to the soot formation. However, this enhancement of the droplet evaporation rate also leads to a reduction of the droplet size and hence the number of droplets that reach the yellow-sooting diffusion flame is lower thus reducing soot formation. Hayashi et al. [22] conducted a detailed experimental and numerical investigation for a n-Decane spray flame in a laminar counterflow field, reporting that as the initial droplet size increased, an initially blue reaction zone transitioned
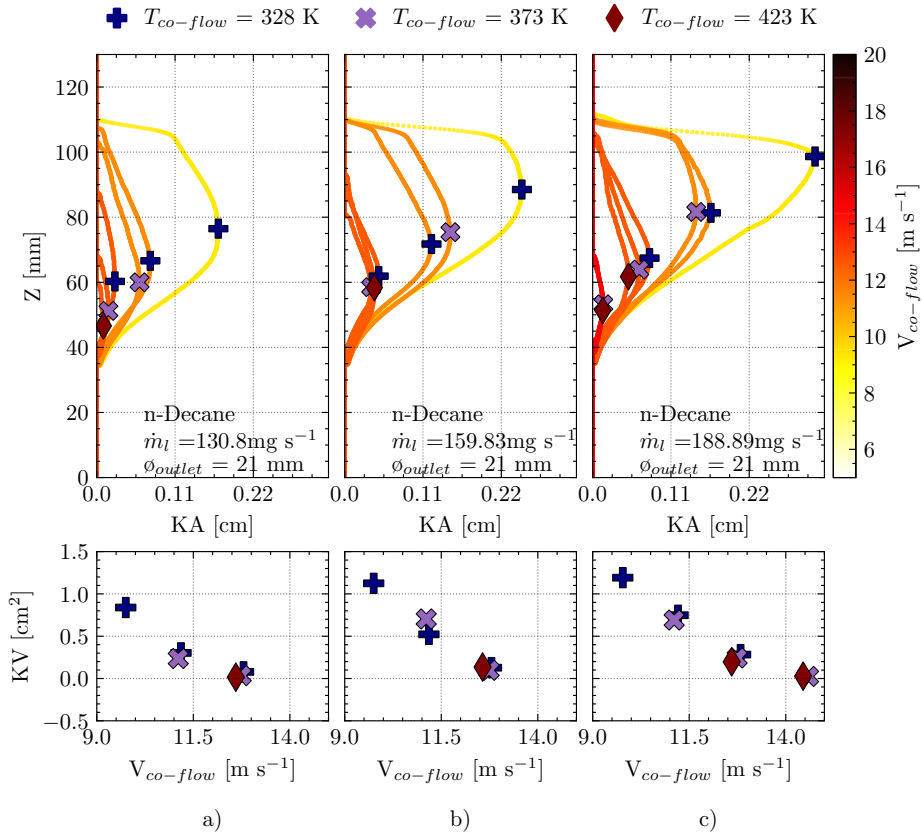
Figure 7.16: *Light attenuation by the soot cloud, in terms of KA and KV, for n-Decane fuel at fuel mass flow rates of 130.8 mg s⁻¹ a), 159.53 mg s⁻¹ b) and 188.89 mg s⁻¹ c). Top images show the KA evolution throughout the flame height and its maximum value, which is pointed out by the location of the symbols. Symbols are in turn related to the co-flow temperature. Bottom images show the total soot, KV, against the co-flow velocity.*

towards yellow flames with increasingly higher luminosity, showing an enhancement of both the peak of soot concentration and the sooting zone area. The two previous facts lead to conclude that during the experiments the effect of the droplet size is higher than the effect of air entrainment, resulting in a balance of both effects. On the contrary, some authors reported [20, 23, 24] that increasing the temperature of the surrounding air also increases the amount of soot, attributing this effect to a reduction of the amount of air entrainment. This suggests that their experiments present a "droplet-driven" flame lift-off height, whereas the present work could be "co-flow driven" (see Figure 7.3.b), considering that the other works were conducted at relatively low co-flow velocities.

- Figure 7.16 also shows the effect of varying the fuel mass flow rate. For a constant co-flow velocity, increasing the fuel mass flow rate significantly increases soot formation. As the fuel mass rate increases the equivalence ratio increases, i.e., rich conditions at the reaction zone just downstream of the flame lift-off height, enhancing the soot formation. The location of the maximum KA is also affected by varying the fuel mass flow rate, as shown in Figure 7.16.

Effect of fuel type on soot formation

Figure 7.17 presents the evolution of KA along the flame height for different operating conditions and the three fuels tested. Figure 7.17 shows that the number of operating conditions that promote the soot formation is higher for n-Decane and n-Dodecane than for n-Heptane fuel and that soot formation increases by increasing the global equivalence ratio (i.e., lower air mass flow rate and higher fuel mass flow rate). In Figure 7.17, comparing the yellow markers (i.e., same global equivalence ratio and same co-flow velocity) for n-Decane and n-Dodecane it becomes evident that the soot formation is larger for n-Dodecane.

In order to observe the effect of the fuel type on soot formation at a constant co-flow velocity, Figure 7.18 was introduced, where KV is plotted against the co-flow velocity for the three fuels. From Figure 7.18, it is again clear that n-Dodecane fuel has a higher sooting tendency, followed by n-Decane and then distantly by n-Heptane, exhibiting for this set of results a slight soot formation only at the lowest co-flow temperature and non-perceptible for the other two co-flow temperatures. As several authors have mentioned, it is natural to suspect that certain fuels are inherently more sooting than others,
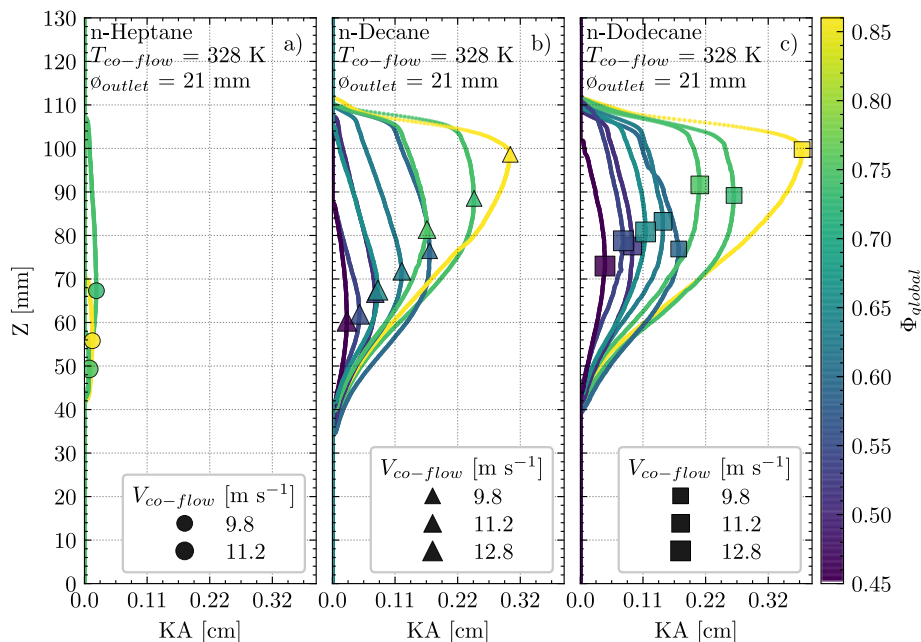
Figure 7.17: KA evolution throughout the flame height for the different fuels, n-Heptane a), n-Decane b), and n-Dodecane c) at a fixed air temperature of 328 K and air outlet diameter of 21 mm. Lines and symbols are colored by the global equivalence ratio and the marker size is related to co-flow velocity.

which is generally accepted since the fuel molecular structure is critical in determining the sooting tendencies of a combustion system [19, 25, 26].

In order to assess the sooting tendencies, different sooting indexes have been developed. Calcote and Manos [27] introduced the threshold soot index (TSI), where higher values mean higher sooting propensity and Mcenally and Pfefferle [28] introduced the yield sooting index (YSI). Olson et al. [25] provided a set of diffusion flame soot threshold data, including both TSIs values and maximum soot volume fraction, $f_v(\text{max})$, for 103 pure hydrocarbons. From this data, it is found that the fuel with higher values of both $f_v(\text{max})$ and TSI is n-Dodecane fuel, followed closely by n-Decane and then n-Heptane with a considerable difference (see Table 7.5). Olson et al. [25] also mentioned that for alkane fuels (e.g., n-Heptane, n-Decane and n-Dodecane) the sooting tendency generally increases in a slight manner with an increase in the number of carbon chains in the molecule. In Figure 7.18, it may be seen that soot formation follows the statement previously mentioned among the
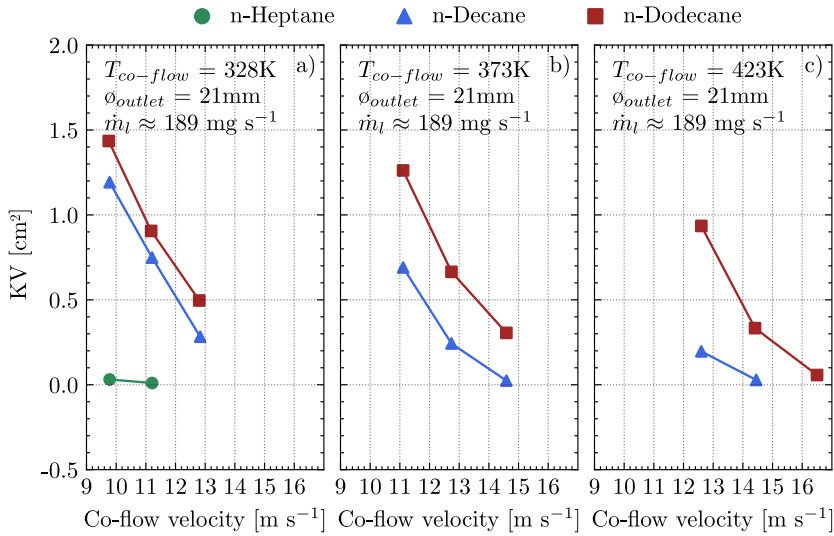
Figure 7.18: KV against co-flow velocity at different co-flow temperatures of 328 K a), 373 K b), and 423 K c) and air outlet diameter of 21 mm (accurate values of fuel mass flow rates for each fuel are listed in Table 6.3).

fuels, evidencing the strong dependence of soot formation on the fuel sooting tendency.

Table 7.5: Sooting tendency values measured by Olson et al. [25] for diffusion flames. For Alkanes the $f_v(max)$ values are seen to be in the range 2 to 7 $\times 10^{-6}$ and TSI in the range 2 to 20.

Properties	n-Heptane	n-Decane	n-Dodecane
Threshold soot index (TSI)	2.0	3.9	5.4
$f_v(max)$ (10^{-6})	2.0	3.4	3.5

Air outlet diameter effect on soot formation

The effect of varying the air outlet diameter on soot formation for n-Decane and n-Dodecane fuels at fixed conditions of fuel mass fuel rate and co-flow temperature is presented in Figure 7.19. For a constant velocity, it can be seen that soot formation increases with a reduction of the outlet cross-section (i.e., air outlet diameter). As was explained previously, a reduction in the air outlet diameter causes a reduction of the flame lift-off height (see Figure 7.6), hence, the amount of air entrainment is reduced (i.e., a reduction of the availability

of the of O_2) to oxidize the fuel molecules, which results in increasing the amount of soot.
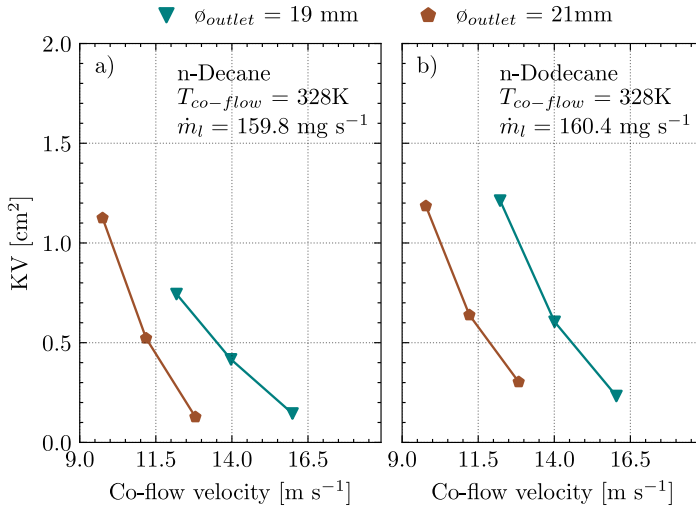
Figure 7.19: Effect of air outlet diameter on soot formation, at fixed conditions of co-flow temperature of 328 K and fuel mas flow rate of 160 mg s^{-1} for n-Decane a) and n-Dodecane b) fuels.

Relationship between soot formation and co-flow velocity

The figures from the previous subsections only show partial sets of results. Hence, Figure 7.20 is introduced as a summary to present all the tested conditions that promote the soot formations. In Figure 7.20, *KV* is plotted against the co-flow velocity, which is divided by fuel type and air outlet diameter. The vertical axis was set on a logarithmic scale due to the large differences in the soot concentration between fuels. Figure 7.20 shows some of the previously described facts, such as the large influence of the co-flow velocity on soot formation for every fuel. An inverse behavior is exhibited: as the co-flow velocity increases the soot formation is reduced. The previous fact is probably due to co-flow velocity playing a significant role in the flame lift-off height limits, and therefore on the amount of air entrainment, which delimits the availability of O_2 to oxidize the fuel molecules. Furthermore, another clear fact is the dependence of the soot formation with the fuel sooting tendency, showing a large formation for n-Dodecane fuel, followed closely by n-Decane, and finally with a notorious difference n-Heptane. Finally, the fuel mass flow rates and

co-flow temperature exhibit a slight effect linked to the commented co-flow velocity and fuel mass flow rate effects.
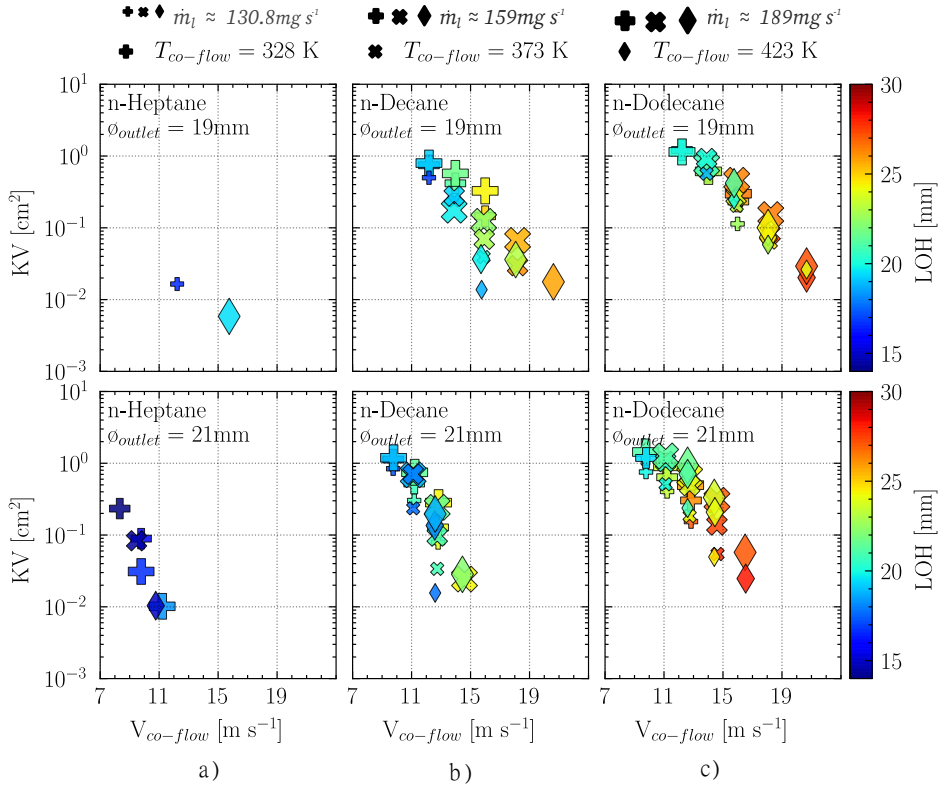
Figure 7.20: Relationship between flame lift-off height and total light attenuation by soot concentration (KV), for all operating conditions and the different fuels: n-Heptane a), n-Decane b), and n-Dodecane c) (accurate values of fuel mass flow rates for each fuel are listed in Table 6.3). Symbols represent the co-flow temperature and its size the fuel mass flow rate, and also colored by the flame lift-off height.

7.5   Summary and conclusions

This chapter collects all the results describing the spray flame combustion for multiple operating conditions. Measurements were carried out in an annular spray burner. Optical setups included a diffused back-illumination to quantify soot, and an intensified CCD camera coupled with a narrow-pass filter to visualize OH* chemiluminescence to measure the stabilized lift-off height of

the spray flame. Fuels were injected through a hollow cone spray injector in a preheated air co-flow. From the findings, it is possible to conclude that:

- For a particular fuel, the flame lift-off height is largely controlled by the co-flow velocity. As co-flow velocity increases, the resultant velocity drives the droplets straight to a downstream position and thus moving the stabilization point of the flame.

- Isolating the effect of the co-flow temperature, it has been observed that flame lift-off height varies inversely with increases in co-flow temperature. The reason is that an increase in the air temperature leads to an increase in the fuel vaporization rate, which results in a reduction in the flame lift-off height.

- The influence of the fuel type on the flame lift-off height seems to be related to both fuel volatility and droplet size, which depend on the fuel physical properties such as density, viscosity, and surface tension. The larger the droplet size and the lower the fuel volatility (e.g., n-Dodecane) the higher the measured lift-off height. As a result, this increases the time necessary to evaporate the fuel droplets and generate enough vapor to stabilize the flame against the incoming reactant stream.

- Isolating the effect of the air outlet diameter, it has been observed that as the air outlet diameter increases, the flame lift-off height is increased. This behavior is attributed to a lower global equivalence ratio, which causes a reduction in the flame speed.

- The statistical analysis performed for each fuel and each outlet diameter evidences the strong dependence of flame lift-off height with the co-flow velocity and co-flow temperature, which affect the resultant velocity of the mixture and evaporation rates, respectively. Additionally, including the SMD in the correlation to predict the flame lift-off height regardless of the fuel type shows good results since it involves the physics properties of the fuel and the effects of the injection pressure and mass flow rate.

- The differences in flame lift-off heights were shown to be a result of two-phase flame speed (S_{spray}), which accounts for both time scale related to the droplet evaporation and pre-vaporized fuel reactivity (S_L). n-Heptane fuel exhibits a higher (S_{spray}), followed by n-Decane and then n-Dodecane. This is likely caused by the smaller droplet sizes of n-Heptane and its higher volatility that enhances the fuel/air mixing.

- By predicting the flame lift-off height with the flame speed through a droplet mist (S_{spray}), co-flow temperature and co-flow velocity exhibit to be a good predictor, with $R^2 = 0.88$ and $R^2 = 0.93$ and p-values quite significant for each variable. Good results are expected since almost all the effects of atomization and evaporation are included in the correlation.

- Soot formation is significantly controlled by the co-flow velocity. As the co-flow velocity increases, the droplets are quickly transported further away from the injector tip, increasing the amount of air entrainment. Thus, a lean mixture is formed further downstream, which results in a less soot formation.

- Isolating the co-flow temperature effect on soot formation it was observed that its influence is almost negligible. This is likely due to the balance of two effects: on the one hand, increasing the co-flow temperature enhances the evaporation rates, which reduces the flame lift-off height (i.e., a reduction of the amount of air entrainment), establishing a rich primary zone that enhances the soot formation. On the other hand, the co-flow temperature leads to a reduction of the droplet size and hence the number of droplets that reach the yellow-sooting region of the flame, resulting in a reduction in the soot formation.

- Isolating the effect of the air outlet diameter on the soot formation, it was observed that reducing the air outlet diameter enhances soot formation. This is likely due to the reduction in the amount of air entrainment before the reaction zone, which promotes a rich reaction zone.

- The trends observed from the experimental results exhibit that soot formation is a complex process that is affected by several parameters such as the amount of air entrainment, fuel evaporation rate, the global equivalence ratio, and mainly the sooting tendency of the fuel since they control the conditions in the reaction zone just downstream of the flame lift-off height.

- Droplet evaporation results exhibit that the smaller droplets take less time to evaporate compared to the larger droplets as a result of the differences in the surface area-to-volume ratio. n-Heptane droplets evaporated faster than n-Decane and n-Dodecane droplets since the differences of both the fuel evaporation properties (lower normal boiling point and higher vapor pressure) and as well as lower initial droplet size, which is generated by lower: density, viscosity, and surface tension.

7.A Appendix: droplet evaporation

This appendix explains how to calculate the droplet diameter before entering the flame, which is used to estimate the fuel vapor volume fraction that enters the flame. In the Figure 7.21, the radius r is the only coordinate variable and has its origin at the droplet center, and the r_s is the radius at the liquid-vapor interface. Far away from the surface of the droplet ($r \to \infty$), the mass fraction of droplet vapor is $Y_{F,\infty}$. The heat from the surrounding environment provides the energy required to evaporate the liquid droplet, and the vapor then diffuses from the droplet surface into the surrounding gas. The droplet radius decreases with time due to mass loss until the droplet is fully evaporated ($r_s = 0$). Knowing the mass flow rate of vapor from the surface at any moment in time allows for the calculation of droplet radius as a function of time as well as droplet lifetime. The following conservation laws are necessary to fully explain this process mathematically:

- Droplet: mass conservation, energy conservation.

- Droplet vapor/ambient gas mixture ($r_s < r < \infty$): overall mass conservation, droplet vapor (species) conservation, and energy conservation.
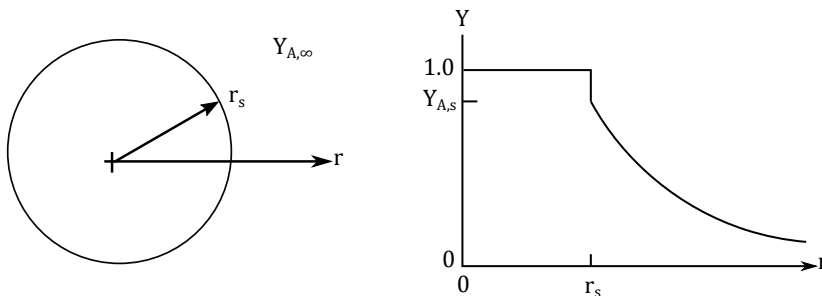
Figure 7.21: Evaporation of liquid droplet in a quiescent environment, where $Y_{A,s}$ is the vapor mass fraction at the droplet surface (Adapted from [29]).

Thus, at least five equations are required for a complete description. Depending on the simplifying assumptions used, these equations can take the form of either ordinary or partial differential equations. Therefore, the d^2 *law* for droplet evaporation can expressed as

$$D^2(t) = D_0^2 - K_e t \tag{7.6}$$

where D_0 is the initial droplet size and K_e is the evaporation constant, which is defined as

$$K_e = \frac{8\rho \mathcal{D}_{AB}}{\rho_l} \ln(1 + B_Y) \qquad (7.7)$$

where the $\mathcal{D}_{AB}$ is the binary diffusion coefficient for the species pair A and B and B_Y is the dimensionless transfer number, and both are calculated as was explained in [29], in which are also described the assumptions to reduce the number unknows and, thus, the number equations to calculate the droplet evaporation.

References

[1]   Reddy, V. M., Trivedi, D., and Kumar, S. "Experimental investigations on lifted spray flames for a range of coflow conditions". In: *Combustion Science and Technology* 184.1 (2012), pp. 44–63. DOI: `10.1080/00102202.2011.615770`.

[2]   Alsulami, R. et al. "Investigating the role of atomization on flame stability of liquid fuels in an annular spray burner". In: *Fuel* 265 (2020). DOI: `10.1016/j.fuel.2019.116945`.

[3]   Kumar, S., Paul, P. J., and Mukunda, H. S. "Prediction of flame liftoff height of diffusion/partially premixed jet flames and modeling of mild combustion burners". In: *Combustion Science and Technology* 179.10 (2007), pp. 2219–2253. DOI: `10.1080/00102200701407887`.

[4]   Payri, R., Salvador, F. J., Gimeno, J., and Cardona, S. "Experimental study of the influence of the boundary conditions on the atomization process in an unconfined atmospheric burner". In: *ILASS-Europe*. Paris, France, 2019, pp. 1–9.

[5]   Alsulami, R. A., Nates, S., Wang, W., Won, S. H., and Windom, B. "Effects of varying liquid fuel and air co-flow rates on spray characterisation of an annular co-flow spray burner". In: *Proceedings of the ASME Turbo Expo*. Vol. 4B-2019. American Society of Mechanical Engineers (ASME), 2019. DOI: `10.1115/GT2019-90989`.

[6]   Myers, G. D. and Lefebvre, A. H. "Flame propagation in heterogeneous mixtures of fuel drops and air". In: *Combustion and Flame* 66.2 (1986), pp. 193–210. DOI: `10.1016/0010-2180(86)90091-X`.

[7]   Reveillon, J. and Vervisch, L. "Analysis of weakly turbulent dilute-spray flames and spray combustion regimes". In: *J. Fluid Mech* 537 (2005), pp. 317–347. DOI: 10.1017/S0022112005005227.

[8]   Réveillon, J. and Vervisch, L. "Partially Premixed Combustion in Spray Flames". In: *18th International Colloquium on The Dynamics of Explosions and Reactive Systems*. 2001, pp. 1–5.

[9]   Benajes, J., Payri, R., Bardi, M., and Martí-aldaraví, P. "Experimental characterization of diesel ignition and lift-off length using a single-hole ECN injector". In: *Applied Thermal Engineering* 58.1-2 (2013), pp. 554–563. DOI: 10.1016/j.applthermaleng.2013.04.044.

[10] Pickett, L. M., Siebers, D. L., and Idicheria, C. A. "Relationship Between Ignition Processes and the Lift-Off Length of Diesel Fuel Jets". In: *SAE Paper*. 724. 2005, pp. 1–18. DOI: 10.4271/2005-01-3843.

[11] Payri, R., Salvador, F. J., Manin, J., and Viera, A. "Diesel ignition delay and lift-off length through different methodologies using a multi-hole injector". In: *Applied Energy* 162 (2016), pp. 541–550. DOI: 10.1016/j.apenergy.2015.10.118.

[12] Faeth, G. M. "Evaporation and combustion of sprays". In: *Progress in Energy and Combustion Science* 9.1-2 (1983), pp. 1–76. DOI: 10.1016/0360-1285(83)90005-9.

[13] Giusti, A. "Development of numerical tools for the analysis of advanced airblast injection systems for lean burn aero-engine combustors". PhD thesis. 2014.

[14] Neophytou, A. and Mastorakos, E. "Simulations of laminar flame propagation in droplet mists". In: *Combustion and Flame* 156 (2009), pp. 1627–1640. DOI: 10.1016/j.combustflame.2009.02.014.

[15] Linstrom, P. J. and Mallard, W. G. "The NIST Chemistry WebBook: A chemical data resource on the Internet". In: *Journal of Chemical and Engineering Data* 46.5 (2001), pp. 1059–1063. DOI: 10.1021/je000236i.

[16] Xu, Y. and Lee, C.-f. F. "Forward-illumination light-extinction technique for soot measurement". In: *Applied Optics* 45.9 (2006), pp. 2046–2057. DOI: 10.1364/AO.45.002046.

[17] De Iuliis, S., Barbini, M., Benecchi, S., Cignoli, F., and Zizak, G. "Determination of the soot volume fraction in an ethylene diffusion flame by multiwavelength analysis of soot radiation". In: *Combustion and Flame* 115.1-2 (1998), pp. 253–261. DOI: 10.1016/S0010-2180(97)00357-X.

[18] Xu, F., Sunderland, P. B., and Faeth, G. M. "Soot formation in laminar premixed ethylene/air flames at atmospheric pressure". In: *Combustion and Flame* 108.4 (1997), pp. 471–493. DOI: `10.1016/S0010-2180(96)00200-3`.

[19] Wang, Y. and Chung, S. H. "Soot formation in laminar counterflow flames". In: *Progress in Energy and Combustion Science* 74 (2019), pp. 152–238. DOI: `10.1016/j.pecs.2019.05.003`.

[20] Payri, R., Gimeno, J., Cardona, S., and Ayyapureddi, S. "Experimental study of the influence of the fuel and boundary conditions over the soot formation in multi-hole diesel injectors using high-speed color diffused back-illumination technique". In: *Applied Thermal Engineering* 158.113746 (2019), pp. 1–16. DOI: `10.1016/J.APPLTHERMALENG.2019.113746`.

[21] Pickett, L. M. and Siebers, D. L. "Soot formation in diesel fuel jets near the lift-off length". In: *International Journal of Engine Research* 7.2 (2006), pp. 103–130. DOI: `10.1243/146808705X57793`.

[22] Hayashi, J., Watanabe, H., Kurose, R., and Akamatsu, F. "Effects of fuel droplet size on soot formation in spray flames formed in a laminar counterflow". In: *Combustion and Flame* 158.12 (2011), pp. 2559–2568. DOI: `10.1016/j.combustflame.2011.05.015`.

[23] Yeganeh, M. G. "Effects of preheated combustion air on laminar coflow diffusion flames under normal and microgravity conditions". PhD thesis. University of Maryland, College Park, 2005.

[24] Ghasemi, A., Moghiman, M., Javadi, S. M., and Hosseini, N. "Effects of droplet size and air preheating on soot formation in turbulent combustion of liquid fuel". In: *ASME 2010 10th Biennial Conference on Engineering Systems Design and Analysis, ESDA2010*. Vol. 1. 2010, pp. 211–217. DOI: `10.1115/ESDA2010-24663`.

[25] Olson, D. B., Pickens, J. C., and Gill, R. J. "The effects of molecular structure on soot formation II. Diffusion flames". In: *Combustion and Flame* 62.1 (1985), pp. 43–60. DOI: `10.1016/0010-2180(85)90092-6`.

[26] Glassman, I. and Yaccarino, P. "The temperature effect in sooting diffusion flames". In: *Symposium (International) on Combustion* 18.1 (1981), pp. 1175–1183. DOI: `10.1016/S0082-0784(81)80122-1`.

[27] Calcote, H. F. and Manos, D. M. "Effect of molecular structure on incipient soot formation". In: *Combustion and Flame* 49.1-3 (1983), pp. 289–304. DOI: `10.1016/0010-2180(83)90172-4`.

[28] Mcenally, C. S. and Pfefferle, L. D. "Improved sooting tendency measurements for aromatic hydrocarbons and their implications for naphthalene formation pathways". In: *Combustion and Flame* 148 (2007), pp. 210–222. DOI: 10.1016/j.combustflame.2006.11.003.

[29] Turns, S. R. *An introduction to combustion: concepts and applications.* 2000, p. 752.

Chapter 8

Summary and future works

This chapter aims at summarizing the work carried out and presented throughout this document. In addition, a list of the potential developments, new studies, and multiple improvements to the methodology used in this thesis are listed as well.

8.1 Summary

This thesis sought to contribute to the fundamental understanding of the effect of the atomization process on combustion performance using different optical diagnostics. A major effort was put into developing a new test rig for studying the spray flames in an annular spray burner, performing experimental measurements for multiple geometrical configurations, several operating conditions and various liquid fuels. Similarly, in implementing new measurement techniques, data processing tools, and image processing routines for the different phenomena.

The work carried out was divided into multiple experimental campaigns, grouped into two chapters based on their specific target, to thoroughly study different aspects of the injection and combustion process. These were:

- Spray characterization, droplet size and droplet velocity.
- Spray flame characterization.

As mentioned before, the first aim of this work was a literature review of the different annular spray burners around the world in order to perform a design of an analogous burner for the study of spray flames in different atmospheric configurations (confine and no confine and also different swirler/venturi configurations). Therefore, a modular design that allows evaluating different geometrical configurations was mandatory. Furthermore, a simplified geometry of the annular burner was used to simulate the airflow behavior inside the combustion chamber, varying the air mass flow rate and also some geometrical configurations, such as swirl angle, venturi angle and cross-section of the combustion chamber. Finally, the annular spray burner was manufactured and set up with its complementary systems (e.g., air supply test bench, electric heater and smoke extraction system) to evaluate different phenomena such as droplet diameter, droplet velocity, and other ones from the combustion process.

All experiments were carried out with a commercially available pressure swirl atomizer, which produces a hollow cone spray pattern. Operating conditions included different fuel mass flow rates, co-flow temperatures, air mass flow rates and two air outlet diameters. Three hydrocarbon fuels were tested (n-Heptane, n-Decane, and n-Dodecane), which present significant differences in physical properties that affect the atomization process.

As mentioned previously, the co-flow of air is supplied through a centrifugal blower which is heated through an electric heater disposed at the main air pipeline up to a maximum temperature of $673\,\mathrm{K}$. The fuel injection system consists of a pressurized vessel that is pressurized with nitrogen at high pressure. An electronic Coriolis mass flow-meter has been arranged at the fuel line to measure the fuel mass flow rate accurately. The fuel spray interacts immediately with the annular co-flow stream that surrounds the injector system, influencing the jet break-up phenomena.

From the results of using a Microscopic diffused back-illumination (MDBI) technique and a configuration similar to the PIV technique principle (i.e., recording two consecutive frames with a very small-time difference), the droplet size and velocity showed that are mainly controlled by the liquid properties and the fuel mass flow rate. By increasing the fuel mass flow rate, on the one hand, the droplet diameter is reduced due to the injection pressure increased, which enhances the atomization quality. On the other hand, the droplet velocity is increased as a result of an increase in the pressure drop across the nozzle that raises the droplet ejection velocity from the nozzle. n-Heptane fuel exhibits smaller droplets since the physical properties (e.g., density, viscosity, and surface tension) are lower, enhancing the atomization

quality and therefore producing small droplets. The results showed agreement with the trends reported in the literature. A diffused back-illumination setup coupled with a microscopic device allowed the visualization and tracking of the droplets. Regarding the evaporation process, the fuel that exhibits higher evaporation rates is the n-Heptane fuel, which also produces small droplets, leading to generate a faster fuel vapor phase.

Measurements of the combustion process in spray flames produced by injecting fuel through a pressure swirl atomizer were carried out in an annular spray burner. To the previous optical setup, an intensified CCD camera coupled with a narrow band-pass filter was added to visualize OH* chemiluminescence and measure the stabilized flame lift-off height. Furthermore, the DBI arrangement was used with a narrow band-pass filter to quantify the soot formation in the spray flame generated during the combustion process. Consequently, the image processing methodology was successfully employed to compare the results from different operating conditions.

From the results regarding the spray flame lift-off height, a definite trend was observed regarding the effects of both co-flow velocity and fuel type. Additionally, isolating the effect of the air co-flow temperature on the flame lift-off height was observed that increasing the co-flow temperature, the flame lift-off length is reduced, as a result, of both the fuel droplet vaporization rate and laminar flame speed are enhanced. The effect of increasing the fuel mass flow rate on the flame lift-off height was associated with the droplet ejection velocity.

From the results regarding soot measurements through the optical thickness, it is noted that soot formation is mainly controlled by the co-flow velocity and sooting tendency of the fuel. The effect of the co-flow temperature on the soot formation is almost negligible, likely due to contrary effects, on the one hand, the reduction of the amount of air entrainment by the enhancement of the droplet evaporation moves the flame stabilization point to an upstream position, on the other hand, by increasing the co-flow temperature the droplet diameter is reducing, avoiding that the big droplets reach the yellow-sooting diffusion flame. Finally, the results exhibit that by increasing the fuel mass flow rate, the soot formation is enhanced, which is probably caused by the rich conditions at the reaction zone just downstream of the flame lift-off height.

As observed throughout the document, the co-flow temperature, co-flow velocity, and fuel type are the parameters that control the flame lift-off height, while the co-flow velocity and the fuel type control the soot formation. Additionally, many results are associated with the flame propagation speed through quiescent multi-droplet mists directly affected by the droplet diameter, which

depends on the fuel's physical properties, fuel mass flow rate, and injector technology.

8.2 Future directions

The spray flames development is very complex, as it comprises numerous phenomena and mechanisms that take place in a very fast event. Optical diagnostics provide an excellent tool for non-intrusive analysis of these processes. As technologies improve, so will the quality and possibilities of the experimental measurements to be carried out. A few examples of the potential developments, additional experiments, or improvements to the current database that could provide fruitful information to assess further the statements of this thesis are:

- Provide the Microscopic diffused back-illumination technique with a motorized system to carry out measurements in different regions in the spray flame. This system should move both the camera and the light source since the technique is arranged in a line-of-sight configuration. New laser configurations developed in the last years can be tested as light sources, which can enhance droplet freezing and contrast between the background and the droplets.

- Using different fuel injector nozzle sizes carefully selected to account for differences in the fuel's physical properties (e.g., density, viscosity, and surface tension) and to minimize the role of the spray process, e.g., SMD, on the flame stability. This unique approach of controlling the atomization process allows a more systematic study of the fuels' volatility and reactivity on flame behavior.

- Employ laser techniques such as PDA to characterize the droplet velocity and droplet diameter, allowing to validate the results obtained through the Microscopic Diffused back-illumination.

- After measuring the flame lift-off height for each operating condition, will be interesting to perform an experimental camping close to this height, which will allow determining the droplet diameter of the droplets that reach the base of the flame.

- Applying OH laser-induced fluoresce technique to investigate the structure and stabilization of the spray flame and also PAH distributions through the PAH-PLIF technique to understand the fundamental implications between soot and soot-precursor (PAH).

- Quantify OH and NO_x formation through laser-induced fluorescence to help in understanding their fundamental implications in the soot-NO_x trade-off in spray flames.

- Carry out studies in a configuration of the swirling co-flow with different swirl angles (e.g., 30° and 60°), studying the effect of the swirl angle on droplet characteristics, flame lift-off height and soot formation. Furthermore, carry out studies of spray flame in confined configuration, testing non-swirled and swirled flows and evaluating their effect on the atomization and combustion performance.

- Perform a computational study of the atomization process for the fuels tested and in homologous operating conditions. They can be validated using the experimental data presented in this work and could provide essential information to improve the fundamental understanding of the spray atomization process.

- Perform an experimental campaign with the real fuels used in aircraft engines in order to compare with the result presented throughout this study as well as the upcoming e-fuels.

Global Bibliography

Abramzon, B. and Sirignano, W. A. "Droplet vaporization model for spray combustion calculations". In: *International Journal of Heat and Mass Transfer* 32.9 (1989), pp. 1605–1618. DOI: `10.1016/0017-9310(89) 90043-4` (cited on pages 45, 46).

Allan, D. B., Caswell, T., Keim, N. C., Wel, C. M. van der, and Verweij, R. W. *Trackpy v0.5.0*. 2021. DOI: `10.5281/ZENODO.4682814` (cited on page 106).

Alsulami, R. A., Nates, S., Wang, W., Won, S. H., and Windom, B. "Effects of varying liquid fuel and air co-flow rates on spray characterisation of an annular co-flow spray burner". In: *Proceedings of the ASME Turbo Expo*. Vol. 4B-2019. American Society of Mechanical Engineers (ASME), 2019. DOI: `10.1115/GT2019-90989` (cited on pages 138, 139, 158).

Alsulami, R. et al. "Investigating the role of atomization on flame stability of liquid fuels in an annular spray burner". In: *Fuel* 265 (2020). DOI: `10.1016/j.fuel.2019.116945` (cited on pages 139, 147, 157, 159–161).

Ashgriz, N. and Yarin, A. L. "Capillary Instability of Free Liquid Jets". In: *Handbook of Atomization and Sprays*. Springer US, 2011, pp. 3–53. DOI: `10.1007/978-1-4419-7264-4_1` (cited on pages 37, 38).

Aubagnac-karkar, D. "Sectional soot modeling for Diesel RANS simulations". PhD thesis. IFP - Energies Nouvelles, 2015, p. 152 (cited on page 57).

Aubagnac-Karkar, D., El Bakali, A., and Desgroux, P. "Soot particles inception and PAH condensation modelling applied in a soot model utilizing a sectional method". In: *Combustion and Flame* 189 (2018), pp. 190–206. DOI: `10.1016/j.combustflame.2017.10.027` (cited on page 58).

Avedisian, C. T. "Recent Advances in Soot Formation from Spherical Droplet Flames at Atmospheric Pressure". In: *Journal of Propulsion and Power* 16.4 (2000), pp. 628–635. DOI: `10.2514/2.5619` (cited on page 56).

Balachandar, S. and Eaton, J. K. "Turbulent Dispersed Multiphase Flow". In: *Annual Review of Fluid Mechanics* 42.1 (2010), pp. 111–133. DOI: `10.1146/annurev.fluid.010908.165243` (cited on page 48).

Bardi, M. "Partial needle lift and injection rate shape effect on the formation and combustion of the Diesel spray". PhD thesis. Valencia (Spain): Universitat Politècnica de València, 2014. DOI: `10.4995/Thesis/10251/37374` (cited on page 114).

Bardi, M. et al. "Engine combustion network: comparison of spray development, vaporization, and combustion in different combustion vessels". In: *Atomization and Sprays* 22.10 (2012), pp. 807–842. DOI: `10.1615/AtomizSpr.2013005837` (cited on page 114).

Benajes, J., Payri, R., Bardi, M., and Martí-aldaraví, P. "Experimental characterization of diesel ignition and lift-off length using a single-hole ECN injector". In: *Applied Thermal Engineering* 58.1-2 (2013), pp. 554–563. DOI: `10.1016/j.applthermaleng.2013.04.044` (cited on pages 114, 162).

H. Bockhorn, ed. *Soot Formation in Combustion*. Vol. 59. Springer Series in Chemical Physics. Berlin, Heidelberg: Springer Berlin Heidelberg, 1994. DOI: `10.1007/978-3-642-85167-4` (cited on page 57).

Borghi, R. "Turbulent combustion modelling". In: *Progress in Energy and Combustion Science* 14.4 (1988), pp. 245–292. DOI: `10.1016/0360-1285(88)90015-9` (cited on pages 53–55).

Borghi, R. "The links between turbulent combustion and spray combustion and their modelling". In: *8th International Symposium on Transport Phenomena in Combustion*. 1996, pp. 1–18 (cited on pages 50, 53, 54).

Bray, K. N. C., Champion, M., and Libby, P. A. "The Interaction Between Turbulence and Chemistry in Premixed Turbulent Flames". In: Springer, New York, NY, 1989, pp. 541–563. DOI: `10.1007/978-1-4613-9631-4_26` (cited on page 49).

Brodkey, R. O. *The Phenomena of Fluid Motions*. Addison-Wesley, 1967, p. 737. DOI: `10.1017/S0022112068222267` (cited on page 38).

Cai, J. "Aerodynamics of Lean Direct Injection Combustor with Multi-Swirler Arrays". PhD thesis. 2006 (cited on page 23).

Calcote, H. F. and Manos, D. M. "Effect of molecular structure on incipient soot formation". In: *Combustion and Flame* 49.1-3 (1983), pp. 289–304. DOI: 10.1016/0010-2180(83)90172-4 (cited on page 177).

Calcote, H. "Mechanisms of soot nucleation in flames - A critical review". In: *Combustion and Flame* 42.C (1981), pp. 215–242. DOI: 10.1016/0010-2180(81)90159-0 (cited on page 59).

Candel, S., Lacas, F., Darabiha, N., and Rolon, C. "Group combustion in spray flames". In: *Multiphase Science and Technology* 11.1 (1999), pp. 1–18. DOI: 10.1615/MultScienTechn.v11.i1.10 (cited on page 53).

Carbonell, D. "Numerical studies of diffusion flames. Special emphasis on flamelet concept and soot formation". PhD thesis. Universitat Politècnica de Catalunya, 2008. DOI: 10.13140/2.1.1581.7924 (cited on page 56).

Castanet, G., Perrin, L., Caballina, O., and Lemoine, F. "Evaporation of closely-spaced interacting droplets arranged in a single row". In: *International Journal of Heat and Mass Transfer* 93 (2016), pp. 788–802. DOI: 10.1016/j.ijheatmasstransfer.2015.09.064 (cited on page 45).

Cavaliere, A., Barbella, R., Ciajolo, A., D'anna, A., and Ragucci, R. "Fuel and soot oxidation in diesel-like conditions". In: *Symposium (International) on Combustion* 25.1 (1994), pp. 167–174. DOI: 10.1016/S0082-0784(06)80641-7 (cited on page 59).

Cessou, A. "Simple description of the combustion structures in the stabilization stage of a spray jet flame". In: *Atomization and Sprays* 9.1 (1999), pp. 1–27. DOI: 10.1615/atomizspr.v9.i1.10 (cited on pages 55, 71).

Chi-Ming, L., Kathleen M., T., and Changleie, W. "High pressure low NOx emissions research: Recent progress at NASA Glenn Research Center". In: *fuel* 4.1 (2007), pp. 1–8. DOI: 10.1007/s13398-014-0173-7.2 (cited on page 70).

Chiu, H. H., Kim, H. Y., and Croke, E. J. "Internal group combustion of liquid droplets". In: *Symposium (International) on Combustion* 19.1 (1982), pp. 971–980. DOI: 10.1016/S0082-0784(82)80273-7 (cited on pages 53, 54).

Choi, M. Y. and Kyeong-Okk, L. "Investigation of sooting in microgravity droplet combustion". In: *Symposium (International) on Combustion* 26.1 (1996), pp. 1243–1249. DOI: 10.1016/S0082-0784(96)80341-9 (cited on page 56).

Cignoli, F., De Iuliis, S., Manta, V., and Zizak, G. "Two-dimensional two-wavelength emission technique for soot diagnostics". In: *Applied Optics* 40.30 (2001), p. 5370. DOI: 10.1364/ao.40.005370 (cited on page 115).

Cléon, G., Honoré, D., Lacour, C., and Cessou, A. "Experimental investigation of structure and stabilization of spray oxyfuel flames diluted by carbon dioxide". In: *Proceedings of the Combustion Institute* 35.3 (2015), pp. 3565–3572. DOI: `10.1016/j.proci.2014.06.028` (cited on pages 72, 125).

Cochet, A. et al. "ONERA test Facilities for Combustion in Aero Gas Turbine Engines, and Associated Optical Diagnostics". In: *AerospaceLab* 11 (2016) (cited on page 70).

Cordier, M. "Allumage et propagation de flamme dans les écoulements fortement swirlés : études expérimentales et numériques". PhD thesis. INSA, 2013 (cited on pages 77, 78, 80, 83).

Correia Rodrigues, H., Tummers, M. J., Veen, E. H. van, and Roekaerts, D. J. "Effects of coflow temperature and composition on ethanol spray flames in hot-diluted coflow". In: *International Journal of Heat and Fluid Flow* 51 (2015), pp. 309–323. DOI: `10.1016/j.ijheatfluidflow.2014.10.006` (cited on pages 74, 75).

Correia Rodrigues, H., Tummers, M. J., Veen, E. H. van, and Roekaerts, D. J. "Spray flame structure in conventional and hot-diluted combustion regime". In: *Combustion and Flame* 162.3 (2015), pp. 759–773. DOI: `10.1016/j.combustflame.2014.07.033` (cited on page 125).

D'Anna, A. "Combustion-formed nanoparticles". In: *Proceedings of the Combustion Institute* 32.1 (2009), pp. 593–613. DOI: `10.1016/j.proci.2008.09.005` (cited on page 58).

Damien, M. D. "Modelisation de la combustion d'un spray dans un bruleur aeronautique". PhD thesis. Université de Toulouse, 2016 (cited on page 52).

Damköhler, G. "Der Einfluss der Turbulenz auf die Flammengeschwindigkeit in Gasgemschen". In: *Zeitschrift für Elektrochemie und angewandte physikalische Chemie* 46.11 (1940), pp. 601–652. DOI: `0.1002/bbpc.18980052102` (cited on page 50).

De Iuliis, S., Barbini, M., Benecchi, S., Cignoli, F., and Zizak, G. "Determination of the soot volume fraction in an ethylene diffusion flame by multiwavelength analysis of soot radiation". In: *Combustion and Flame* 115.1-2 (1998), pp. 253–261. DOI: `10.1016/S0010-2180(97)00357-X` (cited on pages 115, 173).

Dec, J. E. and Espey, C. "Chemiluminescence Imaging of Autoignition in a DI Diesel Engine". In: *SAE Technical Paper* 724 (1998). DOI: `10.4271/982685` (cited on page 114).

Dewanji, D. "Investigation of flow characteristics in lean direct injection combustors". PhD thesis. 2012, pp. 181–196. DOI: `10.2514/1.B34264` (cited on pages 18, 23, 24).

Dietrich, D. L. et al. "Droplet Combustion Experiments Aboard the International Space Station". In: *Microgravity Science and Technology* 26.2 (2014), pp. 65–76. DOI: `10.1007/s12217-014-9372-2` (cited on page 56).

Dikshit, P. S. B., Kulshreshtha, D. D. B., and Channiwala, D. S. A. "Numerical Analysis and Empirical Correlations to Predict SMD of Pressure Swirl Atomizer for Small Scale Gas Turbine Combustion Chamber". In: *International Journal of Applied Engineering Research* 13 (2018), pp. 4531–4537 (cited on page 147).

Doerr, T. "Introduction to aero-engine gas turbine combustion". In: *Aero-engine design: from state of the art turbofans towards innovative architectures.* Rhode Saint Genese, 2008, p. 5 (cited on pages 15, 22).

Domingo, P., Vervisch, L., and Réveillon, J. "DNS analysis of partially premixed combustion in spray and gaseous turbulent flame-bases stabilized in hot air". In: *Combustion and Flame* 140.3 (2005), pp. 172–195. DOI: `10.1016/j.combustflame.2004.11.006` (cited on page 55).

Dumouchel, C. "On the experimental investigation on primary atomization of liquid streams". In: *Experiments in Fluids* 45.3 (2008), pp. 371–422. DOI: `10.1007/s00348-008-0526-0` (cited on pages 35, 36).

Eaton, J. and Fessler, J. "Preferential concentration of particles by turbulence". In: *International Journal of Multiphase Flow* 20.SUPPL. 1 (1994), pp. 169–209. DOI: `10.1016/0301-9322(94)90072-8` (cited on page 49).

Eaves, N., Dworkin, S., and Thomson, M. "The importance of reversibility in modeling soot nucleation and condensation processes". In: *Proceedings of the Combustion Institute* 35.2 (2015), pp. 1787–1794. DOI: `10.1016/j.proci.2014.05.036` (cited on page 58).

Eaves, N. A., Dworkin, S. B., and Thomson, M. J. "Assessing relative contributions of PAHs to soot mass by reversible heterogeneous nucleation and condensation". In: *Proceedings of the Combustion Institute* 36.1 (2017), pp. 935–945. DOI: `10.1016/j.proci.2016.06.051` (cited on page 58).

Elghobashi, S. and Truesdell, G. C. "On the two-way interaction between homogeneous turbulence and dispersed solid particles. I: Turbulence modification". In: *Physics of Fluids A* 5.7 (1992), pp. 1790–1801. DOI: `10.1063/1.858854` (cited on page 49).

Faeth, G. M. "Evaporation and combustion of sprays". In: *Progress in Energy and Combustion Science* 9.1-2 (1983), pp. 1–76. DOI: 10.1016/0360-1285(83)90005-9 (cited on page 166).

Faeth, G. "Current status of droplet and liquid combustion". In: *Progress in Energy and Combustion Science* 3.4 (1977), pp. 191–224. DOI: 10.1016/0360-1285(77)90012-0 (cited on page 45).

Frenklach, M. "Reaction mechanism of soot formation in flames". In: *Physical Chemistry Chemical Physics* 4.11 (2002), pp. 2028–2037. DOI: 10.1039/b110045a (cited on page 59).

Frenklach, M. and Wang, H. "Detailed modeling of soot particle nucleation and growth". In: *Symposium (International) on Combustion* 23.1 (1991), pp. 1559–1566. DOI: 10.1016/S0082-0784(06)80426-1 (cited on page 58).

Friedman, J. A. and Renksizbulut, M. "Investigating a methanol spray flame interacting with an annular air jet using phase-Doppler interferometry and planar laser-induced fluorescence". In: *Combustion and Flame* 117.4 (1999), pp. 661–684. DOI: 10.1016/S0010-2180(98)00136-9 (cited on pages 71, 72).

Gaydon, A. G. *The Spectroscopy of Flames.* Springer Netherlands, 1974. DOI: 10.1007/978-94-009-5720-6 (cited on page 114).

Ghasemi, A., Moghiman, M., Javadi, S. M., and Hosseini, N. "Effects of droplet size and air preheating on soot formation in turbulent combustion of liquid fuel". In: *ASME 2010 10th Biennial Conference on Engineering Systems Design and Analysis, ESDA2010.* Vol. 1. 2010, pp. 211–217. DOI: 10.1115/ESDA2010-24663 (cited on page 176).

Giusti, A. "Development of numerical tools for the analysis of advanced air-blast injection systems for lean burn aero-engine combustors". PhD thesis. 2014 (cited on pages 13, 15, 20–22, 34, 37, 39, 43, 44, 48, 166).

Glassman, I. and Yaccarino, P. "The temperature effect in sooting diffusion flames". In: *Symposium (International) on Combustion* 18.1 (1981), pp. 1175–1183. DOI: 10.1016/S0082-0784(81)80122-1 (cited on page 177).

Glassman, I. and Yetter, R. A. "Environmental Combustion Considerations". In: *Combustion.* Elsevier, 2008, pp. 409–494. DOI: 10.1016/B978-0-12-088573-2.00008-7 (cited on pages 56, 57).

Goix, P. J., Edwards, C. F., Cessou, A., Dunsky, C. M., and Stepowski, D. "Structure of a methanol/air coaxial reacting spray near the stabilization region". In: *Combustion and Flame* 98.3 (1994), pp. 205–219. DOI: 10.1016/0010-2180(94)90236-4 (cited on page 71).

Gore, R. and Crowe, C. "Effect of particle size on modulating turbulent intensity". In: *International Journal of Multiphase Flow* 15.2 (1989), pp. 279–285. DOI: 10.1016/0301-9322(89)90076-1 (cited on page 49).

Gounder, J. D., Kourmatzis, A., and Masri, A. R. "Turbulent piloted dilute spray flames: Flow fields and droplet dynamics". In: *Combustion and Flame* 159.11 (2012), pp. 3372–3397. DOI: 10.1016/j.combustflame.2012.07.014 (cited on pages 73, 74).

Guildenbecher, D. R., López-Rivera, C., and Sojka, P. E. "Secondary atomization". In: *Experiments in Fluids* 46.3 (2009), pp. 371–402. DOI: 10.1007/s00348-008-0593-2 (cited on pages 40, 41).

Harris, S. J. and Weiner, A. M. "Determination of the Rate Constant for Soot Surface Growth". In: *Combustion Science and Technology* 32.5-6 (1983), pp. 267–275. DOI: 10.1080/00102208308923661 (cited on page 59).

Harris, S. J. and Weiner, A. M. "Surface Growth of Soot Particles in Premixed Ethylene/Air Flames". In: *Combustion Science and Technology* 31.3-4 (1983), pp. 155–167. DOI: 10.1080/00102208308923637 (cited on page 59).

Haselbach, F. and Parker, R. "Hot end technology for advanced, low emission large civil aircraft engines". In: *28th Congress of the International Council of the Aeronautical Sciences 2012, ICAS 2012* 3 (2012), pp. 2479–2490 (cited on page 19).

Hayashi, J., Watanabe, H., Kurose, R., and Akamatsu, F. "Effects of fuel droplet size on soot formation in spray flames formed in a laminar counterflow". In: *Combustion and Flame* 158.12 (2011), pp. 2559–2568. DOI: 10.1016/j.combustflame.2011.05.015 (cited on page 174).

Haynes, B. and Wagner, H. "Soot formation". In: *Progress in Energy and Combustion Science* 7.4 (1981), pp. 229–273. DOI: 10.1016/0360-1285(81)90001-0 (cited on page 59).

Hervo, L., Senoner, J. M., Biancherin, A., and Cuenot, B. "Large-Eddy Simulation of Kerosene Spray Ignition in a Simplified Aeronautic Combustor". In: *Flow, Turbulence and Combustion* 101.2 (2018), pp. 603–625. DOI: 10.1007/s10494-018-9924-4 (cited on pages 76, 77).

Heywood, J. *Internal Combustion Engine Fundamentals*. 2018, p. 1056 (cited on page 56).

Hickstein, D. D., Gibson, S. T., Yurchak, R., Das, D. D., and Ryazanov, M. "A direct comparison of high-speed methods for the numerical Abel transform". In: *Review of Scientific Instruments* 90.6 (2019), pp. 1–9. DOI: 10.1063/1.5092635 (cited on page 112).

Higgins, B. and Siebers, D. L. "Measurement of the Flame Lift-Off Location on DI Diesel Sprays Using OH Chemiluminescence". In: *SAE Technical Paper* (2001) (cited on pages 113, 114).

Hinze, J. O. "Fundamentals of the hydrodynamic mechanism of splitting in dispersion processes". In: *AIChE Journal* 1.3 (1955), pp. 289–295. DOI: `10.1002/aic.690010303` (cited on page 40).

Homann, K. and Wagner, H. "Some new aspects of the mechanism of carbon formation in premixed flames". In: *Symposium (International) on Combustion* 11.1 (1967), pp. 371–379. DOI: `10.1016/S0082-0784(67)80161-9` (cited on page 59).

Im, J. H., Kim, D., Han, P., Yoon, Y., and Bazarov, V. "Self-pulsation characteristics of a gas-liquid swirl coaxial injector". In: *Atomization and Sprays* 19.1 (2009), pp. 57–74. DOI: `10.1615/atomizspr.v19.i1.40` (cited on page 147).

Jackson, G. S. and Avedisian, C. T. "The effect of initial diameter in spherically symmetric droplet combustion of sooting fuels". In: *Proceedings of the Royal Society of London. Series A: Mathematical and Physical Sciences* 446.1927 (1994), pp. 255–276. DOI: `10.1098/rspa.1994.0103` (cited on page 56).

Jasuja, A. K. "Atomization of crude and residual fuel oils". In: *Journal of Engineering for Gas Turbines and Power* 101.2 (1979), pp. 250–258. DOI: `10.1115/1.3446480` (cited on pages 142, 147).

Jedelsky, J. and Jicha, M. "Energy considerations in spraying process of a spill-return pressure-swirl atomizer". In: *Applied Energy* 132 (2014), pp. 485–495. DOI: `10.1016/j.apenergy.2014.07.042` (cited on page 147).

Jenny, P., Roekaerts, D., and Beishuizen, N. "Modeling of turbulent dilute spray combustion". In: *Progress in Energy and Combustion Science* 38.6 (2012), pp. 846–887. DOI: `10.1016/j.pecs.2012.07.001` (cited on page 52).

JetX Engineering. *https://www.jet-x.org/* (cited on pages 16, 19).

Kashif, M., Bonnety, J., Matynia, A., Da Costa, P., and Legros, G. "Sooting propensities of some gasoline surrogate fuels: Combined effects of fuel blending and air vitiation". In: *Combustion and Flame* 162.5 (2015), pp. 1840–1847. DOI: `10.1016/j.combustflame.2014.12.005` (cited on page 56).

Kashif, M., Guibert, P., Bonnety, J., and Legros, G. "Sooting tendencies of primary reference fuels in atmospheric laminar diffusion flames burning into vitiated air". In: *Combustion and Flame* 161.6 (2014), pp. 1575–1586. DOI: 10.1016/j.combustflame.2013.12.009 (cited on page 56).

Koch, R. "Spray combustion". In: *Turbulent combustion.* 2011 (cited on pages 41, 47, 48).

Kumar, K., Freeh, J. E., Sung, C. J., and Huang, Y. "Laminar flame speeds of preheated iso-octane/O2/N2 and n-heptane/O2/N2 mixtures". In: *Journal of Propulsion and Power* 23.2 (2007), pp. 428–436. DOI: 10.2514/1.24391 (cited on page 131).

Kumar, S., Paul, P. J., and Mukunda, H. S. "Prediction of flame liftoff height of diffusion/partially premixed jet flames and modeling of mild combustion burners". In: *Combustion Science and Technology* 179.10 (2007), pp. 2219–2253. DOI: 10.1080/00102200701407887 (cited on page 157).

Kumar, S., Ray, A., and Kale, S. R. "A soot model for transient, spherically symmetric n -heptane droplet combustion". In: *Combustion Science and Technology* 174.9 (2002), pp. 67–102. DOI: 10.1080/00102200290021380 (cited on page 56).

LaVision. *https://www.piv.de/index.php* (cited on page 101).

Lee, K. O., Manzello, S. L., and Choi, M. Y. "The effects of initial diameter on sooting and burning behavior of isolated droplets under microgravity conditions". In: *Combustion Science and Technology* 132.1-6 (1998), pp. 139–156. DOI: 10.1080/00102209808952013 (cited on page 56).

Lefebvre, A. and McDonell, V. *Atomization and Sprays.* 2017, p. 300. DOI: 10.1016/0009-2509(90)87140-N (cited on pages 13–15, 32, 36, 42, 43, 52, 142, 147).

Lefebvre, A. H. "Airblast atomization". In: *Progress in Energy and Combustion Science* 6.3 (1980), pp. 233–261. DOI: 10.1016/0360-1285(80)90017-9 (cited on pages 15, 41, 150).

Lefebvre, A. H. and Ballal, D. R. *Turbine Combustion Alternative Fuels and Emissions.* CRC Press, 2010, pp. 1–537 (cited on pages 9–11, 16, 31, 33, 36, 38).

Lewis, B. and Von Elbe, G. "Stability and structure of burner flames". In: *The Journal of Chemical Physics* 11.2 (1943), pp. 75–93. DOI: 10.1063/1.1723808 (cited on page 18).

Linstrom, P. J. and Mallard, W. G. "The NIST Chemistry WebBook: A chemical data resource on the Internet". In: *Journal of Chemical and Engineering Data* 46.5 (2001), pp. 1059–1063. DOI: `10.1021/je000236i` (cited on pages 124, 131, 167).

Liu, H. et al. "Influence of temperature and mixture stratification on HCCI combustion using chemiluminescence images and CFD analysis". In: *Applied Thermal Engineering* 33-34.1 (2012), pp. 135–143. DOI: `10.1016/j.applthermaleng.2011.09.026` (cited on page 113).

Liu, Y. et al. "Review of modern low emissions combustion technologies for aero gas turbine engines". In: *Progress in Aerospace Sciences* 94 (2017), pp. 12–45. DOI: `10.1016/j.paerosci.2017.08.001` (cited on pages 23, 25, 26).

Liu, Z., Zheng, C., and Zhou, L. "A joint PDF model for turbulent spray evaporation/combustion". In: *Proceedings of the Combustion Institute* 29.1 (2002), pp. 561–568. DOI: `10.1016/S1540-7489(02)80072-4` (cited on page 45).

Macian, V., Bermúdez, V., Payri, R., and Gimeno, J. "New technique for determination of internal geometry of a Diesel nozzle with the use of silicone methodology". In: *Experimental Techniques* 27.April (2003), pp. 39–43. DOI: `10.1111/j.1747-1567.2003.tb00107.x` (cited on page 95).

Malbois, P. et al. "Experimental Investigation With Optical Diagnostics of a Lean-Premixed Aero-Engine Injection System Under Relevant Operating Conditions". In: *ASME Turbo Expo 2017*. Vol. 4B. Charlotte, North Carolina: American Society of Mechanical Engineers, 2017. DOI: `10.1115/GT2017-64484` (cited on page 69).

Manin, J., Bardi, M., Pickett, L., Dahms, R., and Oefelein, J. "Microscopic investigation of the atomization and mixing processes of diesel sprays injected into high pressure and temperature environments". In: *Fuel* 134 (2014), pp. 531–543. DOI: `10.1016/j.fuel.2014.05.060` (cited on page 103).

Manin, J., Bardi, M., and Pickett, L. M. "Evaluation of the liquid length via diffused back-illumination imaging in vaporizing diesel sprays". In: *The Proceedings of the International symposium on diagnostics and modeling of combustion in internal combustion engines*. Fukuoka, 2012, pp. 665–673 (cited on page 111).

Manin, J., Pickett, L. M., and Skeen, S. A. "Toward quantitative spray measurements using high-performance high-speed video cameras". In: *ILASS Americas 2016* (2016), pp. 511–518 (cited on page 111).

Manin, J., Skeen, S. A., and Pickett, L. M. "Two-color diffused back-illumination imaging as a diagnostic for time-resolved soot measurements in reacting sprays". In: *SAE Int. J. Engines* 6.4 (2013), pp. 1908–1921. DOI: 10.4271/2013-01-2548 (cited on page 109).

Mansour, M. S., Alkhesho, I., and Chung, S. H. "Stabilization and structure of n-heptane flame on CWJ-spray burner with kHZ SPIV and OH-PLIF". In: *Experimental Thermal and Fluid Science* 73 (2016), pp. 18–26. DOI: 10.1016/j.expthermflusci.2015.08.019 (cited on page 125).

Manzello, S. L. et al. "The burning of large n-heptane droplets in microgravity". In: *Proceedings of the Combustion Institute* 28.1 (2000), pp. 1079–1086. DOI: 10.1016/S0082-0784(00)80317-3 (cited on page 56).

Marchal, C. "Modélisation de la formation et de l'oxydation des suies dans un moteur automobile". PhD thesis. 2009, pp. 1–177 (cited on page 56).

Marchese, A., Dryer, F., and Nayaman, V. "Numerical modeling of isolated n-alkane droplet flames: initial comparisons with ground and space-based microgravity experiments". In: *Combustion and Flame* 116.3 (1999), pp. 432–459. DOI: 10.1016/S0010-2180(98)00109-6 (cited on page 56).

Marley, S. K., Lyons, K. M., and Watson, K. A. "Leading-Edge Reaction Zones in Lifted-Jet Gas and Spray Flames". In: *Flow, Turbulence and Combustion* 72.1 (2004), pp. 29–47. DOI: 10.1023/B:APPL.0000014906.91990.4e (cited on page 72).

Marley, S. K., Welle, E. J., Lyons, K. M., and Roberts, W. L. "Effects of leading edge entrainment on the double flame structure in lifted ethanol spray flames". In: *Experimental Thermal and Fluid Science* 29.1 (2004), pp. 23–31. DOI: 10.1016/j.expthermflusci.2004.01.009 (cited on page 72).

Marmottant, P. and Villermaux, E. "On spray formation". In: *Journal of Fluid Mechanics* 498.498 (2004), pp. 73–111. DOI: 10.1017/S0022112003006529 (cited on page 36).

Marrero-Santiago, J. et al. "Experimental study of aeronautical ignition in a swirled confined jet-spray burner". In: *ASME. J. Eng. Gas Turbines Power*. Vol. 140. American Society of Mechanical Engineers (ASME), 2017, pp. 1–14. DOI: 10.1115/GT2017-64476 (cited on page 77).

Marrero-Santiago, J. et al. "Spray Ignition and Local Flow Properties in a Swirled Confined Spray-Jet Burner: Experimental Analysis". In: *ILASS-Europe 2017, 28th Conference on Liquid Atomization and Spray Systems*. Valencia (Spain), 2017. DOI: 10.4995/ILASS2017.2017.4674 (cited on page 77).

Masri, A. R. and Gounder, J. D. "Turbulent spray flames of acetone and ethanol approaching extinction". In: *Combustion Science and Technology* 182.7 (2010), pp. 702–715. DOI: 10.1080/00102200903467754 (cited on page 73).

Massot, M., Kumar, M., Smooke, M. D., and Gomez, A. "Spray counterflow diffusion flames of heptane: Experiments and computations with detailed kinetics and transport". In: *Symposium (International) on Combustion.* Vol. 27. 2. Elsevier, 1998, pp. 1975–1983. DOI: 10.1016/S0082-0784(98)80042-8 (cited on page 73).

Mcenally, C. S. and Pfefferle, L. D. "Improved sooting tendency measurements for aromatic hydrocarbons and their implications for naphthalene formation pathways". In: *Combustion and Flame* 148 (2007), pp. 210–222. DOI: 10.1016/j.combustflame.2006.11.003 (cited on page 177).

McKinney, R. G., Sepulveda, D., Sowa, W., and Cheung, A. K. "The Pratt & Whitney TALON X low emissions combustor: Revolutionary results with evolutionary technology". In: *Collection of Technical Papers - 45th AIAA Aerospace Sciences Meeting.* Vol. 7. 2007, pp. 4697–4704. DOI: 10.2514/6.2007-386 (cited on page 21).

Mikami, M., Niwa, M., Kato, H., Sato, J., and Kono, M. "Clarification of the flame structure of droplet burning based on temperature measurement in microgravity". In: *Symposium (International) on Combustion* 25.1 (1994), pp. 439–446. DOI: 10.1016/S0082-0784(06)80672-7 (cited on page 56).

Miller, R., Harstad, K., and Bellan, J. "Evaluation of equilibrium and non-equilibrium evaporation models for many-droplet gas-liquid flow simulations". In: *International Journal of Multiphase Flow* 24.6 (1998), pp. 1025–1055. DOI: 10.1016/S0301-9322(98)00028-7 (cited on pages 45–47).

Mitra, T., Zhang, T., Sediako, A. D., and Thomson, M. J. "Understanding the formation and growth of polycyclic aromatic hydrocarbons (PAHs) and young soot from n-dodecane in a sooting laminar coflow diffusion flame". In: *Combustion and Flame* 202 (2019), pp. 33–42. DOI: 10.1016/j.combustflame.2018.12.010 (cited on page 58).

Myers, G. D. and Lefebvre, A. H. "Flame propagation in heterogeneous mixtures of fuel drops and air". In: *Combustion and Flame* 66.2 (1986), pp. 193–210. DOI: 10.1016/0010-2180(86)90091-X (cited on pages 159, 161, 165–167).

Naik, C. V. et al. "Detailed chemical kinetic mechanism for surrogates of alternative jet fuels". In: *Combustion and Flame* 158.3 (2011), pp. 434–445. DOI: 10.1016/j.combustflame.2010.09.016 (cited on page 131).

Neophytou, A. and Mastorakos, E. "Simulations of laminar flame propagation in droplet mists". In: *Combustion and Flame* 156 (2009), pp. 1627–1640. DOI: 10.1016/j.combustflame.2009.02.014 (cited on page 167).

Nonnenmacher, S. and Piesche, M. "Design of hollow cone pressure swirl nozzles to atomize Newtonian fluids". In: *Chemical Engineering Science* 55.19 (2000), pp. 4339–4348. DOI: 10.1016/S0009-2509(00)00043-9 (cited on page 14).

O'Rourke, P. J. and Amsden, A. A. "The tab method for numerical calculation of spray droplet breakup". In: *SAE Technical Papers*. SAE International, 1987, pp. 1–10. DOI: 10.4271/872089 (cited on page 45).

Olson, D. B., Pickens, J. C., and Gill, R. J. "The effects of molecular structure on soot formation II. Diffusion flames". In: *Combustion and Flame* 62.1 (1985), pp. 43–60. DOI: 10.1016/0010-2180(85)90092-6 (cited on pages 177, 178).

Orain, M. and Hardalupas, Y. "Influence du combustible sur la mesure de richesse par chimiluminescence dans les flammes prémélangées". In: *Comptes Rendus - Mecanique* 338.5 (2010), pp. 241–254. DOI: 10.1016/j.crme.2010.05.002 (cited on page 113).

Panoutsos, C. S., Hardalupas, Y., and Taylor, A. M. "Numerical evaluation of equivalence ratio measurement using OH* and CH* chemiluminescence in premixed and non-premixed methane-air flames". In: *Combustion and Flame* 156.2 (2009), pp. 273–291. DOI: 10.1016/j.combustflame.2008.11.008 (cited on page 113).

Park, H. and Heister, S. D. "Nonlinear simulation of free surfaces and atomization in pressure swirl atomizers". In: *Physics of Fluids* 18.052103 (2006), pp. 1–11. DOI: 10.1063/1.2197876 (cited on page 14).

Pastor, J. V., Garcia-Oliver, J. M., Novella, R., and Xuan, T. "Soot Quantification of Single-Hole Diesel Sprays by Means of Extinction Imaging". In: *SAE International Journal of Engines* 8.5 (2015), pp. 2068–2077. DOI: 10.4271/2015-24-2417 (cited on page 109).

Payri, R., Bracho, G., Gimeno, J., and Moreno, A. "Spray Characterization of the Urea-Water Solution (UWS) Injected in a Hot Air Stream Analogous to SCR System Operating Conditions". In: *WCX SAE World Congress Experience*. 1. 2019, pp. 1–9. DOI: 10.4271/2019-01-0738 (cited on page 103).

Payri, R., Bracho, G., Martí-Aldaraví, P., and Viera, A. "Nozzle geometry size influence on reactive spray development: from Spray B to heavy duty applications". In: *SAE Technical Paper 2017-01-0846*. 2017, pp. 1–12. DOI: `10.4271/2017-01-0846` (cited on page 114).

Payri, R., Gimeno, J., Cardona, S., and Ayyapureddi, S. "Measurement of Soot Concentration in a Prototype Multi-Hole Diesel Injector by High-Speed Color Diffused Back Illumination Technique". In: *SAE Technical Paper 2017-01-2255*. 2017, pp. 1–11. DOI: `10.4271/2017-01-2255` (cited on page 109).

Payri, R., Gimeno, J., Cardona, S., and Ayyapureddi, S. "Experimental study of the influence of the fuel and boundary conditions over the soot formation in multi-hole diesel injectors using high-speed color diffused back-illumination technique". In: *Applied Thermal Engineering* 158.113746 (2019), pp. 1–16. DOI: `10.1016/J.APPLTHERMALENG.2019.113746` (cited on pages 174, 176).

Payri, R., Salvador, F. J., Gimeno, J., and Cardona, S. "Experimental study of the influence of the boundary conditions on the atomization process in an unconfined atmospheric burner". In: *ILASS-Europe*. Paris, France, 2019, pp. 1–9 (cited on page 158).

Payri, R., Salvador, F. J., Manin, J., and Viera, A. "Diesel ignition delay and lift-off length through different methodologies using a multi-hole injector". In: *Applied Energy* 162 (2016), pp. 541–550. DOI: `10.1016/j.apenergy.2015.10.118` (cited on pages 114, 162).

Payri, R., Viera, J. P., Pei, Y., and Som, S. "Experimental and numerical study of lift-off length and ignition delay of a two-component diesel surrogate". In: *Fuel* 158 (2015), pp. 957–967. DOI: `10.1016/j.fuel.2014.11.072` (cited on page 114).

PETERS, N. "The turbulent burning velocity for large-scale and small-scale turbulence". In: *Journal of Fluid Mechanics* 384 (1999), pp. 107–132. DOI: `10.1017/S0022112098004212` (cited on page 50).

Peters, N. *Turbulent Combustion*. Cambridge University Press, 2000. DOI: `10.1017/CBO9780511612701` (cited on page 49).

Pickett, L. M., Siebers, D. L., and Idicheria, C. A. "Relationship Between Ignition Processes and the Lift-Off Length of Diesel Fuel Jets". In: *SAE Paper*. 724. 2005, pp. 1–18. DOI: `10.4271/2005-01-3843` (cited on pages 162, 174).

Pickett, L. M. and Siebers, D. L. "Soot formation in diesel fuel jets near the lift-off length". In: *International Journal of Engine Research* 7.2 (2006), pp. 103–130. DOI: `10.1243/146808705X57793` (cited on page 174).

Pilch, M. and Erdman, C. A. "Use of breakup time data and velocity history data to predict the maximum size of stable fragments for acceleration-induced breakup of a liquid drop". In: *International Journal of Multiphase Flow* 13.6 (1987), pp. 741–757. DOI: `10.1016/0301-9322(87)90063-2` (cited on page 39).

Pittermann, R. "Spectroscopic Analysis of the Combustion in Diesel and Gas Engines". In: *MTZ worldwide* 69.7 (2008), pp. 66–73. DOI: `doi.org/10.1007/BF03227907` (cited on page 114).

Poinsot, T. and Veynante, D. *Theoretical and numerical combustion*. 2005 (cited on page 49).

Prasad, A. K., Adrian, R., Landreth, C. C., and Offutt, P. W. "Effect of resolution on the speed and accuracy of particle image velocimetry interrogations". In: *Experiments in Fluids* 13 (1990), pp. 105–116 (cited on page 101).

Prevish, T. D. and Santavicca, D. A. "Turbulent breakup of hydrocarbon droplets at elevated pressures". In: *ILASS Americas, 11th annual conference on liquid atomization and spray systems*. Sacramento, CA, 1998, pp. 1–9 (cited on page 40).

Prieto, L. M. P. "CFD Modeling of Combustion and Soot Production in". PhD thesis. UPV, 2020, pp. 1–157 (cited on pages 58, 59).

Radcliffe, A. "Section D. Fuel Injection". In: *Design and Performance of Gas Turbine Power Plants*. Princeton University Press, 2015, pp. 92–118. DOI: `10.1515/9781400875603-008` (cited on pages 142, 147).

Raffel, M. et al. *Particle Image Velocimetry*. Cham: Springer International Publishing, 2018, pp. 1–664. DOI: `10.1007/978-3-319-68852-7` (cited on page 101).

Rayleigh, L. "On The Instability Of Jets". In: *Proceedings of the London Mathematical Society* s1-10.1 (1878), pp. 4–13. DOI: `10.1112/plms/s1-10.1.4` (cited on page 33).

Reddy, V. M., Trivedi, D., and Kumar, S. "Experimental investigations on lifted spray flames for a range of coflow conditions". In: *Combustion Science and Technology* 184.1 (2012), pp. 44–63. DOI: `10.1080/00102202.2011.615770` (cited on pages 72, 140, 157–159, 162, 163).

Reitz, R. D. *Atomization and other breakup regimes of a liquid jet.* Princeton University, 1978 (cited on page 34).

Reveillon, J. and Vervisch, L. "Analysis of weakly turbulent dilute-spray flames and spray combustion regimes". In: *J. Fluid Mech* 537 (2005), pp. 317–347. DOI: 10.1017/S0022112005005227 (cited on pages 55, 160).

Réveillon, J. and Vervisch, L. "Partially Premixed Combustion in Spray Flames". In: *18th International Colloquium on The Dynamics of Explosions and Reactive Systems.* 2001, pp. 1–5 (cited on page 160).

Rosin, P. and Rammler, E. "The Laws Governing the Fineness of powdered coal". In: *Journal of the Institute of Fuel* 7 (1933), pp. 29–36 (cited on page 42).

Samuelsen, G. S., Brouwer, J., Vardakas, M. A., and Holdeman, J. D. "Experimental and modeling investigation of the effect of air preheat on the formation of NOx in an RQL combustor". In: *Heat and Mass Transfer/Waerme- und Stoffuebertragung* 49.2 (2013), pp. 219–231. DOI: 10.1007/s00231-012-1080-0 (cited on page 19).

Sánchez, A. L., Urzay, J., and Liñán, A. "The role of separation of scales in the description of spray combustion". In: *Proceedings of the Combustion Institute* 35.2 (2015), pp. 1549–1577. DOI: 10.1016/j.proci.2014.08.018 (cited on page 30).

Santiago, J. M. "Experimental study of lean aeronautical ignition. Impact of critical parameters on the mechanisms acting along the different ignition phases." PhD thesis. 2018, pp. 1–215 (cited on page 78).

Schmidt, D. P. et al. "Pressure-swirl atomization in the near field". In: *SAE Technical Papers.* SAE International, 1999. DOI: 10.4271/1999-01-0496 (cited on page 150).

Schneider, D. et al. "A new test rig for laser optical investigations of lean jet engine burners". In: *27th Congress of the International Council of the Aeronautical Sciences 2010, ICAS 2010.* Vol. 4. 2010, pp. 2667–2676 (cited on page 70).

Schuetz, C. A. and Frenklach, M. "Nucleation of soot: Molecular dynamics simulations of pyrene dimerization". In: *Proceedings of the Combustion Institute* 29.2 (2002), pp. 2307–2314. DOI: 10.1016/S1540-7489(02)80281-4 (cited on page 58).

Senecal, P. K. et al. "Modeling high-speed viscous liquid sheet atomization". In: *International Journal of Multiphase Flow* 25.6-7 (1999), pp. 1073–1097. DOI: 10.1016/S0301-9322(99)00057-9 (cited on page 150).

Seyfried, H. et al. "Optical diagnostics applied to a gas turbine pilot burner". In: *AIAA Journal* 45.11 (2007), pp. 2702–2709. DOI: 10.2514/1.30032 (cited on page 70).

Shaw, B., Dryer, F., Williams, F., and Haggard, J. "Sooting and disruption in spherically symmetrical combustion of decane droplets in air". In: *Acta Astronautica* 17.11-12 (1988), pp. 1195–1202. DOI: 10.1016/0094-5765(88)90008-2 (cited on page 56).

Shum-Kivan, F. et al. "Experimental and numerical analysis of a turbulent spray flame structure". In: *Proceedings of the Combustion Institute* 36.2 (2017), pp. 2567–2575. DOI: 10.1016/j.proci.2016.06.039 (cited on pages 126, 133).

Sidey, J. A. M., Giusti, A., Benie, P., and Mastorakos, E. *The Swirl Flames Data Repository* (cited on page 77).

Siebers, D. L. "Liquid-Phase Fuel Penetration in Diesel Sprays". In: *SAE Technical Paper*. 1998, pp. 1–23. DOI: 10.4271/980809 (cited on page 116).

Siegmann, K., Sattler, K., and Siegmann, H. "Clustering at high temperatures: carbon formation in combustion". In: *Journal of Electron Spectroscopy and Related Phenomena* 126.1-3 (2002), pp. 191–202. DOI: 10.1016/S0368-2048(02)00152-4 (cited on page 58).

Skeen, S. A., Manin, J., Dalen, K., and Pickett, L. M. "Extinction-based Imaging of Soot Processes over a Range of Diesel Operating Conditions". In: *8th US National Combustion Meeting*. Utah, USA, 2013, pp. 1–13 (cited on page 109).

Squires, K. D. and Eaton, J. K. "Particle response and turbulence modification in isotropic turbulence". In: *Physics of Fluids A: Fluid Dynamics* 2.7 (1990), pp. 1191–1203. DOI: 10.1063/1.857620 (cited on page 49).

Stanmore, B. R., Brilhac, J. F., and Gilot, P. "The oxidation of soot: a review of experiments, mechanisms and models". In: *Carbon* 39.15 (2001), pp. 2247–2268. DOI: 10.1016/S0008-6223(01)00109-9 (cited on page 59).

Stårner, S. H., Gounder, J., and Masri, A. R. "Effects of turbulence and carrier fluid on simple, turbulent spray jet flames". In: *Combustion and Flame* 143.4 (2005), pp. 420–432. DOI: 10.1016/j.combustflame.2005.08.016 (cited on pages 73, 74).

Sunderland, P. and Faeth, G. "Soot formation in hydrocarbon/air laminar jet diffusion flames". In: *Combustion and Flame* 105.1-2 (1996), pp. 132–146. DOI: 10.1016/0010-2180(95)00182-4 (cited on page 59).

Syred, N. and Beér, J. M. "Combustion in swirling flows: A review". In: *Combustion and Flame* 23.2 (1974), pp. 143–201. DOI: `10.1016/0010-2180(74)90057-1` (cited on page 22).

Tabor, G. *Combustion regimes* (cited on page 17).

Tacina, R., Cai, J., and Jeng, S.-M. "The Structure of a Swirl-Stabilized Reacting Spray Issued from an Axial Swirler". In: *43rd AIAA Aerospace Sciences Meeting & Exhibit.* January. 2005, pp. 1–14 (cited on pages 76, 78–80, 83).

TCS. *Workshop on Measurement and Computation of Turbulent Spray Combustion.* 2015 (cited on page 73).

Thielicke, W. and Sonntag, R. "Particle Image Velocimetry for MATLAB: Accuracy and enhanced algorithms in PIVlab". In: *Journal of Open Research Software* 9 (2021), pp. 1–14. DOI: `10.5334/JORS.334` (cited on page 100).

Tratnig, A. and Brenn, G. "Drop size spectra in sprays from pressure-swirl atomizers". In: *International Journal of Multiphase Flow* 36.5 (2010), pp. 349–363. DOI: `10.1016/j.ijmultiphaseflow.2010.01.008` (cited on page 147).

Turns, S. R. *An introduction to combustion: concepts and applications.* 2000, p. 752 (cited on pages 183, 184).

Verdier, A. "Experimental study of dilute spray combustion". PhD thesis. Normandie Université, 2018, pp. 1–175 (cited on pages 12, 30, 47, 52, 125).

Verdier, A. et al. "Experimental study of local flame structures and fuel droplet properties of a spray jet flame". In: *Proceedings of the Combustion Institute* 36.2 (2017), pp. 2595–2602. DOI: `10.1016/j.proci.2016.07.016` (cited on page 73).

Verdier, A. et al. "Local extinction mechanisms analysis of spray jet flame using high speed diagnostics". In: *Combustion and Flame* 193 (2018), pp. 440–452. DOI: `10.1016/j.combustflame.2018.03.032` (cited on pages 73, 74).

Verma, S. and Basu, S. *Application of Inverse Abel Transform on flame image.* Tech. rep. Indian Institute of Science (cited on page 115).

Veshkini, A., Eaves, N. A., Dworkin, S. B., and Thomson, M. J. "Application of PAH-condensation reversibility in modeling soot growth in laminar premixed and nonpremixed flames". In: *Combustion and Flame* 167 (2016), pp. 335–352. DOI: `10.1016/j.combustflame.2016.02.024` (cited on page 58).

Violi, A., Sarofim, A. F., and Voth, G. A. "Kinetic monte carlo-molecular dynamics approach to model soot inception". In: *Combustion Science and Technology*. Vol. 176. 5-6. Taylor and Francis Inc., 2004, pp. 991–1005. DOI: 10.1080/00102200490428594 (cited on page 58).

Wang, H. "Formation of nascent soot and other condensed-phase materials in flames". In: *Proceedings of the Combustion Institute* 33.1 (2011), pp. 41–67. DOI: 10.1016/j.proci.2010.09.009 (cited on pages 55, 58).

Wang, H. et al. "A comparison study on the combustion and sooting characteristics of base engine oil and n-dodecane in laminar diffusion flames". In: *Applied Thermal Engineering* 158.113812 (2019), pp. 1–6. DOI: 10.1016/j.applthermaleng.2019.113812 (cited on page 58).

Wang, Y. and Chung, S. H. "Soot formation in laminar counterflow flames". In: *Progress in Energy and Combustion Science* 74 (2019), pp. 152–238. DOI: 10.1016/j.pecs.2019.05.003 (cited on pages 56–59, 173, 174, 177).

Warnatz, J., Maas, U., and Dibble, R. W. *Combustion: Physical and chemical fundamentals, modeling and simulation, experiments, pollutant formation.* Springer Berlin Heidelberg, 2006, pp. 1–378. DOI: 10.1007/978-3-540-45363-5 (cited on pages 56, 57, 59).

Wei, X. and Yong, H. "Improved Semiempirical Correlation to Predict Sauter Mean Diameter for Pressure-Swirl Atomizers". In: *Journal of Propulsion and Power* 30.6 (2014), pp. 1628–1635. DOI: 10.2514/1.B35238 (cited on page 147).

Willert, C. E. and Gharib, M. "Digital particle image velocimetry". In: *Experiments in Fluids* 10.4 (1991), pp. 181–193. DOI: 10.1007/BF00190388 (cited on page 101).

Willert, C. et al. "Combined PIV and DGV applied to a pressurized gas turbine combustion facility". In: *Measurement Science and Technology* 17.7 (2006), pp. 1670–1679. DOI: 10.1088/0957-0233/17/7/005 (cited on pages 78, 79, 83).

Xu, F., Sunderland, P. B., and Faeth, G. M. "Soot formation in laminar premixed ethylene/air flames at atmospheric pressure". In: *Combustion and Flame* 108.4 (1997), pp. 471–493. DOI: 10.1016/S0010-2180(96)00200-3 (cited on page 173).

Xu, Y. and Lee, C.-f. F. "Forward-illumination light-extinction technique for soot measurement". In: *Applied Optics* 45.9 (2006), pp. 2046–2057. DOI: 10.1364/AO.45.002046 (cited on page 173).

Yao, G. F., Abdel-Khalik, S. I., and Ghiaasiaan, S. M. "An investigation of simple evaporation models used in spray simulations". In: *Journal of Heat Transfer* 125.1 (2003), pp. 179–182. DOI: 10.1115/1.1517267 (cited on page 46).

Yeganeh, M. G. "Effects of preheated combustion air on laminar coflow diffusion flames under normal and microgravity conditions". PhD thesis. University of Maryland, College Park, 2005 (cited on page 176).

Yuan, R., Kariuki, J., Dowlut, A., Balachandran, R., and Mastorakos, E. "Reaction zone visualisation in swirling spray n-heptane flames". In: *Proceedings of the Combustion Institute* 35.2 (2015), pp. 1649–1656. DOI: 10.1016/j.proci.2014.06.012 (cited on page 76).

Yuen, M. C. and Chen, L. W. "On Drag of Evaporating Liquid Droplets". In: *Combustion Science and Technology* 14.4-6 (1976), pp. 147–154. DOI: 10.1080/00102207608547524 (cited on page 45).

Zonta, F., Marchioli, C., and Soldati, A. "Direct numerical simulation of turbulent heat transfer modulation in micro-dispersed channel flow". In: *Acta Mechanica* 195.1-4 (2008), pp. 305–326. DOI: 10.1007/s00707-007-0552-7 (cited on page 49).